Mahoney, J.J., Fitton, J.G., Wallace, P.J., et al., 2001
Proceedings of the Ocean Drilling Program, Initial Reports Volume 192

3. Site 1183[1]

Shipboard Scientific Party[2]

BACKGROUND AND OBJECTIVES

Site 1183 is near the crest of the Ontong Java Plateau's main or high plateau (Fig. F1), 183 km west-southwest of Deep Sea Drilling Project (DSDP) Site 289. We chose this site because it is in the shallowest region of the high plateau, where the upper crust is thickest but the sediment cover is relatively thin (1130 m). This broad region is where the lava pile of the high plateau originally may have been shallowest and eruptive activity may have been the greatest. Given its central location, the compositional range of basement lavas here might be greater than in previously studied areas located much closer to the margins of the plateau (Malaita, Santa Isabel, Sites 803 and 807). Also, a distinctive sediment package appears above the acoustic basement in this vicinity that might correspond to shallower water deposits than those found elsewhere on the high plateau.

Geophysical Background

The site is located on multichannel seismic (MCS) reflection Line 404 of the *Hakuho Maru* cruise KH98-1, Leg 2, ~18 km east of the intersection of this line with Line 501 (Figs. F2, F3). It lies at a water depth of ~1805 m (drill pipe measurement) in a relatively simple structural setting with coherent basement and no major basement faults nearby (Figs. F4, F5). The 3.5-kHz record shows that the seafloor is rough in places, suggesting a high-energy sedimentary environment. The sedimentary section is interpreted to lie between the seafloor, at 2.4-s two-way traveltime (TWT), and the top of a high-amplitude, continuous reflection at 3.4-s TWT; this section is characterized by parallel to subparallel reflections of high continuity (Figs. F4, F5). Reflection amplitudes are medium to high, and frequency is high. An upper sedimentary megasequence (2.4–3.2 s TWT) appears to be mainly a pelagic drape

F1. Ontong Java Plateau bathymetry, with site locations, p. 44.

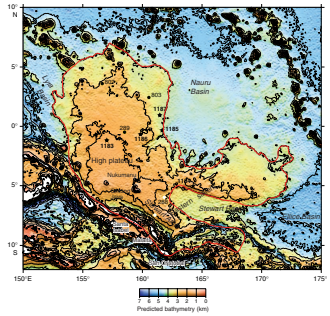

F2. Free-air gravity map of Ontong Java Plateau region, p. 45.

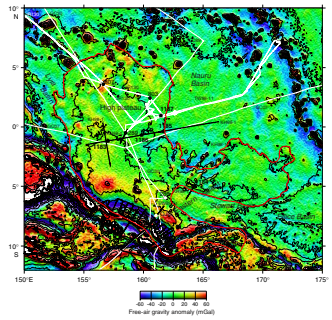

F3. Site 1183 location and site-survey data, p. 46.

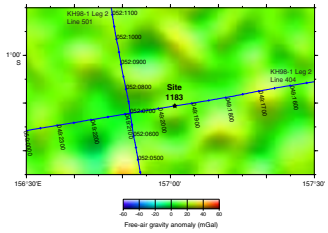

F4. MCS reflection profile, p. 47.

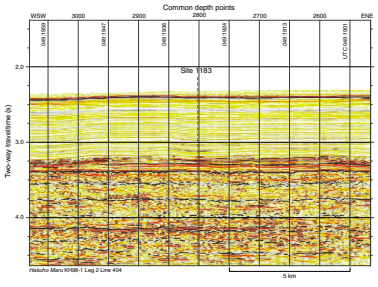

[1]Examples of how to reference the whole or part of this volume.
[2]Shipboard Scientific Party addresses.

that exhibits some differential compaction. A lower sedimentary sequence (3.2–3.4 s TWT) varies significantly in thickness and is cut and thinned by a prominent angular unconformity ~7 km west of Site 1183. This unconformity and variations in reflection amplitude, continuity, and configuration within the lower megasequence suggest a dynamic, perhaps relatively shallow-water, paleoenvironment. The top of acoustic basement is characterized by medium- to high-amplitude moderately discontinuous reflections, and some intrabasement reflections are visible. Seismic structure studies of the entire crust and uppermost mantle employing ocean-bottom seismometer data along MCS lines 404 and 501 are in progress, and preliminary results have been reported by Araki et al. (1998) and Mochizuki et al. (1998).

F5. Close-up of Site 1183 vicinity, p. 48.

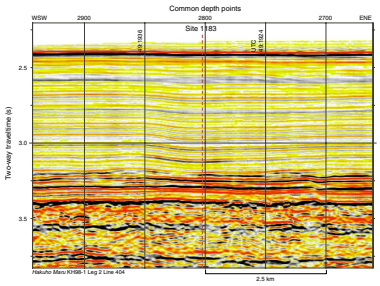

Summary of Objectives

The main objectives at this site were to determine

1. Compositions of basement rocks and compare them with those of basement lavas exposed in Malaita and Santa Isabel and drilled at DSDP Site 289 and Ocean Drilling Program (ODP) Sites 803 and 807;
2. Ages of basement and basal sedimentary rocks to help test the hypothesis that magmatism in most of the high plateau ceased soon after 122 Ma, the age of basement at Site 807 and in Malaita and parts of Santa Isabel;
3. Physical volcanology of basement lavas, the nature of sedimentary interbeds, and the characteristics of basal sedimentary layers in order to deduce the eruptive environment (flow types and approximate depths of eruption);
4. Early subsidence history, as recorded in the basement lava pile and the overlying sedimentary succession;
5. Ages of sequence boundaries observed in the seismic record; and
6. Rates of Cretaceous environmental change as recorded in the sedimentary record.

OPERATIONS

Transit to Site 1183

At 2048 hr on 13 September 2000 the *JOIDES Resolution* departed Guam and began the transit to Site 1183. Calm seas, mild weather, and the absence of any significant currents contributed to better-than-expected speed during the voyage. The 2141-km transit was accomplished at an average speed of 11.1 kt. At 0615 hr on 18 September we deployed a beacon at the Global Positioning System (GPS) coordinates for Site 1183.

Hole 1183A

The planned operational scenario for Site 1183 was for two holes. The first hole was to be a pilot hole drilled and cored to bit destruction; the second was to be a double-cased reentry hole. The purpose of the pilot hole was to determine the amount of 16-in and 10.75-in casing to be deployed in the second hole. The bit tagged the seafloor at 1804.7 meters below sea level (mbsl) and was observed with the vibration-

isolated television (VIT) system. We began a jet-in test at 1700 hr on 18 September and concluded it by 1900 hr. After completing the jet-in test, we washed ahead through the sediment with a core barrel in place to a depth of 328.0 meters below seafloor (mbsf). After recovering the wash barrel, we dropped another core barrel and initiated coring in Hole 1183A at 0300 hr on 19 September. Coring advanced from 328.0 to 452.7 mbsf with 58.6% average recovery. The material recovered from this interval suggested that ~430 m of 10.75-in casing would be appropriate in the cased reentry hole.

We drilled the interval from 452.7 to 752.0 mbsf without coring, using a center bit fitted in the rotary bit. The 299.3-m interval was drilled at an average rate of penetration of 35.4 m/hr with no drilling problems. We then rotary cored Hole 1183A continuously from 752.0 to 1160.6 mbsf. At 1130.4 mbsf we contacted basaltic basement. The average recovery within basement from 1130.4 to 1160.6 mbsf was 60% with an average rate of penetration of 1.2 m/hr.

After the bit had accumulated 59.2 rotating hours, we had to decide whether to deepen the pilot hole using a free-fall funnel (FFF) or terminate Hole 1183A and start the reentry site emplacement in Hole 1183B. After considering the risks entailed by using a FFF, the considerable time and resources needed to set a reentry cone and ~430 m of casing, and, particularly, the excellent hole conditions thus far in Hole 1183A, we decided to attempt to achieve the depth objectives with the pilot hole and forego the reentry hole. We deployed a FFF with three floats, and we used the VIT to observe the FFF during extraction of the drill string from the hole. The bit was smoothly withdrawn from the FFF, after which we recovered the VIT and retrieved the drill string. The worn bit, an RBI C-4 coring bit, was replaced with a harder-formation C-7 bit, and we deployed the drill string and positioned it over the FFF. After a 30-min search, we reentered Hole 1183A at 1900 hr on 24 September. The operation was complicated because the FFF had settled into the sediment, and effluent emanating from the hole obscured the funnel and the glass floats marking the position of the hole. Following the recovery of the VIT, we lowered the drill string to 519.7 mbsf, where it encountered a constriction, suggesting that this part of the hole was closing. We picked up the top drive, and we washed and reamed the hole from 442.5 to 577.4 mbsf. After clearing the tight spots in the hole, we set back the top drive and lowered the drill string to bottom. There was ~2 m of soft fill at the bottom of the hole.

We resumed rotary coring in Hole 1183A at 0530 hr on 25 September, and we advanced from 1160.6 to 1211.1 mbsf at an average rate of penetration of 1.2 m/hr. The average recovery for this interval was 54%. To reduce the chances of the core jamming in the liner, we used no liners and employed a sleeveless core catcher. After the bit had accumulated 44.1 rotating hours, we decided to make another bit change. After circulating a 50-bbl sepiolite mud flush, we pulled back the drill string to 318 mbsf, where we injected a 50-bbl solution of 10.5 lb/gal mud. The heavy mud was to serve as a density cap to prevent effluent exiting the FFF and complicating reentry operations.

We recovered the drill string and replaced the worn bit with a new, harder formation RBI C-9 coring bit. While lowering the drill string, we also launched the VIT and ran it down for the reentry. At 0558 hr on 28 September we reentered Hole 1183A after a 20-min search for the FFF. The FFF was not visible, but we could clearly see the circular sediment pond formed from hole cuttings. The spotting of heavy mud at the top of the hole appeared to have prevented material from the hole from

venting to the water column and obscuring the visibility, as happened during the first reentry.

We lowered the drill pipe to 202 mbsf, where progress was prevented by increasing hole drag. We recovered the VIT and picked up the top drive. After dropping a wash barrel, we washed and reamed the hole in an attempt to work past the tight section. However, the tight hole conditions did not improve. From 0815 hr on 28 September to 0530 hr on 29 September, we advanced the bit to 953 mbsf, where the penetration rate slowed dramatically. We recovered the wash barrel and dropped a center bit to drill ahead through the obstruction. We made no further progress and terminated operations in the hole. We deployed the wireline to recover the center bit, but a failed pin connection on the bottom inner barrel prevented the retrieval of the center bit, inner barrel sub, and landing sub, which remained in the bottom-hole assembly (BHA).

During the washing and reaming of the hole, the relatively rapid rate of advance compared with the rate of coring over the same depth interval strongly suggested that the bit was in the original hole and not drilling a new hole. The drillers commented that it felt as if there was something being pushed ahead of the bit as they tried to advance to 1211 mbsf. We terminated attempts at getting to the bottom 258 m short of the bottom of the hole. We retrieved the drill string with no noticeable resistance experienced on the way out of the hole. Inspection of the bit showed an unusual amount of wear on the tungsten carbide inserts on the nose of each of the cones. After recovering the beacon and retracting the thrusters and hydrophones, we began the transit to Site 1184 at 1430 hr on 30 September 2000.

During operations at Hole 1183A, we cored 583.8 m of sediment and basement (Tables T1, T2) with 260.7 m recovered (44.7% average recovery). An additional 627.3 m of sediment was washed and drilled. In basement, we cored ~80.7 m of basalt and recovered a total of 44.2 m (54.8%).

T1. Site 1183 coring summary, p. 139.

T2. Expanded coring summary, p. 140.

LITHOSTRATIGRAPHY

Overview

We cored the sedimentary sequence at Site 1183 from 328.0 to 452.7 mbsf and from 752 mbsf to basement at 1130.4 mbsf. Aptian through Miocene sediment at Site 1183 is composed of foraminifers and calcareous nannofossils with variable amounts of chert and volcaniclastic material. Bioturbation is pervasive. Diagenetic changes include progressive pressure-solution lithification, partial silicification and chert formation, and redox-mediated migration (mobilization) of iron and manganese. The depositional record has at least two hiatuses of Late Cretaceous age that appear to be regional in extent.

The first section below summarizes the general features of each lithologic facies or subunit. The second section discusses the main trends in the sedimentation history. The third section reviews different interpretations of postdepositional diagenetic alteration.

F6. Lithostratigraphic summary, p. 49.

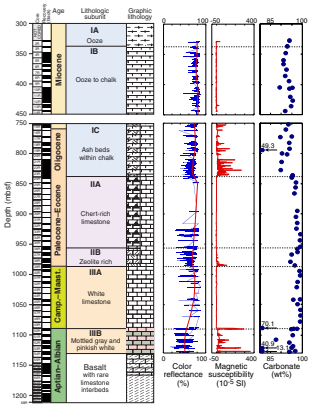

Unit and Subunit Descriptions

The sedimentary succession at Site 1183 is dominated by carbonate facies and was divided into three lithologic units with seven subunits (Fig. F6; Table T3) on the basis of the following criteria:

T3. Lithologic unit characteristics, p. 149.

1. Chalk-ooze transition (Subunit IA vs. IB);
2. Major influxes of volcanic material (Subunits IC and IIB and basement);
3. Significant chertification (Subunit IIA); and
4. Sediment color (Subunit IIIA vs. IIIB).

Stratigraphic divisions in the upper 950 m (middle Eocene–Miocene) generally parallel those used at DSDP Sites 289 and 586 and ODP Sites 803 and 807 on the main Ontong Java Plateau. This stratigraphic framework is also applied to Leg 192 Sites 1185, 1186, and 1187. Our subdivisions of the Cretaceous and Paleogene section at Site 1183 can be recognized in the approximately correlative sediments at DSDP Site 289 and ODP Site 807, where broader divisions were employed. This consistency suggests that these lithologic divisions represent regional trends in paleoceanography, volcaniclastic influxes, and diagenetic processes.

Unit I

Interval: 192-1183A-2R, 0 cm, through 24R-1, 43 cm
Depth: 328.0–838.6 mbsf
Age: Oligocene–Miocene
Lithology: foraminifer nannofossil chalk

Unit I consists predominantly of foraminifer nannofossil ooze to chalk. Priority given to basement basalt objectives, coupled with good recovery of a sedimentary succession in relatively nearby DSDP Sites 289 and 586, resulted in the decision to core only two portions of this thick unit at Site 1183. The ooze-to-chalk transition, which defines the transition between Subunits IA and IB, is at ~337.6 mbsf. The lowest subunit, Subunit IC, is characterized by volcanic ash beds within the chalk. Similar volcanic ash-rich horizons are in coeval sediments at Sites 289 and 807; therefore, our Subunit IC is a regionally recognizable interval. The contact between Subunits IB and IC was not cored in Hole 1183A.

Subunit IA

Interval: 192-1183A-2R-1, 0 cm, through 3R-1, 0 cm
Depth: 328.0–337.6 mbsf
Age: middle Miocene
Lithology: foraminifer nannofossil ooze

Hole 1183A was washed down to 328.0 mbsf, and Core 192-1183A-2R contained carbonate with an ooze texture. The ooze is white to bluish white and homogenized by bioturbation. Foraminifers and calcareous nannofossils have approximately equal abundance by volume, and there are lesser amounts of radiolarians, diatoms, and sponge spicules.

Overprinting the bioturbated texture are faint, colored, horizontal streaks at ~5-cm intervals. These color bands cut across burrows and are interpreted as diagenetic Liesegang banding. Darker patches, possibly of disseminated pyrite or ferromanganese oxide staining, are scattered throughout the ooze.

Subunit IB

Interval: 192-1183A-3R-1, 0 cm, through 14R-CC, 33 cm
Depth: 337.6–444.83 mbsf
Age: earliest Miocene–middle Miocene
Lithology: foraminifer nannofossil chalk

Subunit IB consists of foraminifer nannofossil chalk with minor amounts of siliceous microfossils and sponge spicules. The transition from ooze to chalk is between Cores 192-1183A-2R and 3R at 337.6 mbsf. We cored 115 m of Subunit IB (Cores 192-1183A-3R through 14R), but the underlying 300 m was drilled without coring. The sediment below the coring gap is also chalk but contains common volcanic ash–rich beds and is designated lithologic Subunit IC. The coring gap precludes precise designation of the boundary between "pure" chalk Subunit IB and underlying volcaniclastic-rich Subunit IC.

The chalk of Subunit IB ranges from white to bluish white to very light greenish gray. Carbonate ranges from 90 to 95 wt%, and the noncarbonate component is predominantly biogenic silica. The low magnetic susceptibility (Fig. F6) suggests that no significant volcaniclastic materials are present. Sediments are faintly mottled throughout, suggesting pervasive bioturbation. Discrete burrows include *Zoophycos* and *Planolites*. Mottling aside, color is relatively constant in Cores 192-1183A-3R through 9R. In contrast, Cores 192-1183A-10R through 14R (414–445 mbsf) display subtle color alternations from white to light green at ~75-cm spacing. Burrows in the upper portion of each color type are filled with sediment of the overlying color. Subunit IB contains abundant, thin, crosscutting color bands and streaks of green, blue, and purplish red (Fig. F7).

The lower half of Core 192-1183A-11R includes a thick (3.4 m), homogeneous interval without obvious burrows or color streaks. This interval is unique in having a uniform texture spanning almost 4 m. It appears to contain elongate white "clasts" or filled burrows (1–2 cm long) with a preferential dip of 30° to 45°, in addition to scattered, equant, white clasts. Shipboard biostratigraphy indicates that this bed overlies a hiatus between the early and the middle Miocene, but sedimentological evidence is inadequate to confirm a redeposition or slump origin. Core 192-1183A-12R has similar, but thinner, intervals that display partial bioturbation.

F7. Chalk with crosscutting laminae, Subunit IB, p. 50.

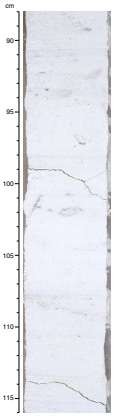

Subunit IC

Interval: 192-1183A-15R-1, 0 cm, through 24R-1, 43 cm
Depth: 752.0–838.6 mbsf
Age: Oligocene–earliest Miocene
Lithology: nannofossil foraminifer chalk, nannofossil foraminifer limestone, and volcanic ash layers

The common presence of volcaniclastic material distinguishes Subunit IC from the ash-free chalk of Subunit IB. Core 192-1183A-15R, recovered below the 300-m coring gap, contains significant amounts of ash; therefore, the upper contact of this subunit is placed within the coring gap. The contact with the underlying Unit II is placed at the uppermost significant chert at 838.6 mbsf (192-1183A-24R-1, 43 cm). Thus, Subunit IC is at least 86 m thick.

T4. Components of sediments, p. 150.

The dominant lithology in Subunit IC is nannofossil foraminifer chalk with small amounts of siliceous microfossils. The carbonate content ranges from 90 to 95 wt%, slightly decreasing downward, with a very low value (49%) recorded from an ash layer (Sample 192-1183A-19R-4, 19 cm; 794.79 mbsf) (Table T4). The lowermost 50 m (below Core 19R at 790 mbsf) is limestone rather than chalk. Thin sections indicate that the average chalk is a packstone containing 50% foraminifers forming a grain-supported fabric with a nannofossil matrix (Fig. F8).

F8. Nannofossil foraminifer chalk, Subunit IC, p. 51.

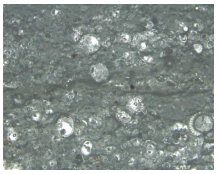

Color varies from white to light greenish gray. Smear slide comparisons suggest that intervals of light greenish gray contain more siliceous microfossils. Pervasive bioturbation includes *Zoophycos* and *Planolites* burrows. Chert-filled burrows (e.g., a 4-cm-long, 1-cm-wide occurrence in Section 192-1183A-18R-1, 49 cm) are rare. As in Subunits IA and IB, color bands and laminae of greenish gray and other colors cut across the bioturbated fabric.

Gray layers with volcaniclastic material are intercalated with the chalk and limestone throughout this subunit (Fig. F9). These layers are rich in glass shards. Thicker ash layers are preserved as discrete bands, but thinner beds have been blurred by burrowing and form diffuse zones of mixed chalk and glass shards. Increased magnetic susceptibility and reduced color reflectance indicate that these discrete and diffuse ash layers are more abundant toward the lower part of this subunit (Fig. F6). Greenish intervals containing a relative abundance of siliceous microfossils are commonly seen above ash-rich horizons.

The intermixed chalk-ash bands display a well-developed array of small-scale textural features from wispy flaser (chalk lenses partially outlined by ash-rich seams) through flaser-nodular (chalk lenses embedded within an ash-rich matrix) to clusters of compacted ash-filled burrows. We interpret these flaser textures in Subunit IC and in other subunits as diagenetic features, and they are discussed in the final part of "Postburial Diagenetic Features," p. 18.

F9. Ash layer in chalk, Subunit IC, p. 52.

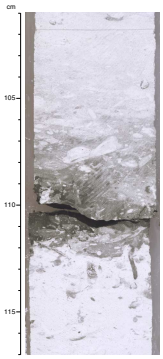

Unit II

Interval: 192-1183A-24R-1, 43 cm, to 39R-4, 15 cm
Depth: 838.6–986.6 mbsf
Age: Paleocene–Eocene
Lithology: limestone, chert, and zeolitic chalk

The top of Unit II is marked by the uppermost chert layer (Section 192-1183A-24R-1, 43 cm; 838.6 mbsf). A similar unit boundary was used in both DSDP Site 289 and ODP Site 807. The highest chert layer in Hole 1183A is 1.5 m above the lowest volcanic ash (Section 192-1183A-24R-2, 90 cm; 840.1 mbsf) typical of overlying Subunit IC. We subdivided Unit II into a relatively chert-rich upper interval (Subunit IIA; 838.6–958.3 mbsf) and a relatively chert-poor lower interval containing common zeolite-rich beds (Subunit IIB; 958.3–986.6 mbsf). The base of Unit II is marked by the lowest zeolite-rich bed at 986.6 mbsf (Section 192-1183A-39R-4, 15 cm).

Subunit IIA

Interval: 192-1183A-24R-1, 43 cm, to 36R-4, 71 cm
Depth: 838.6–958.3 mbsf
Age: Eocene
Lithology: nannofossil foraminifer limestone and chert

Subunit IIA spans 120 m and coincides approximately with the Eocene. Recovery of this subunit was generally <20%, with some cores containing only 10 cm of rock fragments. Recovery of correlative intervals in DSDP Site 289 and ODP Site 807 was similarly low, thus precluding a reliable characterization of the lithologic succession. For example, estimates from wireline-log velocity data at ODP Site 807 indicated a chert content of only 20%, although the recovered sediments were 50% chert (Kroenke, Berger, Janecek, et al., 1991).

Limestone intervals recovered from Subunit IIA are white with faint burrow mottling. The limestone contains an average of 40% foraminifers with a grain-supported fabric in a matrix of calcareous nannofossils and micrite. The limestone from the upper transition between Subunits IIA and IC contains 50%–60% foraminifers in a grain-supported fabric with little intergranular micrite. Even though chert is common, siliceous microfossils are not preserved in the limestone. Carbonate content is 95–99 wt% (Table T4), and the low magnetic susceptibility (Fig. F6) indicates an absence of volcaniclastic material.

The chert is typically light olive-gray to dark olive, but some pinkish gray chert is present in Cores 192-1183A-33R through 35R (Fig. F10). Chert fragments commonly display white rinds, and incompletely silicified, white limestone is incorporated within the chert. White silicified limestone and porcellanite are also present.

Subunit IIB

Interval: 192-1183A-36R-4, 71 cm, to 39R-4, 15 cm
Depth: 958.3–986.6 mbsf
Age: Paleocene
Lithology: foraminifer limestone and zeolitic chalk

Subunit IIB spans only 28 m and contains numerous zeolite-rich beds. Upper and lower boundaries are the highest and lowest zeolitic chalk horizons at 958.3 mbsf (Section 192-1183A-36R-4, 71 cm) and 986.6 mbsf (Section 39R-4, 15 cm), respectively. Similar zeolite-rich beds are present within the Paleocene limestone at DSDP Site 289 and ODP Site 807.

The dominant lithology in this interval is white to very light gray limestone with variable concentrations of foraminifers. In thin section, the limestone is predominantly foraminifers with a grain-supported fabric in a nannofossil matrix (Fig. F11). The limestone is moderately to commonly bioturbated, especially with *Planolites* burrows, with less abundant *Zoophycos* and vertical burrows. Carbonate content is 94–98 wt% (Table T4). In a few intervals, the undersides of burrows are outlined in bluish gray (e.g., interval 192-1183A-37R-3, 135 cm, through 37R–4, 50 cm; Fig. F12). Dark brown chert is a minor lithology within the limestone. The chertification is incomplete, and the chert is spotted with residual limestone and white porcellanite.

Gray 0.5- to 5-cm-wide zones within the limestone are zeolite rich and contain small amounts of glass and traces of biotite. They are less lithified than the limestone and therefore are classified as chalk. The zeolitic chalk zones have diffuse, bioturbated boundaries with the host limestone. Similar zeolite-rich bands were interpreted as altered volcanic ash layers at DSDP Site 289 and ODP Site 807 (Shipboard Scientific Party, 1975; Kroenke, Berger, Janecek, et al., 1991). The center of a typical zone displays a finely laminated texture if thicker than 0.5 cm; otherwise, the center consists of a single seam or group of interwoven seams (Fig. F13). Agglutinated foraminifers, which include feldspar or other noncarbonate grains in their tests, are found in the zeolite-rich zones but not in the host limestone.

A relatively greater abundance of zeolitic chalk beds in the lower part of Subunit IIB is indicated by an increase in average magnetic susceptibility, a darker average color, and a slightly lower carbonate content (Fig. F6). The lowest zeolite-rich bed (interval 192-1183A-39R-4, 14–15 cm) is 1 cm wide, greenish gray, and indistinctly laminated (Fig. F14). No zeolite-rich layers are present in the underlying white limestone of

F10. Limestone interbedded with chert, Subunit IIA, p. 53.

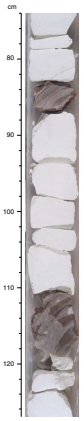

F11. Packed foraminifers within micrite matrix, Subunit IIB, p. 54.

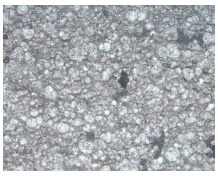

F12. Blue-gray staining underlining burrows, Subunit IIB, p. 55.

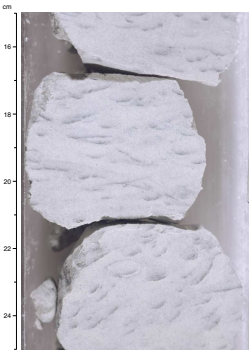

F13. Microflaser and anastomosing seams in limestone, Subunit IIB, p. 56.

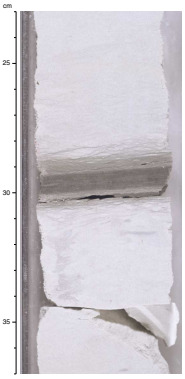

the Maastrichtian; therefore, this lowest zeolite-rich bed was used to mark the base of Subunit IIB.

Unit III

Interval: 192-1183A-39R-4, 15 cm, through 54R-3, 120 cm
Depth: 986.6–1130.4 mbsf
Age: Aptian–earliest Danian
Lithology: limestone

Unit III spans ~144 m from the contact with the lowest zeolite-rich bed at 986.6 mbsf (Section 192-1183A-39R-4, 15 cm) to the contact with basalt at 1130.4 mbsf (Section 54R-3, 120 cm). The unit is predominantly Cretaceous but includes ~70 cm of lowermost Danian sediments at the top. The upper 102 m of the succession consists of white limestone, and the lower 42 m is mottled grayish and pinkish white limestone with minor clay and volcaniclastic beds. This color difference divides the unit into two subunits, and the subunit contact at 1088.8 mbsf seems to correspond to a major hiatus between Santonian and Campanian strata. Core descriptions indicate that both subunits of Unit III are also present at DSDP Site 289 and ODP Site 807.

Subunit IIIA

Interval: 192-1183A-39R-4, 15 cm, through 50R-1, 60 cm
Depth: 986.6–1088.8 mbsf
Age: Campanian to earliest Danian
Lithology: white limestone

Subunit IIIA consists of light-colored foraminifer nannofossil limestone with abundant bioturbation and scattered black stylolites. The subunit spans a 102-m-thick interval from the zeolitic chalk at 986.6 mbsf (Section 192-1183A-39R-4, 15 cm) to a marked color change at 1088.8 mbsf (Section 50R-1, 60 cm). The limestone contains recrystallized foraminifers in decreasing abundance downhole. Carbonate content of the limestone is generally 98–100 wt% (Fig. **F6;** Table **T4**). Burrows are dominated by *Planolites* and vertical types and are filled by white, finer grained limestone. Chert is present as rare replacement nodules or lenses of reddish brown to dark brown (Fig. **F15**).

The upper half of Subunit IIIA (Core 192-1183A-39R through 44R) consists of white to very light gray limestone with abundant foraminifers. In Sections 192-1183A-39R-4 through 40R-3, the limestone contains bluish burrow mottles, has individual trace fossils up to a centimeter in diameter that penetrate as much as 10 cm, and is a foraminifer limestone with ~40% foraminifers in a grain-supported fabric. In Sections 192-1183A-40R-3 through 44R-CC, the limestone contains ~20%–30% foraminifers. In Sections 192-1183A-40R-3 through 41R-1 and Cores 43R and 44R, the limestone is white, relatively soft, and quite homogeneous with very faint burrow mottling. The limestone in Core 192-1183A-42R and most of Core 41R has a slight greenish tinge, and the burrows are usually parallel to bedding planes.

The lower half of Subunit IIIA (Cores 192-1183A-45R through 49R) displays subtle color alternations at a 30- to 40-cm scale between white and pale yellow limestone (Fig. **F16**). Bioturbation is especially visible at the color transitions. In thin section, the white limestone contains more foraminifers (10%; Fig. **F17**) than the pale yellow limestone (<5%).

F14. Lowest zeolite-rich band defining base of Unit II, p. 57.

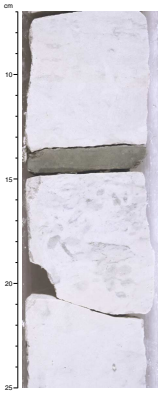

F15. Typical Maastrichtian facies, Subunit IIIA, p. 58.

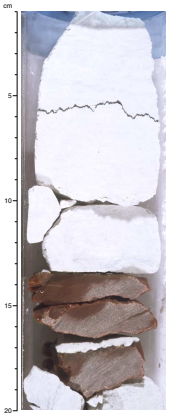

F16. Alternating light yellowish brown and white bands, Subunit IIIA, p. 59

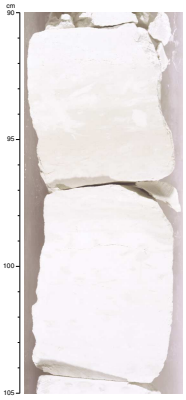

F17. Micrite limestone with foraminifers, Subunit IIIA, p. 60.

The Cretaceous/Paleogene boundary is ~70 cm below the top of Subunit IIIA in a piece of white siliceous limestone in interval 192-1183A-39R-4, 87–90 cm. Burrows filled with foraminifers of earliest Danian are present in foraminifer limestone of late Maastrichtian age.

Subunit IIIB

Interval: 192-1183A-50R-1, 60 cm, through 54R-3, 120 cm
Depth: 1088.8–1130.4 mbsf
Age: Santonian–Coniacian and Aptian–Albian
Lithology: mottled gray and pinkish white limestone

Subunit IIIB consists of ~42 m of varicolored micritic limestone with interbeds of dark ferruginous calcareous claystone and vitric tuff in the lowest 10 m.

There is a complex transition interval in Core 192-1183A-50R, and the subunit boundary was assigned to the highest level of bioturbated reddish limestone at 1088.8 mbsf (Section 50R-1, 60 cm). The overlying 60 cm of Core 50R displays a downward change from white to pinkish tints. The highest gray-mottled limestone that is typical of most of Subunit IIIB is nearly 1.7 m below this level. The intervening 1.7-m interval (interval 50R-1, 60 cm, to 50R-2, 87 cm) was recovered completely and contains three dramatic alternations between bioturbated clayey limestone and 10-cm-thick beds of calcareous claystone. The limestone is intensely pink to reddish brown, whereas the claystone is very dark reddish brown (Fig. **F18**). The claystone has a high magnetic susceptibility (Fig. **F6**). Pronounced dark stains extend from the claystone into the adjacent limestone intervals. Biostratigraphy indicates that this 1.7-m transition interval includes early Campanian, Santonian, and late Coniacian strata. The reddish brown bed of late Coniacian age directly overlies a hardground on light pink limestone of latest Albian age (see **"Biostratigraphy,"** p. 21). Clasts of this pink Albian limestone are found within the reddish brown Coniacian bed.

F18. Santonian–Coniacian facies overlying hardground, p. 61.

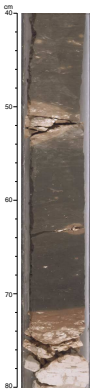

Below this transition interval, the Aptian–Albian limestone in Subunit IIIB is characterized by color alternations and mottles of lighter pink and of darker gray, although some intervals are a uniform light yellowish gray. The darker gray intervals seem to have more *Chondrites* burrows, whereas the lighter pink zones contain more *Planolites* burrows. Anastomosing pressure-solution seams are present in both colors but seem more prevalent in gray intervals. Color changes are variously sharp to gradational and cut across burrow fillings, pressure-solution seams, and chertification horizons. Patches of lighter pink occur within darker gray intervals and vice versa. Superimposed on the mottles are diffuse black spots.

The carbonate content of the limestone is typically 95 wt%, with no significant difference between the color facies. Foraminifers generally comprise <5% of the limestone, and calcified radiolarians are abundant in the basal 50 cm above the basalt. Magnetic susceptibility displays closely spaced oscillations on a generally elevated background (Fig. **F6**), indicating that iron oxyhydroxides are a constituent of the abundant fine-grained opaque and brownish semiopaque particles observed in thin sections. The noncarbonate components are concentrated along pressure-solution seams.

A combination of compacted subhorizontal burrows, subhorizontal streaks, discontinuous planar to irregular laminations, and thin elongate lenses imparts a distinctive "woody" texture to most of the Aptian–

Albian limestone. This woody texture grades into microflasers and anastomosing pressure-solution seams within the limestone (Fig. F19).

Chert is present as irregular bands and as nodules partially replacing limestone. Red chert is associated with pinkish limestone, and dark brown chert with grayish limestone. Pressure shadows are present adjacent to some chert nodules (e.g., Section 192-1183A-52R-1, 97 cm), indicating that initial silicification preceded the final stages of compaction and lithification.

Two beds of laminated calcareous claystone lie at ~10 m and 4 m above the base of Subunit IIIB. The upper bed (interval 192-1183A-53R-3, 115 cm, to 53R-4, 85 cm) is a 1.2-m-thick, reddish brown to black, ferruginous nannofossil claystone containing scattered horizontal stringers and lenses of packed foraminifer tests and fine sand–size clasts (Fig. F20). The lower bed (Section 192-1183A-54R-1, 50–60 cm) is a very dark brown claystone that was poorly recovered. In sharp contrast to the pervasive burrowing of the adjacent limestone pieces, these claystone beds display virtually no bioturbation. Both beds have high magnetic susceptibility (Fig. F6). Clay- to silt-size, brown, semiopaque particles of goethite and perhaps other iron oxyhydroxides are predominant in smear slides, thin section, and X-ray diffraction (XRD) data (Table T4). Carbonate content is ~40 wt%. The scattered laminations are concentrations of calcite-filled foraminifers and phosphatic fish debris; these components are also dispersed within the clay-rich matrix. Foraminifer tests and fragments are partially replaced and filled by opaques, which appear to be iron oxyhydroxides that may have replaced pyrite or precipitated in place. Planktonic foraminifers are common throughout the claystone, but benthic foraminifers are conspicuously absent.

The basal 5 m of limestone has a variety of primary and secondary colors, including white, gray, yellow, pink, reddish brown, and olive-brown. Darker shades form faint halos around some *Chondrites* burrows.

The lowest 2 m of Subunit IIIB contains two intervals of olive-gray to reddish brown vitric tuff (Fig. F21). The lowermost of the two intervals is separated from the underlying basalts by a 25-cm-thick limestone bed. The main component of the tuff, identified in thin section, is basaltic ash consisting of partly glassy to tachylitic fragments with abundant plagioclase microlites. Texturally, many of the fragments are similar to aphanitic pillow margins in the underlying basalts. Most fragments are nonvesicular, but some have vesicles or scalloped margins. Altered brown glass shards are also present; most are blocky and nonvesicular, but some are moderately vesicular. The tuff is composed of at least eight normally graded beds, several of which have scoured bases. The uppermost layer grades up through parallel-laminated to cross-laminated beds, indicating deposition by turbidity currents or reworking by currents. There is a thin layer of bioturbated limestone above the fourth depositional layer.

The base of Subunit IIIB is placed at the top of the uppermost basalt unit at 1130.4 mbsf (Section 192-1183A-54R-3, 120 cm), but the sediment/basalt contact was not recovered. The lowermost sediment recovered above the basalt (interval 54R-3, 95–120 cm) is the typical bioturbated nannofossil limestone of Subunit IIIB (Fig. F22).

Basement

Interval: 192-1183A-54R-3, 120 cm, through 68R-1, 46 cm
Depth: 1130.4–1211.1 mbsf
Age: Aptian

F19. Typical Aptian–Albian facies, Subunit IIIB, p. 62.

F20. Laminated dark calcareous claystone, Subunit IIIB, p. 63.

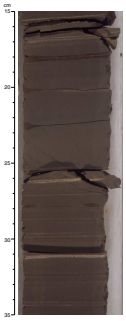

F21. Vitric tuff, lower Subunit IIIB, p. 64.

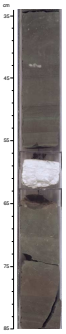

F22. Bioturbated limestone overlying basalt, p. 65.

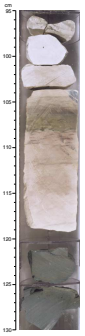

Lithology: basalt flows with rare beds of ferruginous micrite limestone

Basement consists of eight pillow-basalt units with thin limestone interbeds. The basalt is described in detail in "Igneous Petrology," p. 25, "Alteration," p. 29, and "Structural Geology," p. 32. The limestone is partially recrystallized and light yellow to very pale brown. The limestone beds recovered between pillow-basalt flows comprise Piece 2A above hyaloclastite in Section 192-1183A-54R-4 (Fig. F23), two pieces at the top of Core 55R, one piece in Section 55R-2 at 80 cm, and one piece at the top of Section 56R-1.

The sediment is thermally altered ferruginous micrite limestone with foraminifers and radiolarians. Calcite-filled foraminifers and radiolarians are in a micrite matrix that has been partially recrystallized to fine-grained spar and that contains abundant fine-grained opaque and brown semiopaque particles. Sedimentary structures are difficult to distinguish. XRD data show that the limestone fragment in Core 192-1183A-60R includes glauconite.

F23. Partially recrystallized limestone above hyaloclastite, p. 66.

Sedimentation History of Site 1183

The Maastrichtian through Pleistocene sedimentation record is quite consistent across the main Ontong Java Plateau (e.g., Berger et al., 1991). The succession is predominantly calcareous sediments composed of foraminifers and calcareous nannofossils. Deposition was punctuated by episodes of relative enrichment in siliceous microfossils and in volcaniclastic material and by major regional hiatuses. Only the Aptian–Campanian stratigraphy displays significant local variability.

Noteworthy aspects of Site 1183 sedimentation history include the following:

1. Depositional setting on the seafloor was primarily deep, oxygenated (pervasively bioturbated, no organic-carbon preservation), and quiet (no significant currents or redeposition events after the Aptian).
2. Two beds of laminated, ferruginous calcareous clay with planktonic foraminifers of late Aptian age (~115 Ma) indicate a seafloor that was temporarily devoid of burrowing organisms or benthic foraminifers. These episodes could reflect bottom-water dysoxia and/or hyperoligotrophic (low surface productivity) conditions.
3. The preserved sediment was deposited above the calcite compensation depth (CCD) and generally above the foraminifer lysocline. However, the regional pattern of the Cenomanian–Campanian (100–70 Ma) condensation or hiatus is consistent with a relative rise of the CCD through the Aptian and Albian to a level above the summit of the plateau, followed by a progressive descent of the CCD during the Campanian and Maastrichtian. These trends reflect the posteruption subsidence history of the plateau, combined with oscillations in the Pacific CCD.
4. Input of volcaniclastic material into the sedimentary succession is concentrated in two main periods: Paleocene to early Eocene (65–50 Ma) and late Eocene to Oligocene (40–20 Ma). The initiation of the latter episode is similar in age to that inferred for the basaltic volcaniclastic sequence recovered at Site 1184 on the

southeastern extension of the plateau, but the Oligocene ash layers probably are derived from the Melanesian arc.
5. The middle Eocene (50–40 Ma) chalk is chert rich and corresponds to a lull in the input of volcaniclastic material.

Aptian Basal Limestone and Vitric Tuff

The Aptian–Albian section is relatively thick at Site 1183, where it is represented by 42 m of mottled grayish and pinkish white limestone (Subunit IIIB) and by rare pockets of ferruginous micrite limestone within the underlying pillow basalt flows. This subunit at Site 1186 has a similar thickness (see **"Lithostratigraphy,"** p. 4, in the "Site 1186" chapter). In contrast, only a thin veneer of basal limestone overlain by noncalcareous radiolarian claystone was found at Site 807 on the plateau's northern flank.

Following the last flow of pillow basalt at Site 1183, a minimum of 25 cm of bioturbated limestone was deposited before deposition of at least eight beds of vitric tuff. The minor, moderately vesicular basaltic glass shards in these tuff beds indicate formation by relatively shallow submarine eruptions, whereas the partly glassy basaltic ash that constitutes the dominant component could have been derived from shallow-water to subaerial hydroclastic eruptions or by erosion of a volcanic source somewhere in the summit region of the main Ontong Java Plateau. These beds and possibly a vitric tuff of similar age just above basement basalt at DSDP Site 289 (Andrews, Packham, et al., 1975) are the only evidence that a portion of the main plateau was relatively shallow and possibly subaerial.

Aptian Laminated Intervals

The Aptian–Albian limestone is thoroughly bioturbated and light pink (with secondary gray staining, as explained later). These characteristics indicate oxygenated waters at this depth in the Pacific basin. However, there are two important exceptions.

Above the Aptian/Albian boundary interval is a 1.2-m-thick, reddish brown to black, ferruginous nannofossil claystone (interval 192-1183A-53R-3, 115 cm, to 53R-4, 85 cm; Fig. **F24**). Another, but poorly recovered, very dark brown claystone is ~6 m lower, within the middle Aptian (interval 192-1183A-54R-1, 50–60 cm). The moderate abundance of planktonic foraminifers indicates depositional depths above the foraminifer lysocline.

Some components of these intervals suggest a period of condensed sedimentation. The abundance of phosphatic fish debris and enrichment in fine-grained noncalcareous components suggest a slow rate of sediment accumulation. Iron oxyhydroxides and clay (identified as goethite and nontronite in XRD patterns) form abundant, brown, semiopaque particles within the claystone (Fig. **F25**). These may be related to red-brown semiopaque objects (RSOs) that are common in pelagic brown clays at deeper Pacific sites (e.g., Yeats, Hart, et al., 1976; Shipboard Scientific Party, 1990). RSOs are considered to be iron oxyhydroxides formed during intense early diagenetic processes accompanying low sedimentation rates (Karpoff, 1989, and references therein). Other opaque particles, which may be pyrite replacements that were later altered, partially fill some foraminifer tests and have shapes similar to radiolarian and foraminifer tests.

F24. Base of laminated dark calcareous claystone, Subunit IIIB, p. 67.

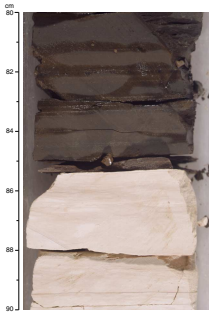

F25. Microfacies of laminated dark calcareous claystone, Subunit IIIB, p. 68.

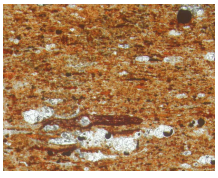

Other observations suggest that the Aptian and Albian environment on the plateau during these episodes was unfavorable for bottom life. No bioturbation disrupts the numerous stringers and laminae of concentrated planktonic foraminifers and fish debris (Fig. F26). The laminae of concentrated foraminifers may represent periodic winnowing by bottom currents or surface productivity blooms. Despite the abundance of planktonic foraminifers, there are no benthic foraminifers. Possible causes of unfavorable environments include low oxygen levels on the bottom and/or an inadequate food supply.

Four oceanic anoxic events (OAEs) have been proposed as global or widespread episodes during the Aptian and Albian (e.g., Schlanger and Jenkyns, 1976; Bralower et al., 1993). These events are a mid–early Aptian OAE1a (Selli level), an Aptian/Albian boundary OAE1b (Paquier level), an early late Albian OAE1c, and a latest Albian OAE1d. Organic-rich laminated shale is the typical signature of OAEs in the Atlantic-Tethys seaway. However, except for the OAE1a event, which is recognized in the Mid-Pacific Mountains as three laminated organic carbon–rich intervals (Shipboard Scientific Party, 1981; Bralower et al., 1993), the record of these events in the Pacific basin is patchy. High-resolution biostratigraphic correlation and carbon isotope stratigraphy may establish whether the laminated ferruginous claystone layers at Site 1183 coincide with any of these postulated global OAEs.

An alternative hypothesis is that low sedimentation rates during deposition of the claystone were a result of very low surface productivity (hyperoligotropic). A low flux of planktonic tests and associated organic material to the bottom would limit benthic communities. Under this scenario, the broad summit region of the Ontong Java Plateau became a biological "desert" during part of the Aptian because of reduced circulation of nutrient-rich water.

F26. Microfacies of laminated calcareous claystone, p. 69.

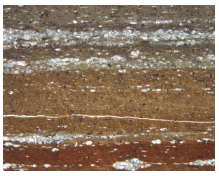

Aptian–Maastrichtian CCD

The Cretaceous sediment succession overlying basalt basement on the main Ontong Java Plateau has been recovered from a total of seven sites during DSDP Leg 30 and ODP Legs 130 and 192. These sites span the lower flank to the summit of the plateau and record different ages both for the termination of calcareous sediment deposition during the Aptian–Albian interval and for the return to carbonate deposition during the Campanian–Maastrichtian interval. We interpret this pattern as the result of a rise and fall of the CCD relative to the depositional surface of the plateau.

We obtained an estimate of relative CCD trends by applying a simple backtracking and subsidence procedure (e.g., Berger and Winterer, 1974; Tucholke and Vogt, 1979) uniformly to all basement sites on the main Ontong Java Plateau to estimate the paleodepth of the sediment surface through time (Fig. F27). This procedure incorporates progressive sediment accumulation with time as the underlying basement undergoes thermal subsidence and sediment loading.

The compensation for sediment loading assumes a local Airy isostatic depression of the mantle:

$$\text{Loading adjustment} = \text{sediment thickness} \cdot (\text{mantle density} - \text{sediment density})/(\text{mantle density} - \text{seawater density})$$

in which we used the values of Tucholke and Vogt (1979) for mantle density (3.3 g/cm³), average carbonate sediment density (1.8 g/cm³),

F27. Estimated CCD on Ontong Java Plateau through time, p. 70.

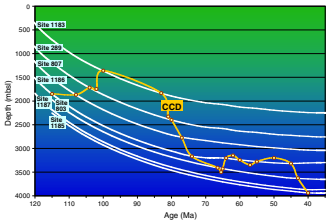

and seawater density (1.03 g/cm^3). The resulting loading adjustment is ~0.66 of the sediment thickness, implying for each 1 m of average sediment accumulation, the basement is depressed by 0.33 m and the depositional surface rises by 0.66 m.

The backstripped depths of the current sediment-basement interface, adjusted for removal of the total sediment loading, are as follows:

ODP Hole 1183A = 2563 mbsl
DSDP Site 289 = 3058 mbsl
ODP Hole 1186A = 3380 mbsl
ODP Hole 807C = 3717 mbsl
ODP Hole 803D = 3826 mbsl
ODP Hole 1187A = 4036 mbsl
ODP Hole 1185A = 4103 mbsl

These backstripped basement depths are slightly deeper than the array shown in Figure **F37,** p. 73, in the "Leg Summary" chapter because here we apply a slightly lower average density for the typical chalk sediment.

We estimated the initial depth and progressive deepening of basement by backtracking, following a generalized version of the global depth and heat flow (GDH1) model of Stein and Stein (1993). In this empirical fit to global seafloor depth data, the lithosphere behaves as the cold upper boundary layer of a cooling half-space for the first 20 m.y., followed by an asymptotic approach to observed maximum depths for old crust. The equation for the total subsidence of crust ≥ 20 m.y. is:

$$d(t) = 3051 - 2473 \exp(-0.0278t)$$

where $d(t)$ = total subsidence (in meters), and t = elapsed time (in m.y.) since the initial thermal age.

Application of this equation, assuming that the initial thermal age is the same as the age of the erupted basalts, would imply 2968 m of total subsidence in the past 122 m.y. This would place the uppermost basalt at Hole 1183A at an initial altitude of 405 m above sea level. This result is incompatible with the submarine, nonvesicular nature of the pillow basalts. Similar discrepancies in subsidence models have been noted for sites on the Kerguelen Plateau (Coffin, 1992), Mid-Pacific guyot carbonate platforms (Röhl and Ogg, 1996) and other volcanic edifices constructed on older crust. Detrick and Crough (1978) proposed that the subsidence of a volcanic edifice emplaced on older oceanic crust behaves as if the initial thermal age is intermediate between the edifice age and the age of the underlying and partially cooled oceanic lithosphere. This concept fits the accumulation history of Aptian–Albian carbonate platforms of the Mid-Pacific Mountains and MIT guyot (Röhl and Ogg, 1996) where subsidence rates (rates of shallow-water carbonate accumulation) were constrained by coring during Legs 143 and 144.

An initial thermal age ~2.5 m.y. older than the assumed 122-Ma age of the uppermost basalt flows on the main Ontong Java Plateau would mean that the lithosphere would have subsided by ~600 m (using $d(t) = 365t^{1/2}$ for the initial 2.5-m.y. period) before the emplacement of the plateau (see Stein and Stein, 1993). This would satisfy both of the following:

1. A possible eruption depth of ~1300 m at Hole 807C, as estimated from the abundance of CO_2 and H_2O in glass of the topmost basalt unit, Unit A (Michael, 1999), and
2. A middle- to upper-shelf benthic foraminifer assemblage in the basal sediment in Hole 1183A (see "Biostratigraphy," p. 21).

This depth zone is consistent with the calculated 1100-m bathymetric offset between the compensated basement depths of Holes 807C and 1183A, as computed above (see also Fig. F37, p. 73, in the "Leg Summary" chapter). However, the implied 200-m paleodepth of the final eruptive phase of Site 1183 conflicts with the nonvesicular texture of the basalts, which would generally indicate an eruptive water depth >800 mbsl (Moore and Schilling, 1973).

Implicit in applying this model to the Ontong Java Plateau is the simplifying assumption that no later underplating or reheating episodes (e.g., tectonic model of Ito and Clift, 1998) caused deviations from a thermal subsidence curve typical of an edifice emplaced on older oceanic crust.

The accumulated sediment thickness at each successive 5-m.y. interval was added to the computed subsidence of basement and isostatically compensated, as explained above. The resulting trends of estimated sediment surface paleodepth display a rapid initial deepening, followed by a semiconstant or even slightly shallowing depth as the rapid sedimentation rates in the Cenozoic balance thermal subsidence (Fig. F27).

We assumed that the major hiatuses in the Cretaceous carbonate record were produced when the seafloor at each of the sites was below the CCD and connected these age-depth intersections to derive an estimated history of the Cretaceous and Paleogene CCD. Although the general trends produced by this model may be indicative of the CCD history, the absolute estimates of paleodepths may be in error.

According to this subsidence model and the carbonate successions at the different sites, the CCD on the Ontong Java Plateau rose during the Aptian through Albian, then descended during the Campanian and Maastrichtian. Contributing to the apparent relative rise of the CCD during the Aptian–Albian was the thermal subsidence of the main Ontong Java Plateau. A similar major rise of the CCD during the Aptian–Albian, followed by rapid descent during the Campanian–Maastrichtian, is recorded in the North Atlantic and Indian Ocean basins (e.g., van Andel, 1975; Tucholke and Vogt, 1979; Thierstein, 1979). The CCD oscillations during the Cretaceous may be related to global paleoceanographic and biological trends (e.g., Berger, 1979; Sclater et al., 1979; Barrera and Savin, 1999; Frank and Arthur, 1999; MacLeod and Huber, 2001). Shore-based studies of carbon isotope data coupled with characterization of the planktonic assemblages might provide clues to changing surface-water conditions and circulation patterns on the Ontong Java Plateau.

Cretaceous/Paleogene Event and Paleocene Zeolitic Limestone

In Hole 1183A, burrows of earliest Danian (planktonic foraminifer Zone P0) penetrating chalk of middle–late Maastrichtian age represent the Cretaceous/Paleogene boundary (Sample 192-1183A-39R-4, 87–90 cm). A depositional hiatus or end-Maastrichtian erosion episode trun-

cated the final 2 m.y. of the Cretaceous record (see "Biostratigraphy," p. 21).

An abundance of zeolite-rich horizons characterizes Subunit IIB, which spans only 30 m. Similar zeolite-rich bands within the Paleocene limestone at DSDP Site 289 and ODP Site 807 have been interpreted as altered volcanic ash layers (Kroenke et al., 1993). The lowest zeolite-rich layer is 70 cm above the Cretaceous/Paleogene boundary at interval 192-1183A-39R-4, 81–85 cm (987.1 mbsf). A similar coincidence of a lithified volcanic ash just above the Cretaceous/Paleogene boundary is present at Site 807 (interval 130-807C-54R-3, 135–136 cm).

A potential source of the ash beds is the Paleogene volcanic arc that developed behind the Papua–New Caledonia–Norfolk Ridge subduction zone ~2000 km southwest of the Ontong Java Plateau (Kroenke, 1984, 1996). Activity along this subduction system may have begun when the Pacific plate changed direction at ~65 Ma (polarity Chron C29) and continued until ~40 Ma (Duncan and Clague, 1985; Kroenke et al., 1993). Alternatively, the volcaniclastic material may have had a closer source, perhaps the formation of one or more of the seamounts on top of the Ontong Java Plateau, such as the edifice below the immense Ontong Java atoll (see Fig. F1). Because the glass shards in the original ash have been pervasively altered to zeolite, no information is available from shard morphology or color to help distinguish between these possible sources.

Eocene Chert and Lull in Input of Volcaniclastic Material

Eocene sedimentation in the world's oceans is characterized by a high accumulation rate of biogenic silica (from diatoms and radiolarians) and abundant chert (e.g., Lancelot, 1971; Jansa et al., 1979; Riech and von Rad, 1979; Emery and Uchupi, 1984). Increased siliceous volcanic activity during the Eocene is a common hypothesis invoked to explain the surge in silica deposition and chert formation (e.g., Gibson and Towe, 1971; Mattson and Pessagno, 1971; Tucholke and Mountain, 1979; Mélières et al., 1981; Emery and Uchupi, 1984). Volcanism is postulated to stimulate siliceous plankton productivity by supplying the nutrients Si and Fe and to enhance preservation by increasing the silica saturation in deep waters. However, this postulated relationship between volcanic activity and elevated silica and chert abundance in sediments is contradictory to the trends recorded on the Ontong Java Plateau.

Hole 1183A penetrated 120 m of interbedded Eocene chert and limestone (Subunit IIA). The chert-rich interval of the Eocene is ash poor but is sandwiched between ash-rich, chert-poor Paleocene and Oligocene sediments. This large-scale inverse relationship suggests that increased input of volcanic material is not a major factor contributing to the formation of chert. We favor an alternative hypothesis that silica is enriched in the oceans during periods of warm humid climate, when intensified chemical weathering leaches silica from continental rocks (e.g., Millot, 1964). The early and middle Eocene was the warmest period in the Cenozoic (e.g., review by Crowley and North, 1991) and coincides with this anomalous episode of worldwide siliceous sedimentation.

The top of the chert capping Unit II at all sites on the Ontong Java Plateau is the seismic reflector terminating the "Ontong Java Series" (Berger et al., 1991). This reflector is analogous to the Eocene seismic Horizon A^c capping the chert-rich Bermuda Rise Formation of the

North Atlantic basin (Tucholke, 1979). A global cooling trend and associated shift of diatom productivity to circum-Antarctic seas and coastal upwelling zones, plus a reduction in global volcanic activity, contributed to silica "starvation" after 40 Ma in tropical seas (reviewed by Berger et al., 1991). However, on the Ontong Java Plateau, regional volcanic activity increased, rather than decreased, at the top of the chert beds. Therefore, we suggest that regional volcanic input to the Ontong Java Plateau inhibited, rather than aided, chertification.

This inhibition of chert formation by volcanism seems to occur both at the large scale of the lithologic subunits and at the individual bed scale. Within the Paleocene limestone, individual beds of volcaniclastic zeolites and localized chertification are never associated. One contributing factor is the process of chert formation during diagenesis. Zeolite and clay from altered volcanic material dispersed in biogenic sediment are sources for easily exchangeable cations which inhibit chert precipitation (e.g., Millot, 1964; Lancelot, 1971).

Oligocene–Miocene Volcanic Ash Input and Chalk Cycles

The second major Cenozoic episode of ash-rich sediment deposition began in the late Eocene and continued into the Miocene. Chalk that is rich in volcaniclastic material was recovered from similar age intervals at Site 1183, DSDP Site 289 (e.g., Shipboard Scientific Party, 1975), and ODP Site 807 (e.g., Kroenke, Berger, Janecek, et al., 1991, fig. 19 on p. 393). Kroenke et al. (1993) did not include this episode in their tephrachronology for the Ontong Java Plateau because the published Site 289 and Site 807 core description sheets did not give details on the numbers of Oligocene ash horizons.

The first appearance of the volcanic ash beds at ~40 Ma is similar in age to both the basaltic volcaniclastic rocks at Site 1184 (see **"Biostratigraphy,"** p. 11, in the "Site 1184" chapter) to the southeast of the main plateau and the initiation of Melanesian arc volcanism, when the southern side of the Ontong Java Plateau was converging obliquely with the Melanesian Trench (Kroenke et al., 1993). The Melanesian volcanic arc remained active throughout the Oligocene until the completion of docking of the Ontong Java Plateau with the Melanesian arc at ~23 Ma (Kroenke, 1984, 1996).

Light greenish gray intervals with a relative enrichment of siliceous microfossils are found within the white nannofossil chalk of Subunit IC, where they commonly overlie ash-rich horizons. This association may indicate either a preferential preservation of biogenic silica caused by ash-influenced interstitial water chemistry or an enhanced productivity of siliceous plankton. The influence of volcanic ash may be superimposed on a subtle primary cyclicity in the Oligocene. Portions of the Miocene Subunit IB display alternations from white to light green at ~75-cm spacing, which may correspond to oscillations in paleoceanographic conditions caused by Milankovitch cycles and/or episodic minor influxes of fine volcanic ash.

Postburial Diagenetic Features

Following deposition and mixing by bioturbation, the carbonate ooze underwent compaction, progressive pressure-solution lithification, partial silicification, and late-stage redox reactions of iron and manganese compounds. These diagenetic effects created a variety of

features. Studies of similar features at DSDP Site 289 and from ODP Leg 130 resulted in different interpretations.

The approximate succession of selected diagenetic effects with time and depth is as follows:

1. Progressive lithification of ooze to chalk to limestone.
2. Early (within 5 m.y.) formation of Liesegang color banding.
3. Dissolution and reprecipitation of biogenic silica, with partial chertification of limestone.
4. Progressive pressure-solution of the carbonates, creating seams of insoluble residue, stylolites, and microflaser textures.
5. Late-stage (during or after pressure solution) color staining and mottling.

These processes progress with depth within Site 1183 and overlap in their effects (e.g., Fig. F28).

F28. Silicification and redox diagenesis, Subunit IIIB, p. 71.

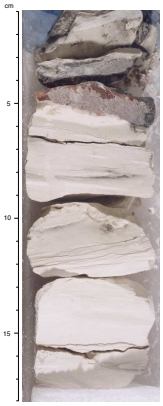

Ooze-to-Chalk Transition (Subunits IA to IB)

The ooze-to-chalk transition (Subunits IB/IA boundary) in Hole 1183A is based subjectively on the finger-press test, and we assigned this transition to ~337.6 mbsf. Other sites at 2- to 3-km water depths on the Ontong Java Plateau have the ooze-to-chalk transition at a similar depth within the sediment column. In deeper water, the ooze-to-chalk transition is at progressively shallower levels within the sediment column (Berger et al., 1991). For example, at Site 803 in 3410 m of water, this transition is at 217 mbsf. However, many factors besides water depth are involved in this early lithification process (van der Lingen and Packham, 1975).

Color Laminae and Dark Spots in Cenozoic Chalk (Unit I)—Redox or Volcanic?

Overprinting the bioturbated texture of the white chalk and ooze throughout the Oligocene and Miocene (lithologic Unit I) are abundant (~5-cm intervals), thin (~1 mm), faint horizontal bands and streaks of green, blue, or purplish red (Fig. F29). Similar Liesegang color laminae and streaks within coeval chalk at ODP Sites 803 and 807 were interpreted in two ways.

F29. Color laminae on white chalk, Subunit IB, p. 72.

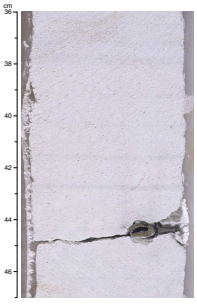

The first interpretation is that these color laminae are a diagenetic enhancement of subtle primary compositional differences (especially organic carbon content) by preferential redox reactions of iron and manganese (e.g., Kroenke, Berger, Janecek, et al., 1991; Berger et al., 1991). The second interpretation is that the color bands develop as minor concentrations of volcanic ash are transformed during diagenesis (Lind et al., 1993). This interpretation was based primarily on comparison of appearance and frequency to color laminae in Oligocene–Pleistocene chalk of Lord Howe Rise. Those laminae contain smectite and have a temporal pattern resembling other records of Cenozoic volcanism in the southwest Pacific (Gardner et al., 1986). In the ODP holes on the Ontong Java Plateau, the greenish laminae are associated with Fe- and Al-bearing silicates, whereas the purplish laminae are caused by finely disseminated iron sulfide (Lind et al., 1993). However, direct evidence of a volcanic component, such as glass or thicker ash horizons adjacent to color bands, was not demonstrated in any of the previous studies.

Chertification in Limestone (Units II and III)

Silicification of deep-sea sediments is a progressive process involving phase transitions from biogenic-skeletal opal-A through opal-CT to quartz. The transformation rates depend on host lithology, concentration of siliceous microfossils, elapsed time, and burial depth (e.g., Lancelot, 1971; Hein et al., 1981; Behl and Smith, 1992). The first stage is preferential silicification of burrows; the amount and types of burrowing may control the initial loci of formation of chert nodules and bands (Hein et al., 1981). The shallowest chertification in Hole 1183A occurs as rare chert-filled burrows in the Oligocene (Subunit IC). In addition, the relative concentrations of siliceous microfossils may be affected by periodic oscillations in surface fertility driven by Milankovitch climate cycles (e.g., Ogg et al., 1992).

Formation of chert within host limestone typically requires between 30 and 50 m.y., according to Behl and Smith (1992), but this interpretation may be partially biased by the global pattern of chert formation during the Eocene (35–50 Ma). Chertification of limestone is completed when all biogenic silica has dissolved from zones within the host siliceous carbonate sediment and has reprecipitated as bands or nodules (Fig. F30). Within Eocene Subunit IIA, all siliceous microfossils have been dissolved from the surrounding carbonate. This striking contrast between pure carbonate and silicified limestone was also noted at ODP Site 807.

F30. Chertification in limestone, Subunit IIA, p. 73.

Wispy Flaser to Woody Textures in Chalk and Limestone (Subunit IC and Units II and III)—Diagenesis or Currents?

The limestone from Hole 1183A displays a suite of small-scale features, including wispy flaser (chalk lenses partially outlined by volcaniclastic clay seams), flaser-nodular (chalk lenses embedded within a volcaniclastic clay matrix; Fig. F31), and a woody texture (subhorizontal streaks, thin lenses, burrows, and laminations). Many intervals closely resemble microflaser and nodular limestone structures within the English Chalk and other Upper Cretaceous limestone (e.g., Kennedy and Garrison, 1975; Scholle et al., 1983). These structures are most evident in bands that are enriched in volcanic ash, zeolite, or another noncarbonate component.

F31. Flaser texture, Subunit IC, p. 74.

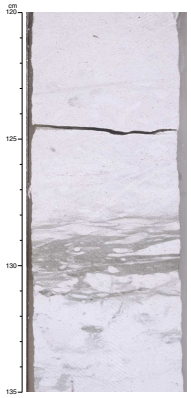

Two contrasting interpretations have been proposed for such flaser textures. DSDP Leg 30 sedimentologists inferred bottom currents with a superimposed tidal component. Flaser textures are a common feature of storms and tide-influenced ripples, and tides may influence sedimentation to great depths (Lonsdale et al., 1972a, 1972b). Therefore, microflasers in the limestone implied that the surface of the Ontong Java Plateau was affected by deep-sea tidal currents or periodic major storms during the Aptian–Oligocene (e.g., Klein, 1975; Shipboard Scientific Party, 1975). However, at Site 1183, we observed no evidence of current laminations within the foraminifer chalk lenses to support a ripple origin.

In contrast, the Leg 130 sedimentologists postulated a recrystallization and pressure-solution origin for the microflasers at Site 807 (Kroenke, Berger, Janecek, et al., 1991). Earlier, Bathurst (1987) concluded that stylolites are typical of pressure-solution affecting carbonate having <8%–10% clay, whereas greater proportions of clay will result in dissolution seams. However, even though the limestone throughout the flaser-bearing facies from Hole 1183A (and at Site 807) contains <10%

clay, stylolite horizons are rare, yet bands of microflasers surrounded by anastomosing seams are common. Therefore, Lind (1993) proposed that microstylolites and flasers develop if the clay and other noncarbonate minerals are finely disseminated, whereas clay concentrated in a narrow zone tends to give rise to a stylolite.

We propose a modified diagenetic process in which heterogeneity, not uniformity, plays an important role in creating the array of diagenetic features at Site 1183 and other sites. We observed a continuum of textures in Hole 1183A, from differential cementation and compaction of burrow fillings to chalk lenses isolated by anastomosing and braided clay seams, to "floating" chalk nodules embedded within volcaniclastic claystone. If bioturbation has redistributed material from volcaniclastic horizons into the adjacent chalks, then there would be an irregular patchy distribution of the noncarbonate minerals. During pressure solution, carbonate dissolves from relatively clay-rich zones, then reprecipitates in more carbonate-rich zones. The insoluble residue left behind forms wavy clay-rich streaks that act as conduits for continued pressure solution of the adjacent carbonate (Fig. F32). The process continues with accumulating overburden and time and results in the wispy flaser structures within these bands. Pressure solution may eventually concentrate the insoluble ash or zeolites into a central seam or anastomosing set of seams surrounded by microflaser textures in the adjacent chalk, as found within some bands in the Paleocene (Subunit IIB). Under further differential compaction and pressure-solution mediation of lithification of the bioturbated sediment, the microflaser and anastomosing clay-seam features grade into the woody texture of the Aptian–Albian limestone (Fig. F33). A similar pressure-solution process was proposed for the woody texture in the lower Cretaceous clay-rich radiolarian sediments at ODP Site 801 (Shipboard Scientific Party, 1990; Ogg et al., 1992, pp. 591–592).

F32. Microstylolite, Subunit IC, p. 75.

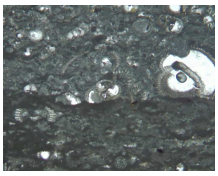

F33. Diagenetic woody texture of seams and microflasers, Subunit IIIB, p. 76.

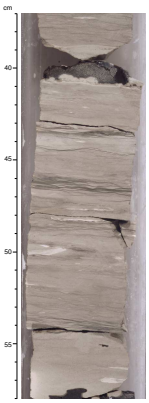

Color Staining in Middle Cretaceous Limestone (Unit III)

The Aptian–Albian limestone has pink and gray mottling. The color differences are partially a diagenetic feature because the color changes cut across burrow fillings, clay seams, and chertification horizons; are variously sharp to gradational; and are also present as patches within the opposite color facies. The most striking dark color fronts extend from volcaniclastic claystone bands in Core 192-1183A-50R into the adjacent limestone intervals. These color stains are probably a redox mobilization of manganese or iron from the claystone or altered volcaniclastic material. Similar mottling features in Lower Cretaceous sediment in the Pigafetta Basin were ascribed to mobilization and differential staining by iron-manganese oxyhydroxides (Lancelot, Larson, Fisher, et al., 1990; Ogg et al., 1992). Migrating Fe-Mn compounds, either from the volcaniclastic beds or from the underlying plateau basalt, probably also caused the variety of colors (reddish brown, olive, yellow, etc.) in the basal 5 m of limestone in Hole 1183A.

BIOSTRATIGRAPHY

Lower–middle Miocene (328–445 mbsf) and mid-Aptian to terminal Oligocene sections (752–1130.37 mbsf) were cored at Hole 1183A (Table T5). By using planktonic foraminifers and calcareous nannofossils, we detected the presence of 11 unconformities (Table T6), of which the

T5. Depth-age summary, p. 152.

T6. Unconformity depths and estimated durations, p. 153.

longest are intra-Albian (~10.6 m.y.) and Albian/Coniacian (~13.2 m.y.). The upper Coniacian to lower Campanian section overlies the younger of these two unconformities and is extremely condensed (0.3 m/m.y. accumulation rate), devoid of planktonic foraminifers, and contains sparse, atypical nannofossil assemblages. The Eocene/Oligocene and Cretaceous/Paleogene boundaries were recovered in Sections 192-1183A-24R-2 and 39R-4, respectively. The Cretaceous/Paleogene boundary is unconformable, but the Eocene/Oligocene boundary interval is condensed and appears relatively complete. Most significantly, microfossils (*Eprolithus floralis* and *Leupoldina cabri*) limit the age of the sediment immediately above basaltic basement to a short stratigraphic interval straddling the lower/upper Aptian boundary.

Foraminifer abundance at Hole 1183A is high overall, except for rare intervals associated with low-oxygen deposition and/or deposition near or below the foraminifer lysocline; foraminifer preservation generally worsens downsection. Calcareous nannofossils are abundant and poorly preserved throughout most of the section; only the basal 73 cm of the Danian section is barren of nannofossils.

We have completed a preliminary, integrated biostratigraphic framework for both the Cenozoic (Table **T7**) and Cretaceous (Table **T8**) intervals. The emphasis is on the Cretaceous–Eocene interval.

T7. HO and LO of Cenozoic foraminifers and nannofossils, p. 154.

T8. HO and LO of Cretaceous foraminifers and nannofossils, p. 156.

Cenozoic

We applied the standard Cenozoic biozonations for planktonic foraminifers (Berggren et al., 1995) and calcareous nannofossils (Martini, 1971) to Hole 1183A sediments. We examined the Paleogene portion of the sediments (Cores 192-1183A-19R through 39R) in detail for foraminifers, whereas only the Paleocene–Eocene portion (Cores 24R through 39R) was examined in detail for calcareous nannofossils. We examined single samples from individual cores for both microfossil groups.

Our preliminary results demonstrate one major difference in calibration between these two microfossil groups relative to the Berggren et al. (1995) timescale. In Hole 1183A, the occurrences of *Sphenolithus heteromorphus* and *Globorotalia fohsi fohsi* overlap for 28 m. However, Berggren et al. (1995) reported that the extinction of *S. heteromorphus* preceded the appearance of *G. fohsi fohsi* by 0.82 m.y. We also encountered minor calibration differences around the Eocene/Oligocene boundary in Section 192-1183A-24R-2 and within the middle Eocene (see Table **T7**).

Cretaceous/Paleogene Boundary

The Danian (lower Paleocene) interval is ~2.3 m thick in Hole 1183A (Table **T5**) and is bounded by unconformities (Table **T6**). The basal Danian planktonic foraminifer zone (P0) is extremely thin (5 cm); it is characterized in Sample 192-1183A-39R-4, 83–87 cm, by dominant, tiny *Guembelitria cretacea* and also very rare *Hedbergella holmsdelensis, Heterohelix globulosa,* and *Woodringina hornerstownensis*. A thin section from the terminal Cretaceous limestone (Sample 192-1183A-39R-4, 87–90 cm) contains abundant planktonic foraminifers and laminae with graded bioclasts disrupted by common horizontal burrowing. This thin section also bisected a vertical burrow that was filled with microfossils of the Zone P0 Danian assemblage. Planktonic foraminifers and calcare-

ous nannofossils indicate that the upper Maastrichtian interval in Hole 1183A is unconformable with the overlying Danian interval.

Cretaceous

Calcareous microfossils can be used to subdivide the Cretaceous section in Hole 1183A into three parts:

1. Microfossil-rich mid-Campanian to Maastrichtian limestones of lithologic Subunit IIIA (see "Lithostratigraphy," p. 4), between interval 192-1183A-39R-4, 87–90 cm, and Section 50R-1, 60 cm;
2. Condensed upper Coniacian to lower Campanian claystones between Section 192-1183A-50R-1, 60 cm, and 50R-2, 75 cm; and
3. Mid-Aptian to upper Albian limestones between Section 192-1183A-50R-2, 75 cm, and 54R-3, 120 cm.

The mid-Campanian to Maastrichtian limestone is rich in both foraminifers and calcareous nannofossils. The Campanian/Maastrichtian boundary is associated with a possible unconformity (Table T6) located between Cores 192-1183A-44R and 45R (top of nannofossil Zone CC24). This unconformity is marked, in part, by the highest occurrences of the calcareous nannofossils *Quadrum trifidum* and *Quadrum gothicum* in Sample 192-1183A-45R-1, 56 cm. The highest occurrences of these two species are 10 m above the base of the Maastrichtian in the new boundary stratotype section near Tercis, France (J. Bergen, unpubl. data). A second unconformity is suggested by the highest occurrences of three nannofossil taxa in Section 192-1183A-46R-2 at 1051.22 mbsf (see Table T8).

Sparse calcareous nannofossil assemblages dominated by nannolith taxa (e.g., *Assipetra* and *Marthasterites*) were recovered from samples taken from the condensed interval between Section 192-1183A-50R-1, 60 cm, and 50R-2, 75 cm. This interval is nearly devoid of planktonic foraminifers, indicating deposition below the foraminifer lysocline. Recovered nannofossils indicate that almost the entire upper Coniacian to lower Campanian interval may be present within this 1.65-m section, although a Santonian/Campanian hiatus may be present (see Table T6).

Approximately 40 m of mid-Aptian to upper Albian limestone was recovered below the major unconformity with the upper Coniacian. Within these mid-Cretaceous sediments, calcareous microfossils indicate a significant mid-Albian unconformity between Sample 192-1183A-52R-2, 105 cm, and 52R-3, 107 cm. In contrast, the Albian/Aptian boundary appears conformable. A small unconformity is inferred within the upper Aptian section (between Sample 192-1183A-54R-2, 28-31 cm, and 54R-2, 35 cm) because the calcareous nannofossil Subzone NC7B and foraminifer *G. ferreolensis* Zone (see Bralower et al., 1995) are missing.

Basement Age

There is ~2 m of limestone between the intra–upper Aptian hiatus and basalt basement (Samples 192-1183A-54R-2, 34 cm, and 54R-3, 119 cm). The calcareous nannofossil *Eprolithus floralis* is present in the sample taken immediately above basement (Sample 192-1183A-54R-3, 119 cm) and the foraminifer *Leupoldina cabri* extends only 23 cm higher in the section. The co-occurrence of these two microfossils defines Zone IC25 of Bralower et al. (1995), who placed this short zone at the base of the upper Aptian (~121 Ma) ~3.5 m.y. younger than their estimate for

the basal Aptian. In the historical lower Aptian stratotype (see Moullade et al., 1998), the lowest occurrence of *Eprolithus floralis* is ~5 m below the base of the upper Aptian and immediately below the base of the *Dufrenoyia furcata* ammonite zone (Zone IC25 straddles the lower/upper Aptian boundary at this locality). Gradstein et al. (1995) estimated the base of the *D. furcata* ammonite zone to be ~118 Ma, which they placed ~3.3 m.y. above their estimate for the basal Aptian.

The presence of the foraminifer index *Praehedbergella sigali* within limestones intercalated with lava flows in the upper 6 m of the basement section (Samples 192-1183A-54R-4, 7–9 cm, and 55R-1, 6–9 cm) indicates an early Aptian age.

Paleoenvironment

Paleoenvironmental analysis was often hampered in Hole 1183A by generally poor recovery of benthic foraminifers in pelagic limestone and chalk. Nevertheless, intensive examination of washed residues and thin sections allowed us to make a reasonable paleoenvironmental interpretation for most of the section. Most of the interval is indicative of normal, deep-water, pelagic carbonate mud deposition. However, we also noted several indications of variation in sedimentation rate and bottom-water oxygenation, as well as sporadic occurrences of allochthonous facies distributed through most of the section. Postcruise studies will be necessary to establish the full distribution of these less common facies. Our initial examination of the section, however, allowed an estimation of paleobathymetric trends for Hole 1183A through time (Table T9). These trends proved to be more variable than we originally anticipated.

T9. Relative paleobathymetric trend, p. 157.

Relatively shallow-water benthic foraminifers were recovered from Aptian limestone immediately above basaltic basement, dominated by nodosariids such as *Lenticulina gaultina, Dentalina nana,* and *Astacolus incurvata,* as well as *Gavelinella barremiana* and indeterminate species of *Polymorphinidae*. Relatively shallow water depths, comparable to the middle to outer shelf in continental margin environments, are indicated by these species. The appearance of common small, spherical radiolarians in the upper Aptian section marked the beginning of a rapid deepening that continued into the Late Cretaceous, probably caused by a rapid subsidence of this part of the Ontong Java Plateau. In the lower Albian, the nodosariid assemblage mixed with slope species of agglutinated foraminifers such as *Dorothia filiformis* and hyaline species such as *Gyroidinoides primitiva* and *Valvulineria loetterlei*. Farther upsection within the Albian, the nodosariid species decline and robust agglutinates such as *Gaudryina dividens* and common *Gyroidinoides infracretacea* and *Osangularia* spp. appear, indicating continued deepening to depths comparable to the lower half of the slope in continental margin environments. The condensed Coniacian to basal Campanian interval marks the climax of the initial stage of subsidence at Site 1183. Abyssal benthic foraminifers characterize the section, including *Gaudryina pulvina* and *Eggerellina* sp. 1 Moullade (Sikora and Olsson, 1991).

Evidence of shallowing paleobathymetry and uplift of Site 1183 is present in the overlying thick Campanian to Maastrichtian section. The shallowing is first evident in an increase in benthic foraminifer diversity in the middle Campanian section, with a mixture of deep-water agglutinated species, such as *Kalamopsis grzybowskii* and *Verneuilina cretacea,* and shallower-water slope species such as *Dorothia oxycona, Nuttallides bronnimanni,* and *Pleurostomella*. Deposition at depths corre-

sponding to the lower half of the slope on continental margins is indicated, and the abyssal species of the condensed zone are absent. The upper Campanian through mid-Paleocene section indicates further shallowing as species of *Gyroidinoides*, *Globorotalites*, and *Osangularia* become more common. The peak of this late Cretaceous shallowing occurred in the late Campanian with a reappearance of rare nodosariids such as *Lenticulina munsteri* and *Dentalina communis*.

Our analysis of the post–mid-Paleocene section indicates a resumption of rapid deepening in the late Paleocene, with a reoccurrence of lower slope species such as *Nuttallides truempyi* and *Clavulinoides paleocenica*. Abyssal taxa, including *Cibicidoides grimsdalei* and *Bulimina callahani*, replaced the slope assemblage by the middle Eocene. Abyssal conditions continued through deposition of the younger section, as indicated by facies markers such as *Melonis pompilioides* forma *sphaeroides* in the Oligocene and *Planulina wuellerstorfi* and *Laticarinina pauperata* in the Miocene.

IGNEOUS PETROLOGY

Introduction

We encountered basement at 1130.37 mbsf (curated depth) at Hole 1183A and drilled 80.7 m of basalt flows that have been divided into eight separate basement units (Table **T10**) primarily on the basis of limestone and/or hyaloclastite interbeds (see **"Igneous Petrology,"** p. 12, in the "Explanatory Notes" chapter and **"Lithostratigraphy,"** p. 4). The interbeds were designated as "A" subunits and the basalt beneath as "B" subunits. The age of the sediment directly overlying basement Unit 1 is early Aptian (see **"Biostratigraphy,"** p. 21; Table **T5,** p. 152). The limestone interbeds never exceeded 12 cm (in curated thickness) (see Figs. **F34, F35; "Lithostratigraphy,"** p. 4; Table **T10**), but the contacts with the overlying and underlying basalt were not recovered, so these interbeds may be thicker. They are extensively recrystallized, but an approximate age of early Aptian was determined for the limestone interbed forming Unit 3A (see **"Biostratigraphy,"** p. 21). The boundary between Units 5 and 6 was defined by the presence of small pieces of hyaloclastite. The boundary between Units 6 and 7 was defined by the presence of a thin (~2 cm) calcite-cemented hyaloclastite breccia containing clasts of basalt glass and recrystallized limestone (Fig. **F35**). The boundary between Unit 7 and 8 was defined by the presence of highly altered, calcite-cemented hyaloclastite. There is an indication of variations in magnetic inclination in Units 5B and 7 (see **"Paleomagnetism,"** p. 32), but we saw no petrologic evidence to subdivide these units. The basement units range in thickness from 0.36 m (Unit 1) to 25.7 m (Unit 6; Table **T10**). Although the drilling rate became progressively slower as we penetrated deeper into basement, recovery was generally good, averaging 56% and ranging from 25% to 94% (see Fig. **F36**).

Macroscopic Description

The basement units are typically aphyric to moderately phyric, aphanitic to fine-grained basalts that are slightly to moderately altered (see **"Alteration,"** p. 29). Olivine (completely pseudomorphed by smectites with subordinate calcite and/or pyrite) is the dominant phenocryst phase, with smaller amounts of unaltered plagioclase (Fig. **F36**). Glassy

T10. Basement unit boundaries and thicknesses, p. 158.

F34. Top of Unit 5, p. 77.

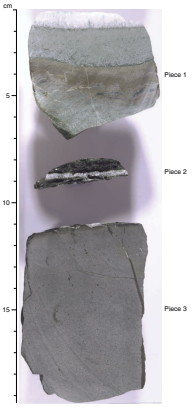

F35. Contact between Units 6 and 7, p. 78.

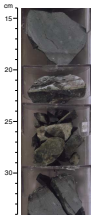

F36. Summary of basement units, p. 79.

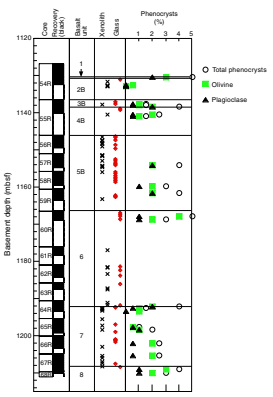

rinds are present throughout the recovered basement section (Fig. F36), and some of the glass is unaltered (e.g., Figs. F37, F38). Immediately adjacent to the glassy rinds are zones of aphanitic basalt 1–2 cm wide; slightly farther from the rind is a 1- to 2-cm sparsely vesicular zone (Fig. F37). Elongate vesicles in this zone are generally aligned perpendicular to the glassy rind and rarely exceed 0.5 cm in length. Grain size increases to fine grained farther from the narrow vesicular zone (Fig. F39). Based on these observations, we concluded that we had cored through a sequence of pillow basalts (see Fig. F40, in which a curved pillow margin is illustrated). Where the glassy rind was not recovered, the same morphology was evident, allowing us to identify aphanitic pillow rims and fine-grained pillow interiors. Core 192-1183A-68R, Unit 8 (Fig. F41), shows evidence of pillow inflation. Apart from the narrow (1–2 cm), sparsely to moderately vesicular zones that are adjacent to pillow margins, the basement units are generally nonvesicular.

Round to subround plagioclase-rich xenoliths ranging from 0.5 to 3 cm in diameter are present throughout the basement sequence (Figs. F36, F42, F43). They are most common in Units 5B and 7 (Fig. F36) but are found in all units except Unit 1, where only 0.36 m was recovered, and Unit 8, the base of which was not reached.

One of the objectives for Site 1183 was to determine the eruptive environment (subaerial, shallow submarine, or deep submarine) of the final volcanic activity in the shallowest part of the Ontong Java Plateau. Based on the recovery of an essentially nonvesicular series of pillow basalts, volcanism was entirely submarine and either eruption took place at depths that prevented abundant vesicle formation (probably >800 m; Moore and Shilling, 1973) and/or the magma was volatile poor.

Petrography

We described 22 thin sections from both pillow rims and interiors, including some samples selected for xenolith and alteration features. The degree of alteration is highly dependent on the proximity to secondary veins but is generally slight to moderate (see "Alteration," p. 29). For the complete thin section descriptions see "Site 1183 Thin Sections," p. 99.

The textures exhibited in thin section demonstrate the different cooling rates between pillow rims and interiors. In order to save the glassy rinds for shore-based studies, we did not sample this material on the ship. Early-crystallizing olivine and plagioclase phenocrysts are best observed in the aphanitic pillow rims (Fig. F44) and are sometimes difficult to identify in the pillow interiors where the groundmass is more coarsely crystalline (e.g., Fig. F45). Thin sections demonstrate that the majority of the basalt flows are sparsely olivine (±plagioclase) phyric and all are essentially nonvesicular. Small (0.1–1.2 mm) euhedral to subhedral pseudomorphs after olivine were observed in all thin sections. The dominant replacement minerals include smectite (nontronite group), celadonite, saponite, and calcite (e.g., Figs. F44, F46, F47; see "Alteration," p. 29). Calcite replacement becomes more prevalent at greater depths. Rare localized accumulations of olivine phenocrysts result in some samples being classified as moderately olivine (±plagioclase) phyric. Plagioclase phenocrysts (0.1–0.4 mm wide) are less abundant than olivine; they form euhedral to subhedral tabular crystals that usually exhibit oscillatory zoning. Some plagioclase phenocrysts contain minute, partly devitrified glass inclusions (Fig. F48). Rarely, olivine

F37. Section through basaltic pillow with glassy rind and vesicular zone, p. 80.

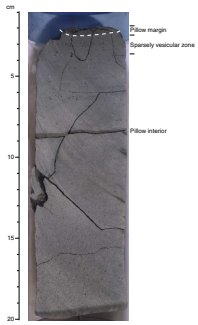

F38. Outer and cut surfaces of pillow rim glass and contact between pillows, p. 81.

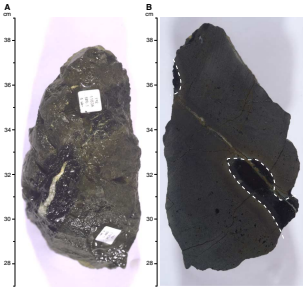

F39. Basaltic pillow section with glassy rind and vesicular zone in pillow rim, p. 82.

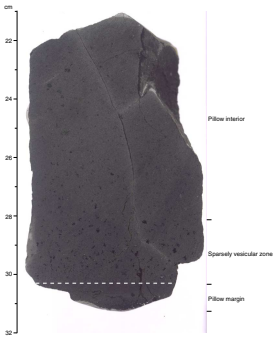

F40. Curved pillow margins, p. 83.

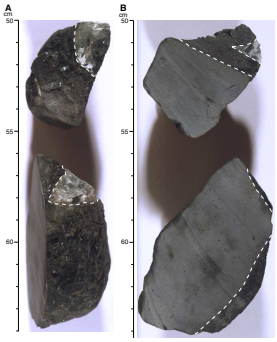

and plagioclase are found together as glomerocrysts (Fig. F44), and a clinopyroxene-plagioclase glomerocryst is present in one thin section (Sample 192-1183A-64R-2 [Piece 2, 15–17 cm]; Fig. F49). Strained and partially resorbed clinopyroxene crystals observed in three thin sections (e.g., Sample 192-1183A-65R-3 [Piece 2, 18–19 cm]; Fig. F50) are probably xenocrysts. Titanomagnetite is a minor yet ubiquitous groundmass phase (e.g., Fig. F51); it is unaltered and exhibits skeletal to dendritic or trellis morphology. Primary sulfide is rare in all but three of the thin sections; one from Unit 5B (Sample 192-1183A-59R-1 [Piece 7C, 107–109 cm]) and two from Unit 7 (Samples 192-1183A-64R-2 [Piece 10B, 136–138 cm] and 65R-3 [Piece 2, 18–19 cm]). In these sections, sulfide is found as ≤0.01-mm subround to elongate blebs in the groundmass and as inclusions in groundmass clinopyroxene and plagioclase; it is tentatively identified as pentlandite and/or possibly troilite. Otherwise, primary sulfide is found only as <0.005-mm inclusions (too small for accurate petrographic identification) in groundmass clinopyroxene and plagioclase.

The groundmass in thin sections of pillow rims close to glassy rinds ranges from partly to totally glassy and exhibits subvariolitic, variolitic or spherulitic (cryptocrystalline) textures with skeletal plagioclase and mesostasis. The mesostasis consists of elongate plagioclase, fibrous clinopyroxene, and glass (e.g., Figs. F51, F52), which is altered to brown clay (smectite group?). Rare, irregularly shaped cavities (≤1.5 mm) filled with green clay (nontronite and/or celadonite) are also present (see "Alteration," p. 29).

Fine-grained samples from pillow interiors typically have subophitic, intergranular, and/or intersertal textures (e.g., Figs. F53, F54). Quenched domains showing a subvariolitic texture are present locally, as is subtrachytic alignment of plagioclase. The groundmass consists of plagioclase and clinopyroxene, with minor titanomagnetite and mesostasis composed of devitrified and altered glass. Plagioclase is generally slightly more abundant than clinopyroxene and ranges in morphology from acicular-skeletal to elongate laths. Clinopyroxene is anhedral to subhedral and mainly equant. Some clinopyroxene exhibits classic bow-tie intergrowths with plagioclase.

One interesting feature is the grain-size banding exhibited in Sample 192-1183A-68R-1 (Piece 3A, 32–35 cm) from Unit 8 (Fig. F41). This core section is from a fine-grained pillow interior and shows alternating hypohyaline and hypocrystalline layers with subvariolitic to intersertal textures and localized subtrachytic patches. This banding is consistent with differential cooling rates during repeated pillow inflation through magma injection. In Sample 192-1183A-67R-1 (Piece 2C, 46–48 cm), the glass-rich layers are subparallel with the elongate subtrachytic patches. Olivine phenocrysts are concentrated in the more crystalline bands and plagioclase laths are aligned around these crystals (Fig. F55).

Thin sections of xenoliths demonstrate an interlocking network of medium to coarse grains of plagioclase (1–10 mm) with interstitial patches consisting of devitrified glassy mesostasis containing crystallites of clinopyroxene and plagioclase with brown clay and titanomagnetite. The plagioclase crystals exhibit fine-scale, complex, oscillatory zoning with truncations indicative of resorption (Fig. F56). One interstitial patch in Sample 192-1183A-57R-3 (Piece 2, 15–17 cm) contains a partially resorbed clinopyroxene crystal (Fig. F57), but, in most cases, the interstitial material appears to consist of quenched (devitrified) basaltic glass. Rarely, these interstitial patches have shapes suggesting that mafic phases may originally have been present (Fig. F58). Elsewhere,

F41. Pillow inflation structures, p. 84.

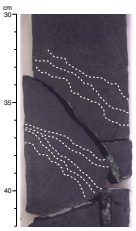

F42. Subround plagioclase-rich xenolith, p. 85.

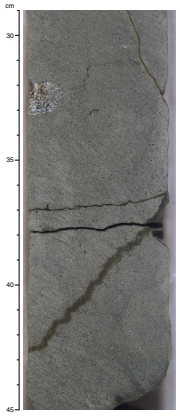

F43. Subround plagioclase-rich xenolith on core's outer surface, p. 86.

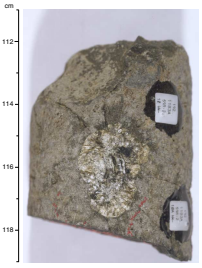

F44. Aphanitic pillow rim, p. 87.

F45. Pillow interior texture, p. 88.

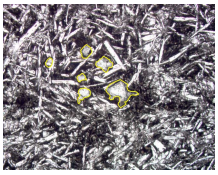

the shape of the interstitial space is controlled by the large, interlocking plagioclase crystals (Fig. F59), producing subhedral to anhedral outlines similar to that of the partially resorbed clinopyroxene in Figure F57. At the perimeter of the xenolith in Sample 192-1183A-57R-3 (Piece 2, 15–17 cm), we again observed partially resorbed clinopyroxene crystals (Fig. F60). Disaggregation of these xenoliths may be responsible for the presence of rare, large, partially resorbed clinopyroxene xenocrysts (see Fig. F50).

Geochemistry

We selected 11 samples for whole-rock analysis by inductively coupled plasma–atomic emission spectrometry (ICP-AES). Weight loss on ignition (LOI) data suggest that the degree of alteration decreases downhole in the basement sequence; LOI values decrease from 2.4 wt% in Units 1–3B to <0.6 wt% in the rest of the sequence (Table T11). All basalts analyzed are tholeiitic, and all but one (Sample 192-1183A-64R-2 [Piece 2, 15–17 cm]) are olivine normative (Table T11).

Comparison with Other Ontong Java Plateau Basalts

The sequence of basalts and limestone interbeds recovered at Site 1183 is similar to the sequences recovered at Sites 803 and 807, except that we did not encounter thick, massive basalt flows like those reported at Site 807 (e.g., Unit F, a 28-m-thick flow) (Kroenke, Berger, Janecek, et al., 1991). At Site 803, the basalt was described as fine grained and sparsely phyric with plagioclase, clinopyroxene, and olivine phenocrysts (Kroenke, Berger, Janecek, et al., 1991). In three instances we observed rare large phenocrysts of plagioclase and clinopyroxene (up to 1 cm). At Site 807, Unit A basalt was described as very fine grained with rare euhedral plagioclase phenocrysts up to 3 mm long. Basalt forming Units C–G was described as very fine grained to fine grained with olivine (pseudomorphs), plagioclase, and clinopyroxene phenocrysts (Kroenke, Berger, Janecek, et al., 1991) (see Fig. F61). At Site 1183, the phenocryst phases are olivine (altered to smectites, celadonite, and subordinate calcite) and plagioclase. Basalt from Site 807 seems to be slightly more evolved than that recovered from Site 1183. Basalt from both Sites 807 and 1183 contains clinopyroxene-plagioclase glomerocrysts (cf. Figs. F62, F49) and partially resorbed clinopyroxene xenocrysts (cf. Figs. F63, F50), although xenocrysts and glomerocrysts appear to be more abundant at Site 807. The one feature that sets the basalt recovered during Leg 192 apart from that recovered during previous drilling legs is the apparently ubiquitous presence of plagioclase-rich xenoliths (Fig. F36). However, small (3–5 mm) clusters of plagioclase crystals are present in one thin section from the Units C–G basalt of Site 807 (e.g., Sample 130-807C-93R-1 [Piece 39, 137–139 cm]; see Fig. F64), indicating that plagioclase-rich xenoliths are present, if not abundant, at Site 807.

Plagioclase-rich xenoliths are also present on the island of Malaita in the Solomon Islands, nearly 1000 km southeast of Site 1183. These xenoliths are present only in basalt of the Kwaimbaita Formation, with which the Units C–G basalt at Site 807 has been linked by Tejada et al. (in press). The xenoliths appear cumulate in nature, and the compositional zoning in the plagioclase (e.g., Fig. F56) indicates complex magma chamber processes. The presence of these xenoliths in petrographically similar basalt from widely separated areas of the plateau has

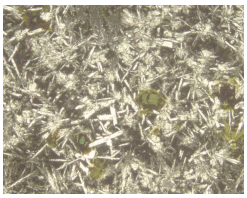

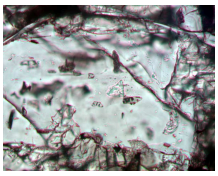

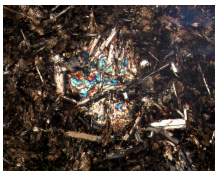

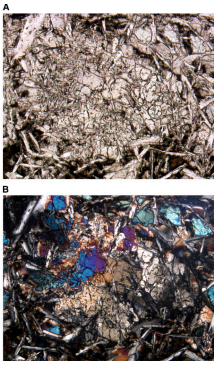

implications for magma chamber size, processes, and/or the geographical extent of these flows.

The similarity between Site 1183 basalt and that from Units C–G at Site 807 is also evident from the geochemical data. The 11 basalt samples that we analyzed by shipboard ICP-AES are all low-K tholeiities (Fig. F65) and have slightly lower (on average) incompatible trace element abundances than the basalt of Units C–G (Fig. F66). Generally, however, the compositions of Site 1183 lava flows are virtually identical to those of Units C–G (Figs. F66, F67). Furthermore, the geochemical analyses (Table T11) show that lava flows comparable to Unit A basalts of Site 807 and the Singgalo Formation basalts of Malaita, both of which form the upper parts of their respective lava piles, are apparently absent from Site 1183.

ALTERATION

The entire section of basaltic basement recovered from Hole 1183A has undergone low-temperature water-rock interactions, resulting in complete replacement of olivine and almost complete replacement of glassy mesostasis. Clinopyroxene and plagioclase only show alteration in some halos close to veins and miarolitic cavities. The overall alteration of the basalt pieces ranges from 5 to 30 vol%, estimated visually by color distribution and not taking into account the veins. Throughout this section we refer to volume percentages of the various alteration types, veins, hyaloclastite, etc.; our assumption is that the area occupied by these features on the sawed surfaces of the cores is equivalent to volume percent of the cores.

Clay minerals (tentatively identified as nontronite, saponite, and celadonite) are the most abundant secondary minerals. Secondary phyllosilicates in rocks from Hole 1183A were identified by color and hardness in hand specimen and by optical properties in thin section with occasional use of the XRD. For instance, we distinguished nontronite from saponite on the basis of absorption color: yellow-green vs. brownish tan to colorless, respectively. Celadonite was distinguished from the other clay minerals on the basis of its pleochroism and anomalous birefringence. We compared the phyllosilicates observed in rocks from Hole 1183A with well-studied clay minerals identified in other sections of the oceanic crust (Böhlke et al., 1980; Honnorez, 1981; Alt and Honnorez, 1984; Alt et al., 1986). The identification of the phyllosilicates in Leg 192 basalts remains tentative pending shore-based analyses with XRD, electron microprobe, and scanning electron microscope. Calcite, pyrite, chalcedony, and quartz are less abundant and have more restricted distributions. No zeolite minerals were identified in basaltic samples.

Low-Temperature Alteration Processes

Based on core descriptions and thin section observations, we have identified three types of low-temperature alteration.

Pervasive Alteration

All of the basalts recovered from Hole 1183A show signs of pervasive alteration. Color ranges from dark to light gray in pieces affected by pervasive alteration (Fig. F68). Most pieces also exhibit colored halos re-

F51. Skeletal plagioclase laths in groundmass, p. 94.

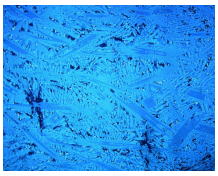

F52. Basalt with variolitic texture around phenocrysts, p. 95.

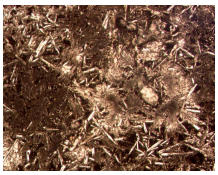

F53. Pillow interior, Sample 192-1183A-60R-1, p. 96.

F54. Pillow interior, Sample 192-1183A-67R-1, p. 97.

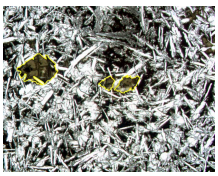

F55. Subtrachytic texture, p. 98.

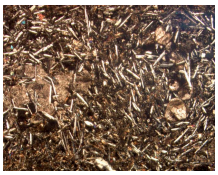

F56. Compositional zonation in plagioclase from a xenolith, p. 99.

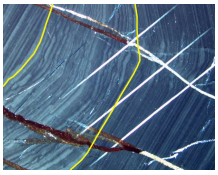

sulting from one or both of the other two alteration processes described below. We identified these colors on wet, cut surfaces of the core. Gray basalts are the most abundant, and the abundance of this color does not vary downhole. Secondary minerals in gray basalts are clay minerals (predominantly saponite with subordinate nontronite and celadonite) replacing interstitial glass and mesostasis in the groundmass. Clay minerals (celadonite, saponite, or minor nontronite) and (less commonly) Fe oxyhydroxides and calcite or (more rarely) pyrite replace euhedral olivine microphenocrysts (Figs. F69, F70, F71, F72, F73, F74, F75, F76) and, rarely, plagioclase phenocrysts. Overall alteration in pervasively altered basalts ranges from <5 to 20 vol%. Pervasive alteration results from extended interaction between basalt and seawater-derived fluid (evolved seawater) under anoxic to suboxic conditions at low temperature (probably 10°–50°C). Pervasive alteration ceases once secondary minerals fill fluid pathways (i.e., open cracks).

Black Halos

We observed black halos along surfaces previously exposed to seawater and, less commonly, along the margins of veins (Figs. F72, F73). Olivine phenocrysts are most commonly altered to clay minerals (including celadonite [Fig. F74] and/or nontronite [Fig. F76]) and Fe oxyhydroxides. In a few instances, pyrite is associated with celadonite in olivine pseudomorphs (Fig. F75). Fine-grained pyrite is also commonly disseminated in the groundmass of the adjacent gray rock beyond the edges of black halos. Calcite is less common in these halos than in pervasively altered basalt. The contact between black halos and the dark gray interior is very sharp both in hand specimen and in thin section (Fig. F69). This is a result of strong changes in chemical conditions across the alteration front during the formation of the black halos.

This stage of alteration results from low temperature (<60°C) interaction between basalt and seawater mixed with hydrothermal solutions. Black halos are characteristic of an early alteration process initiated during cooling of the lava within 1–2 m.y. of basalt emplacement (Böhlke et al., 1980; Honnorez, 1981; Laverne, 1987). Black halos decrease in abundance downhole but less so than the olive halos described below (Fig. F68).

Olive Halos

Olive halos are olive-brown discolorations, in zones <1 to 5 mm thick, of the host rock adjacent to Fe oxyhydroxide–bearing veins. They are caused by Fe oxyhydroxides staining and partly replacing the primary minerals of the basalt groundmass and filling the interstitial voids in the groundmass (Fig. F77). Olive halos result from a basalt-seawater reaction corresponding to halmyrolysis or submarine weathering, which takes place at bottom seawater temperature (i.e., ~2°C), in oxidizing conditions, and generally with large water/rock ratios. The halos represent the last alteration stage, which ceases when the oceanic crust is sealed off from the overlying seawater by a sufficiently thick and comparatively impermeable sediment cover. Olive halos decrease in abundance downhole (Fig. F68) and almost disappear below 1180 mbsf, except for three occurrences in Sections 192-1183A-65R-2, 65R-3, and 67R-2.

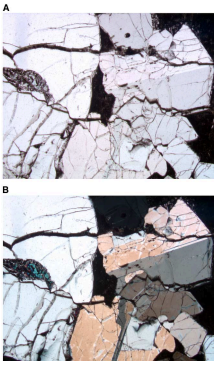

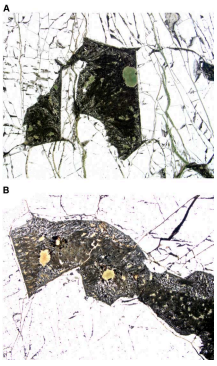

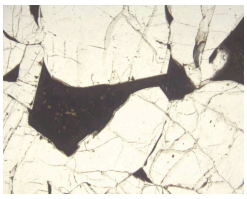

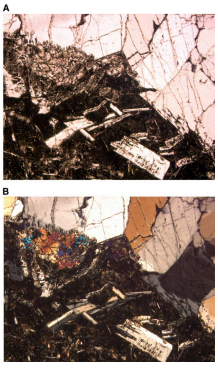

Glass Alteration

Alteration of glass to phyllosilicates ranges from 20 to 100 vol%. Basaltic glass is present either in pillow rims or as shards in hyaloclastites. Glassy mesostasis is rarely present in the pillow-basalt groundmass. Pillow-rim glass is generally the least altered because of its low permeability. Glass shards in the hyaloclastites, because of their large reactional surface areas, are almost always completely replaced by phyllosilicates. One exception is a hyaloclastite found in Section 192-1183A-60R-1 (Piece 1) that contains pillow-rim material composed mostly of unaltered glass cemented by calcite. The association of unaltered glass clasts cemented by calcite is commonly observed in the oceanic crust, regardless of the age of the hyaloclastite or the environment in which it formed (Honnorez, 1967, 1972).

Veins and Miarolitic Cavity Fillings

We counted 849 veins in the 80.7 m of basement penetrated in Hole 1183A. This number represents an average of 19 veins/m for the 44.8 m of basalt recovered at the site. Most of the veins result from symmetrical infilling of open cracks with minor or no replacement of the wall rock. Evidence for the successive reopening and filling of veins is often clear, particularly in the case of calcite deposition, because of the contrast in color between the carbonate and the other vein-filling secondary minerals (Fig. F73). The vast majority of the veins contain the following succession of secondary minerals, from vein walls to centers: smectite and/or celadonite, Fe oxyhydroxide (Fig. F78) or pyrite, and calcite. Disseminated pyrite grains commonly line the walls of smectite and/or celadonite veins cracked open during drilling. When observed within veins in thin section, pyrite completely fills the width of the vein. Pyrite is also associated with black halos as grains scattered in the gray basalt groundmass beyond the alteration front.

The downhole distribution of calcite and smectite (i.e., either or both nontronite and saponite) in veins (Fig. F79) does not show any systematic variation with depth. The presence of celadonite is greatly underestimated because both smectite and celadonite appear black on wet, cut core surfaces; hence the plot of downhole distribution of celadonite is misleading. Pyrite first appears at 1146 mbsf and shows a slight increase in abundance with depth. Conversely, Fe oxyhydroxides seem to be distributed unevenly, with only one occurrence above 1145 mbsf and an apparent absence between 1148 and 1156 mbsf and between 1169 and 1181 mbsf.

Rare occurrences of native copper are restricted to smectite-bearing veins in the uppermost basement cores, whereas we only observed chalcedony and quartz in the lower part of the cored basement: Section 192-1183A-66R-1 (Pieces 6 and 7), Section 66R-2 (Piece 4) (Figs. F80, F81), and Section 67R-1 (Piece 2C) (Figs. F82, F83).

Vein width does not show any downhole trend (see Fig. F84) except for the 2- to 5-mm-wide veins that seem to be more abundant above 1167 mbsf. Hairline, <1-mm- or 1-mm-wide veins are uniformly present through the entire basement section. The observed number of >5-mm-wide veins is not statistically significant. Miarolitic voids are common throughout the cores, whereas vesicles are present only rarely. The maximum dimension of the miarolitic cavities ranges from a few tenths of a millimeter to 4 mm (Fig. F85). The cavities are generally completely

F61. Phenocrysts of clinopyroxene, olivine, and plagioclase, p. 104.

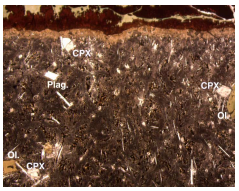

F62. Clinopyroxene-plagioclase glomerocryst in groundmass, p. 105.

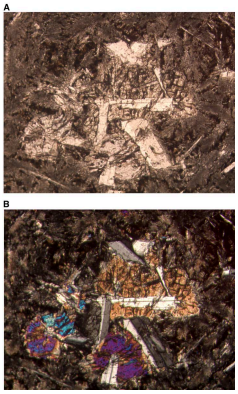

F63. Clinopyroxene xenocryst, p. 106.

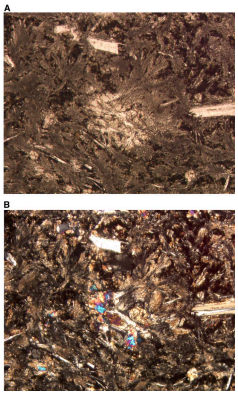

F64. Plagioclase glomerocrysts, p. 107.

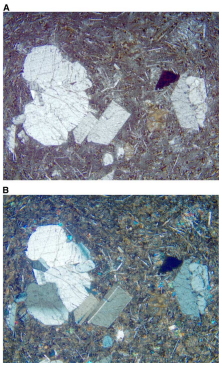

filled by the same secondary minerals as those observed in the veins (Fig. F86).

STRUCTURAL GEOLOGY

Rocks from Site 1183 exhibit relatively few structural features. The sedimentary rocks that overlie basaltic basement are characterized by horizontal bedding planes and appear to have experienced little tilting or faulting (see "Lithostratigraphy," p. 4). Veins are common in the basaltic basement, which has been subdivided into eight units on the basis of sedimentary interbeds, basalt texture, and phenocryst abundance and size (see "Igneous Petrology," p. 25; Fig. F36). No ductile or cataclastic fault zones, or tectonic breccias were encountered in the cores.

Location, vein width, and mineral filling were documented for 849 veins at this site. A total of 303 calculated and measured vein orientations are included in this data set. The graphic presentation of true dip, fracture density, and vein abundance in Figure F87 provides some information about the relation between vein characteristics and basement depth. This figure graphically depicts the measured and calculated dip inclinations vs. depth. Fracture density has been calculated per meter of core section (see "Structural Geology," p. 18, in the "Explanatory Notes" chapter). Vein abundance has been calculated by determining the total thickness of the veins in millimeters per meter. For veins defined as hairline, we assigned a thickness of 0.25 mm, assumed to be a representative average for these types of veins.

The distribution of true vein dip shows no systematic variation with depth in basement (Fig. F87). Although the graph is affected by a pronounced data gap in Core 192-1183A-60R, which was followed by a change of the drill bit, the fracture density appears to be high at 1145–1165 and ~1195–1210 mbsf. These zones of high fracture density are also distinct in the graph of vein abundance, which shows maxima in approximately the same intervals.

The absence of downhole logging information and structural marker planes (e.g., sedimentary bedding and basaltic layering) precludes reorientation of the measured veins and the calculation of dip azimuths. Paleomagnetic results may enable the reorientation of some of the veins on the larger pieces during shore-based analysis of the data (see "Paleomagnetism," p. 32) and allow calculation of true dip azimuths.

PALEOMAGNETISM

Introduction

We took pass-through magnetometer measurements on all split-core archive sections. Sediment cores were measured at 5-cm intervals. Coherent basalt pieces that could be oriented unambiguously with respect to the top were measured at 1-cm intervals. We took pass-through magnetic susceptibility measurements on all unsplit core sections at 4-cm intervals.

In order to isolate the characteristic remanent magnetization (ChRM), we subjected the cores to alternating-field (AF) cleaning. The

F65. Total alkalies vs. silica, p. 108.

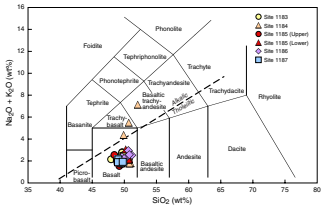

F66. Zr vs. TiO_2, p. 109.

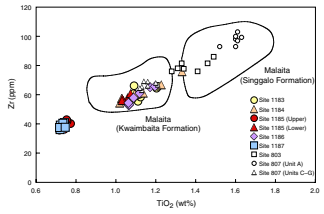

F67. TiO_2 vs. Mg#, p. 110.

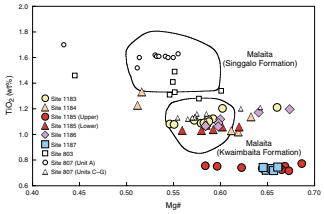

F68. Basement rock color distribution, p. 111.

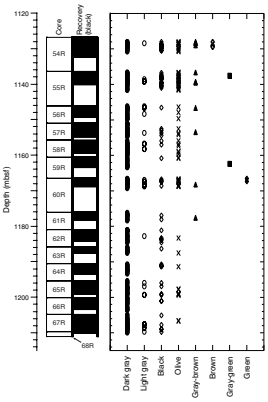

F69. Alteration front between (black) halo and (gray) interior, p. 112.

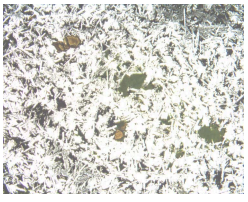

number of AF demagnetization steps and peak-field intensity varied depending on lithology, the natural remanent magnetization (NRM) intensity, and the amount of time available. On average, sediment half-cores were demagnetized using three AF steps in addition to the measurement of NRM. The basalt half-cores were demagnetized using a minimum of six AF steps. The maximum applied field ranged between 20 and 50 mT. We analyzed the results in Zijderveld and stereoplot diagrams, and, where possible, we calculated the ChRM direction using principal component analysis (Kirschvink, 1980). Examples of good-quality AF demagnetization results are shown in Figure **F88.**

Results from Sedimentary Units

Magnetic susceptibility and NRM intensity variations through the sedimentary section are closely correlated (Fig. **F89;** Table **T12**). In general, we find that the magnetic properties of sediments recovered from Hole 1183A correlate with the lithostratigraphy (see **"Lithostratigraphy,"** p. 4). Below we describe the magnetic characteristics of the lithostratigraphic subunits:

1. Subunits IA and IB have low NRM intensity and magnetic susceptibility. The few discrete peaks of high NRM and susceptibility values could in many cases be tied directly to the visible presence of pyrite nuggets. By analogy to previous studies of sediments from the Ontong Java Plateau (ODP Leg 130), we speculate that primary magnetite in these subunits has suffered diagenetic reduction to pyrite, thereby destroying the primary remanent magnetization. For these reasons, reliably defining the primary remanent magnetization of Subunits IA and IB was impossible.
2. Subunit IC has relatively high NRM intensity and magnetic susceptibility, caused by the presence of numerous ash beds with high concentrations of magnetic minerals. Glass from the ash layers appears fresh in smear slides, indicating only minor diagenetic alteration. Burrowing has disseminated the ash layers of Subunit IC. The subunit proved ideal for paleomagnetic work, leading to precise determinations of the ChRM direction.
3. Recovery from Subunit IIA was low. Although the NRM intensity of the intervals that could be measured was low, we were able to define the ChRM direction from the few intact cores.
4. Subunit IIB has high NRM intensity and magnetic susceptibility, related to input of volcanic material. Although Subunit IIB is somewhat altered, the ChRM direction is easily defined.
5. Subunit IIIA has low NRM intensity. Once again, the ChRM direction is easily defined using stepwise demagnetization.
6. Subunit IIIB contains dark clay-rich chalks with goethite. We suspect the magnetic remanence in these black chalks to be secondary and have chosen not to include these data in our analysis.

Magnetostratigraphy

Based on biostratigraphic data (see **"Biostratigraphy,"** p. 21), we were able to correlate certain parts of the magnetic polarity recorded in the sediments with the geomagnetic reversal timescale (Berggren et al., 1995). In particular, the polarity intervals in Cores 192-1183A-17R to

F70. Olivine pseudomorph and miarolitic void filled with saponite, p. 113.

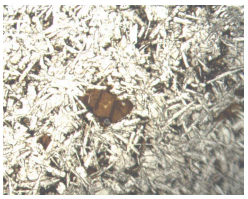

F71. Euhedral olivine pseudomorph in basalt interior, p. 114.

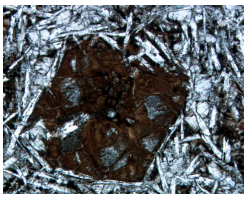

F72. Black halos on sides of hairline vein filled with smectite, p. 115.

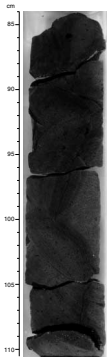

F73. Black halos on sides of vertical vein, p. 116.

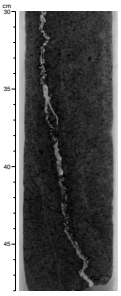

F74. Euhedral olivine (celadonite) pseudomorph in black halo, p. 117.

25R could be tied with reversals in the late Eocene–early Oligocene (e.g., Chrons C12N and C12R). We also obtained reasonable correlations of polarity intervals in Cores 192-1183A-32R to 48R with the middle Eocene–Campanian polarity chrons. In some cases, polarity reversals were recorded in an individual core (e.g., Core 192-1183A-39R contains the Cretaceous/Paleogene boundary; Fig. F90), and we were able to tie the depth interval closely to the geomagnetic polarity timescale. Elsewhere, entire cores recorded a single polarity, and we had difficulty uniquely identifying the corresponding chron. Figure F90 shows the polarity intervals recorded in Cores 192-1183A-36R through 41R and our proposed correlation with the polarity timescale.

Paleolatitudes

The high quality of paleomagnetic data from many of the sedimentary cores allowed a precise determination of the ChRM using principal component analysis. For the analysis of paleolatitudes we accepted only those directions that had maximum angular deviation values <5°. Several cores (e.g., Core 192-1183A-21R; Fig. F91) showed consistent magnetic directions (declination and inclination values) over intervals of 15 cm (i.e., four sample points at 5-cm sampling intervals) to >1 m. We used the method of Kono (1980) on data from these consistent intervals to calculate the mean paleoinclination for each core. Where there were insufficient consistent values for an individual core or the core was short, we combined inclination values from successive cores to produce a paleoinclination for that depth interval. We obtained paleolatitudes from the inclination data using the axial dipole assumption

$$\tan(\text{latitude}) = 0.5 \times \tan(\text{inclination}).$$

In determining paleolatitude, we have interpreted positive inclinations as those corresponding to reversely magnetized samples in the Southern Hemisphere. We used ages determined from the biostratigraphic data (see "Biostratigraphy," p. 21) supplemented with ages determined from the magnetostratigraphy (see above) to provide ages for the paleolatitudes (Fig. F92). There is a gradual increase in (southerly) latitude with increasing age, which we interpret to reflect the motion of the Pacific plate during the past ~120 m.y. The paleolatitudes obtained are consistent with previously published paleomagnetic data for the Pacific plate (listed by Petronotis and Gordon, 1999). If the paleolatitudes are confirmed by shore-based studies of discrete samples, then they imply a position of ~25°–30°S for the plateau at the time of major igneous activity at ~120 Ma. This is less southerly than the paleoposition implied by the plate reconstruction of Neal et al. (1997), which was made in a stationary hot-spot reference frame.

Magnetic inclinations derived from sediments are sometimes influenced by compaction, producing values that are too shallow. Until the influence of compaction can be determined from shore-based studies, we believe that the inclination values should be treated with caution. However, it is encouraging that the magnetic inclinations obtained from basalt samples in Cores 192-1183A-54R and 55R (Table T13) produce very similar inclination values. The inclination values may also be influenced by any tilting of the sedimentary formations, but we found the sedimentary layers to be horizontal where depositional surfaces were apparent, indicating that there has been no major systematic tilting.

F75. Euhedral olivine (celadonite and pyrite) pseudomorph in black halo, p. 118.

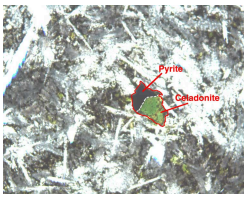

F76. Euhedral olivine pseudomorphs in pillow basalt interior, p. 119.

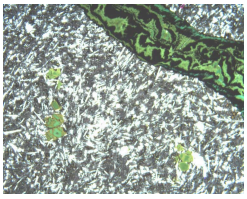

F77. Olive halos on sides of vein, p. 120.

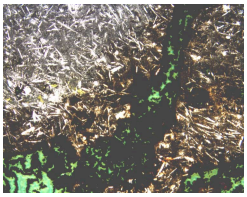

F78. Vein filled with goethite and celadonite, p. 121.

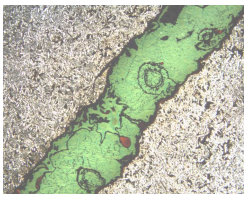

F79. Vein-mineral distribution with depth, p. 122.

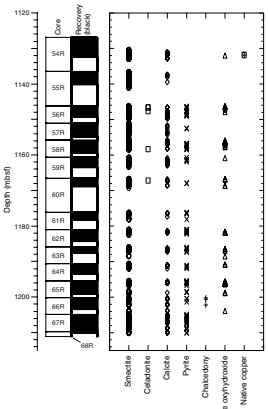

Results from Basaltic Units

We performed detailed AF demagnetization on all coherent basalt pieces that could be oriented unambiguously with respect to the top of the core. All pieces contained a vertical secondary component most likely induced during drilling. In almost all cases, we were able to remove this secondary magnetization by 10- to 20-mT AF demagnetization and isolate the ChRM direction at higher fields (e.g., Fig. F88B). Another problem encountered during half-core measurements on basalt pieces relates to the broken nature of the basalt cores. Because the short pieces have no relative azimuthal orientation, we observed a magnetic interference of one piece on the next within the relatively large (~15 cm) measurement region of the pass-through magnetometer. This problem is exemplified by data from Section 192-1183A-55R-1 (Pieces 4A–4E) (Fig. F93). Principal component analysis for all measured points in this interval reveals that the pieces have different declinations (i.e., the pieces have no relative azimuthal orientation). Pieces 4A–4C are <10 cm in length, and there is significant interference, leading to low NRM intensities and varying inclinations. Pieces 4D and 4E are sufficiently long (>15 cm), so that, in the middle of these pieces, we can define the characteristic inclination. Note that pieces 4D and 4E both give a consistent estimate of inclination of –47°.

We used the following criteria to select only reliable inclination values. The pieces had to be at least 15 cm long, the maximum angular deviation of the principal component analysis had to be <3°, and the pieces had to be homogeneously magnetized. Of the 181 pieces analyzed, only 25 fulfilled these criteria (Table T13). In order to test the half-core data, we demagnetized one discrete sample from Section 192-1183A-65R-1 (Piece 3). This discrete sample yielded an inclination of –38.8°, in good agreement with –38.7° for the half-core measurement.

Although the NRM intensities are quite variable, we identified a distinct difference between the upper and lower basement units. The upper units (Units 2B–4B) are generally more weakly magnetized and have Koenigsberger ratios (Q in Table T13) of <10. Units 5B to 7, however, are more magnetic and, although variable, have many Q values >10. Whereas on the basis of the NRM intensities we are able to distinguish only two units in the basement samples, stable magnetic directions indicate considerably more variation both between units and, more importantly, within units, indicating that the basement units as defined (see "Igneous Petrology," p. 25) contain many distinct subunits. Significant changes in inclination values within Units 5B and 7 suggest that these units contain at least three subunits with thicknesses of ~5 m.

PHYSICAL PROPERTIES

Introduction

Index properties, including wet bulk density, grain density, dry bulk density, water content, void ratio, and porosity, were all measured on discrete samples taken from each core recovered in Hole 1183A. Whole sections of all cores were run through the multisensor track (MST), which measured magnetic susceptibility, gamma ray attenuation (GRA) bulk density, and natural gamma radiation (NGR). We measured sonic

F80. Calcite vein with chalcedony and quartz (plane-polarized light), p. 123.

F81. Calcite vein with chalcedony and quartz (crossed polars), p. 124.

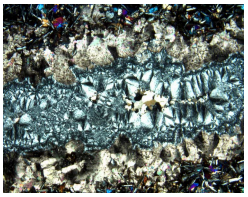

F82. Calcite vein (plane-polarized light), p. 125.

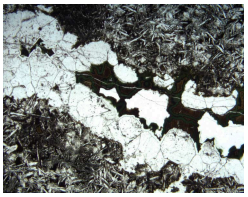

F83. Calcite vein (crossed polars), p. 126.

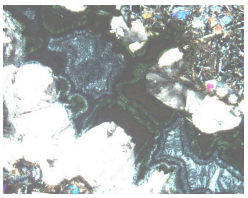

F84. Vein-width distribution with depth, p. 127.

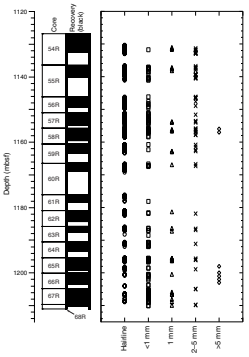

compressional (*P*-wave) velocities on cut samples and, where possible, in more than one direction on oriented cubes to investigate velocity anisotropy. Thermal conductivity was measured in unsplit sediment sections and on split rock samples from each core.

Index Properties

We measured the wet mass, dry mass, and dry volume of each sample taken from the core and calculated wet and dry bulk density, water content, grain density, and porosity (Table T14; Fig. F94). The general downhole increase in wet bulk density corresponds to a decrease in porosity and water content with depth of burial. As shown in Figure F94, porosity decreases from 64% to 56% in the ooze and chalk of lithologic Subunits IA and IB (see "Lithostratigraphy," p. 4), to 56%–42% in the ash-bed-bearing chalks of Subunit IC, to 52%–25% in the chert- and zeolite-bearing limestone of Unit II, to 45%–14% in the white and gray limestone of Unit III and, finally, to 19%–3% in the basalts of the basement. Little variation in grain density (between 2.6 and 2.8 g/cm^3, with a mean value ~2.7 g/cm^3) occurs in the sedimentary units (Fig. F94), which agrees with the high and relatively constant $CaCO_3$ content observed downhole (see "Lithostratigraphy," p. 4). Bulk density increases sharply near 987 mbsf (the boundary between Subunits IIB and IIIA). This increase appears to correlate with a zeolite-rich chalk zone in the lowest part of Subunit IIB, near the Cretaceous/Paleogene boundary (see "Lithostratigraphy," p. 4), where both water content and porosity (Table T14; Fig. F94) also decrease.

Multisensor Track Measurements

Magnetic Susceptibility

We determined magnetic susceptibility with the Bartington meter at 4-cm intervals along all whole-core sections. The results are shown in Figure F95. Magnetic susceptibility was also measured independently every 2 cm on the point-susceptibility meter (see "Lithostratigraphy," p. 4). The two magnetic susceptibility data sets compare well with each other. Susceptibility peaks in sedimentary units commonly correlate with lithologic changes, such as the ash layers found in Subunits IC and IIIB. Detailed results are discussed in "Paleomagnetism," p. 32, in conjunction with discussion of the NRM pass-through and discrete paleomagnetic sample measurements.

Gamma Ray Attenuation Bulk Density

We estimated bulk densities from whole-core GRA measurements, which were made in all sections (Fig. F95). The maximum GRA densities give the best estimate for the true bulk densities of the sediments (Blum, 1997). In the ooze and chalk interval of Unit 1, between 328.1 and 836.8 mbsf, the average estimated maximum density is 1.6 g/cm^3. Below 838.6 mbsf, which is the boundary between lithologic Units I and II (see "Lithostratigraphy," p. 4), the estimated maximum bulk density increases to an average of 1.8 g/cm^3 in Unit II. Maximum density abruptly increases at the lithologic unit boundary between sediment and basalt (Fig. F95). In basement, below 1131 mbsf, estimated maximum bulk density reaches an average of 2.6 g/cm^3. Comparison of the downhole maximum GRA bulk density profile (Fig. F95) with bulk

F85. Miarolitic cavities filled with smectite and calcite, p. 128.

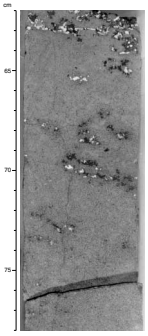

F86. Miarolitic cavity filled with nontronite and celadonite, p. 129.

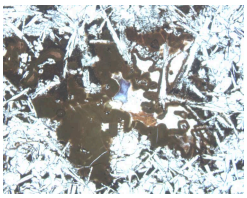

F87. Graph of true dip, fracture density, and vein abundance, p. 130.

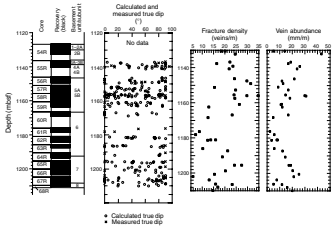

F88. Zijderveld diagrams for sediments and basalts, p. 131.

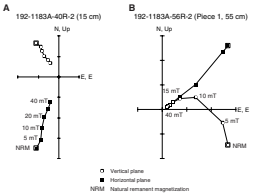

density data obtained from discrete samples (Fig. F94) demonstrates that the two measurements generally correlate, despite the consistently lower values of the GRA density data. The larger scatter in the GRA bulk density data for the basalts probably is a result of the fractured nature and narrow diameter of the basalt cores, which do not completely fill the core liner. Based on comparison with discrete sample measurements, GRA values <1.6 g/cm³ generally can be disregarded.

Natural Gamma Radiation

NGR measurements on unsplit sections of cores show local peaks of >120 cps, centered at ~420, ~800, and ~965 mbsf (Fig. F95), in the Miocene ooze to chalk of Subunit IB, the Oligocene chalk with ash beds of Subunit IC, and the Paleocene–Eocene zeolite-rich limestone of Subunit IIB. A slight but noticeable increase in NGR counts (256 cps) occurs at 986.3 mbsf, above the Cretaceous/Paleogene boundary in Core 192-1183A-39R. In the basement basalts (1130.4–1211.1 mbsf), the NGR counts generally average 35 cps.

P-Wave Velocity

Downhole variations in *P*-wave velocity commonly correlate with changes in lithology. In general, *P*-wave velocity varies directly with increasing wet bulk density and grain density and varies inversely with water content and porosity. We calculated *P*-wave velocity from discrete measurements obtained on both split-core sections and cut samples (Fig. F95) using the contact probe systems. Measurements were generally made in the x-direction, although some oriented cube samples were also measured in the y- and z-directions to investigate velocity anisotropy (Table T15). *P*-wave velocities in the ooze and chalk sections of Unit I gradually increase from a mean of 1699 m/s in Subunits IA and IB to a mean of 2236 m/s in Subunit IC. A marked velocity increase occurs in Unit II at ~950 mbsf, marking the boundary between the chert-rich limestone of Subunit IIA and the zeolite-rich limestone of Subunit IIB. Above 950 mbsf, *P*-wave velocities are typically <2500 m/s. Except for portions of Subunit IIIA, velocities below 950 mbsf are typically >3000 m/s (Fig. F95), with the highest values of 3500–4400 m/s at the bottom of Unit II. Although no clear trend in anisotropy is recognizable in Unit I (anisotropy generally is <5%), sediments in Units II and III display velocity anisotropies up to 20% (Table T15). The high *P*-wave velocities (>5000 m/s) in the basement basalts are associated with high bulk and grain densities and very low porosity values (Fig. F94).

Thermal Conductivity

We determined thermal conductivity in unsplit soft sediment cores and on selected samples of lithified sediments and basalt (Table T16). In Subunits IA and IB, thermal conductivity generally is <1.2 W/(m·K), with a median value of 1.1 W/(m·K). In Subunit IC, thermal conductivity generally is >1.5 W/(m·K), with a median value of 1.6 W/(m·K). In the limestone of Subunits IIA, IIB, IIIA, and IIIB, thermal conductivity, although highly variable, generally increases with depth, exhibiting a maximum value of 2.9 W/(m·K) in the bottom of Subunit IIB near the Cretaceous/Paleogene boundary. In basement, the basalts are characterized by somewhat lower thermal conductivity values, ranging between

F89. Magnetic susceptibility and NRM variations for sedimentary units, p. 132.

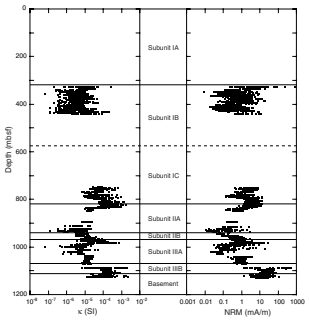

F90. Magnetic polarity and biostratigraphic data and correlation with polarity timescale, p. 133.

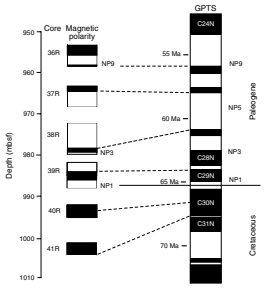

T12. Average NRM intensity and magnetic susceptibility for subunits, Hole 1183A, p. 160.

F91. Remanent magnetization variation, p. 134.

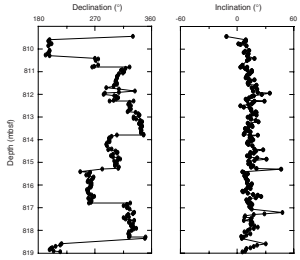

F92. Paleolatitude vs. age, p. 135.

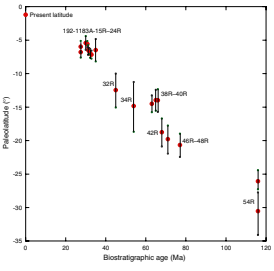

1.4 and 2.5 W/(m·K) in the depth interval from 1130.3 to 1210.0 mbsf (Fig. **F94**).

F93. Declination and inclination variations and NRM intensity, p. 136.

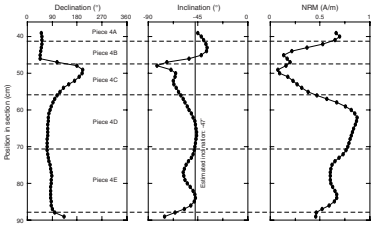

T13. Properties of basalt pieces, p. 161.

T14. Index properties, Hole 1183A, p. 162.

F94. Index properties and thermal conductivity vs. depth, p. 137.

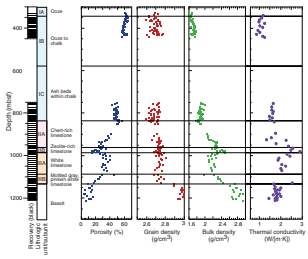

T15. *P*-wave velocity, Hole 1183A, p. 165.

T16. Thermal conductivity values, Hole 1183A, p. 169.

F95. Whole-core measurements vs. depth, p. 138.

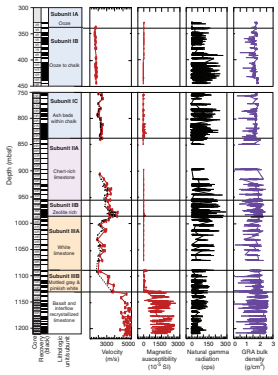

REFERENCES

Alt, J.C., and Honnorez, J., 1984. Alteration of the upper oceanic crust, DSDP Site 417: mineralogy and chemistry. *Contrib. Mineral. Petrol.,* 87:149–169.

Alt, J.C., Honnorez, J., Laverne, C., and Emmermann, R., 1986. Hydrothermal alteration of a 1 km section through the upper oceanic crust, Deep Sea Drilling Project Hole 504B: mineralogy, chemistry, and evolution of seawater-basalt interactions. *J. Geophys. Res.,* 91:10309–10335.

Andrews, J.E., Packham, G., et al., 1975. *Init. Repts. DSDP,* 30: Washington (U.S. Govt. Printing Office).

Araki, E., Mochizuki, K., Suyehiro, K., Taira, A., Yoneshima, S., Shinohara, M., Miura, S., and Hino, R., 1998. Seismic structure of Ontong Java Plateau crust. *Eos,* 79:F869.

Barrera, E., and Savin, S.M., 1999. Evolution of Campanian–Maastrichtian marine climates and oceans. *In* Barrera, E., and Johnson, C.C. (Eds.), *Evolution of the Cretaceous Ocean-Climate System,* Geol. Soc. Amer. Special Paper, 332:245–282.

Bathurst, R.G.C., 1987. Diagenetically enhanced bedding in argillaceous platform limestones: stratified cementation and selective compaction. *Sedimentology,* 34:749–778.

Behl, R.J., and Smith, B.M., 1992. Silicification of deep-sea sediments and the oxygen isotope composition of diagenetic siliceous rocks from the western Pacific, Pigafetta and East Mariana basins, Leg 129. *In* Larson, R.L., Lancelot, Y., et al., *Proc. ODP, Sci. Results,* 129: College Station, TX (Ocean Drilling Program), 81–117.

Berger, W.H., 1979. Impact of deep-sea drilling on paleoceanography. *In* Talwani, M., Hay, W., and Ryan, W.B.F. (Eds.), *Deep Drilling Results in the Atlantic Ocean: Continental Margins and Paleoenvironment.* Am. Geophys. Union, Maurice Ewing Ser., 3:297–314.

Berger, W.H., Kroenke, L.W., Mayer, L.A., and Shipboard Scientific Party, 1991. Ontong Java Plateau, Leg 130: synopsis of major drilling results. *In* Kroenke, L.W., Berger, W.H., Janecek, T.R., et al., *Proc. ODP, Init. Repts.,* 130: College Station, TX (Ocean Drilling Program), 497–537.

Berger, W.H., and Winterer, E.L., 1974. Plate stratigraphy and the fluctuating carbonate line. *In* Hsü, K.J., and Jenkyns, H.C. (Eds.), *Pelagic Sediments on Land and Under the Sea.* Spec. Publ. Int. Assoc. Sedimentol., 1:11–48.

Berggren, W.A., Kent, D.V., Swisher, C.C., III, and Aubry, M.-P., 1995. A revised Cenozoic geochronology and chronostratigraphy. *In* Berggren, W.A., Kent, D.V., Aubry, M.-P., and Hardenbol, J. (Eds.), *Geochronology, Time Scales and Global Stratigraphic Correlation.* Spec. Publ.—Soc. Econ. Paleontol. Mineral. (Soc. Sediment. Geol.), 54:129–212.

Blum, P., 1997. Physical properties handbook: a guide to the shipboard measurement of physical properties of deep-sea cores. *ODP Tech. Note,* 26. [Online]. Available from World Wide Web: <http://www-odp.tamu.edu/publications/tnotes/tn26/INDEX.HTM>. [Cited 2000-09-08]

Böhlke, J.K., Honnorez, J., and Honnorez-Guerstein, B.M., 1980. Alteration of basalts from site 396B, DSDP: petrographic and mineralogical studies. *Contrib. Mineral. Petrol.,* 73:341–364.

Bralower, T.J., Leckie, R.M., Sliter, W.V., and Thierstein, H.R., 1995. An integrated Cretaceous microfossil biostratigraphy. *In* Scholle, P.A. (Ed.), *Geochronology, Time Scales, and Global Stratigraphic Correlation.* Spec. Publ.—Soc. Econ. Paleontol. Mineral. (Soc. Sediment. Geol.), 54:65–79.

Bralower, T.J., Sliter, W.V., Arthur, M.A., Leckie, R.M., Allard, D.J., and Schlanger, S.O., 1993. Dysoxic/anoxic episodes in the Aptian-Albian (Early Cretaceous). *In* Pringle, M.S., Sager, W.W., Sliter, M.V., and Stein, S. (Eds.), *The Mesozoic Pacific: Geology, Tectonics, and Volcanism.* Geophys. Monogr., Am. Geophys. Union, 77:5–37.

Coffin, M.F., 1992. Emplacement and subsidence of Indian Ocean Plateaus and submarine ridges: synthesis of results from scientific drilling in the Indian Ocean. *Geophys. Monogr., Am. Geophys. Union,* 70:115–125.

Crowley, T.J., and North, G.R., 1991. *Paleoclimatology: Oxford Monographs on Geology and Geophysics:* New York (Oxford Univ. Press).

Detrick, R.S., and Crough, S.T., 1978. Island subsidence, hot spots, and lithospheric thinning. *J. Geophys. Res.,* 83:1236–1244.

Duncan, R.A., and Clague, D.A., 1985. Pacific plate motion recorded by linear volcanic chains. *In* Nairn, A.E.M., Stehli, F.G., and Uyeda, S. (Eds.), *The Ocean Basins and Margins* (Vol. 7A): *The Pacific Ocean:* New York (Plenum), 89–121.

Emery, K.O., and Uchupi, E., 1984. *The Geology of the Atlantic Ocean:* New York (Springer-Verlag).

Frank, T.D., and Arthur, M.A., 1999. Tectonic forcings of Maastrichtian ocean-climate evolution, *Paleoceanography,* 14:103–117.

Gardner, J.V., Nelson, C.S., and Baker, P.A., 1986. Distribution and character of pale green laminae in sediment from Lord Howe Rise: a probable late Neogene and Quaternary tephrostratigraphic record. *In* Kennett, J.P., von der Borch, C.C., et al., *Init. Repts. DSDP,* 90 (Pt. 2): Washington (U.S. Govt. Printing Office), 1145–1159.

Gibson, T.G., and Towe, K.M., 1971. Eocene volcanism and the origin of Horizon A. *Science,* 172:152–154.

Gradstein, F.M., Agterberg, F.P., Ogg, J.G., Hardenbol, J., van Veen, P., Thierry, J., and Huang, Z., 1995. A Triassic, Jurassic and Cretaceous time scale. *In* Berggren, W.A., Kent, D.V., Aubry, M.P., and Hardenbol, J. (Eds.), *Geochronology, Time Scales and Global Stratigraphic Correlation.* Spec. Publ.—Soc. Econ. Paleontol. Mineral., 54:95–126.

Hein, J.R., Vallier, T.L., and Allan, M.A., 1981. Chert petrology and geochemistry mid-Pacific Mountains and Hess Rise, Deep Sea Drilling Project Leg 62. *In* Thiede, J., Vallier, T.L., et al., *Init. Repts. DSDP,* 62: Washington (U.S. Govt. Printing Office), 711–748.

Honnorez, J., 1967. La palagonitisation: l'alteration sous-marine du verre volcanique basique de Palagonia (Sicile) [Ph.D. dissert.]. Université Libre de Bruxelles.

————, 1972. La Palagonitisation: l'alteration sous-marine du verre volcanique basique de Palagonia (Sicile) [Palagonitization: the submarine alteration of basic volcanic glass in Palagonia, Sicily]. *Publ. Vulkaninst. Immanuel Friedlaender,* 9.

————, 1981. The aging of the oceanic crust at low temperature. *In* Emiliani, C. (Ed.), *The Sea* (Vol. 7): *The Oceanic Lithosphere:* New York (Wiley), 525–587.

International Hydrographic Organization/Intergovernmental Oceanographic Commission (IHO/IOC), 1997. *General Bathymetric Chart of the Ocean (GEBCO) Digital Atlas:* London (British Oceanographic Data Centre).

Ito, G., and Clift, P.D., 1998. Subsidence and growth of Pacific Cretaceous plateaus. *Earth Planet. Sci. Lett.,* 161:85–100.

Jansa, L.F., Enos, P., Tucholke, B.E., Gradstein, F.M., and Sheridan, R.E., 1979. Mesozoic-Cenozoic sedimentary formations of the North American Basin, western North Atlantic. *In* Talwani, M., Hay, W., and Ryan, W.B.F. (Eds.) *Deep Drilling Results in the Atlantic Ocean: Continental Margins and Paleoenvironment.* Am. Geophys. Union, Maurice Ewing Ser., 3:1–57.

Karpoff, A.M., 1989. Les faciès pélagiques condensés Cénozoiques des océans Pacifique et Atlantique: témoins des grandes crises géodynamiques [Thèse Doc. Sci.]. Univ. Louis Pasteur, Strasbourg.

Kennedy, W.J., and Garrison, R.E., 1975. Morphology and genesis of nodular chalks and hardgrounds in the upper Cretaceous of southern England. *Sedimentology,* 22:311–386.

Kirschvink, J.L., 1980. The least-squares line and plane and the analysis of palaeomagnetic data. *Geophys. J. R. Astron. Soc.,* 62:699–718.

Klein, G. deV., 1975. Depositional facies of Leg 30 Deep Sea Drilling Project Sediment cores. *In* Andrews, J.E., Packham, G., et al., *Init. Repts. DSDP,* 30: Washington (U.S. Govt. Printing Office), 423–442.

Kono, M., 1980. Statistics of paleomagnetic inclination data. *J. Geophys. Res.,* 85:3878–3882.

Kroenke, L.W., 1984. *Cenozoic Tectonic Development of the Southwest Pacific.* Tech. Bull.—U.N. Econ. Soc. Comm. Asia Pac., Comm. Co-ord. Jt. Prospect Miner. Resour. South Pac. Offshore Areas, 6.

Kroenke, L.W., 1996. Plate tectonic development of the western and southwestern Pacific: Mesozoic to the present. *In* Keast, A., and Miller, S.E. (Eds.), *The Origin and Evolution of Pacific Island Biotas, New Guinea to Eastern Polynesia: Patterns and Processes:* Amsterdam (Academic Publishing), 19–34.

Kroenke, L.W., Berger, W.H., Janecek, T.R., et al., 1991. *Proc. ODP, Init. Repts.,* 130: College Station, TX (Ocean Drilling Program).

Kroenke, L.W., Resig, J.M., and Leckie, R.M., 1993. Hiatus and tephrochronology of the Ontong Java Plateau: correlation with regional tectono-volcanic events. *In* Berger, W.H., Kroenke, L.W., Mayer, L.A., et al., *Proc. ODP, Sci. Results,* 130: College Station, TX (Ocean Drilling Program), 423–444.

Lancelot, Y., 1973. Chert and silica diagenesis in sediments from the central Pacific. *In* Winterer, E.L., Ewing, J.I., et al., *Init. Repts. DSDP,* 17: Washington (U.S. Govt. Printing Office), 377–405.

Lancelot, Y., Larson, R.L., et al., 1990. *Proc. ODP, Init. Repts.,* 129: College Station, TX (Ocean Drilling Program).

Laverne, C., 1987. Les altérations des basaltes en domaine océanique: minéralogie, pétrologie et géochimie d'un système hydrothermal: le puits 504B, Pacifique oriental [Thèse]. Univ. Aix-Marseille III.

Le Bas, M.J., Le Maitre, R.W., Streckeisen, A., and Zanettin, B., 1986. A chemical classification of volcanic rocks based on the total alkali-silica diagram. *J. Petrol.,* 27:745–750.

Lind, I.L., 1993. Stylolites in chalk from Leg 130, Ontong Java Plateau. *In* Berger, W.H., Kroenke, L.W., Mayer, L.A., et al., *Proc. ODP, Sci. Results,* 130: College Station, TX (Ocean Drilling Program), 445–451.

Lind, I.L., Janecek, T.R., Krissek, L.A., Prentice, M.L., and Stax, R., 1993. Color bands in Ontong Java Plateau carbonate oozes and chalks. *In* Berger, W.H., Kroenke, L.W., Mayer, L.A., et al., *Proc. ODP, Sci. Results,* 130: College Station, TX (Ocean Drilling Program), 453–470.

Lonsdale, P., Malfait, B.T., and Spiess, F.N., 1972a. Abyssal sand waves on the Carnegie Ridge. *Geol. Soc. Am. Abstracts with Programs,* 4:579–580. (Abstract)

Lonsdale, P., Normark, W.R., and Newman, W.A., 1972b. Sedimentation and erosion on Horizon Guyot. *Geol. Soc. Am. Bull.,* 83:289–315.

Macdonald, G.A., and Katsura, T., 1964. Chemical composition of Hawaiian lavas. *J. Petrol.,* 5:82–133.

Macleod, K.G., and Huber, B.T., 2001. The Maastrichtian record at Blake Nose (western North Atlantic) and implications for global palaeoceanographic and biotic changes. *In* Kroon, D., Norris, R.D., and Klaus, A. (Eds.), *Western North Atlantic Paleogene and Cretaceous Paleoceanography,* Spec. Publ.—Geol. Soc. London, 183:111–130.

Mahoney, J.J., Storey, M., Duncan, R.A., Spencer, K.J., and Pringle, M.S., 1993. Geochemistry and age of the Ontong Java Plateau. *In* Pringle, M.S., Sager, W.W., Sliter, W.V., and Stein, S. (Eds.), *The Mesozoic Pacific: Geology, Tectonics, and Volcanism.* Geophys. Monogr., Am. Geophys. Union, 77:233–262.

Martini, E., 1971. Standard Tertiary and Quaternary calcareous nannoplankton zonation. *In* Farinacci, A. (Ed.), *Proc. 2nd Int. Conf. Planktonic Microfossils Roma:* Rome (Ed. Tecnosci.), 2:739–785.

Mattson, P.H., and Pessagno, E.A., 1971. Caribbean Eocene volcanism and the extent of horizon A. *Science,* 174:138–139.

Mélières, F., Deroo, G., and Herbin, J.-P., 1981. Organic-matter-rich and hypersiliceous Aptian sediments from western Mid-Pacific Mountains, Deep Sea Drilling Project Leg 62. *In* Thiede, J., Vallier, T.L., et al., *Init. Repts. DSDP,* 62: Washington (U.S. Govt. Printing Office), 903–915.

Michael, P.J., 1999. Implications for magmatic processes at Ontong Java Plateau from volatile and major element contents of Cretaceous basalt glasses. In *Geochem., Geophys., Geosys.,* 1: Paper no. 1999GC000025 [Online]. Available from the World Wide Web: <http://gcubed.magnet.fsu.edu/publicationsfinal/articles/1999GC000025/fs1999GC000025.html>. [Cited 2000-08-03] [**N1**]

Millot, G., 1964. *Géologie des Argiles:* Paris (Masson).

Mochizuki, K., Coffin, M., and Eldholm, O., 1998. Upper crustal structure along an E-W transect from the Nauru Basin to the north-central Ontong Java Plateau. *Eos,* 79:F869.

Moore, J.G., and Schilling, J.G., 1973. Vesicles, water, and sulfur in Reykjanes Ridge basalts. *Contrib. Mineral. Petrol.,* 41:105–118.

Moullade, M., Masse, J.P., Tronchetti, G., Kuhnt, W., Ropolo, P., Bergen, J.A., Masure, E., and Renard, M., 1998. Le stratotype historique de l'Aptien inférieur (région de Cassis-La Bedoule): synthèse stratigraphique. *Géol. Méditerranéenne,* 3/4:289–298.

Neal, C.R., Mahoney, J.J., Kroenke, L.W., Duncan, R.A., and Peterson, M.G., 1997. The Ontong Java Plateau. *In* Mahoney, J.J., and Coffin, M.J. (Eds.), *Large Igneous Provinces: Continental, Oceanic, and Planetary Flood Volcanism.* Am. Geophys. Union, Geophys. Monogr., 100:183–216.

Ogg, J.G., Karl, S.M., and Behl, R.J., 1992. Jurassic through Early Cretaceous sedimentation history of the central equatorial Pacific and of Sites 800 and 801. *In* Larson, R.L., Lancelot, Y., et al., *Proc. ODP, Sci. Results,* 129: College Station, TX (Ocean Drilling Program), 571–613.

Petronotis, K.E., and Gordon, R.G., 1999. A Maastrichtian palaeomagnetic pole for the Pacific plate from a skewness analysis of marine magnetic anomaly 32. *Geophys. J. Int.,* 139:227–247.

Riech, V., and von Rad, U., 1979. Silica diagenesis in the Atlantic Ocean: diagenetic potential and transformations. *In* Talwani, M., Hay, W., and Ryan, W.B.F. (Eds.), *Deep Drilling Results in the Atlantic Ocean: Continental Margins and Paleoenvironment.* Am. Geophys. Union, Maurice Ewing Ser., 3:315–340.

Röhl, U., and Ogg, J.G., 1996. Aptian-Albian sea level history from guyots in the western Pacific, *Paleoceanography,* 11:595-624.

Sandwell, D.T., and Smith, W.H.F., 1997. Marine gravity anomaly from Geosat and ERS-1 satellite altimetry. *J. Geophys. Res.,* 102:10039–10054.

Schlanger, S.O., and Jenkyns, H.C., 1976. Cretaceous oceanic anoxic events: causes and consequences. *Geol. Mijnbouw,* 55:179–184.

Scholle, P.A., Arthur, M.A., and Ekdale, A.A., 1983. Pelagic environments. *In* Scholle, P.A., Bebout, D.G., and Moore, C.H. (Eds.), *Carbonate Depositional Environments.* AAPG Mem., 33:620–691.

Sclater, J.G., Boyle, E., and Edmond, J.M., 1979. A quantitative analysis of some factors affecting carbonate sedimentation in the oceans. *In* Talwani, M., Hay, W., and Ryan, W.B.F. (Eds.), *Deep Drilling Results in the Atlantic Ocean, Continental Margins and Paleoenvironment.* Am. Geophys. Union, Maurice Ewing Ser., 3:235–248.

Shipboard Scientific Party, 1975. Site 289. *In* Andrews, J.E., Packham, G., et al., *Init. Repts. DSDP,* 30: Washington (U.S. Govt. Printing Office), 231–398.

————, 1981. Site 463: western Mid-Pacific Mountains. *In* Thiede, J., Vallier, T.L., et al., *Init. Repts. DSDP,* 62: Washington (U.S. Govt. Printing Office), 33–156.

————, 1990. Site 801: Pigafetta Basin, western Pacific. *In* Lancelot, Y., Larson, R.L., Fisher, A., et al., *Proc. ODP, Init. Repts,* 129: College Station, TX (Ocean Drilling Program), 91-170.

Sikora, P.J., and Olsson, R.K., 1991. A paleoslope model of late Albian to early Turonian foraminifers of the west Atlantic Margin and North Atlantic Basin. *Mar. Micropaleontol.,* 8:25–72.

Smith, W.H.F., and Sandwell, D.T., 1997. Global seafloor topography from satellite altimetry and ship depth soundings. *Science,* 277:1956–1962.

Stein, C.A., and Stein, S., 1993. Constraints on Pacific midplate swells from global depth-age and heat flow-age models. *In* Pringle, M.S., Sager, W.W., Sliter, W.V., and Stein, S. (Eds.), *The Mesozoic Pacific: Geology, Tectonics, and Volcanism*. Am. Geophys. Union, Geophys. Monogr., 77:53–76.

Tejada, M.L.J., Mahoney, J.J., Neal, C.R., Duncan, R.A., and Petterson, M.G., in press. Basement geochemistry and geochronology of central Malaita, Solomon Islands, with implications for the origin and evolution of the Ontong Java Plateau. *J. Petrol.*

Thierstein, H.R., 1979. Paleoceanographic implications of organic carbon and carbonate distribution in Mesozoic deep sea sediments. *In* Talwani, M., Hay, W., and Ryan, W.B.F. (Eds.), *Deep Drilling Results in the Atlantic Ocean*. Am. Geophys. Union, Maurice Ewing Ser., 3:249–274.

Tucholke, B.E., 1979. Relationship between acoustic stratigraphy and lithostratigraphy in the western North Atlantic. *In* Tucholke, B.E., Vogt, P.R., et al., *Init. Repts. DSDP,* 43: Washington (U.S. Govt. Printing Office), 827–846.

Tucholke, B.E., and Mountain, G.S., 1979. Seismic stratigraphy, lithostratigraphy, and paleosedimentation patterns in the North American Basin. *In* Talwani, M., Hay, W., and Ryan, W.B.F. (Eds.), *Deep Drilling Results in the Atlantic Ocean: Continental Margins and Paleoenvironment.* Am. Geophys. Union, Maurice Ewing Ser., 3:58–86.

Tucholke, B.E., and Vogt, P.R., 1979. Western North Atlantic: sedimentary evolution and aspects of tectonic history. *In* Tucholke, B.E., Vogt, P.R., et al., *Init. Repts. DSDP,* 43: Washington (U.S. Govt. Printing Office), 791–825.

van Andel, T.H., 1975. Mesozoic/Cenozoic calcite compensation depth and the global distribution of calcareous sediments. *Earth Planet. Sci. Lett.,* 26:187–194.

van der Lingen, G.J., and Packham, G.H., 1975. Relationships between diagenesis and physical properties of biogenic sediments of the Ontong-Java Plateau (Sites 288 and 289, Deep Sea Drilling Project). *In* Andrews, J.E., Gradstein, F.M., et al., *Init. Repts. DSDP,* 30: Washington (U.S. Govt. Printing Office), 443–481.

Yeats, R.S., Hart, S.R., et al., 1976. *Init. Repts DSDP,* 34: Washington (U.S. Govt. Printing Office).

Figure F1. Predicted bathymetry (after Smith and Sandwell, 1997) of the Ontong Java Plateau showing the locations of Site 1183 and other sites drilled during Leg 192 (stars). The plateau is outlined. Black dots = previous ODP and DSDP drill sites that reached basement; white dots = Site 288, which did not reach basement but bottomed in Aptian limestone, and Site OJ-7, which was proposed for Leg 192 but not drilled. The bathymetric contour interval is 1000 m (IHO/IOC, 1997).

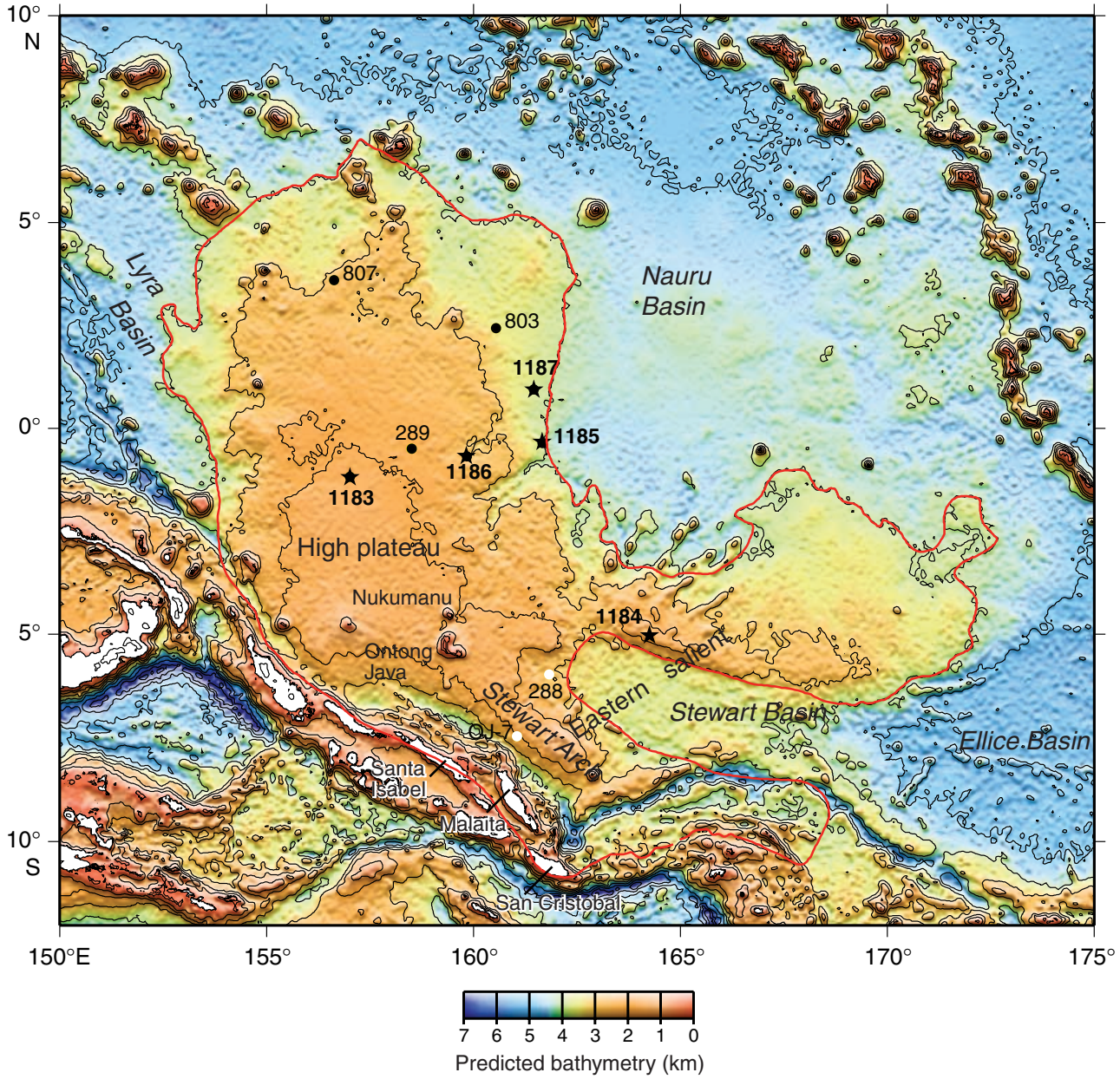

Figure F2. Satellite-derived free-air gravity map of the Ontong Java Plateau region (after Sandwell and Smith, 1997). Stars = locations of Site 1183 and other sites drilled during Leg 192. Black dots = previous ODP and DSDP drill sites that reached basement; white dots = Site 288, which did not reach basement but bottomed in Aptian limestone, and Site OJ-7, which was proposed for Leg 192 but not drilled. Black lines = surveys providing multichannel seismic control: *Hakuho Maru* KH98-1 Leg 2 (1998) and *Maurice Ewing* EW95-11 (1995). White lines = surveys providing single-channel seismic control: *Glomar Challenger* Leg 7 GC07 (1969), *Glomar Challenger* Leg 30 GC30 (1973), *Glomar Challenger* Leg 89 GC89 (1982), *Thomas Washington* TW-11 (1988), and *JOIDES Resolution* Leg 130 JR130 (1990). The bathymetric contour interval is 1000 m (IHO/IOC, 1997).

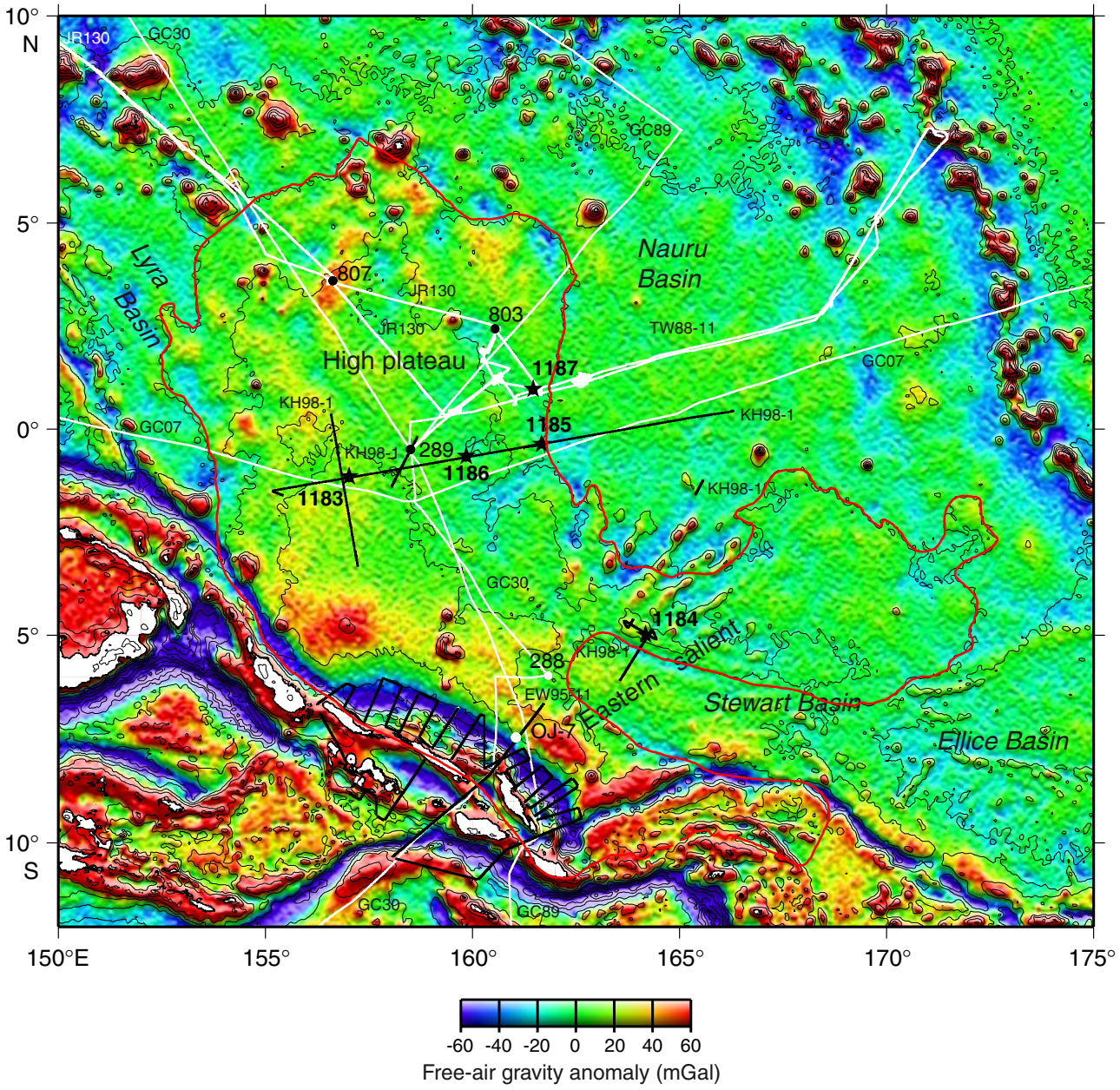

Figure F3. Location of Site 1183 and site-survey data on satellite-derived free-air gravity map (after Sandwell and Smith, 1997). Navigation for *Hakuho Maru* KH98-1 Leg 2 survey, lines 404 and 501, is shown in Julian-day time. Water depths in the survey area are between 1500 and 2000 m (IHO/IOC, 1997).

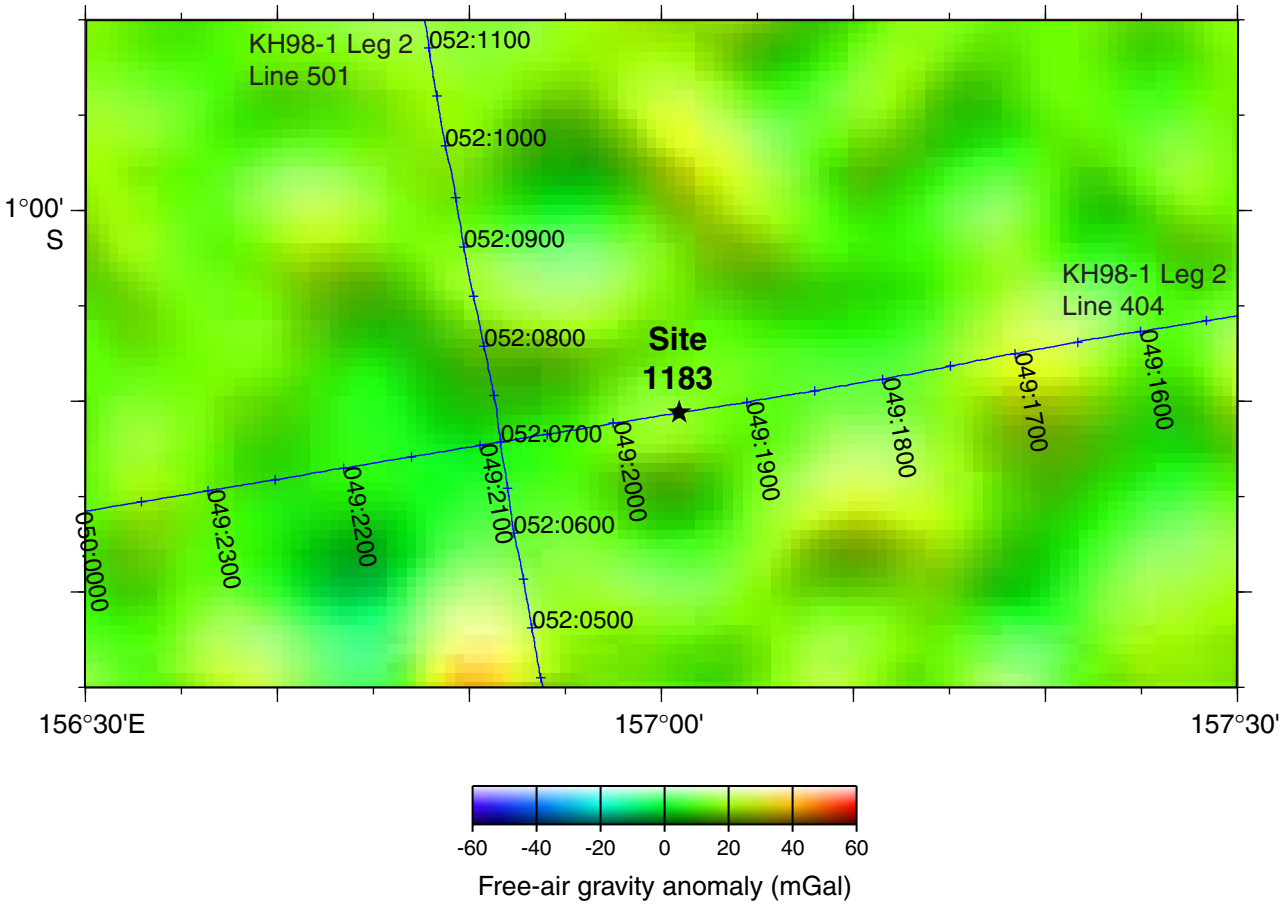

Figure F4. Multichannel seismic reflection profile across Site 1183. Vertical exaggeration is ~4.2 at seafloor. UTC = Universal Time Coordinated.

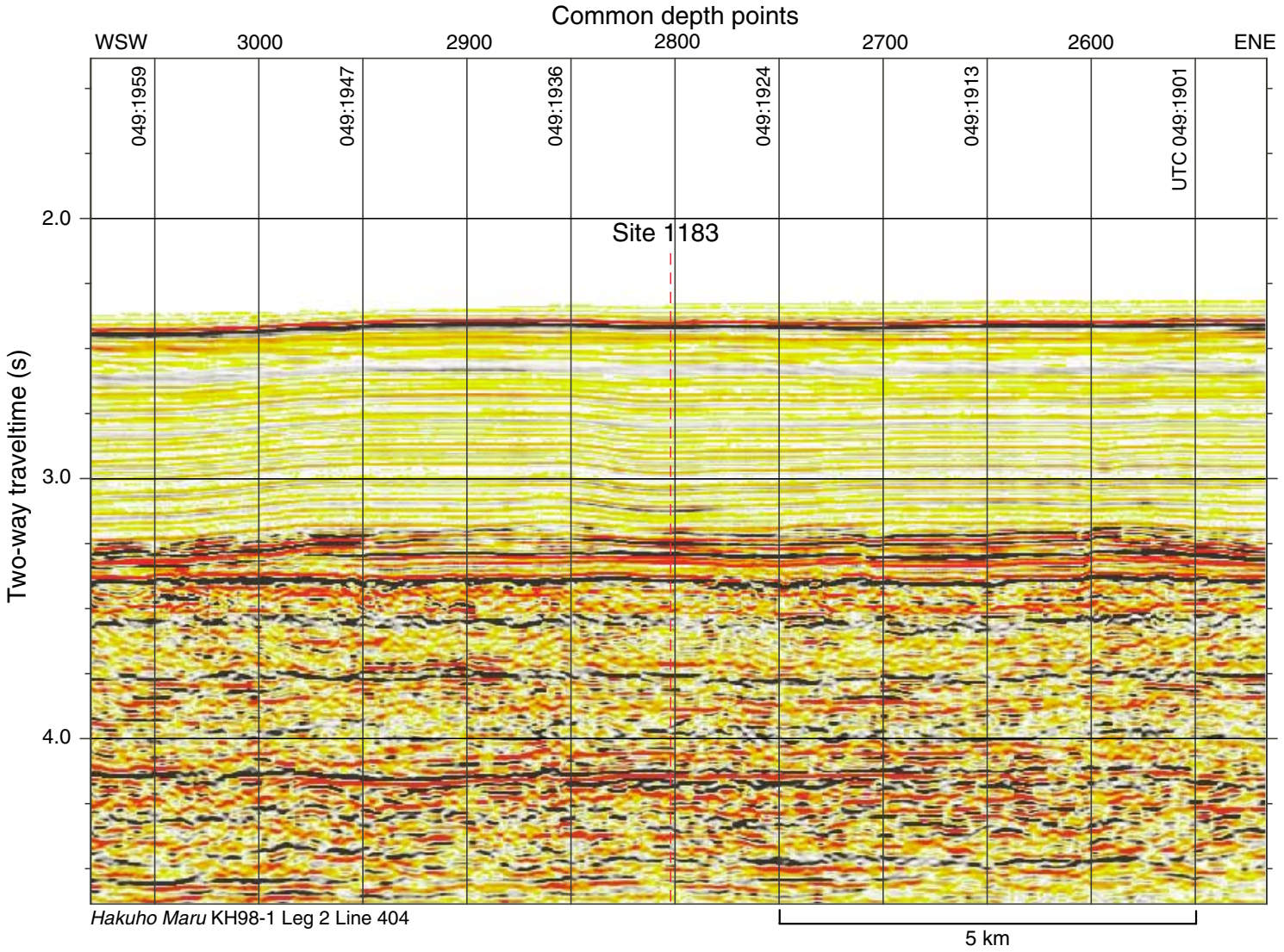

Figure F5. Close-up of Site 1183 vicinity shown in Figure F4, p. 47. UTC = Universal Time Coordinated.

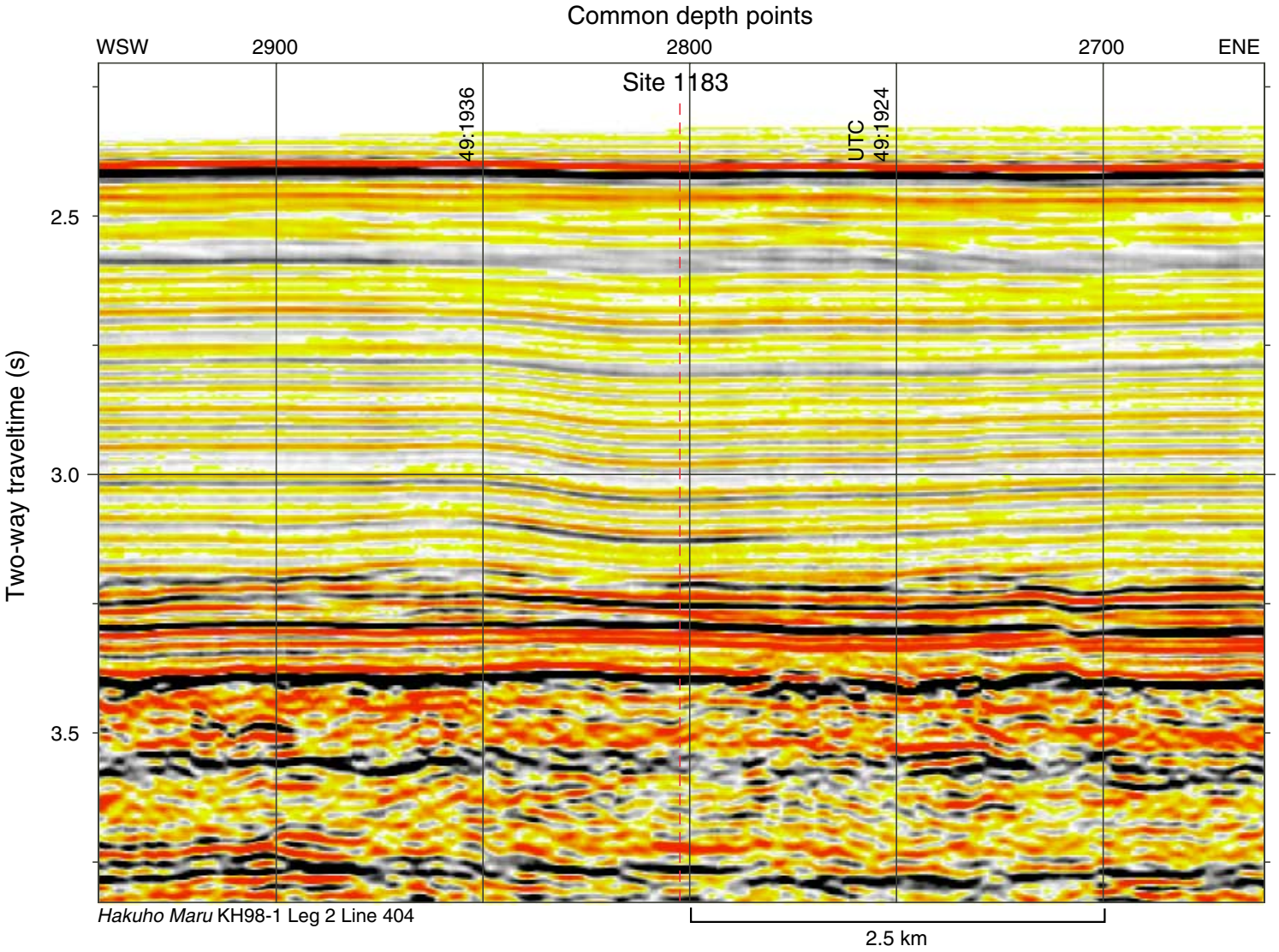

Figure F6. Lithostratigraphy and selected lithologic properties of sediments in Hole 1183A. Depths are in meters below seafloor (mbsf). There was no coring from 0 to 320 mbsf and 450 to 750 mbsf. Camp. = Campanian, Maast. = Maastrichtian. High values of the color reflectance or lightness variable correspond to light-colored sediment, but many of the spikes to relatively darker colors are caused by gaps among cored pieces or other artifacts. Higher values of magnetic susceptibility generally correlate with bands rich in volcanic ash.

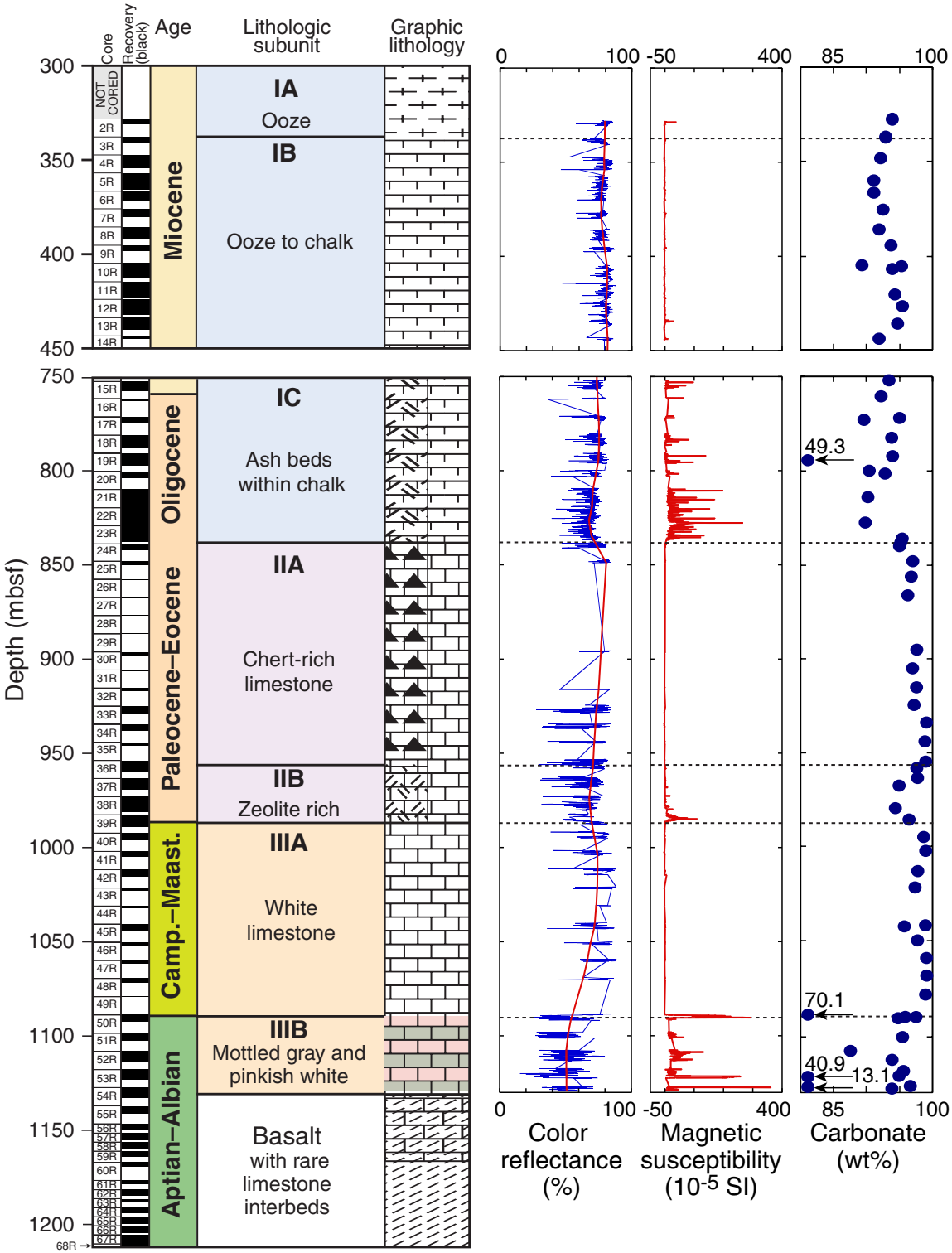

Figure F7. Typical white bioturbated chalk facies of Subunit IB (Miocene) with thin, crosscutting, color laminae of green, blue, and purple (interval 192-1183A-4R-4, 88–116 cm).

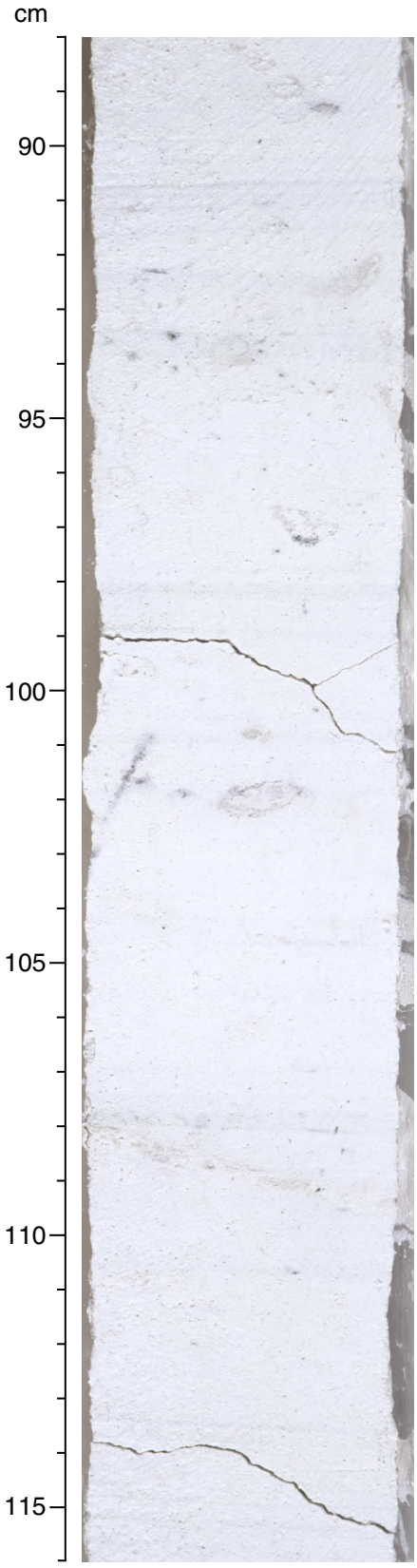

Figure F8. Nannofossil foraminifer chalk (Subunit IC; Oligocene; Sample **192-1183A-20R-CC, 2–6 cm;** plane-polarized light; field of view = 2.8 mm; photomicrograph ID# 1183AS_2). Anastomosing microstylolites (subhorizontal dark streaks in image) are associated with the formation of flaser-nodular texture.

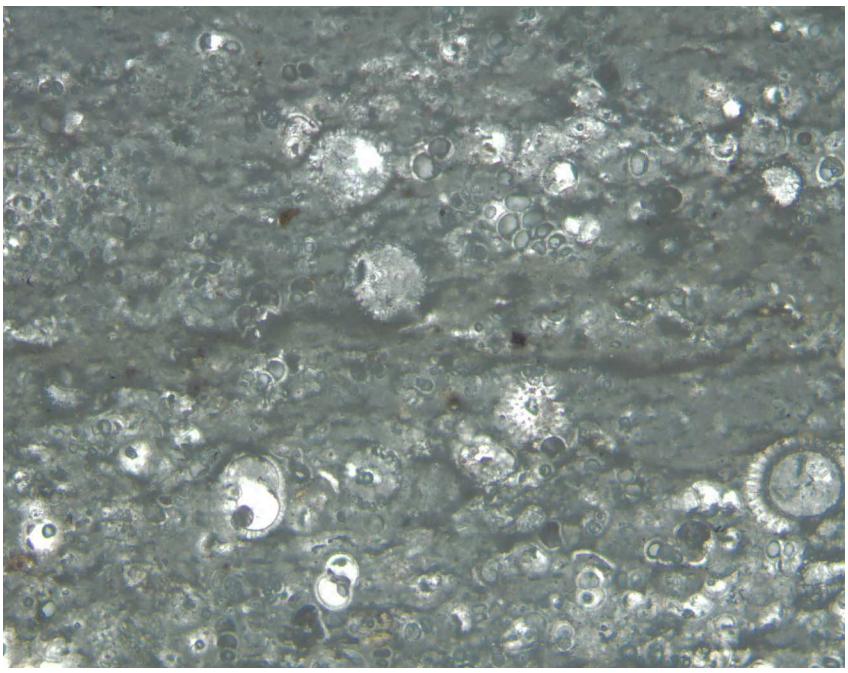

Figure F9. Ash layer in bioturbated chalk of Subunit IC (Oligocene; interval 192-1183-15R-1, 101–117 cm). Volcanic ash has been dispersed upward by bioturbation mixing and partially fills the underlying burrows.

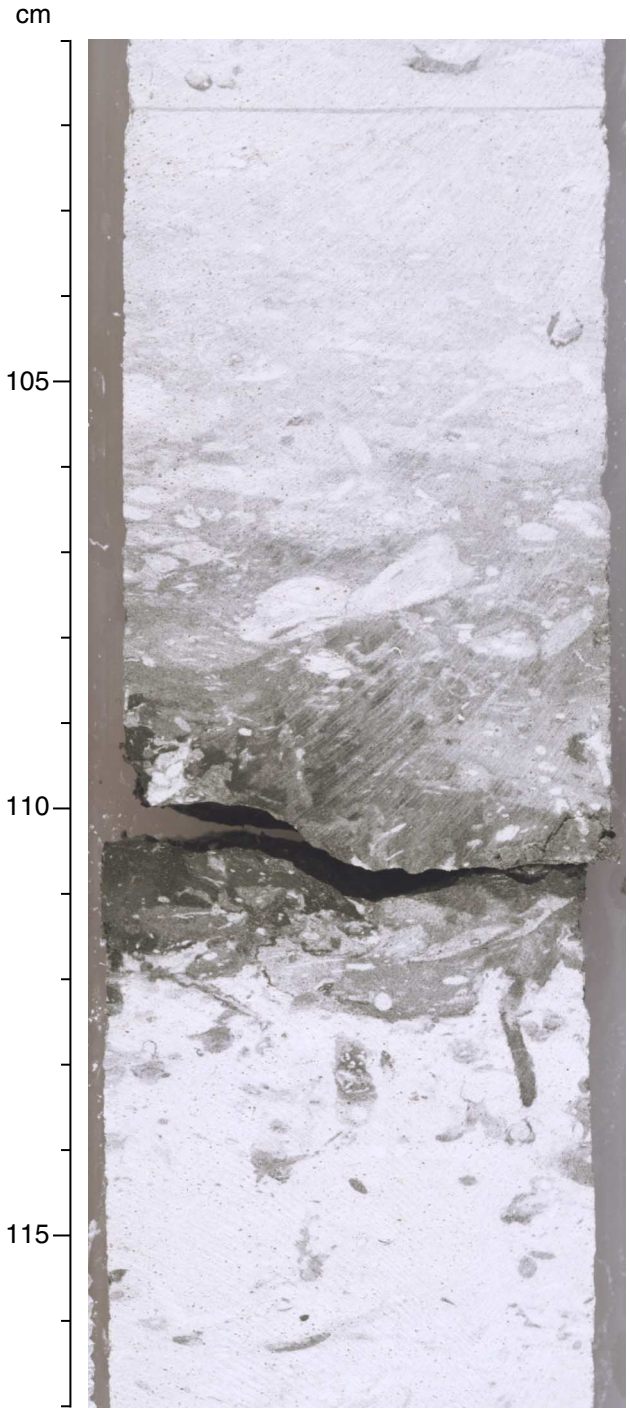

Figure F10. White limestone interbedded with chert is the typical facies of Subunit IIA (middle Eocene, interval 192-1183A-33R-2, 74–127 cm).

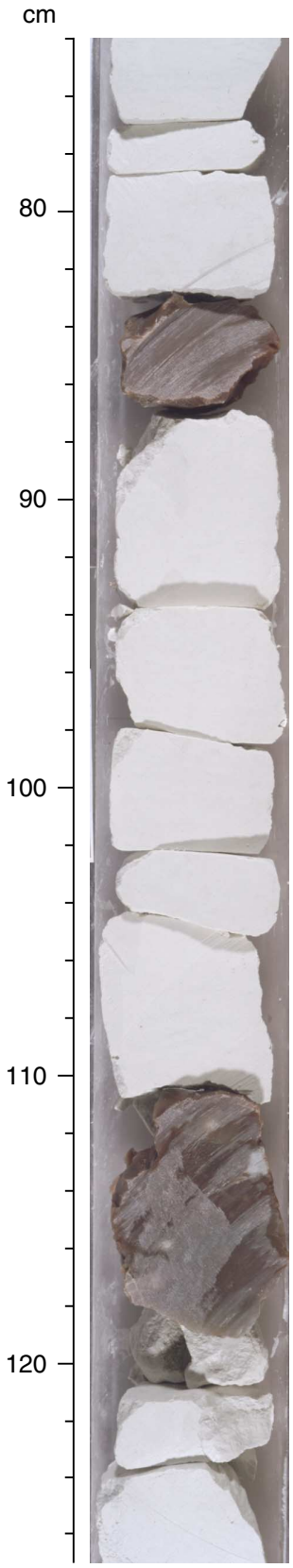

Figure F11. The lower portion of Subunit IIB consists of packed foraminifers within a matrix of nannofossils and micrite (lower Danian; Sample **192-1183A-39R-1, 37–39 cm;** plane-polarized light; field of view = 2.8 mm; photomicrograph ID# 1183AS_10).

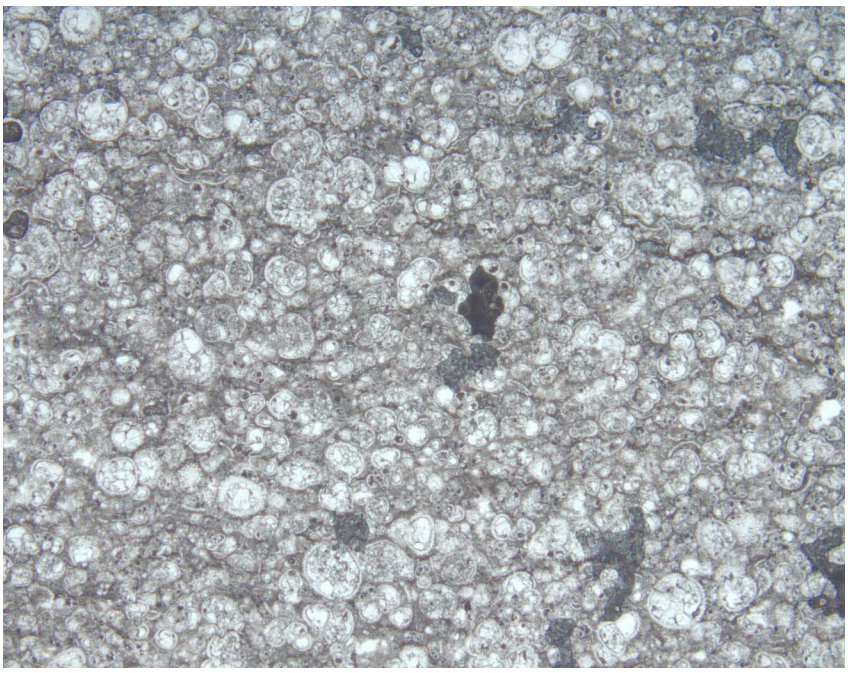

Figure F12. Blue-gray staining is preferentially on undersides of burrows in limestone (Subunit IIB; Paleocene; interval 192-1183A-37R-4, 15–25 cm).

Figure F13. Microflaser and anastomosing seams in limestone of Subunit IIB (Paleocene; interval 192-1183A-38R-1, 23–37 cm). The 1-cm-thick dark layer at 29–30 cm contains a concentration of zeolite and is streaked with light gray chalk. Outward from this layer is a progression from flaser-nodular chalk to thin anastomosing seams. These textures are probably produced under pressure-solution lithification of an altered volcanic ash bed that had been mixed with surrounding calcareous sediment by bioturbation. Such intervals are characteristic of Subunit IIB.

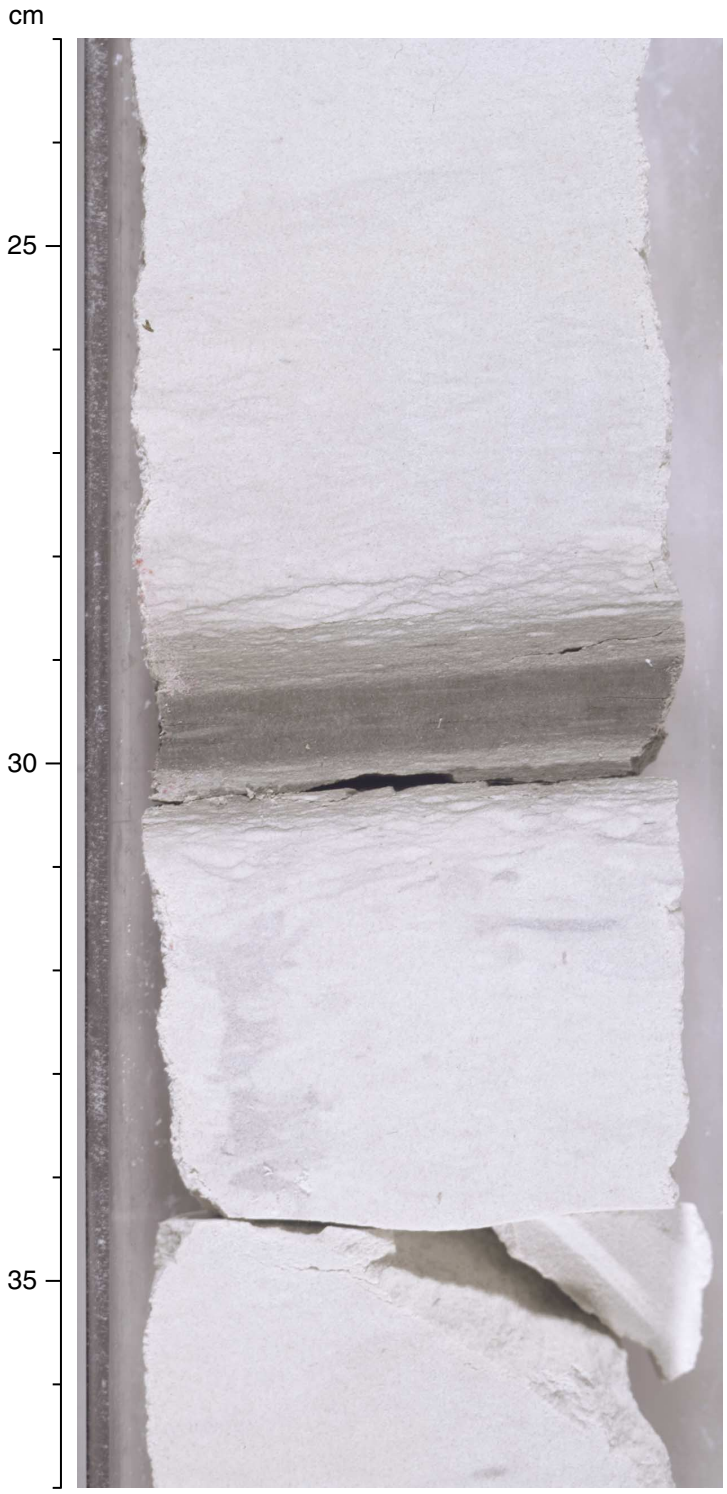

Figure F14. The lowest zeolite-rich band defines the contact between lithologic Units II and III (interval 192-1183A-39R-4, 7–25 cm). The Cretaceous/Paleogene boundary is ~70 cm below this diagenetically concentrated, altered volcanic ash.

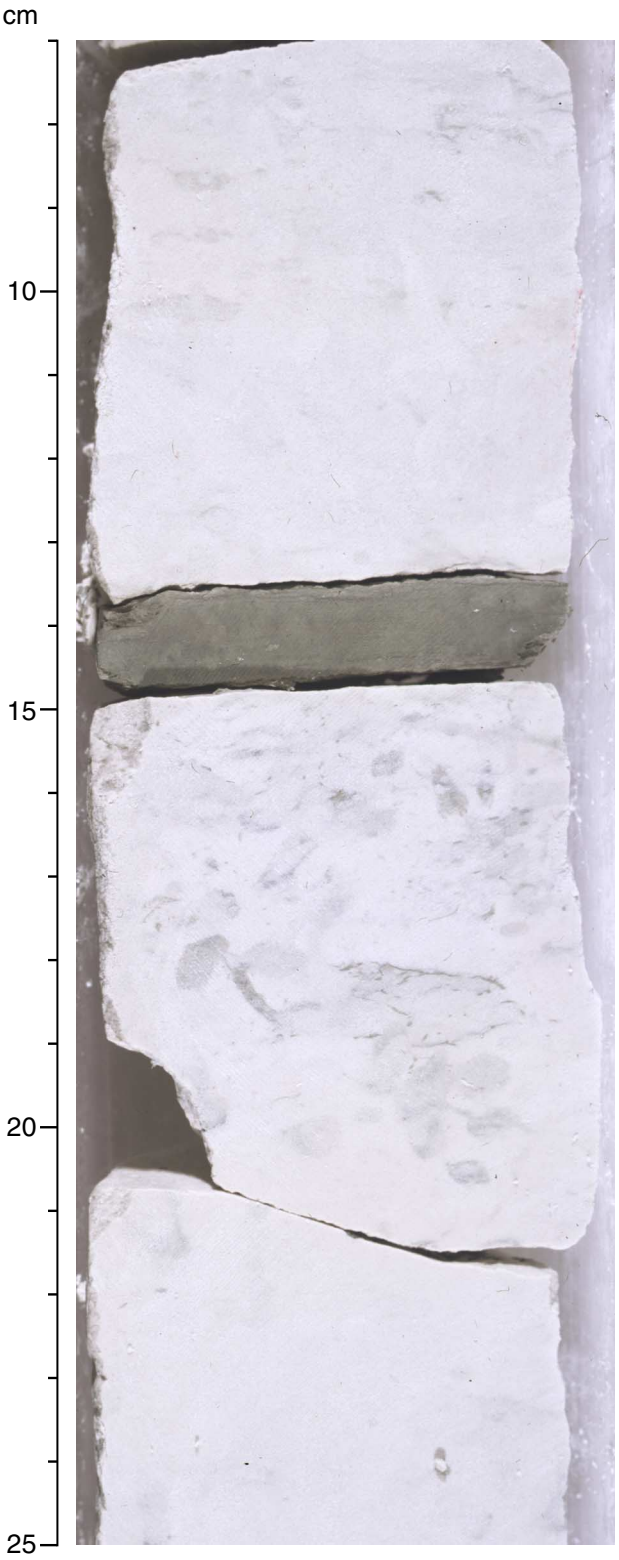

Figure F15. Typical Maastrichtian facies of bioturbated limestone with scattered chert nodules and pressure-solution stylolites (Subunit IIIA; interval 192-1183A-40R-1, 1–20 cm).

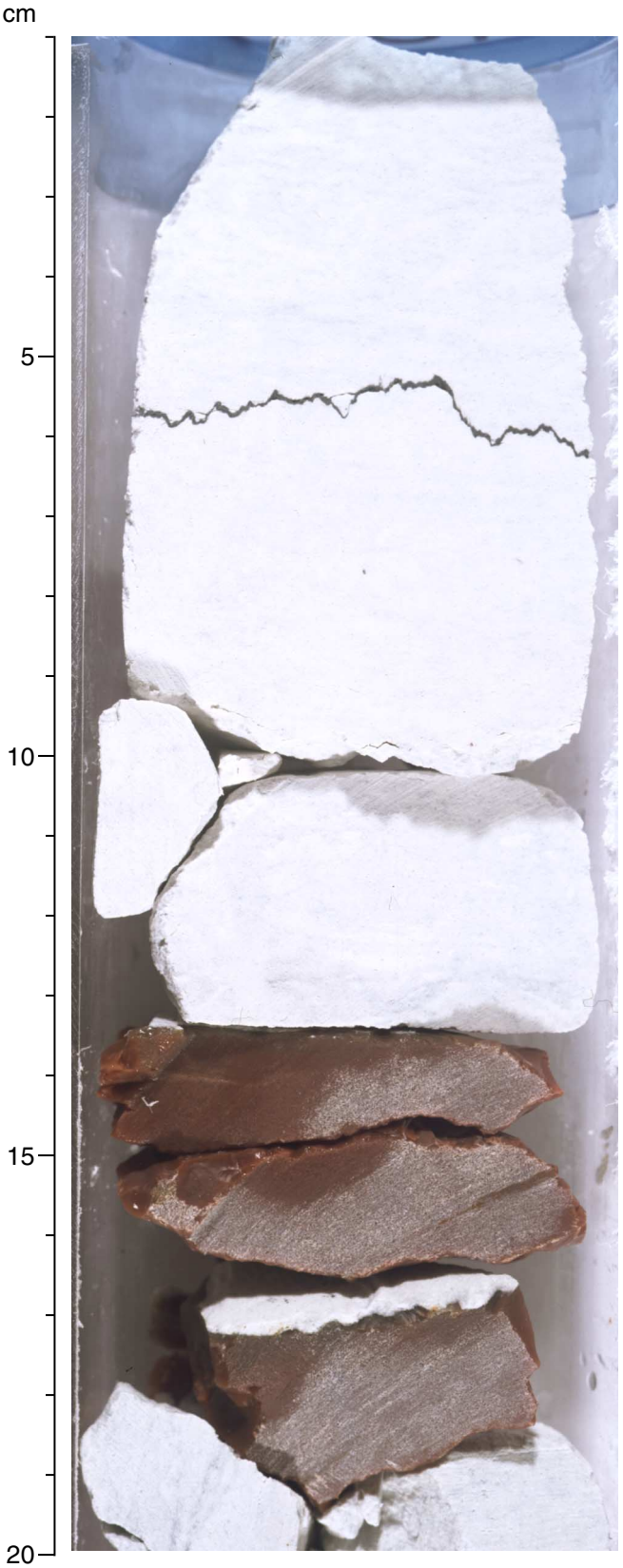

Figure F16. Cycles of light yellowish brown bands within white limestone (lower Subunit IIIA; early Maastrichtian; interval 192-1183A-45R-2, 90–105 cm). Burrows carry sediment of each color downward into the lower facies, implying that the color bands are not diagenetic staining.

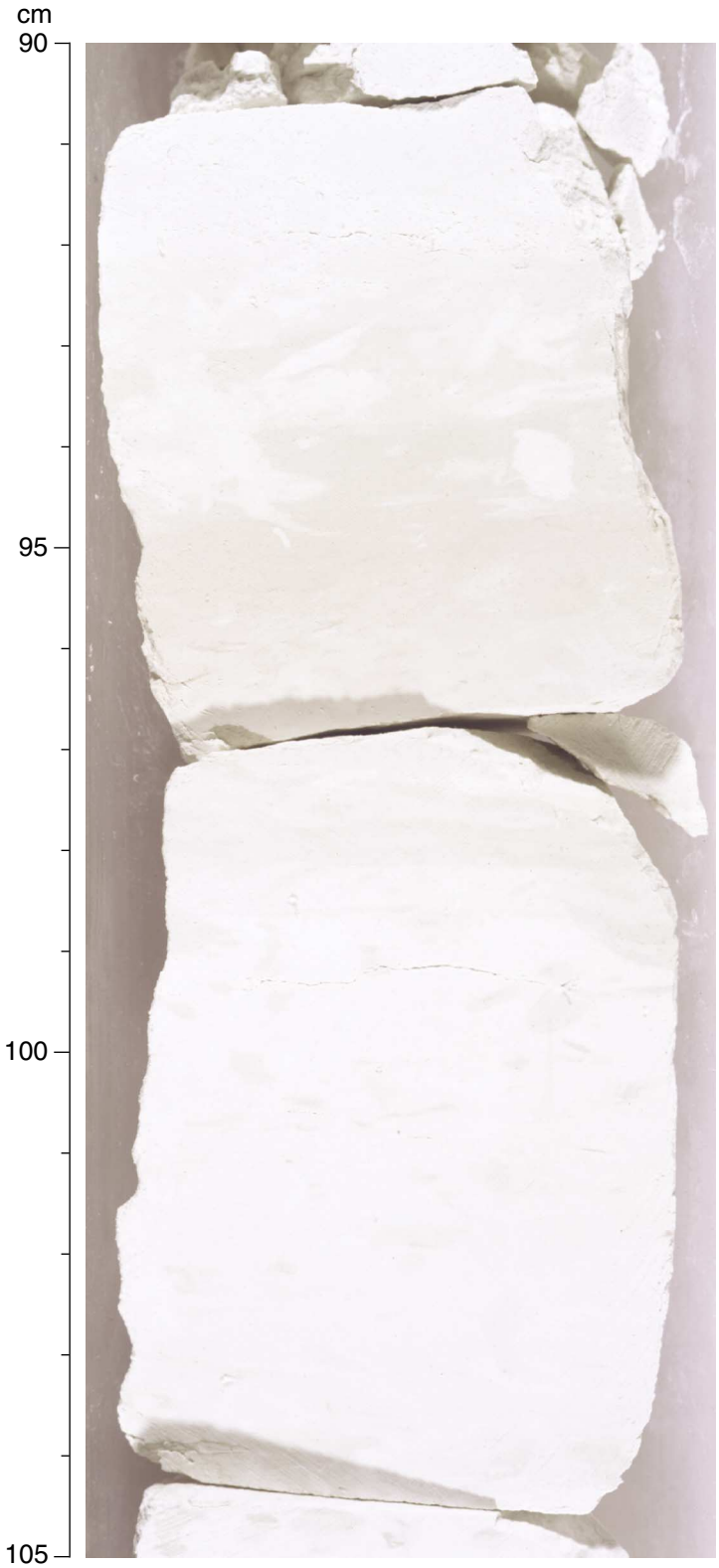

Figure F17. Typical micrite limestone with foraminifers in lower Subunit IIIA (early Maastrichtian; Sample **192-1183A-45R-1, 18–20 cm;** plane-polarized light; field of view = 2.8 mm; photomicrograph ID# 1183AS_15).

Figure F18. Santonian–Coniacian facies (red at base) overlying the hardground at 77 cm developed on light pink Albian limestone (uppermost Subunit IIIB; interval 192-1183A-50R-2, 40–80 cm). Santonian–Campanian facies has interbedded dark claystone and bioturbated reddish limestone. Dark redox fronts from the claystone have stained the adjacent limestone (e.g., sharp color change at 72 cm) and have surrounded pockets of reddish limestone (e.g., at 63 cm).

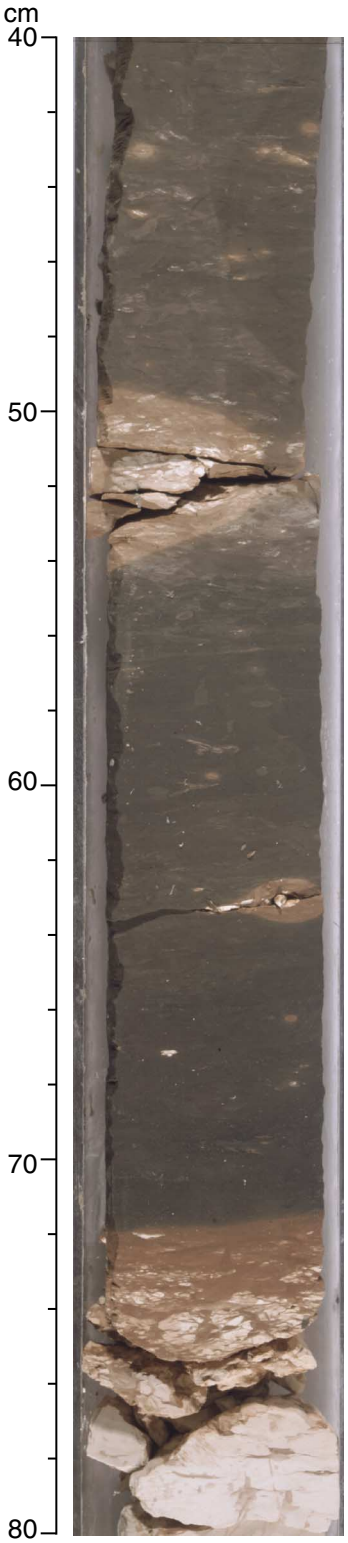

Figure F19. Typical appearance of limestone in Subunit IIIB (Aptian–Albian; interval 192-1183A-53R-2, 109–127 cm). The woody texture consists of compacted bioturbation, microflasers, anastomosing seams, and subhorizontal discontinuous seams. Mottles of gray and pink formed after these diagenetic textures.

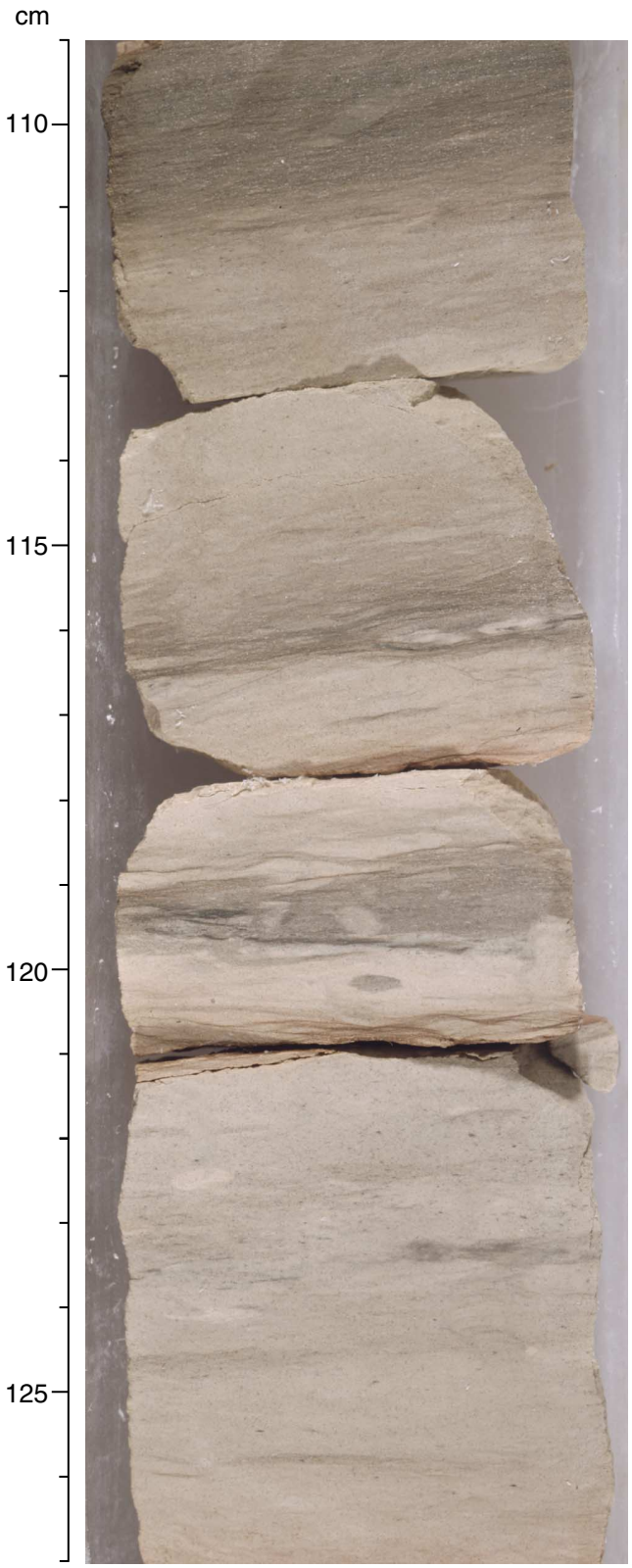

Figure F20. Laminated dark calcareous claystone in Subunit IIIB (Aptian–Albian; interval 192-1183A-53R-4, 15–35 cm). Discrete laminae are composed of concentrated foraminifers or of fine-sand material. Claystone composition is dominated by iron oxyhydroxides (goethite) and nontronite with ~30% nannofossils and scattered planktonic foraminifers. The absence of bioturbation contrasts with adjacent beds of bioturbated limestone.

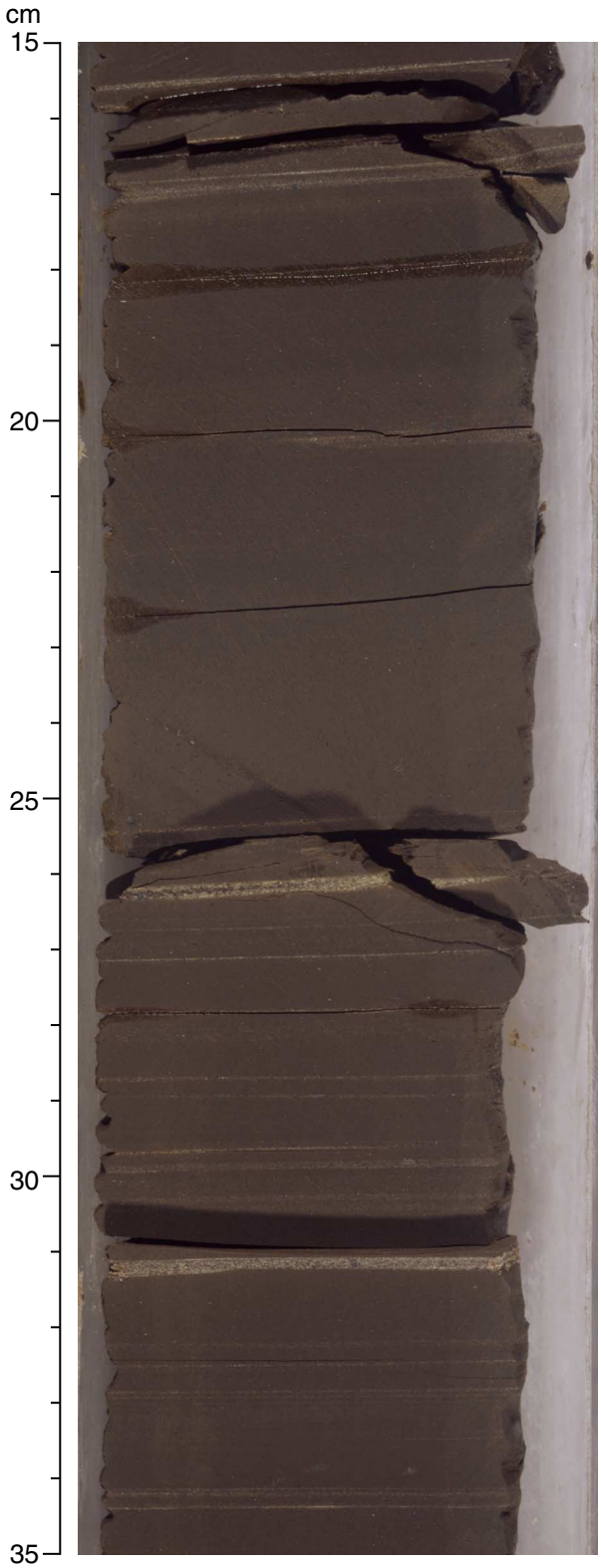

Figure F21. Vitric tuff with normal-graded layers (in lowest meter of Subunit IIIB, Aptian; interval 192-1183A-54R-3, 34–85 cm). Bioturbated limestone interbed is at 58–63 cm.

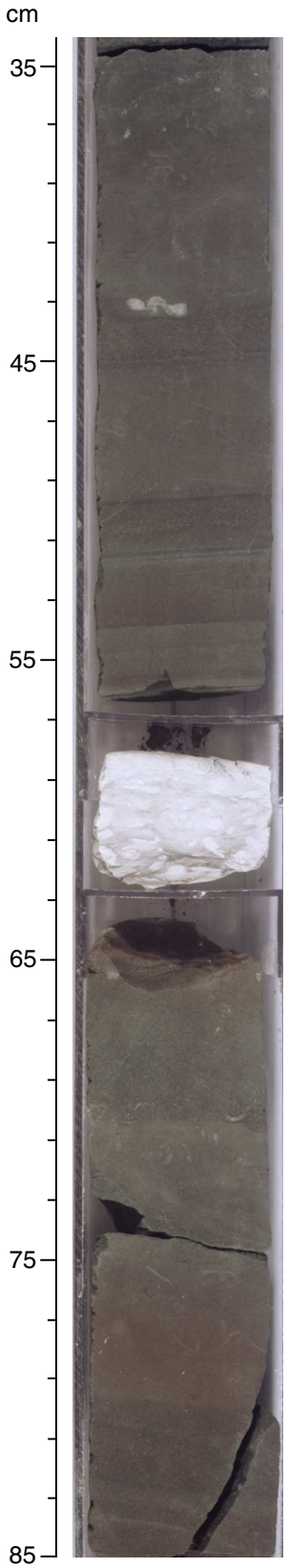

Figure F22. Bioturbated reddish limestone overlying uppermost basalt flow (base of Subunit IIIB; Aptian; interval 192-1183A-54R-3, 95–130 cm).

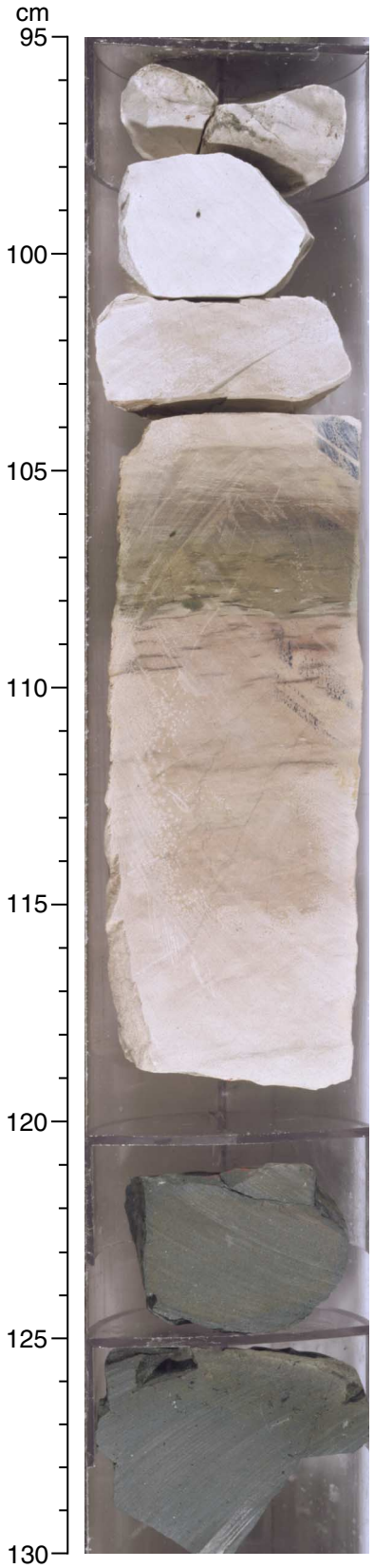

Figure F23. Partially recrystallized foraminifer-bearing limestone above hyaloclastite at top of basement Unit 2 (Aptian; interval 192-1183A-54R-4, 9–18 cm).

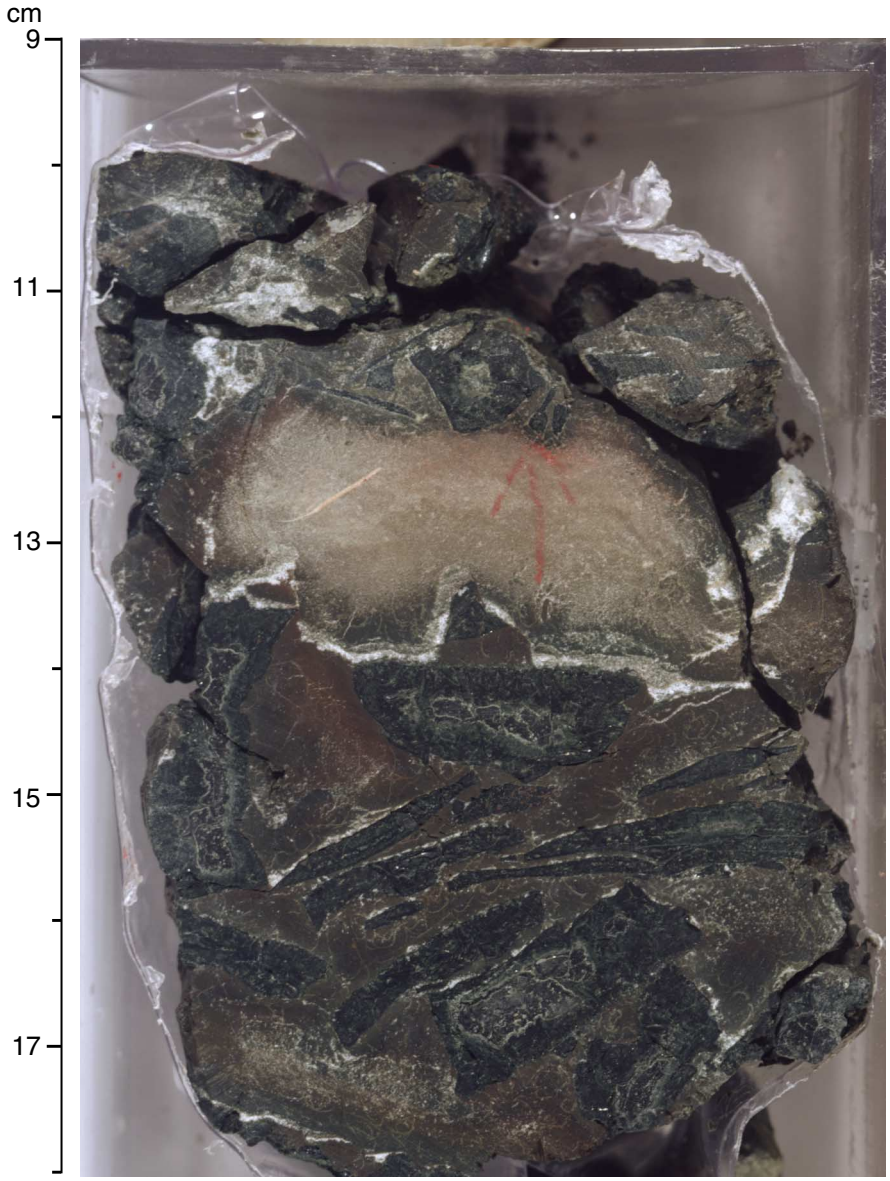

Figure F24. Base of laminated dark calcareous claystone (Subunit IIIB; Aptian–Albian; interval 192-1183A-53R-4, 80–90 cm). The laminated claystone contrasts with the underlying bioturbated pinkish white limestone. Laminae in this interval are composed of concentrations of planktonic foraminifers.

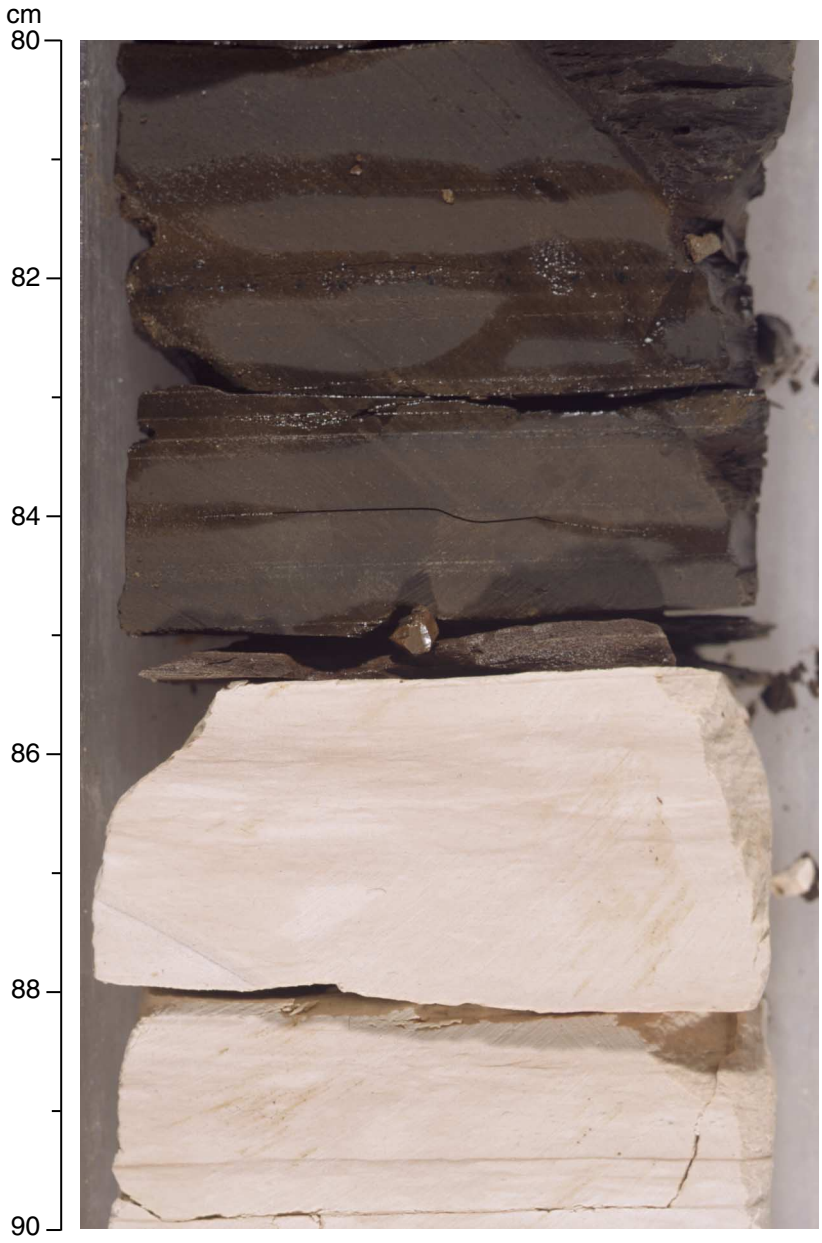

Figure F25. Microfacies texture of laminated dark calcareous claystone (Subunit IIIB; Aptian–Albian; Sample **192-1183A-53R-3, 112–114 cm;** plane-polarized light; field of view = 0.7 mm; photomicrograph ID# 1183AS_18). Planktonic foraminifers have been partially replaced or filled with dark opaque mineral (perhaps pyrite that was later altered to iron oxyhydroxide) and calcite.

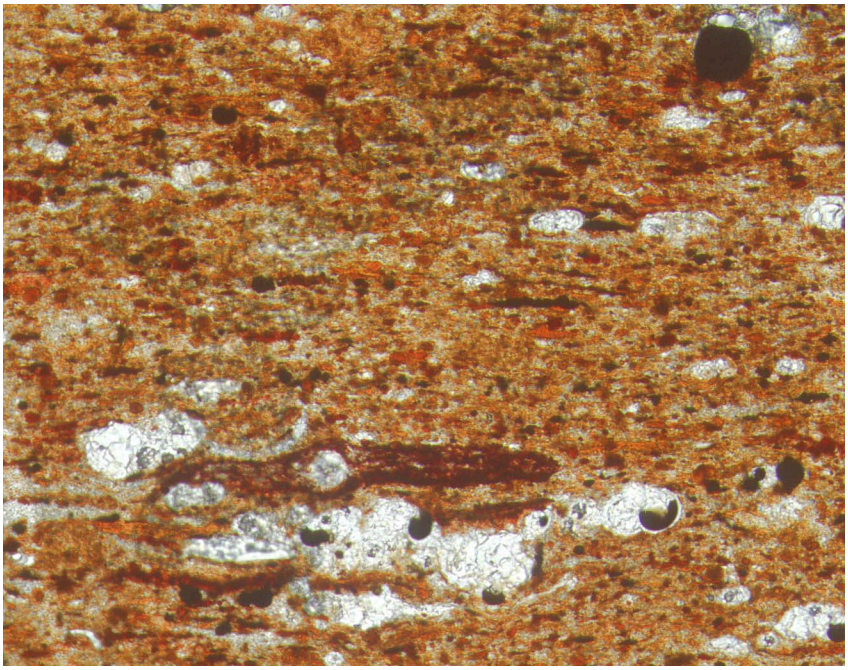

Figure F26. Microfacies of laminated dark calcareous claystone (Subunit IIIB; Aptian–Albian; Sample **192-1183A-53R-3, 112–114 cm;** plane-polarized light; field of view = 2.8 mm; photomicrograph ID# 1183AS_21). Reddish brown matrix consists of fine particles of iron oxyhydroxides with variable proportions of calcareous nannofossils in each band. White laminae are concentrations of planktonic foraminifers and phosphatic fish debris.

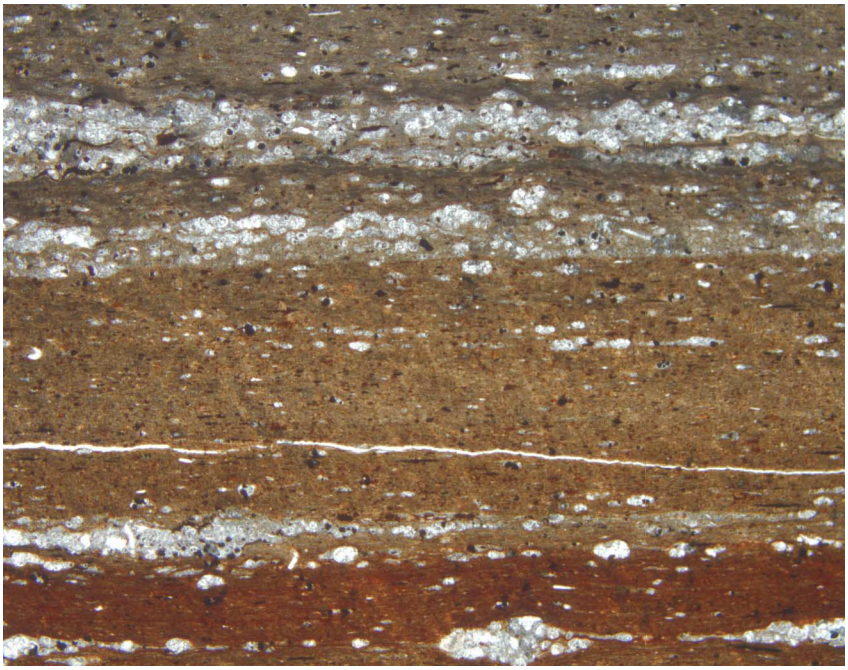

Figure F27. A model of estimated calcite compensation depth (CCD; gray or yellow line) on the Ontong Java Plateau through time. Paleodepths (white lines) of the sediment surface through time at each site were calculated from present depths and assuming simple thermal subsidence and isostatic compensation relative to the accumulating sedimentary cover (see "Aptian–Maastrichtian CCD," p. 14). The CCD curve was constructed assuming that carbonate sediments of a given age indicate deposition above the CCD.

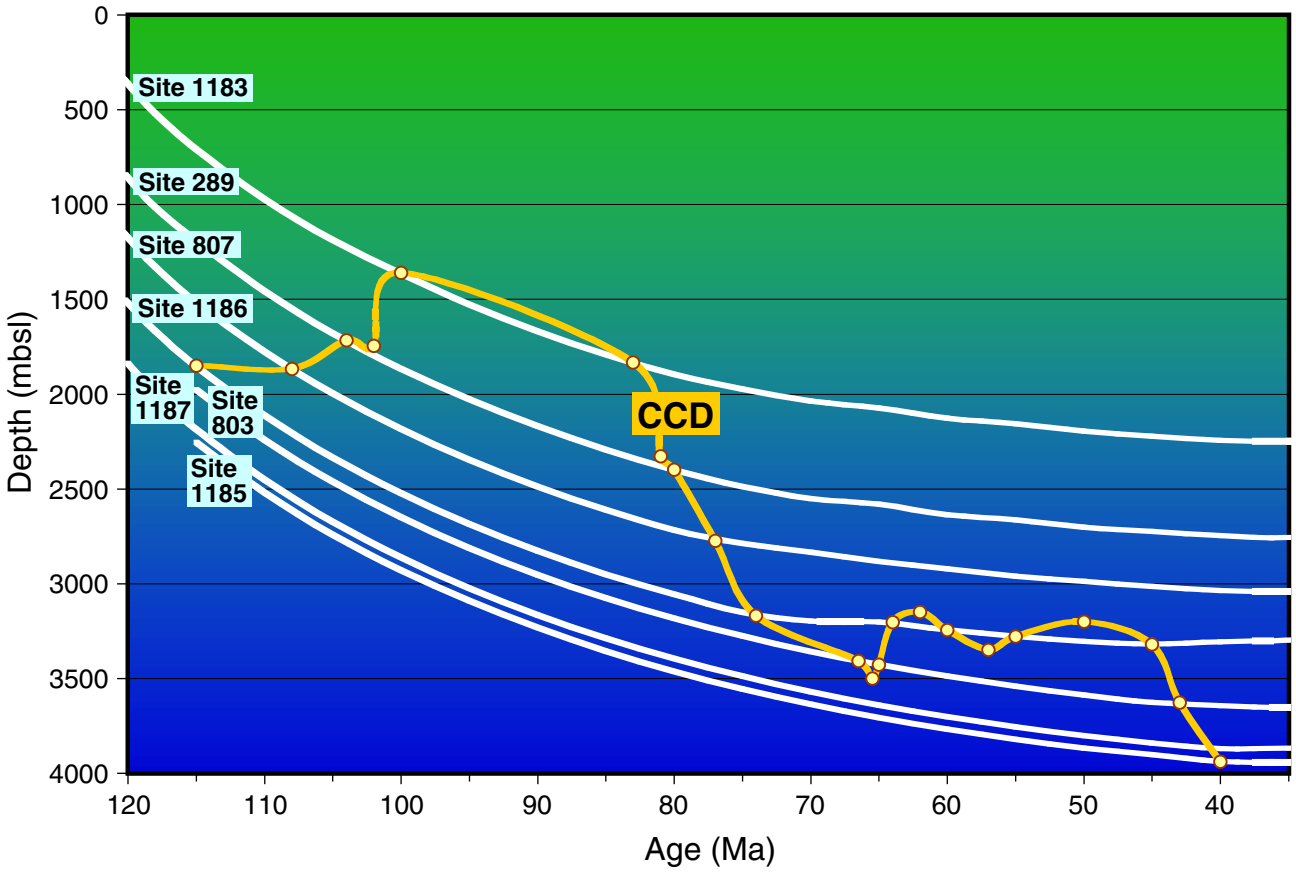

Figure F28. Multiple and overlapping diagenetic features (upper Subunit IIIB; Albian; interval 192-1183A-50R-CC, 1–18 cm). The piece of pinkish limestone at 4–7 cm was partially silicified by a red chertification front descending from the top. Superimposed on both the limestone and the chert is a dark gray mottle (right) caused by late-stage redox migration of oxides.

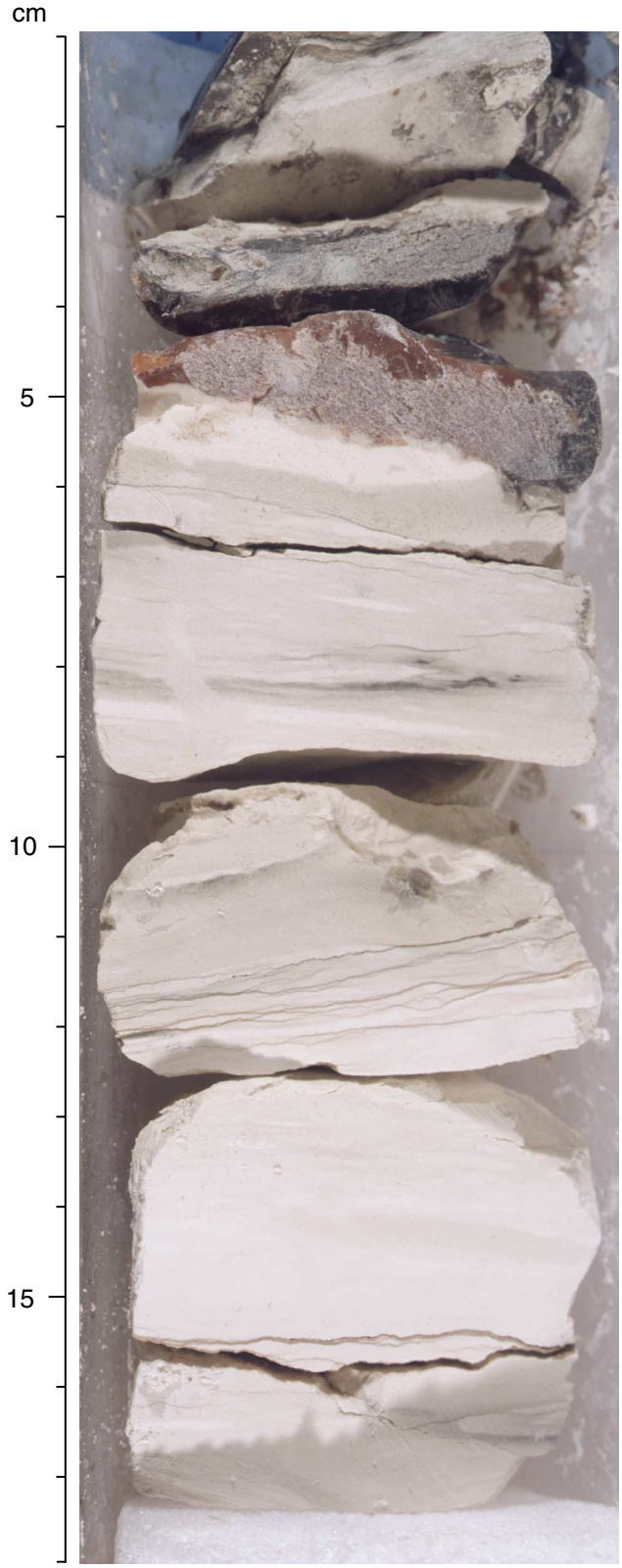

Figure F29. Color laminae superimposed on bioturbated white chalk (Subunit IB; Miocene; interval 192-1183A-8R-2, 36–47 cm). Pyritized burrow at 44 cm indicates postburial redistribution of iron. Color laminae are analogous to Liesegang banding produced by diagenetic redox fronts.

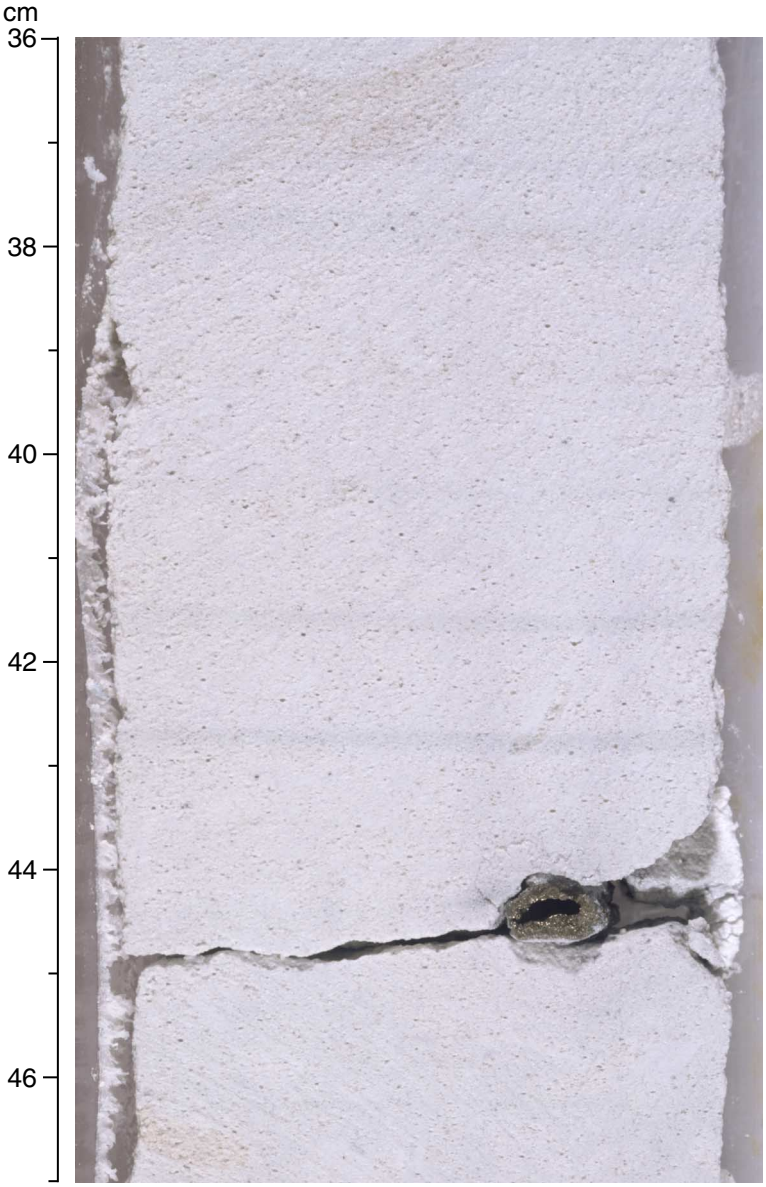

Figure F30. Chertification in limestone (Subunit IIA; Eocene; interval 192-1183A-24R-2, 121–136 cm). Silicification front is at 123 cm. White pockets within dark chert are partially silicified limestone or porcellanite.

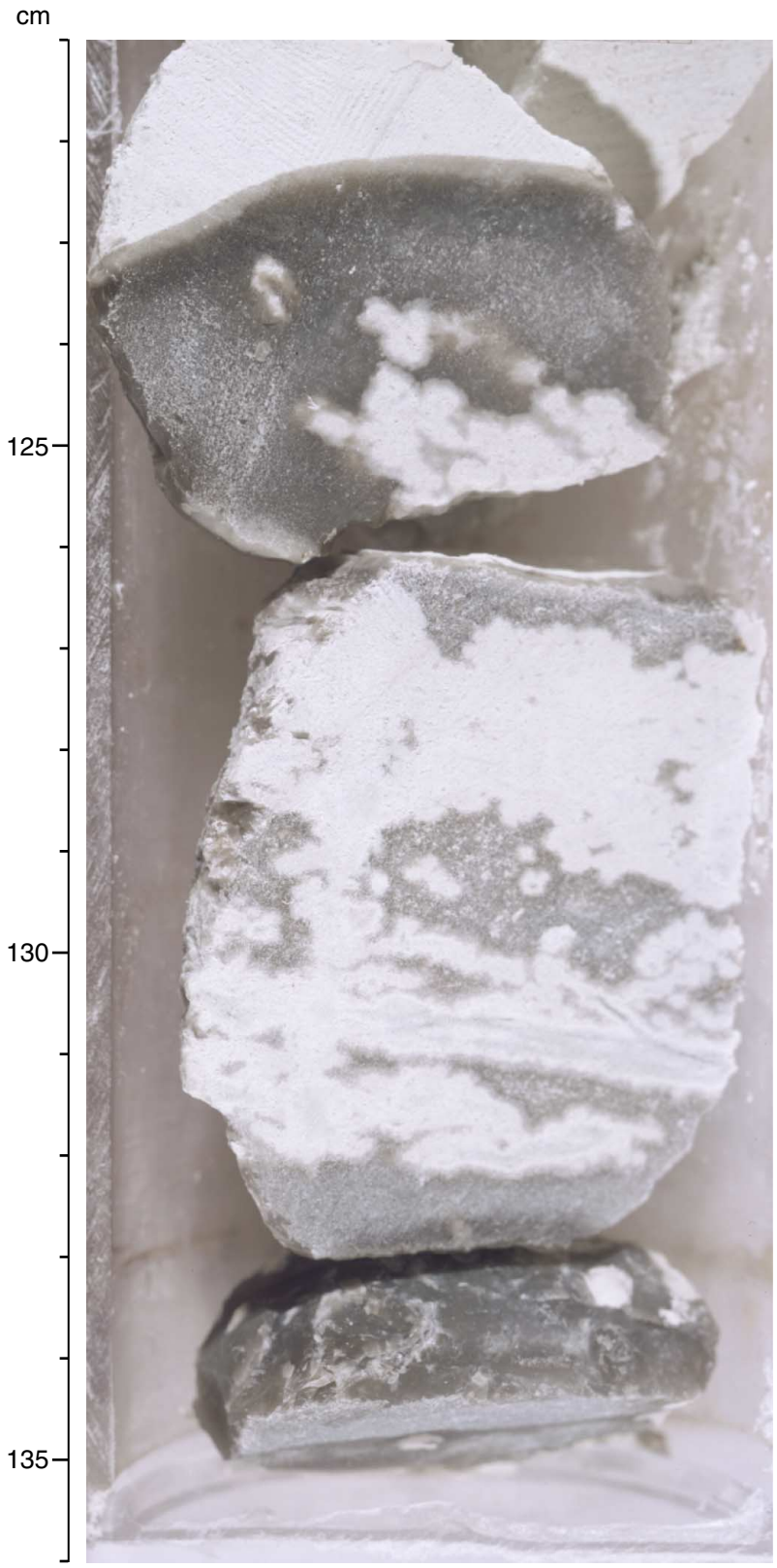

Figure F31. Flaser texture produced by pressure-solution diagenesis of a partially bioturbated volcanic ash (Subunit IC; Oligocene; interval 192-1183A-17R-1, 120–135 cm). The highest concentrations of volcanic ash were concentrated into seams, whereas wispy microstylolites in more carbonate-rich intervals produce a nodular chalk texture.

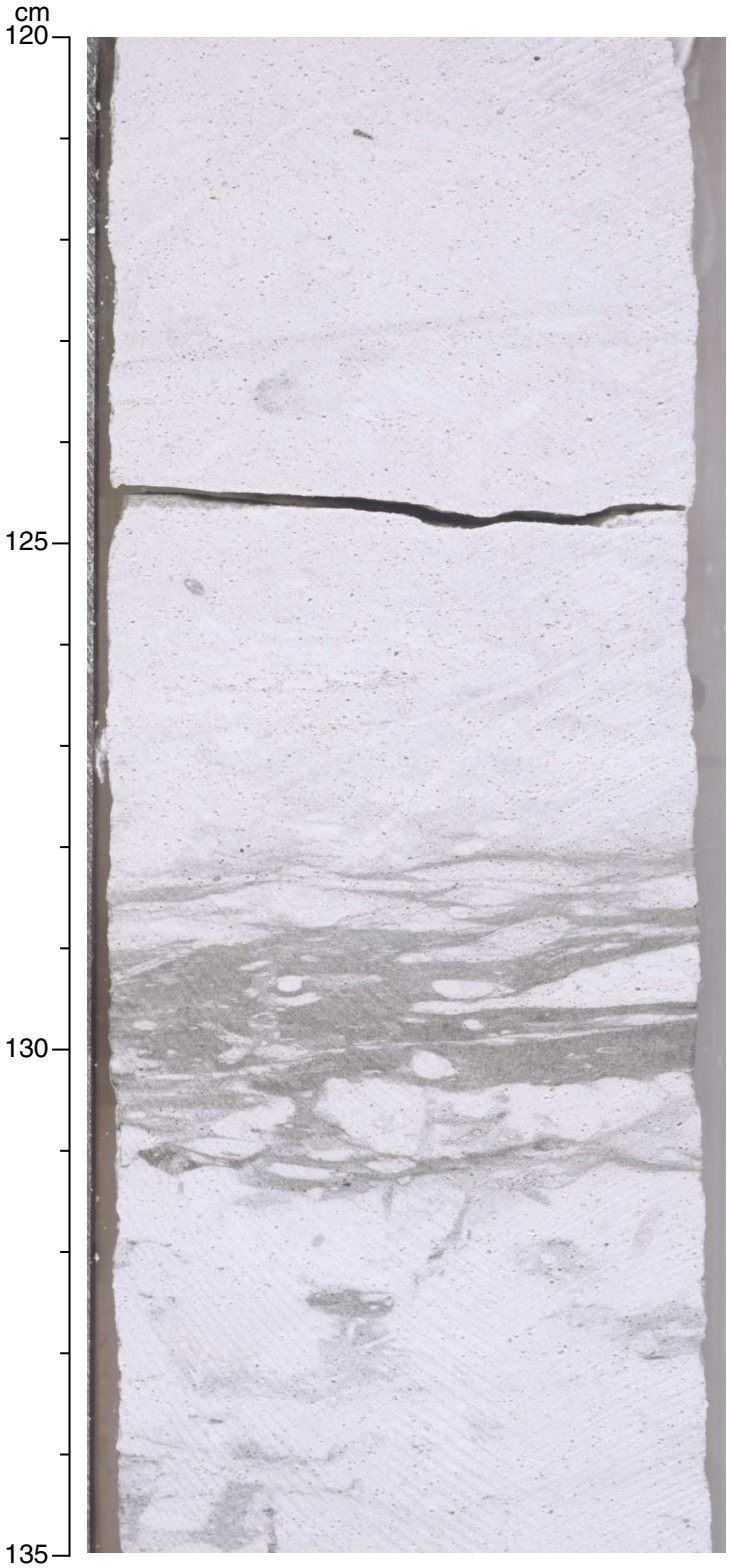

Figure F32. Microstylolite produced by pressure solution of foraminifer chalk (Subunit IC; Oligocene; Sample 192-1183A-20R-CC, 2–6 cm; plane-polarized light; field of view = 1.4 mm; photomicrograph ID# 1183AS_1). Foraminifers are truncated by enhanced dissolution adjacent to the thin clay seam in the middle of the image.

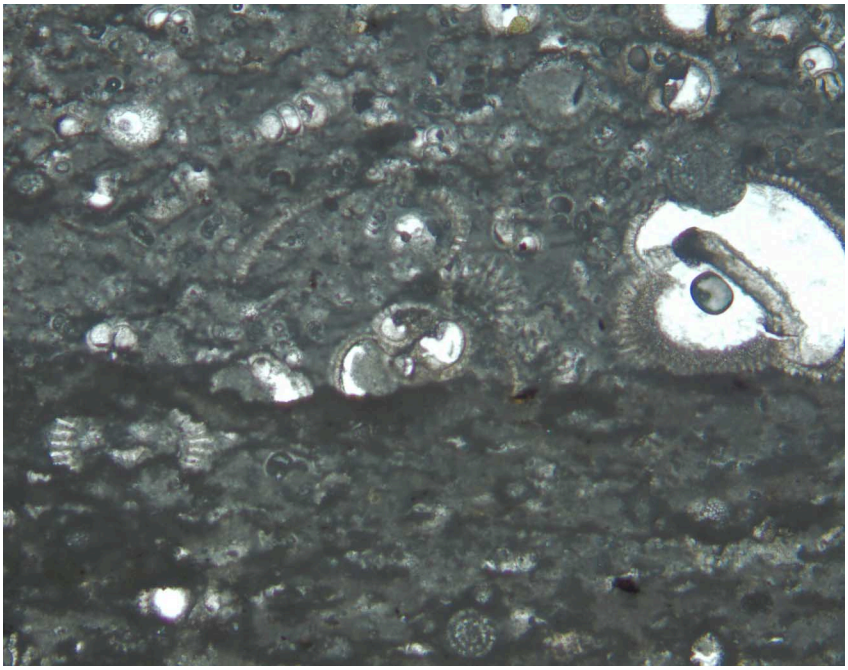

Figure F33. Diagenetic woody texture of anastomosing and discontinuous seams and microflasers developed by pressure-solution lithification of a bioturbated limestone containing minor volcanic ash (Subunit IIIB; Albian; interval 192-1183A-51R-2, 37–58 cm). Partial chertification fronts into the limestone are at 40- and 58-cm levels.

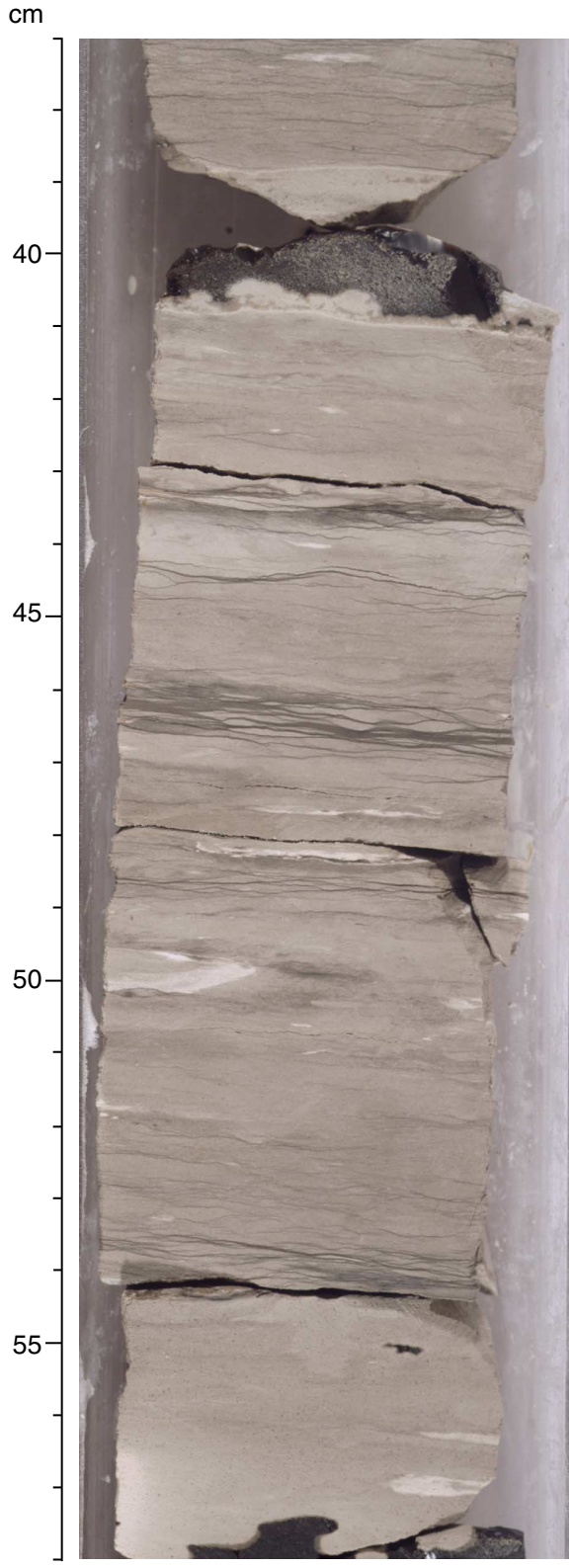

Figure F34. Interval 192-1183A-56R-1 (Pieces 1–3, 1–19 cm) showing the top of Unit 5. Piece 1 (1–7 cm) is a recrystallized limestone cobble (Unit 5A), Piece 2 (8–9 cm) is a glassy pillow rim of Unit 5B, and Piece 3 (11–19 cm) is the chilled upper surface of basalt of Unit 5B.

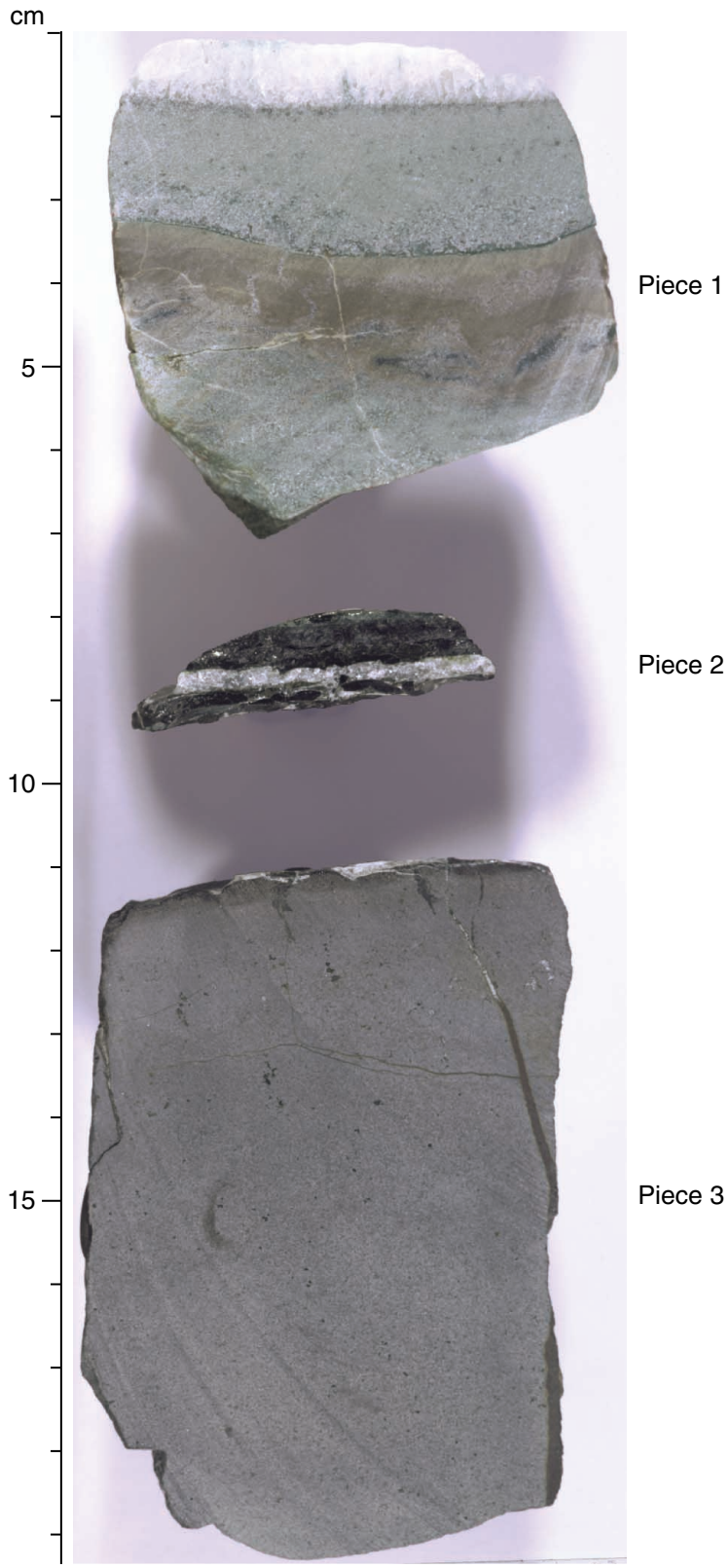

Figure F35. Interval 192-1183A-64R-2 (Pieces 2–5, 14–34 cm) showing the contact between Units 6 and 7 defined by a calcite-cemented hyaloclastite breccia.

Figure F36. A summary of the basement units at Hole 1183A that illustrates core number and recovery (black boxes, on left) for the basaltic sequence. Also shown are the locations of xenoliths (×), glassy pillow rinds (red diamonds), and the approximate percentages of phenocrysts as estimated from thin sections.

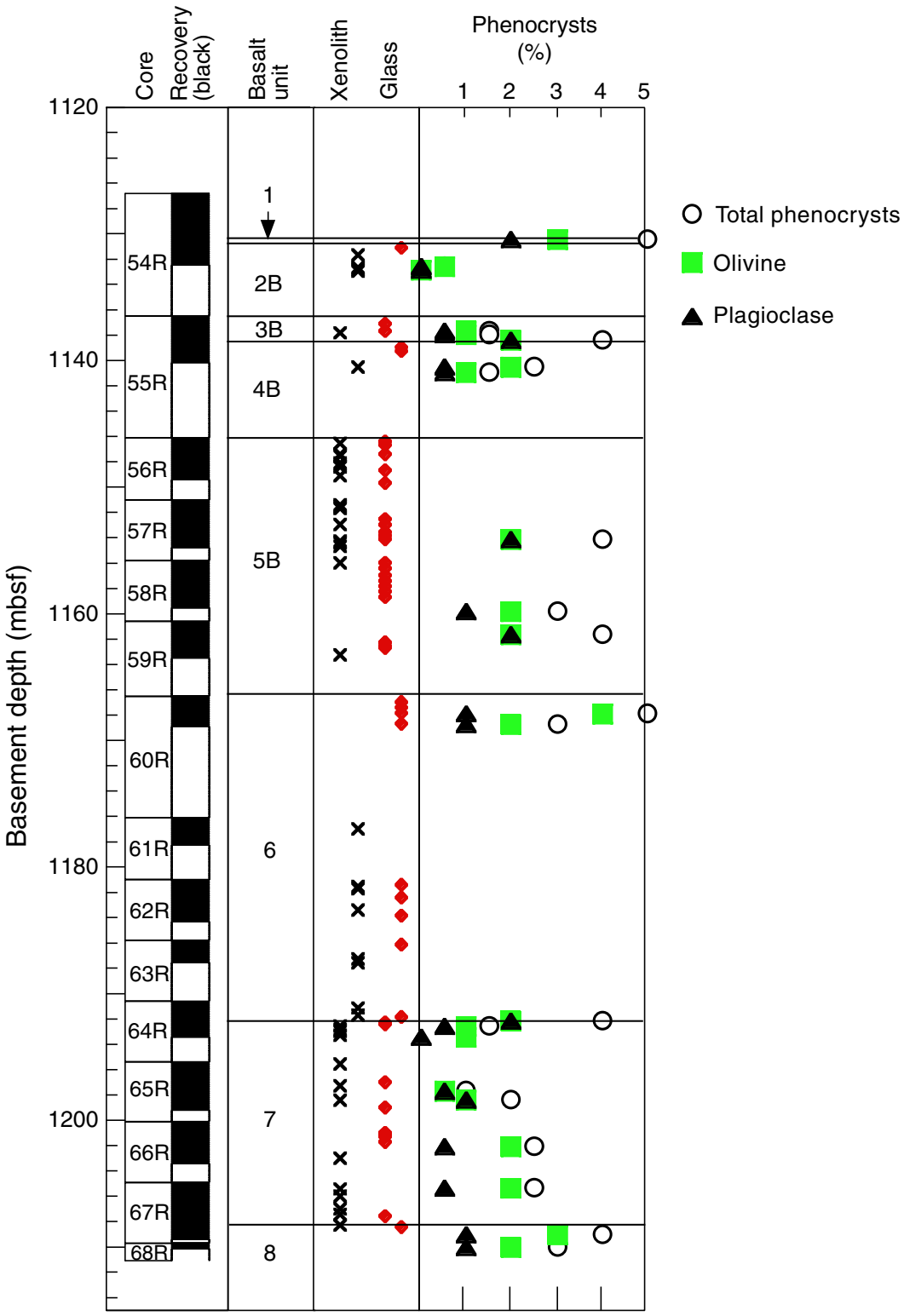

Figure F37. Interval 192-1183A-62R-2 (Pieces 1A–1C, 1–20 cm) illustrating a section through a basaltic pillow with a glassy rind and a 1- to 2-cm sparsely vesicular zone ~1 cm from the glass.

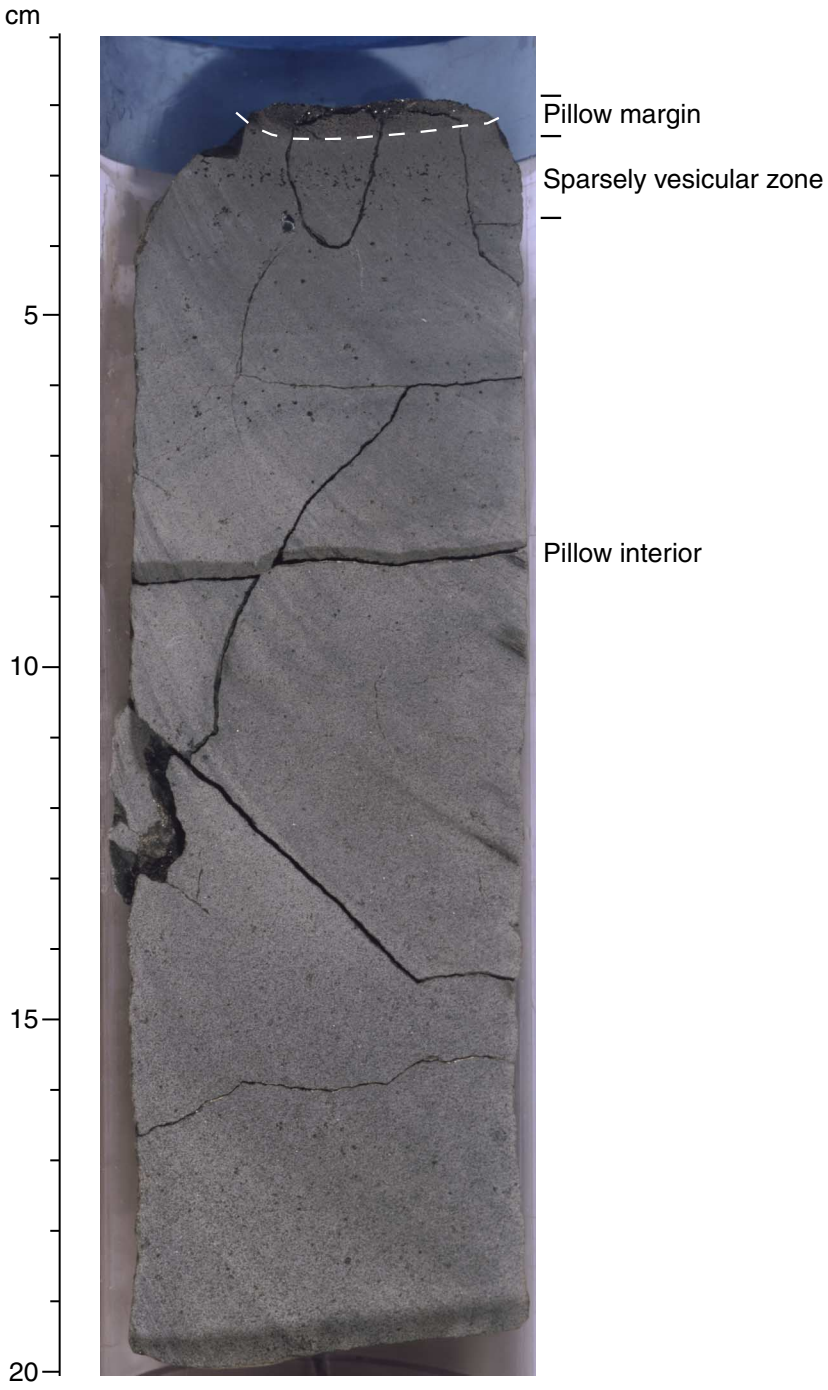

Figure F38. Interval 192-1183A-60R-1 (Piece 5, 27–38.5 cm) showing relatively unaltered pillow rim glass and the contact between two pillows. The margin is discontinuous because of the breakout of one of the pillows. **A.** Outer surface. **B.** Cut surface.

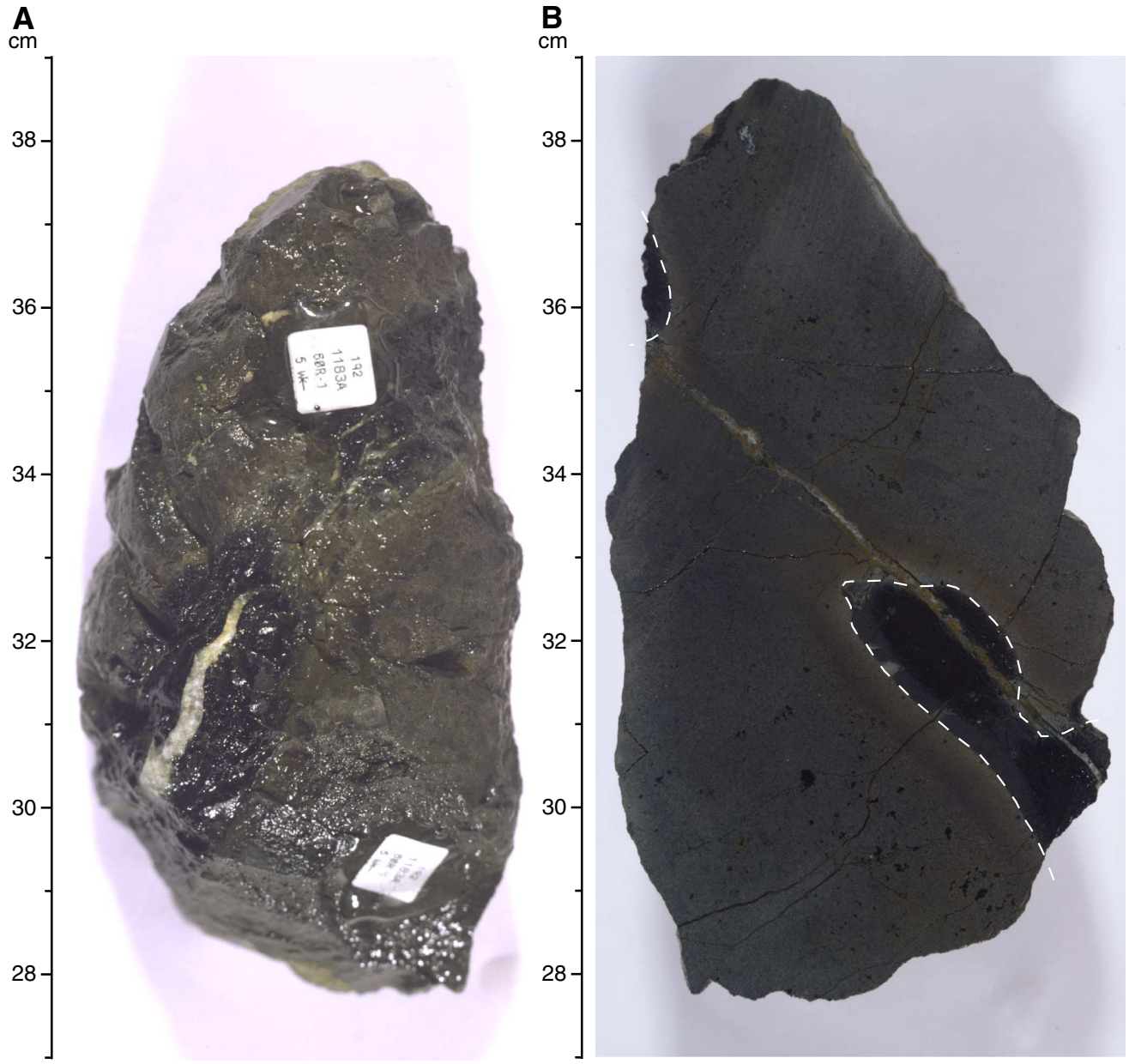

Figure F39. Interval 192-1183A-57R-2 (Piece 3, 21–31 cm) showing a section through a basaltic pillow with a glassy rind and a 1- to 2-cm sparsely vesicular zone in the aphanitic pillow rim, which grades to the fine-grained pillow interior.

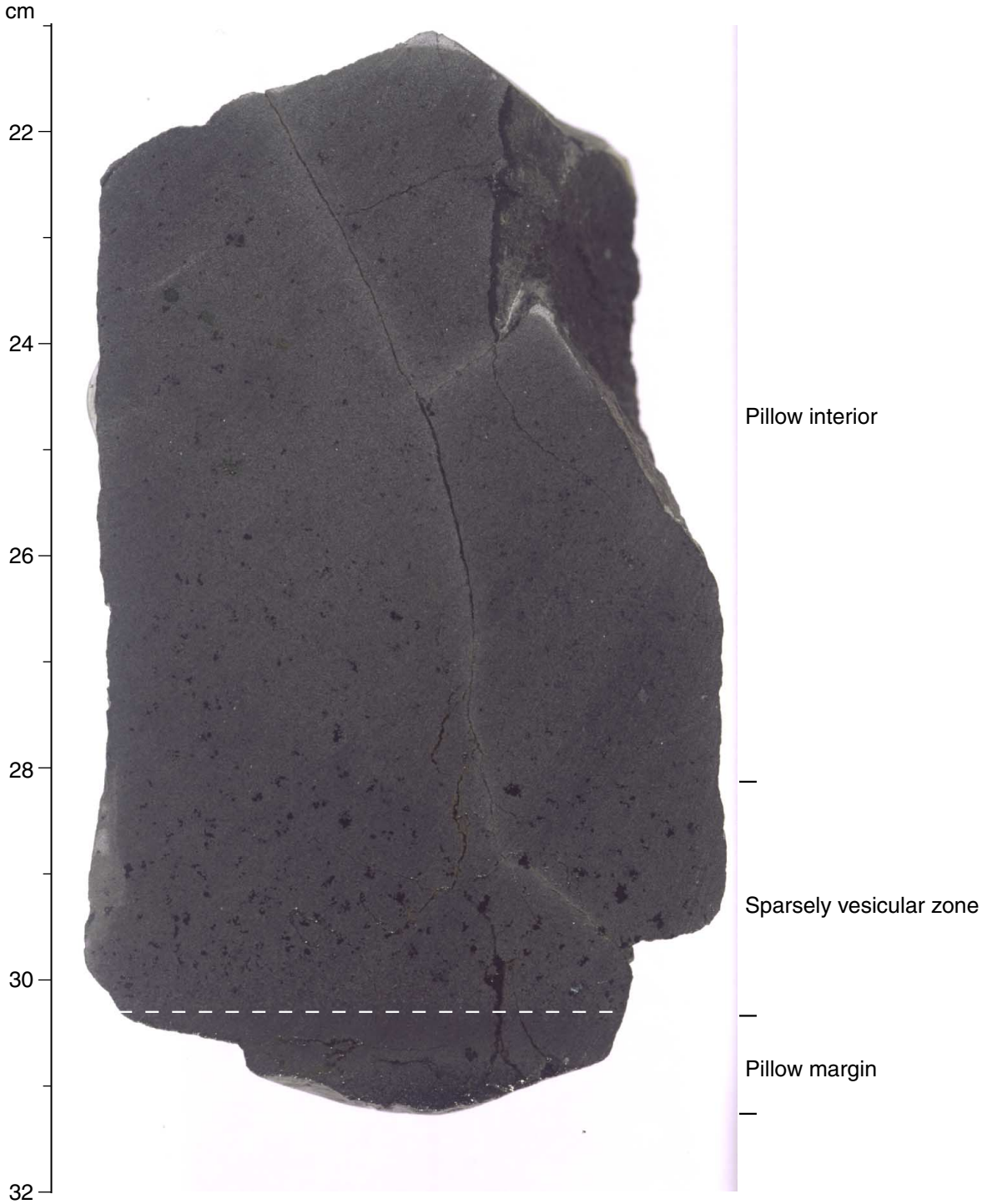

Figure F40. Interval 192-1183A-67R-3 (Pieces 8–9, 50–64 cm) showing curved pillow margins and the presence of interpillow sediment. Glassy margins and sediment are highlighted. **A.** Outer surface. **B.** Cut surface.

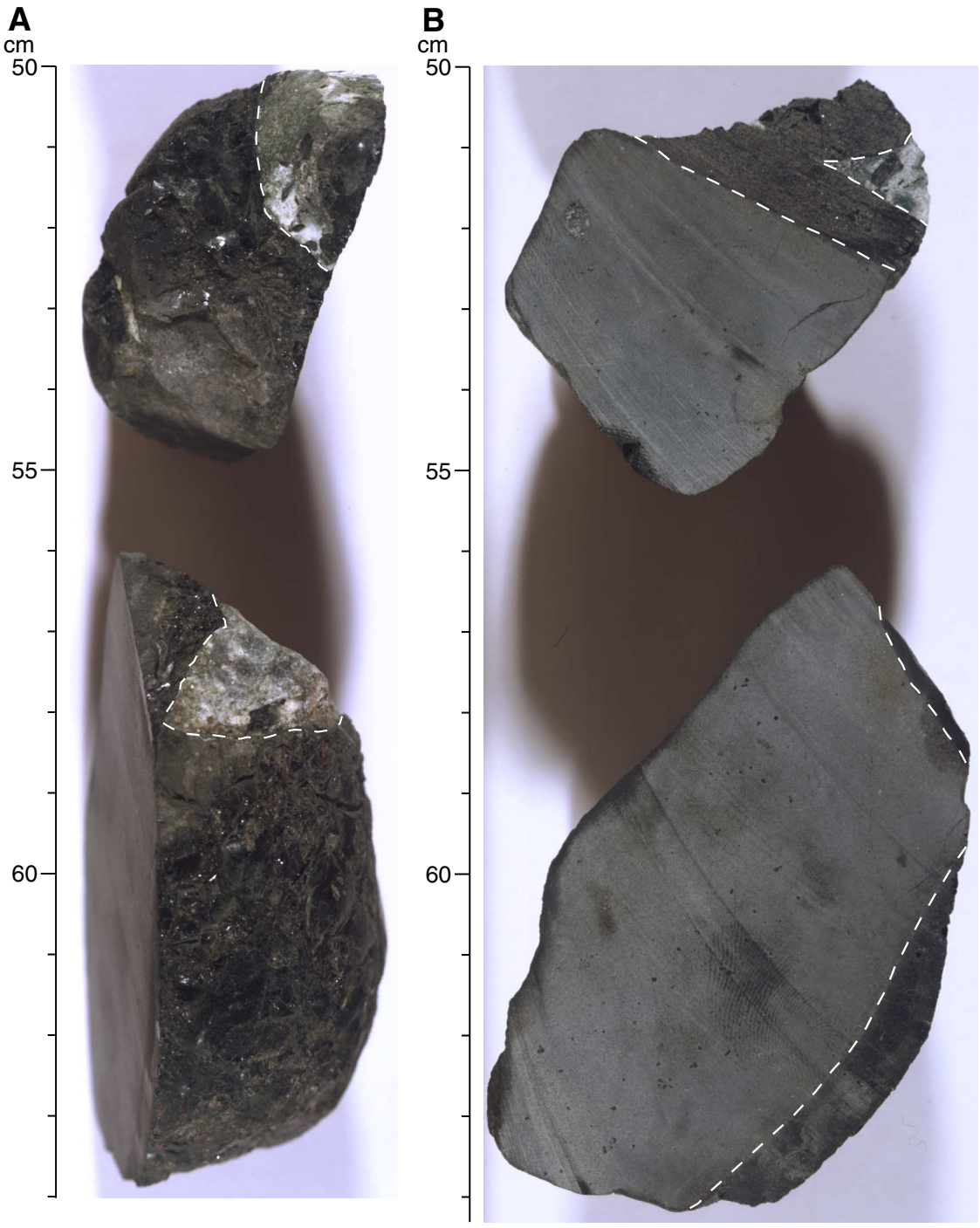

Figure F41. Interval 192-1183A-68R-1 (Pieces 3A–3C, 30–42 cm) showing pillow inflation structures in which subparallel aphanitic and fine-grained textures are juxtaposed in response to repeated magma pulses.

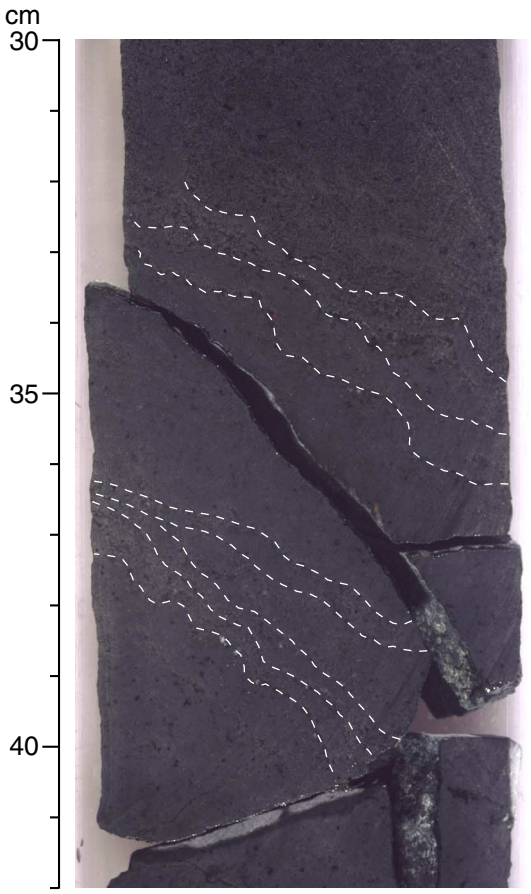

Figure F42. Interval 192-1183A-54R-5 (Piece 4A, 29–45 cm) showing a 1 cm × 2 cm subround, plagioclase-rich xenolith on the cut surface of the core.

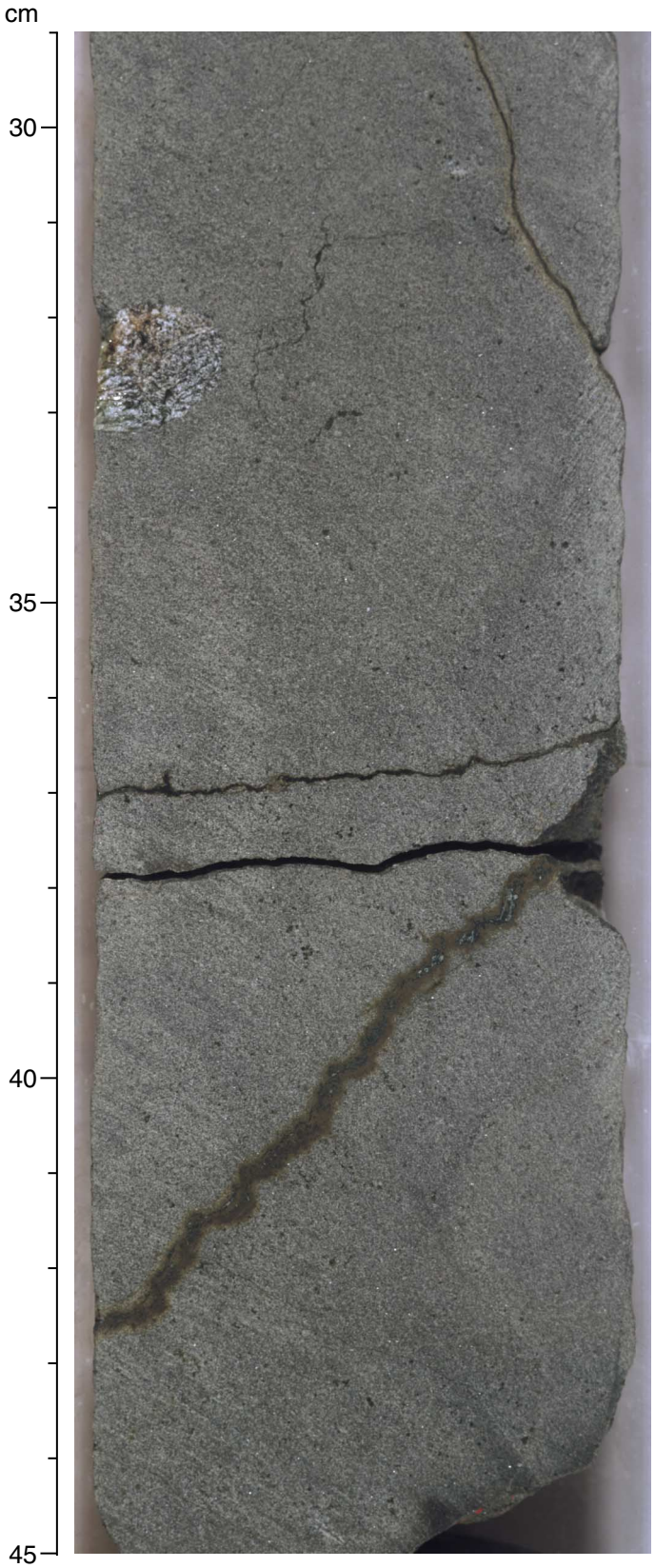

Figure F43. Interval 192-1183A-59R-2 (Piece 10A, 112–119 cm) showing a 1.5 cm × 3 cm subround, plagioclase-rich xenolith on the outer surface of the core.

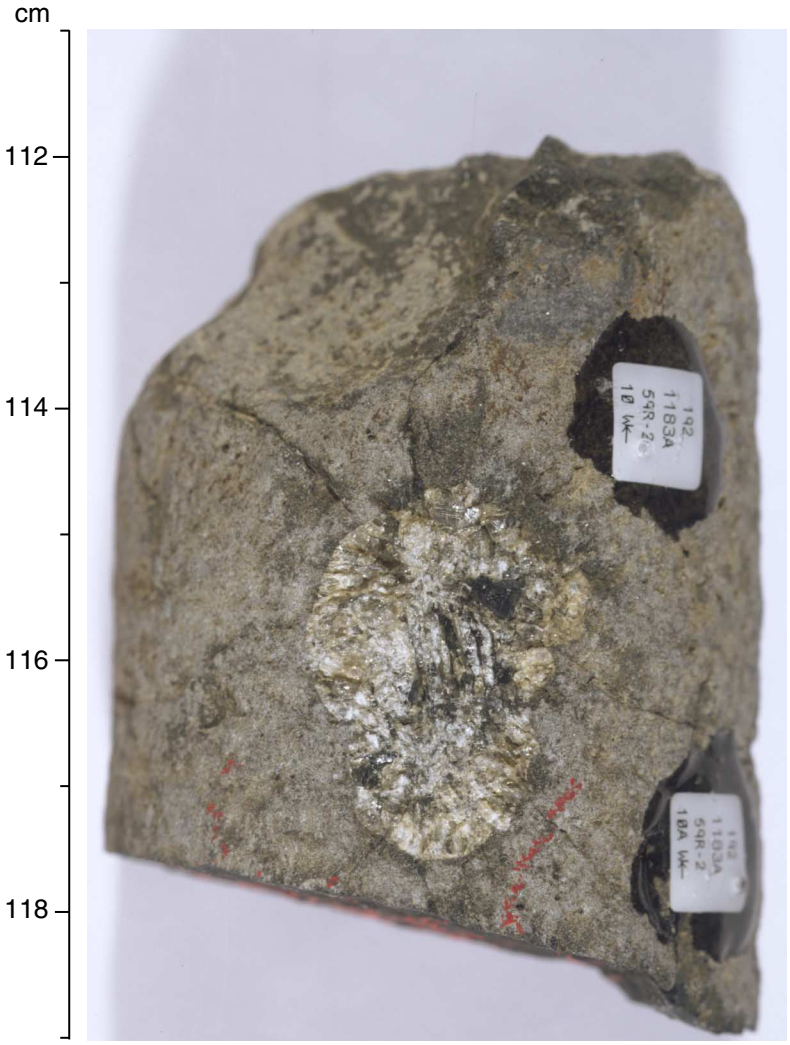

Figure F44. An aphanitic pillow rim at the edge of the sparsely vesicular zone in Unit 1 (Sample **192-1183A-54R-3 [Piece 5, 125–127 cm]**). Euhedral olivine phenocrysts and a glomerocryst of olivine and plagioclase are present (arrow). Olivine is pseudomorphed by green clay, which also partially fills the irregular vesicles in this thin section. The groundmass consists of quench-textured plagioclase and glass (field of view = 2.8 mm; plane-polarized light; photomicrograph ID# 1183A_003).

Figure F45. Fine-grained intersertal to subophitic texture of a pillow interior in Sample **192-1183A-55R-3 (Piece 5B, 128–129 cm),** Unit 4B. Euhedral to subhedral olivine phenocrysts (highlighted) are completely replaced by clay (field of view = 2.8 mm; plane-polarized light; photomicrograph ID# 1183A_007).

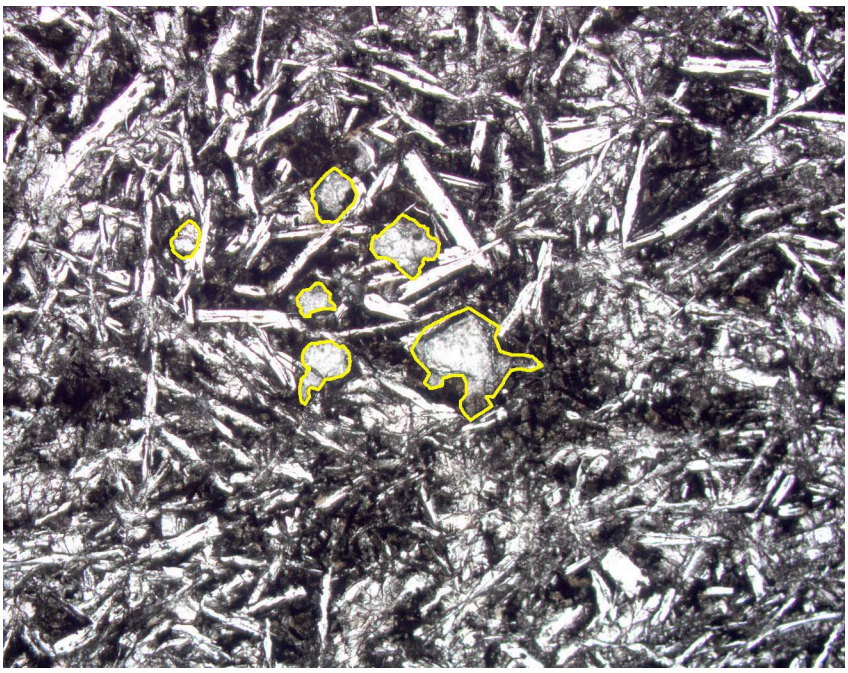

Figure F46. Texture of a fine-grained to partly glassy, sparsely olivine-phyric basalt in Sample **192-1183A-55R-4 (Piece 4, 38–41 cm),** Unit 4B. Olivine phenocrysts, visible in the quench-textured groundmass, are replaced by clay (field of view = 2.8 mm; plane-polarized light; photomicrograph ID# 1183A_004).

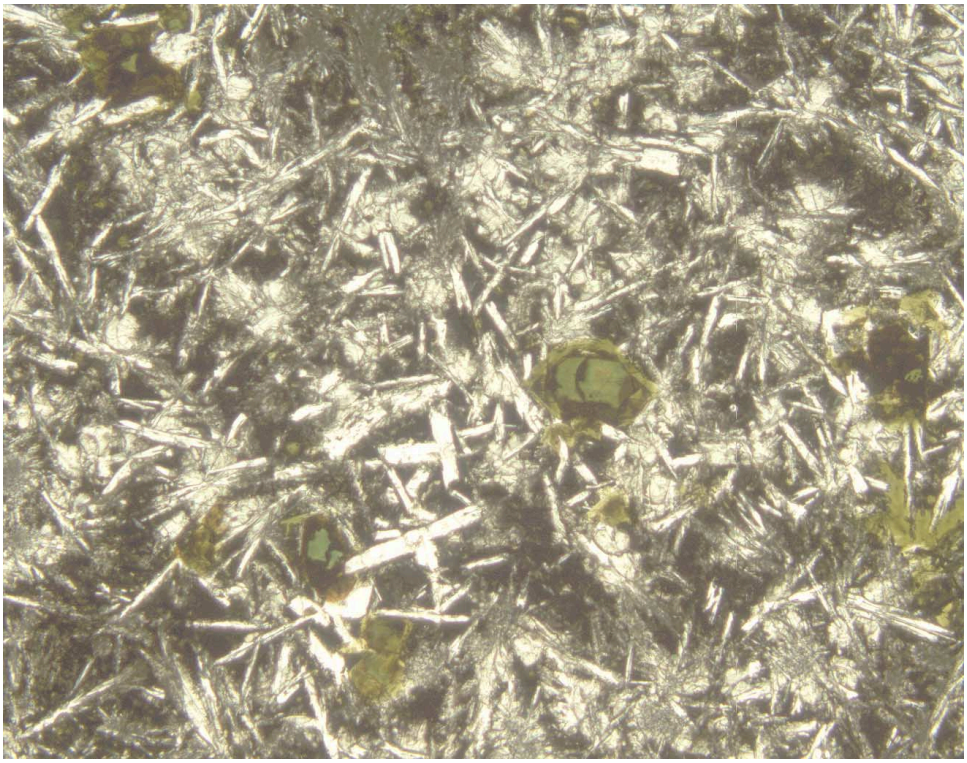

Figure F47. Olivine phenocrysts pseudomorphed by celadonite in a quenched, partly glassy pillow rim in Sample **192-1183A-58R-3 (Piece 13, 109–112 cm),** Unit 5B (field of view = 1.4 mm; plane-polarized light; photomicrograph ID# 1183A_005).

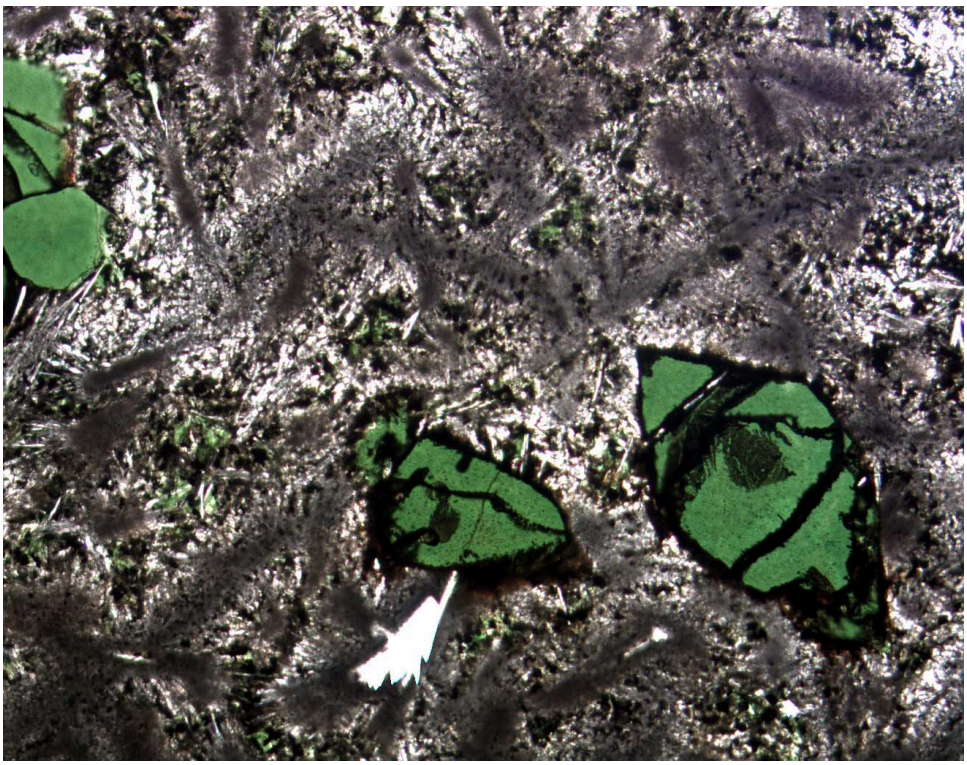

Figure F48. Partly devitrified glass inclusions in a plagioclase phenocryst in Sample **192-1183A-60R-1 (Piece 19, 139–141 cm),** Unit 6 (field of view = 0.35 mm; plane-polarized light; photomicrograph ID# 1183A_012).

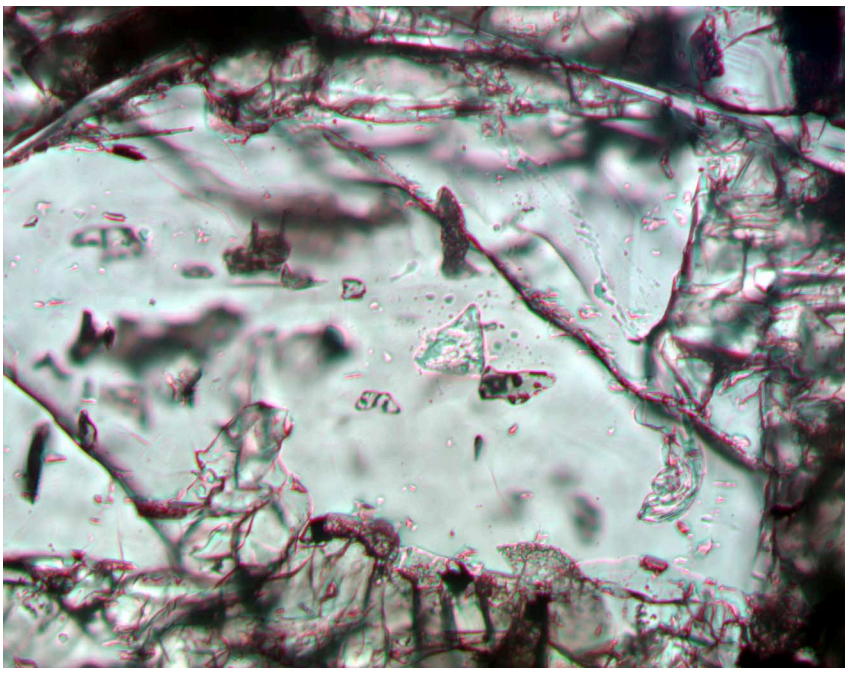

Figure F49. A glomerocryst of clinopyroxene and plagioclase in Sample **192-1183A-64R-2 (Piece 2, 15–17 cm),** Unit 6 (field of view = 1.4 mm; crossed polars; photomicrograph ID# 1183A_021).

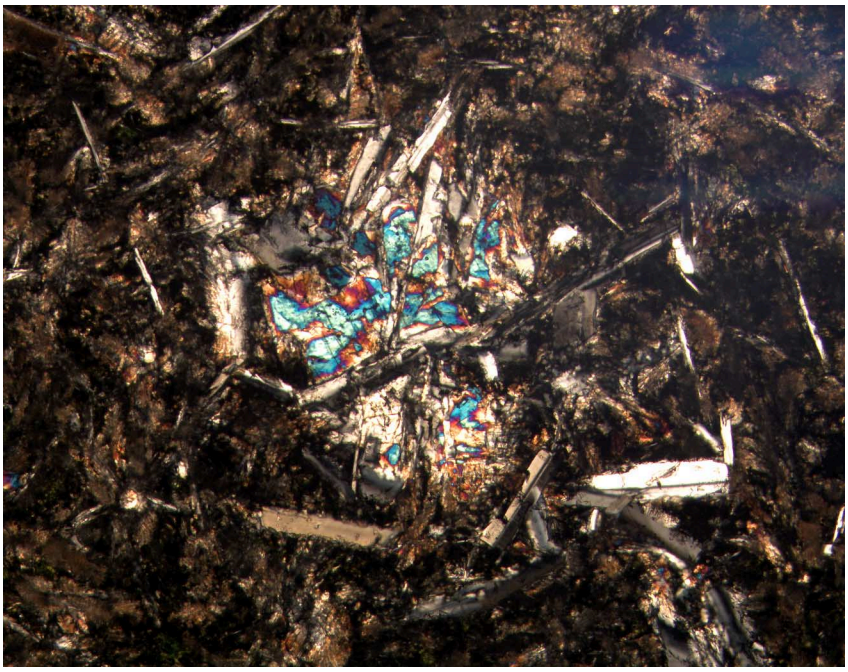

Figure F50. Clinopyroxene xenocryst in Sample **192-1183A-65R-3 (Piece 2, 18–19 cm),** Unit 7, partly resorbed by the host basalt. Such xenocrysts could have been derived from disaggregated plagioclase-clinopyroxene xenoliths of the types seen throughout the basalt from Hole 1183A (field of view = 1.4 mm; photomicrograph ID#s 1183A_022 and 1183A_023). **A.** Plane-polarized light. **B.** Crossed polars.

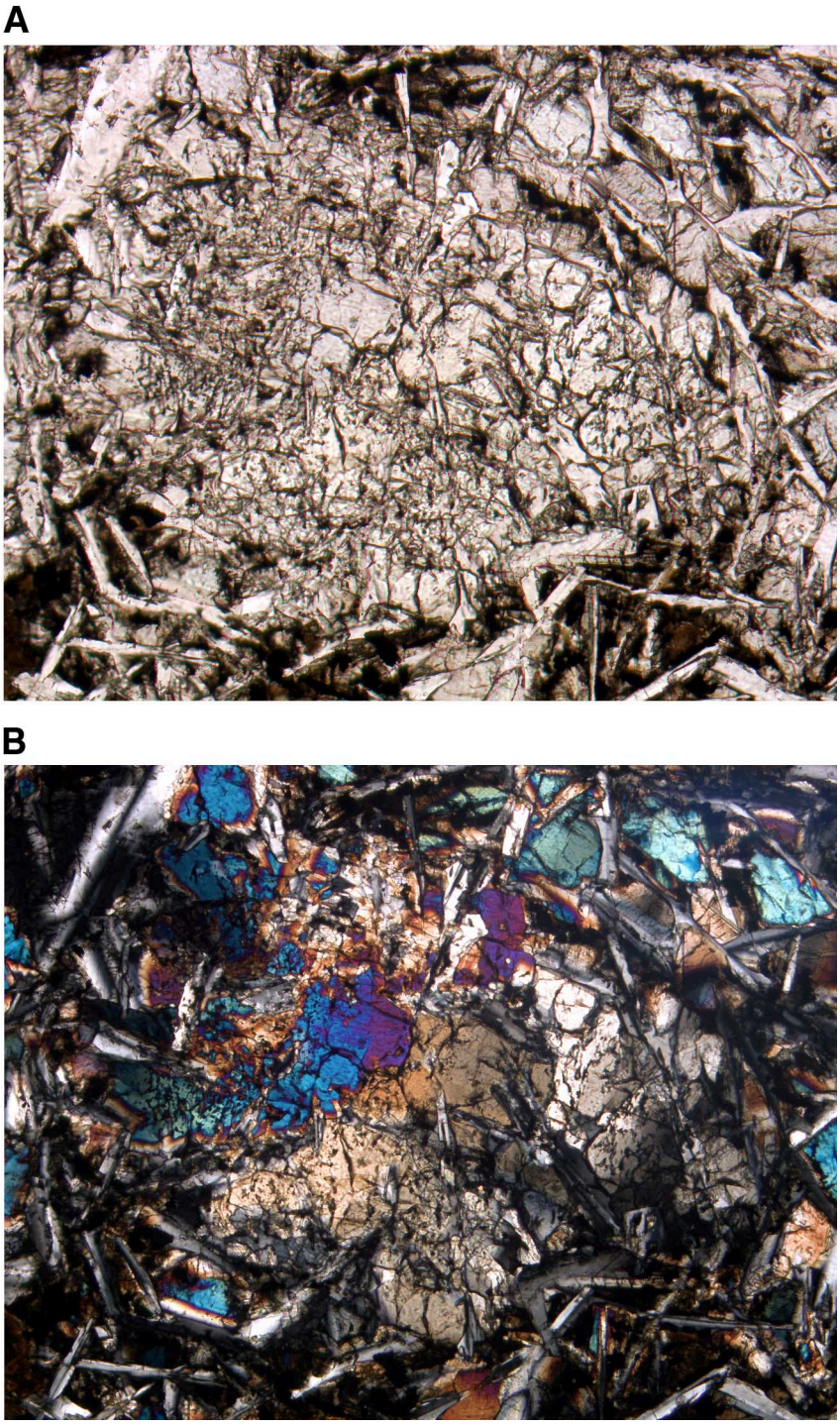

Figure F51. Skeletal plagioclase laths set in a quench-textured groundmass of clinopyroxene, plagioclase, and glass (altered to clay) in Sample **192-1183A-58R-3 (Piece 13, 109–112 cm),** Unit 5B. Groundmass titanomagnetite (the small, bright grains) is unaltered (field of view = 0.7 mm; taken in plane-polarized reflected light with a blue filter; photomicrograph ID#1183A_008).

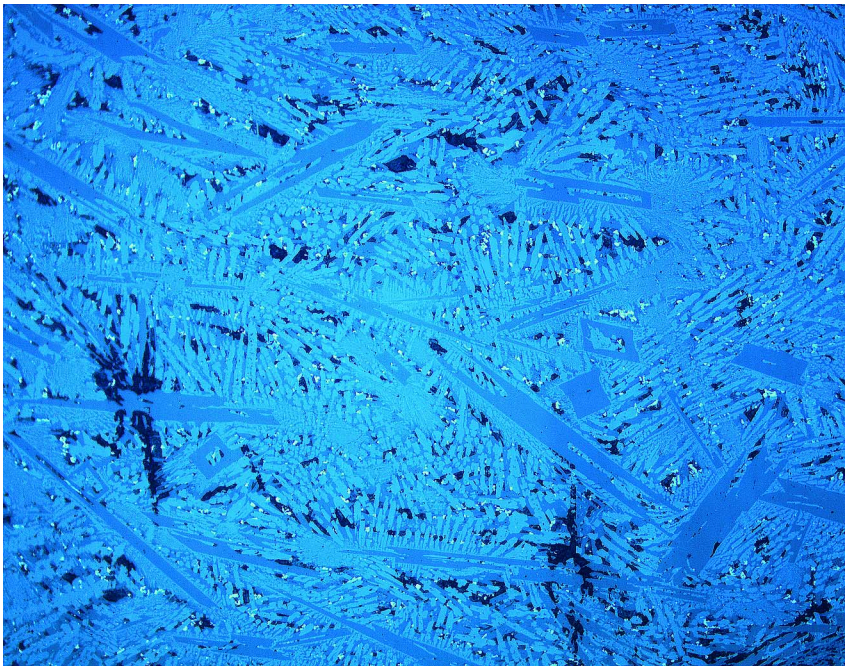

Figure F52. A partly glassy, sparsely olivine-phyric basalt exhibiting a variolitic texture around olivine phenocrysts in Sample **192-1183A-55R-2 (Piece 1A, 15–17 cm),** Unit 3B (field of view = 1.4 mm; plane-polarized light; photomicrograph ID# 1183A_020).

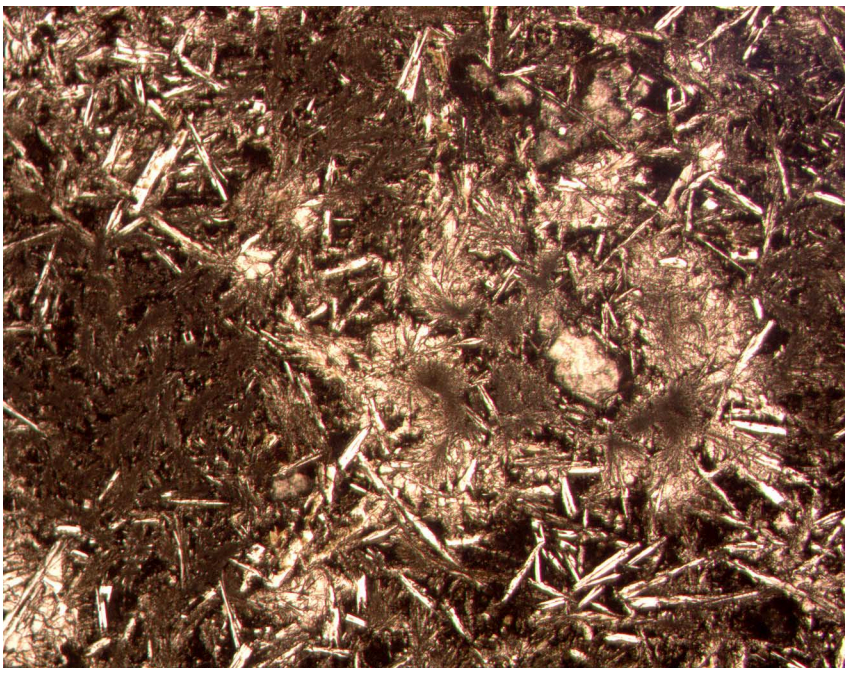

Figure F53. A fine-grained, moderately olivine-plagioclase-phyric pillow interior with a subophitic to slightly intersertal texture in Sample **192-1183A-60R-1 (Piece 19, 139–141 cm),** Unit 6. Olivine phenocrysts are highlighted (field of view = 1.4 mm; plane-polarized light; photomicrograph ID# 1183A_009).

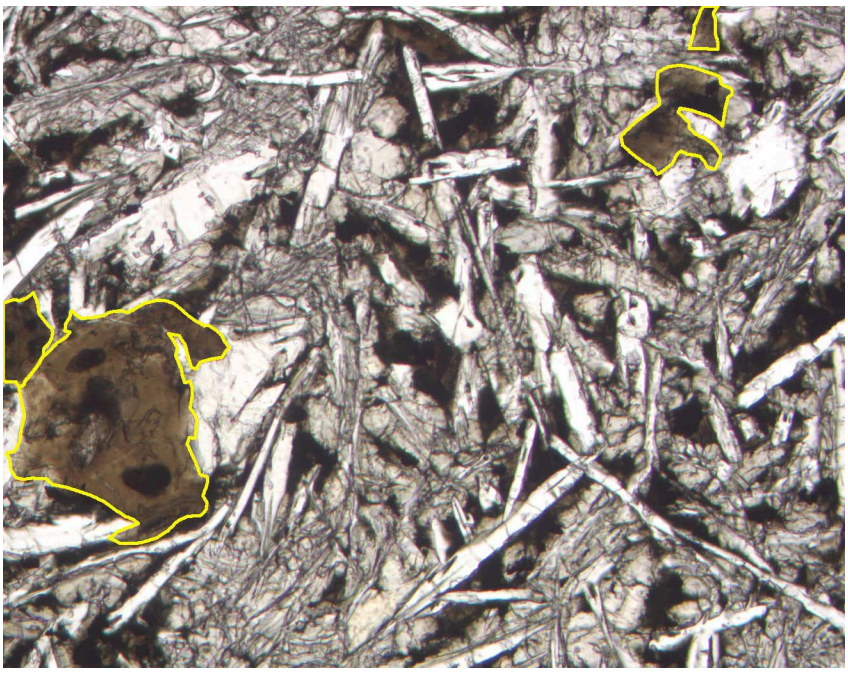

Figure F54. A fine-grained, moderately olivine-phyric pillow interior with a subophitic to intersertal texture in Sample 192-1183A-67R-1 (Piece 2C, 46–48 cm), Unit 7. Olivine phenocrysts are highlighted (field of view = 2.8 mm; plane-polarized light; photomicrograph 1183A_016).

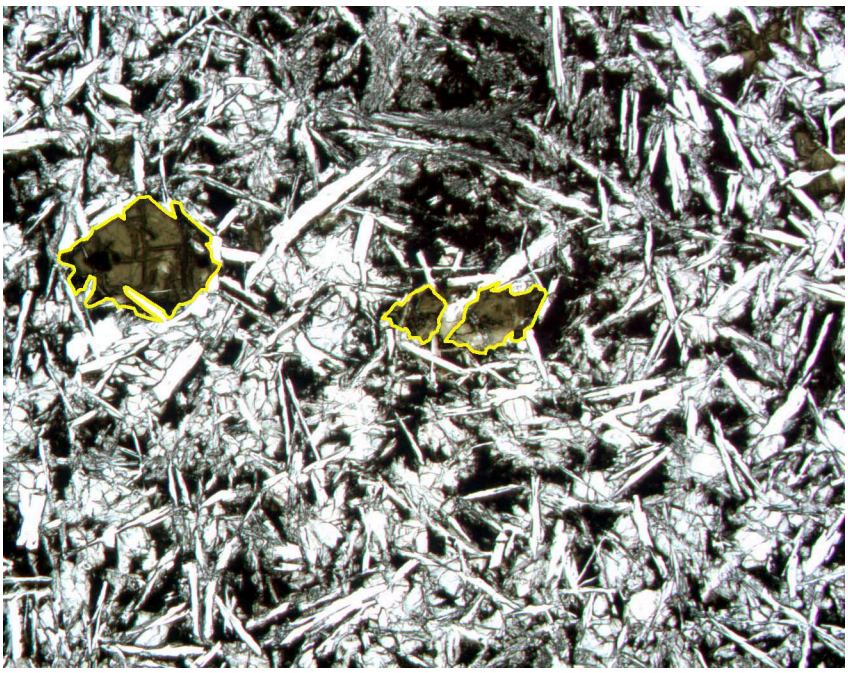

Figure F55. Subtrachytic plagioclase groundmass crystal alignment around glomerophyric olivine pseudomorphs in Sample **192-1183A-68R-1 (Piece 3A, 32–35 cm),** Unit 8. This sample is from the area depicted in Figure **F41,** p. 84, that illustrates a pillow inflation texture. The groundmass grain size variations shown here are consistent with this interpretation (field of view = 2.8 mm; crossed polars; photomicrograph ID# 1183A_017).

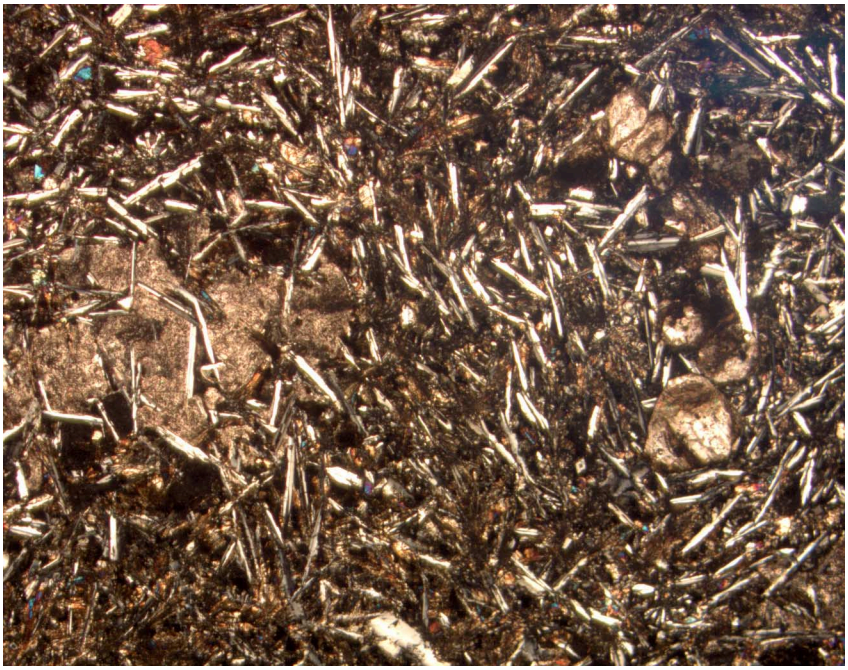

Figure F56. Compositional zonation in plagioclase from a xenolith in Sample **192-1183A-54R-5 (Piece 4A, 32–35 cm),** Unit 2B. Note the truncations of the interior compositional bands (highlighted), suggesting periods of resorption (field of view = 2.8 mm; crossed polars; photomicrograph ID#1183A_006).

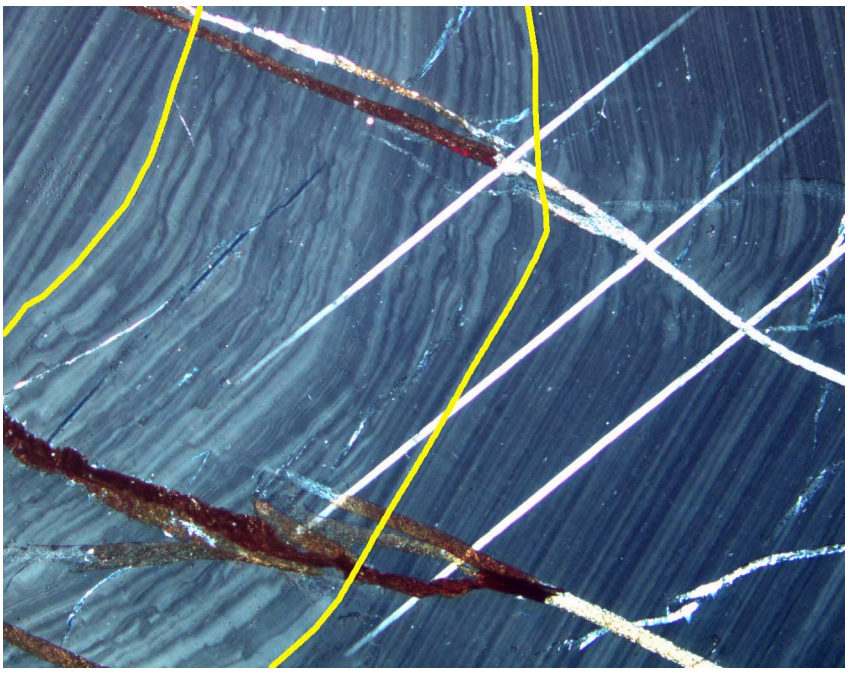

Figure F57. A partially resorbed interstitial clinopyroxene crystal (middle left) in a plagioclase-rich xenolith in Sample 192-1183A-57R-3 (Piece 2, 15–17 cm), Unit 5B. Other interstices are filled with quenched glass (now devitrified and altered to clay). **A.** Plane-polarized light. **B.** Crossed polars. (Field of view = 2.8 mm; photomicrograph ID#s 1183A_13 and 1183A_014.)

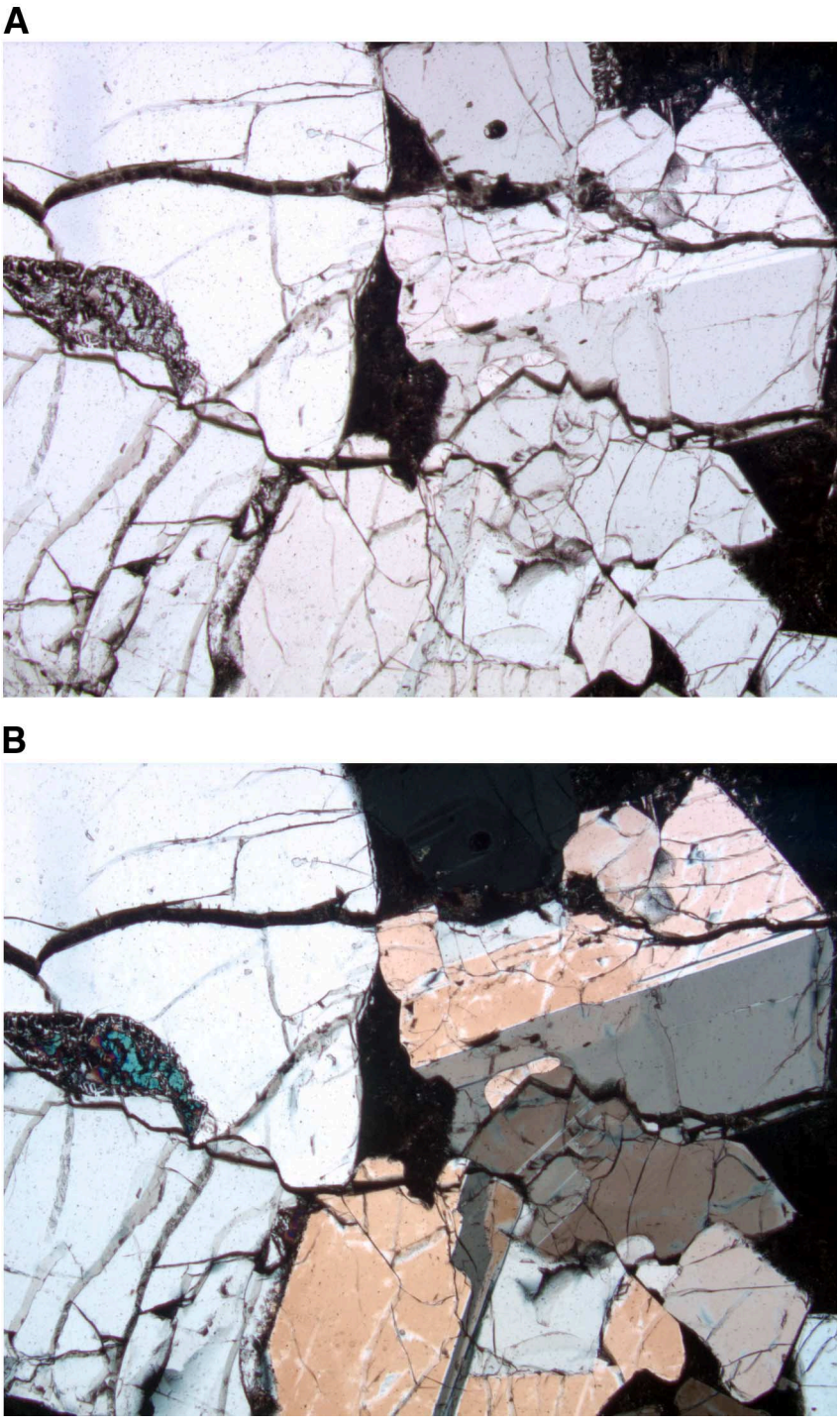

Figure F58. A. Plagioclase-rich xenolith in Sample **192-1183A-54R-5 (Piece 4B, 64–66 cm),** Unit 2B, showing interstitial glass-filled (devitrified) patches between plagioclase crystals. Other areas in the xenolith contain more irregular glass-filled areas (Fig. **F59,** p. 102). **B.** Another example of interstitial patches from the same xenolith. (Field of view = 2.8 mm; plane-polarized light; [A] photomicrograph ID# 1183A_001 and [B] photomicrograph ID#1183A_002.)

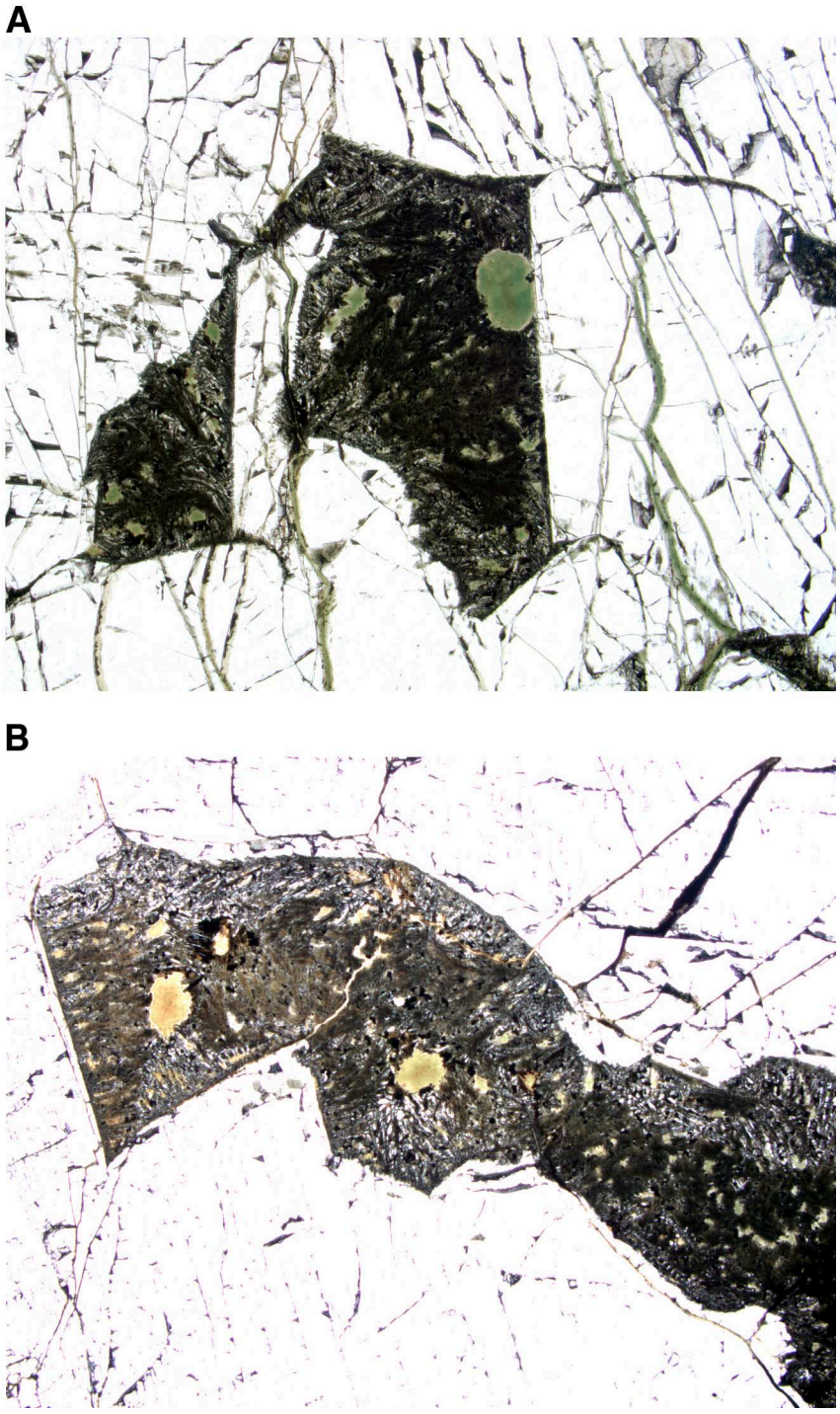

Figure F59. Interstitial material in a plagioclase-rich xenolith in Sample **192-1183A-55R-1 (Piece 6B, 111–113 cm),** Unit 3B. The shape of the interstices is controlled by the surrounding plagioclase crystals (field of view = 2.8 mm; plane-polarized light; photomicrograph ID# 1183A_010).

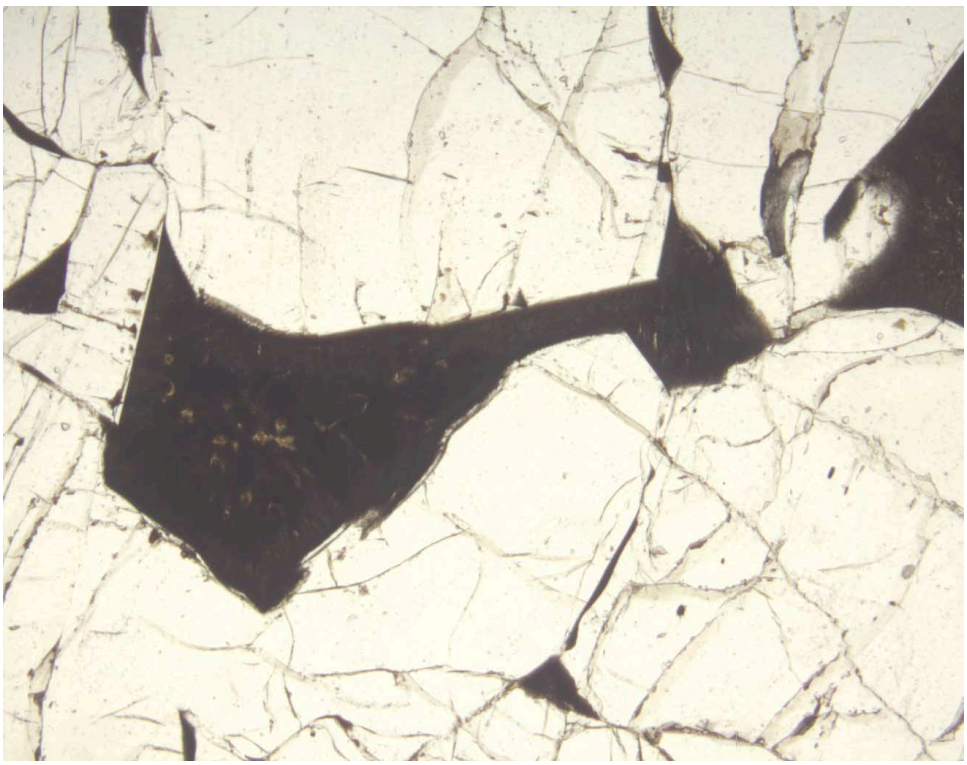

Figure F60. Clinopyroxene at the edge of the plagioclase-rich xenolith in Sample 192-1183A-57R-3 (Piece 2, 15–17 cm) (see Fig. F57, p. 100), Unit 5B, showing resorption by the host basalt. The edges of the plagioclase crystals in contact with the basalt also show slight resorption. **A.** Plane-polarized light. **B.** Crossed polars. (Field of view = 2.8 mm; [A] photomicrograph ID# 1183A_018 and [B] photomicrograph ID# 1183A_019.)

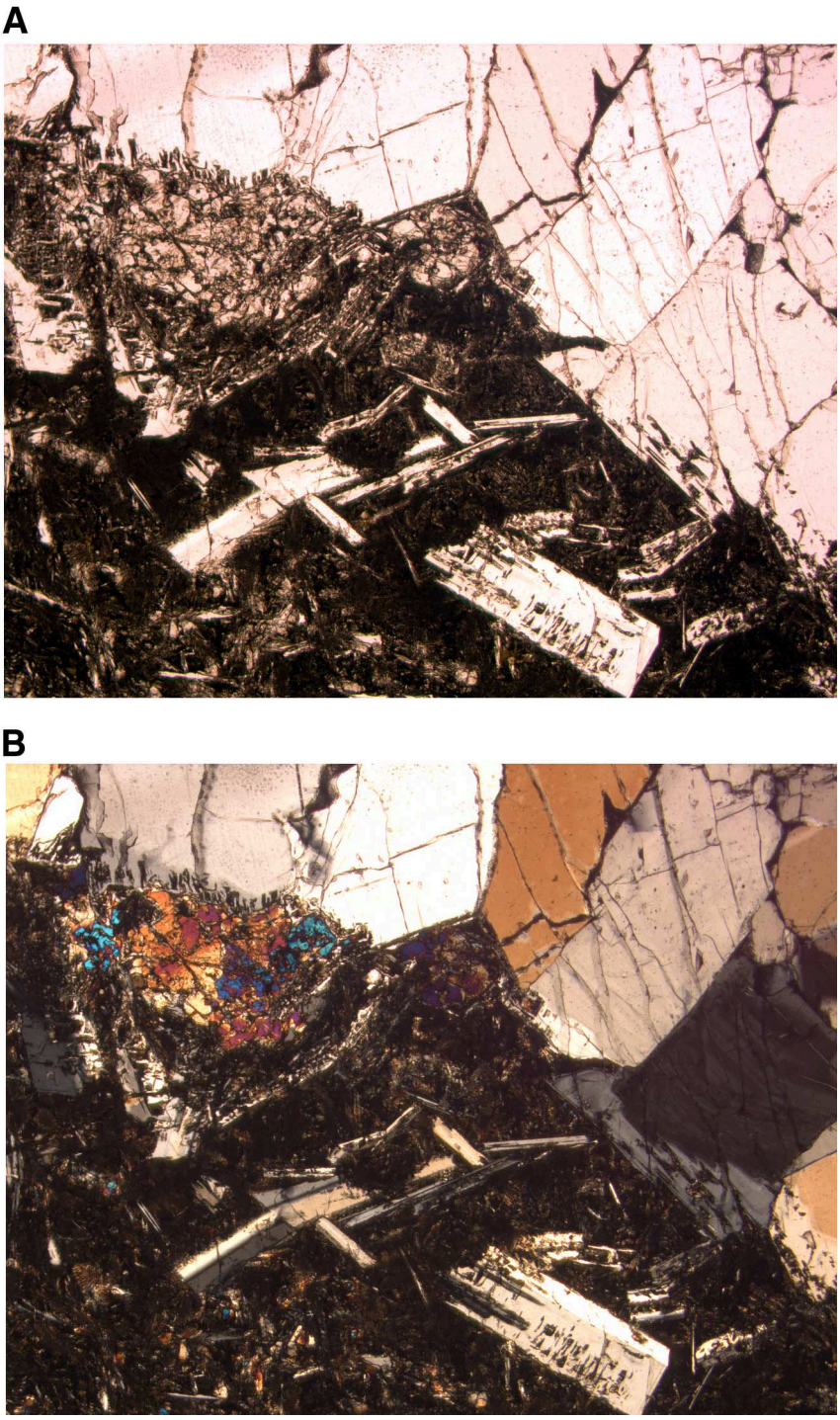

Figure F61. Basalt Sample 130-807C-89R-3, 7–9 cm, illustrating the presence of clinopyroxene phenocrysts (CPX), along with olivine (Ol.) and plagioclase (Plag.) (field of view = 2.8 mm; plane-polarized light; photomicrograph ID# 807C_003).

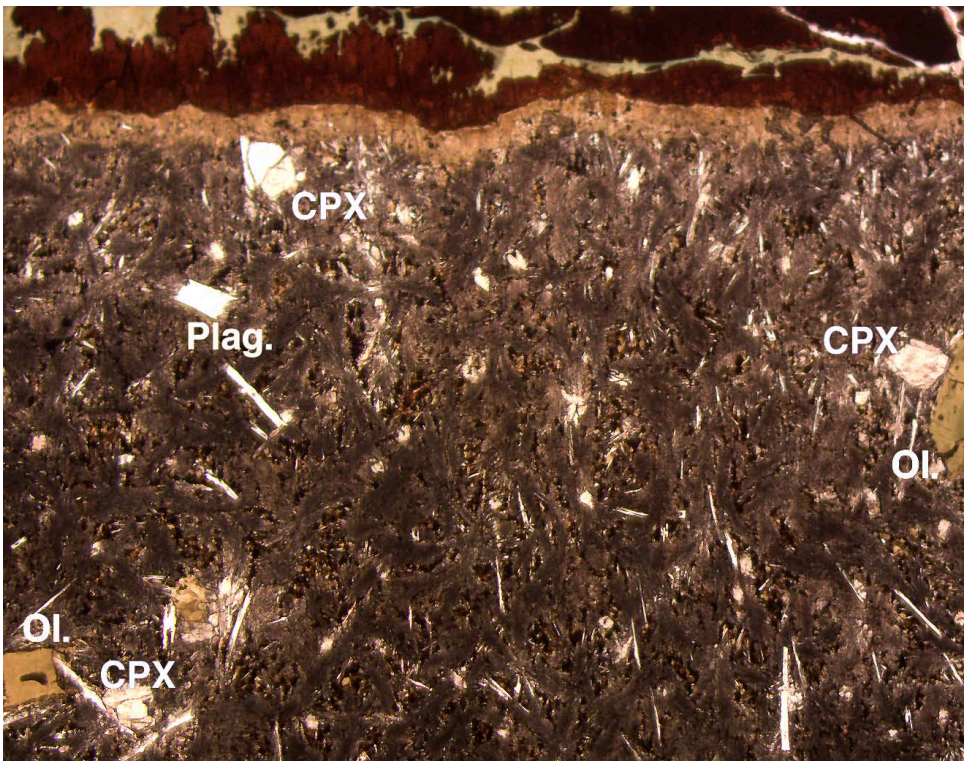

Figure F62. Basalt Sample 130-807C-89R-3, 7–9 cm, showing a clinopyroxene-plagioclase glomerocryst in a quenched, devitrified groundmass. Such glomerocryst associations are relatively common in basalts from Units C–G at Site 807, compared to those from Hole 1183A. **A.** Plane-polarized light. **B.** Crossed polars. (Field of view = 1.4 mm; [A] photomicrograph ID# 807C_005 and [B] photomicrograph ID# 807C_006.)

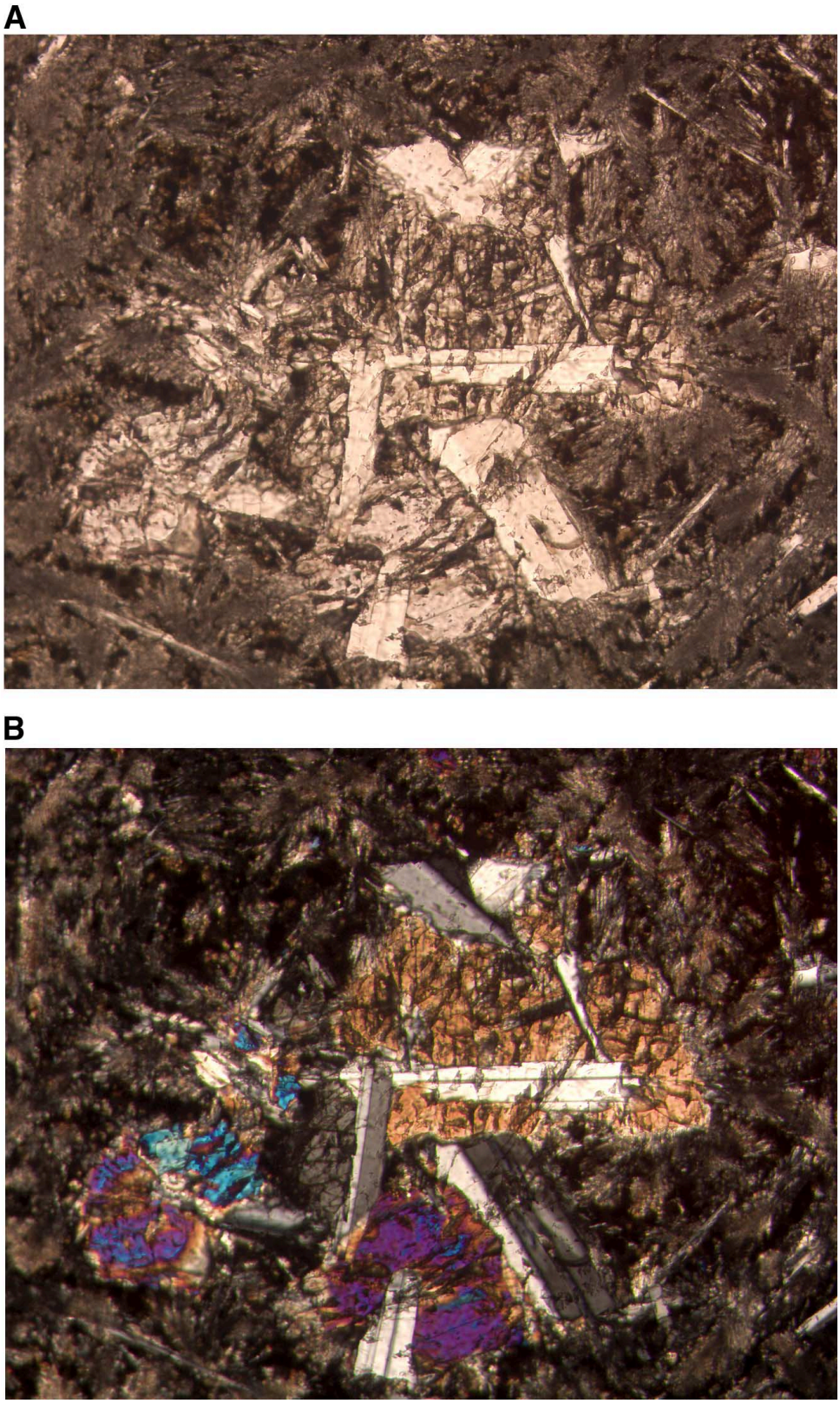

Figure F63. Basalt Sample 130-807C-89R-3, 7–9 cm, showing a partially resorbed clinopyroxene xenocryst similar to those in basalts from Hole 1183A. **A.** Plane-polarized light. **B.** Crossed polars. (Field of view = 1.4 mm; [A] photomicrograph ID# 807C_001 and [B] photomicrograph ID# 807C_002.)

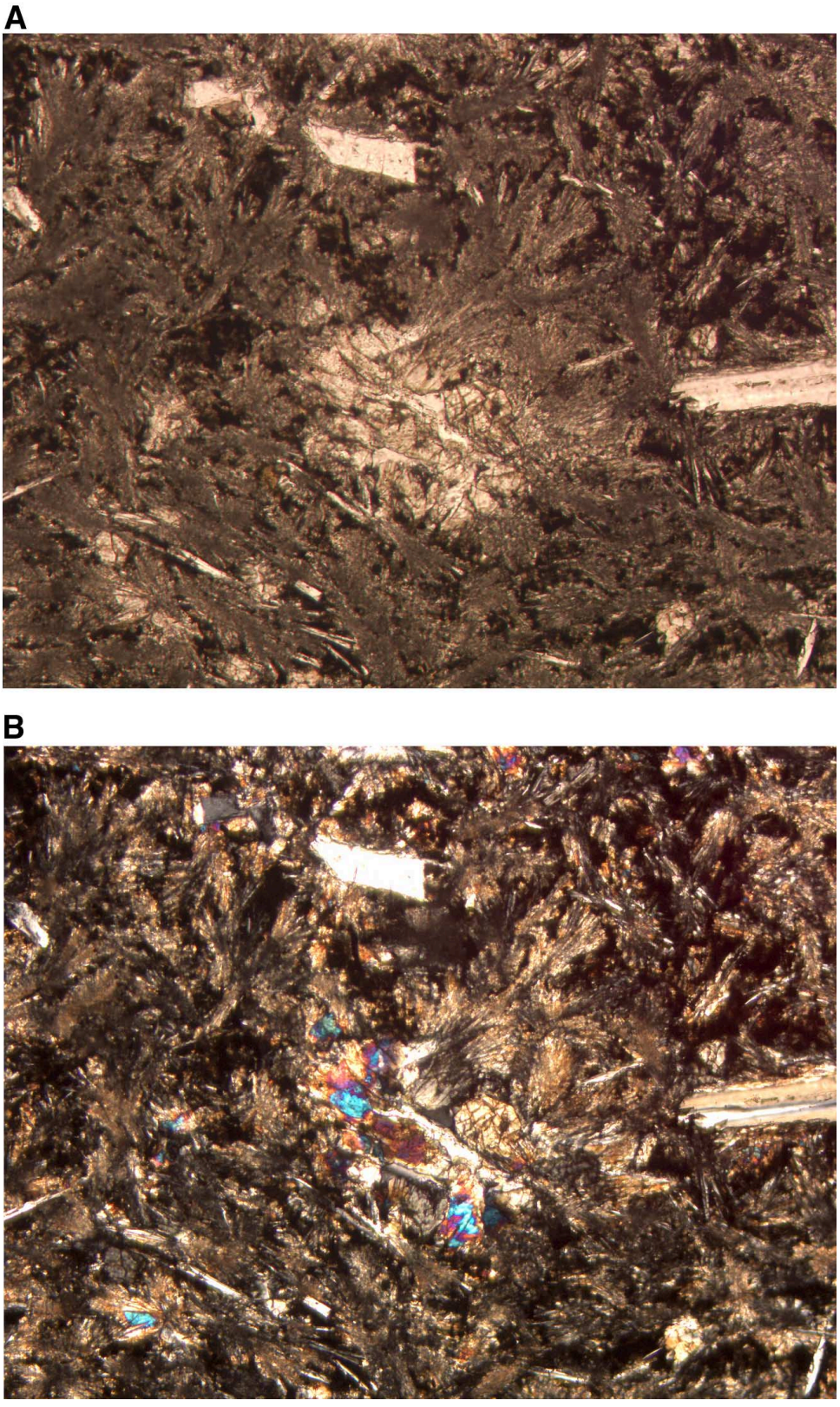

Figure F64. Basalt Sample 130-807C-93R-1, 137–139 cm, showing plagioclase glomerocrysts from Site 807 Units C–G basalts that have a similar morphology to the larger plagioclase-rich xenoliths in the basalts from Hole 1183A. **A.** Plane-polarized light. **B.** Crossed polars. (Field of view = 5.6 mm; [A] photomicrograph ID# 807C_009 and [B] photomicrograph ID# 807C_010.)

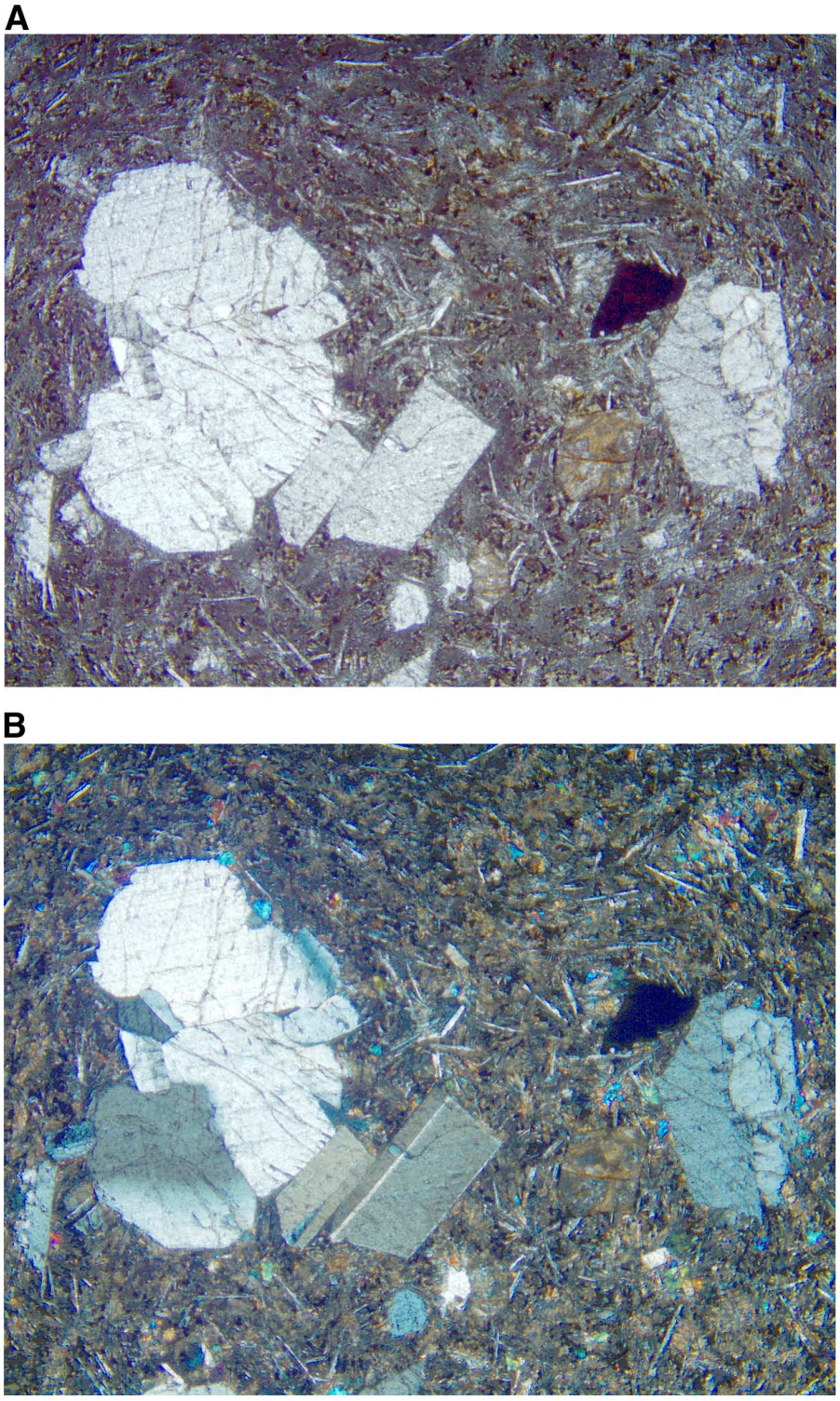

Figure F65. Total alkalies vs. silica diagram (after Le Bas et al., 1986) illustrating the tholeiitic nature of Hole 1183A basalts. The dashed line separates Hawaiian tholeiitic and alkalic lavas (Macdonald and Katsura, 1964).

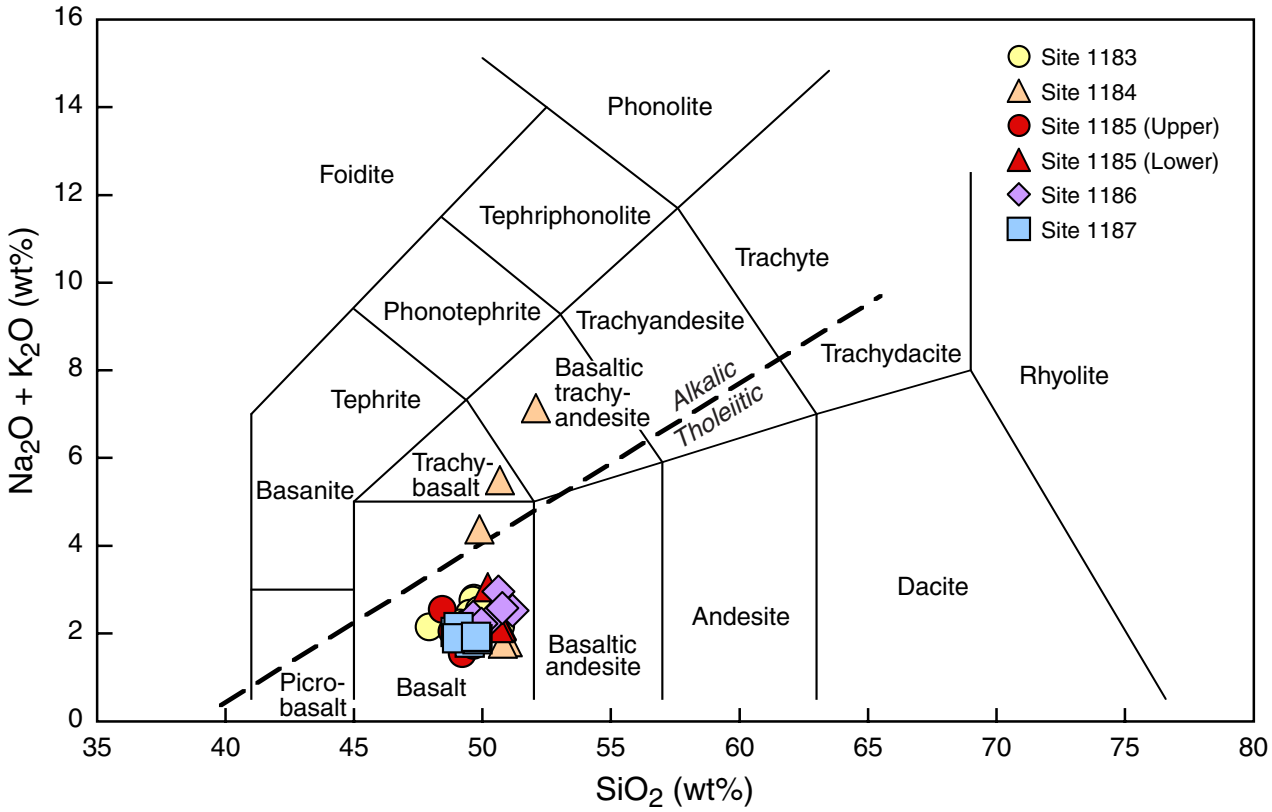

Figure F66. Zr vs. TiO_2 showing that the basalt units from Hole 1183A have broadly similar abundances of incompatible elements to Units C–G at Site 807 (Mahoney et al., 1993) and to the basalt flows of the Kwaimbaita Formation on Malaita (Tejada et al., in press).

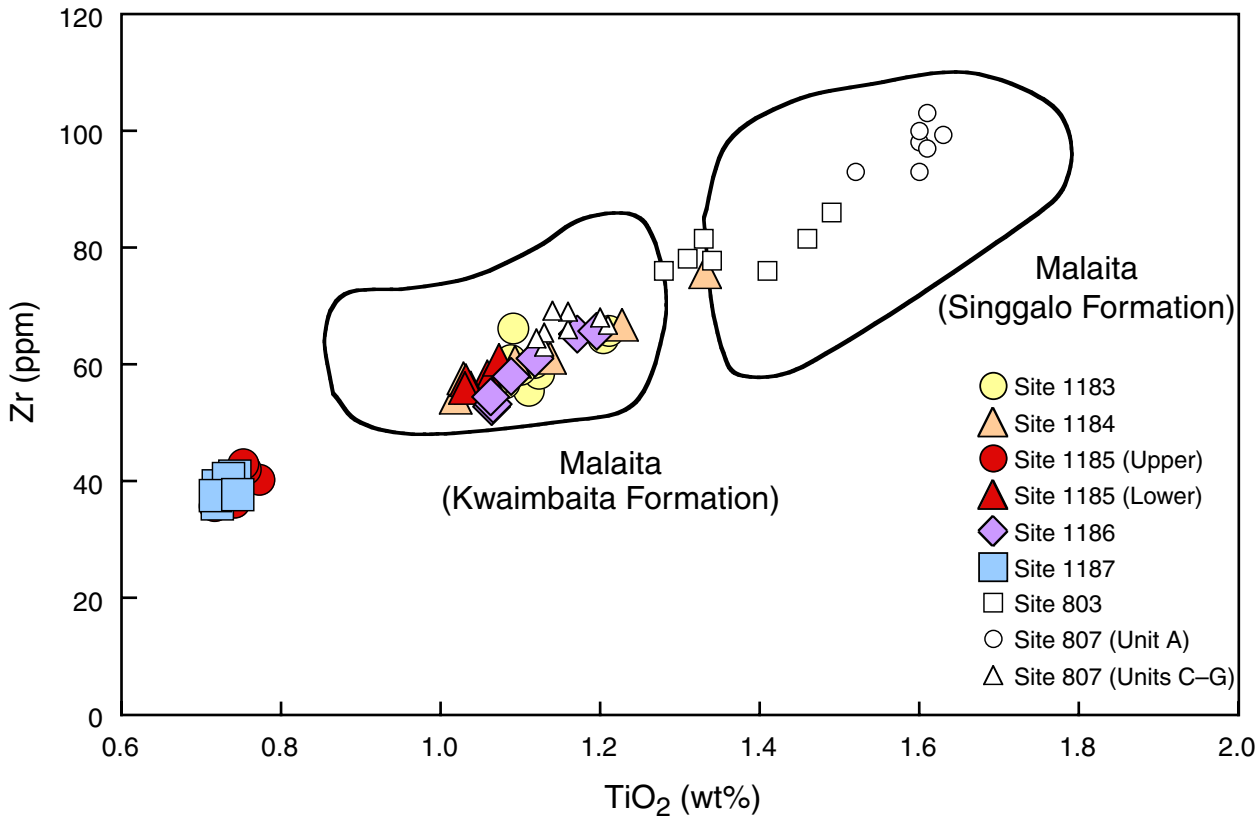

Figure F67. TiO_2 vs. Mg# showing the similarity between the major element compositions of basalt units from Hole 1183A and those of Units C–G at Site 807 (Mahoney et al., 1993) and the Kwaimbaita Formation on Malaita (Tejada et al., in press). Mg# is calculated assuming that 12% of the iron is Fe^{3+}, which is equivalent to $Fe_2O_3/(Fe_2O_3 + FeO) = 0.13$ or $Fe_2O_3/FeO = 0.15$.

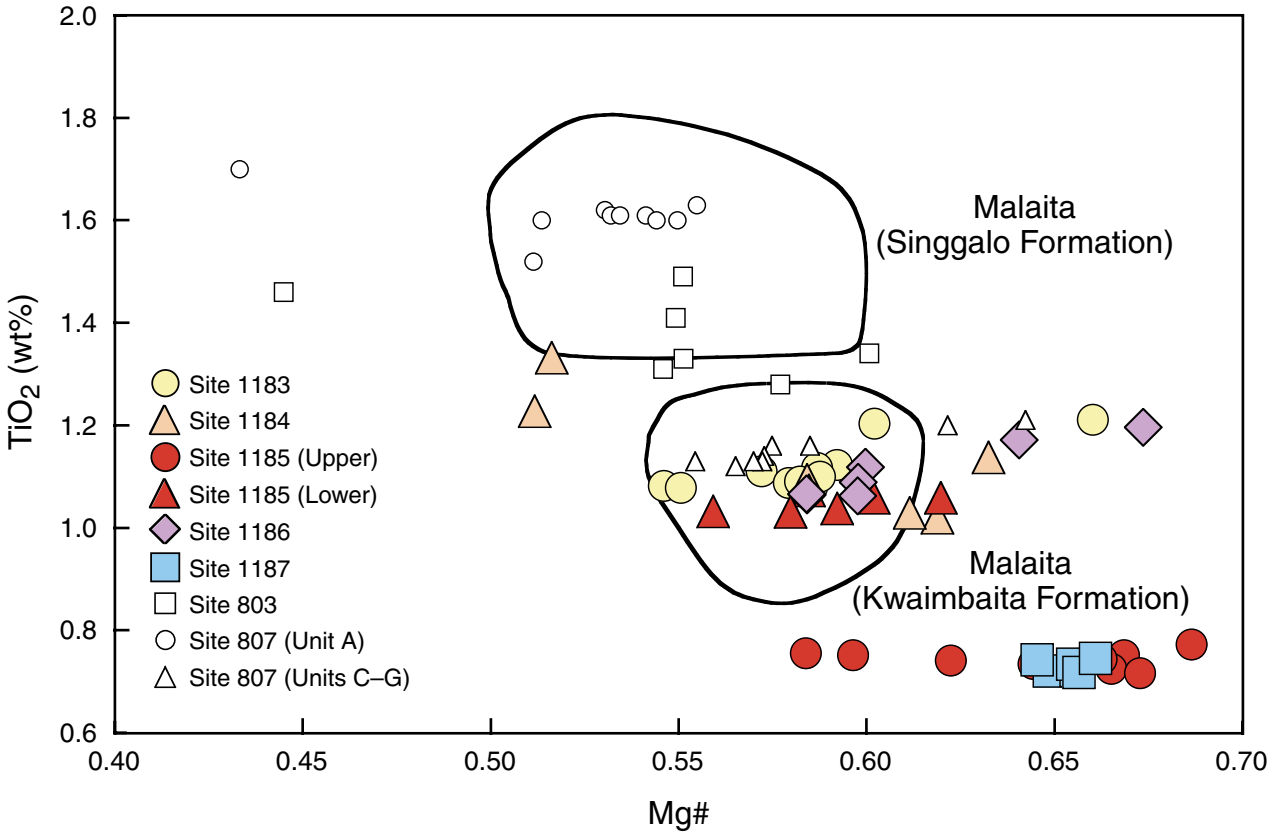

Figure F68. Distribution of basement rock color, Hole 1183A.

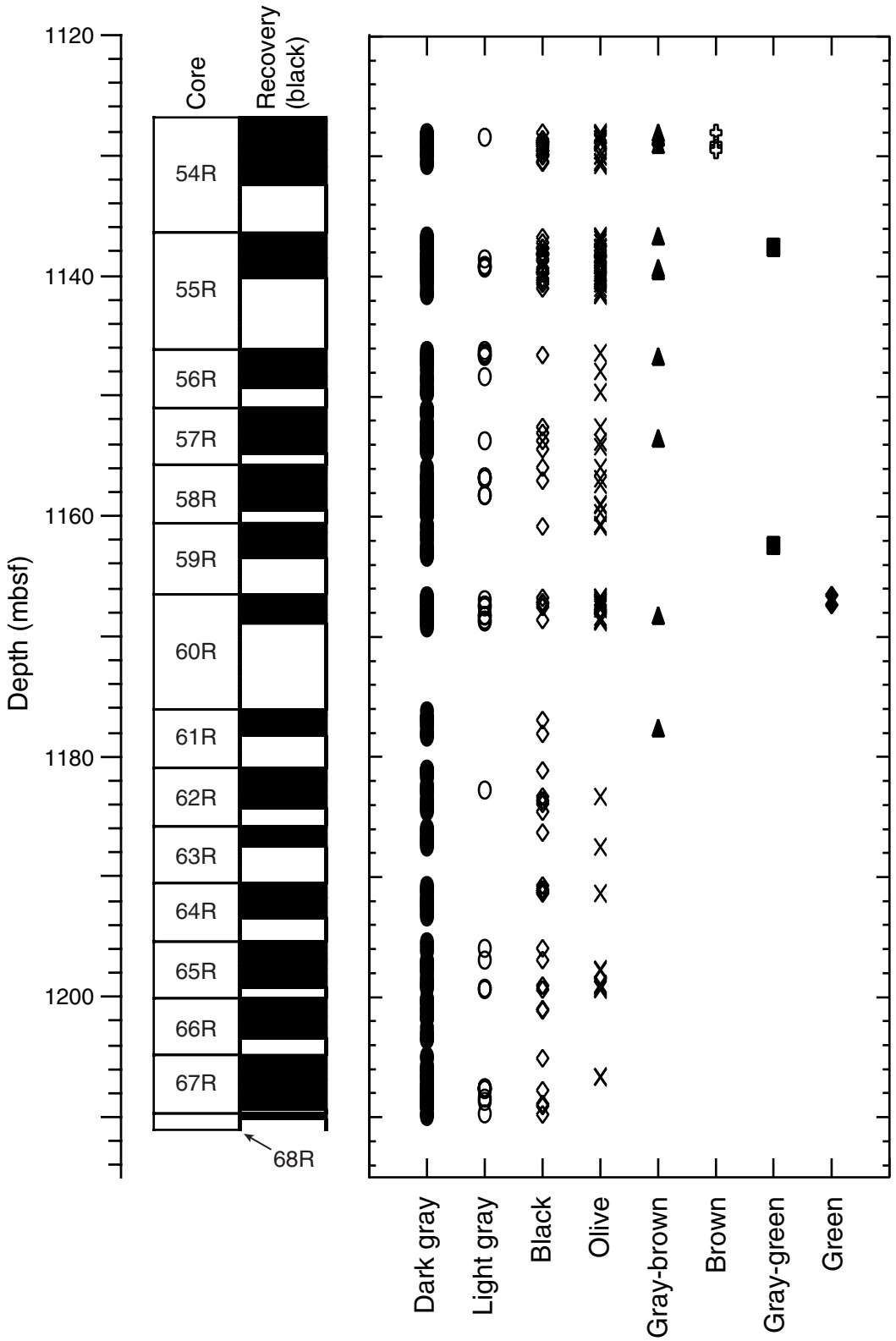

Figure F69. Alteration front between a black halo (two euhedral olivine phenocrysts replaced by nontronite, lower right) and the gray basalt interior (two euhedral olivine phenocrysts replaced by saponite, upper left) in Sample **192-1183A-67R-1 (Piece 2C, 46–48 cm)** (field of view = 5.5 mm; plane-polarized light; photomicrograph ID# 1183A_030).

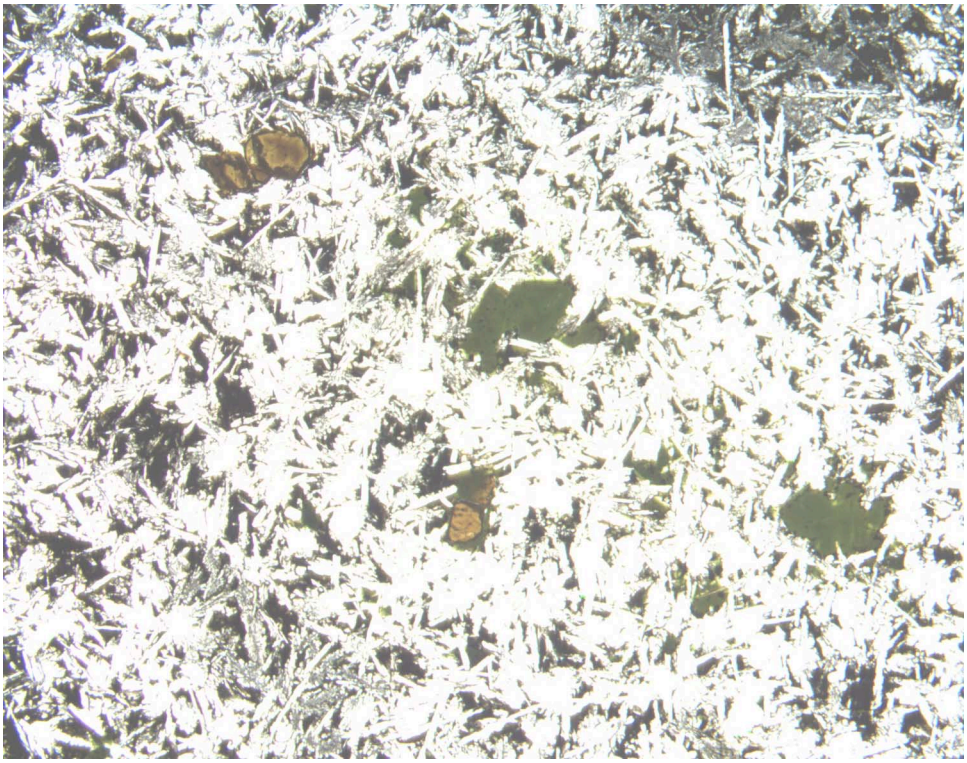

Figure F70. Euhedral olivine pseudomorph (saponite) in a gray basalt interior in Sample **192-1183A-64R-2 (Piece 10, 136–138 cm)** (field of view = 2.8 mm; plane-polarized light; photomicrograph ID# 1183A_036).

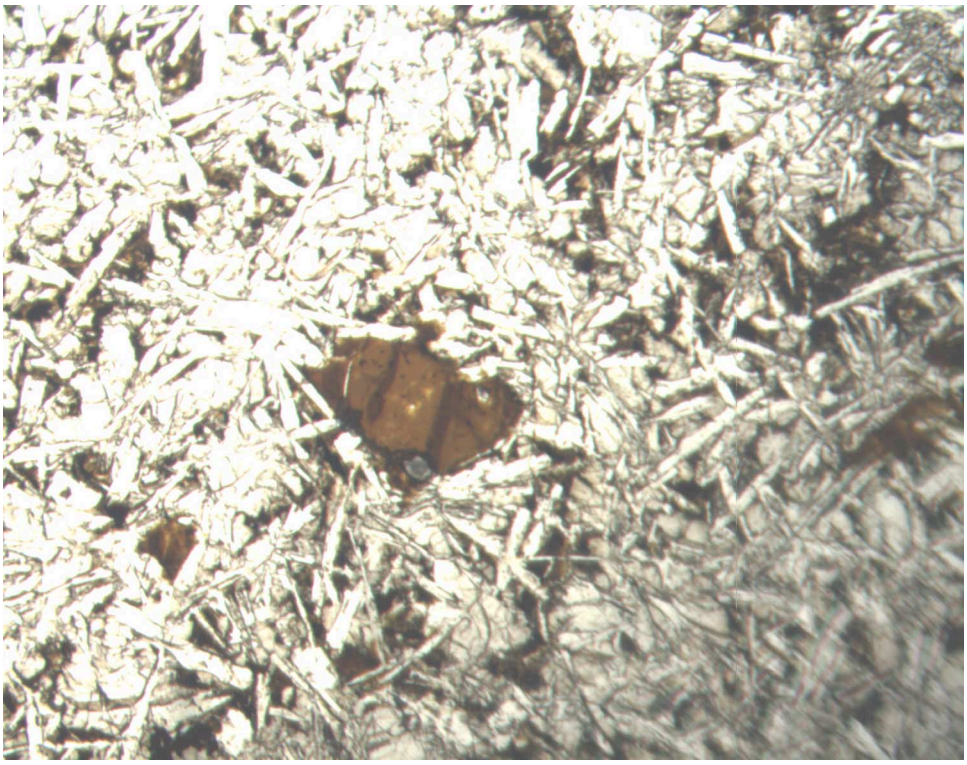

Figure F71. Euhedral olivine pseudomorph (saponite and calcite) in a gray basalt interior in Sample 192-1183A-65R-3 (Piece 2, 18–19 cm) (field of view = 1.4 mm; plane-polarized light; photomicrograph ID# 1183A_025).

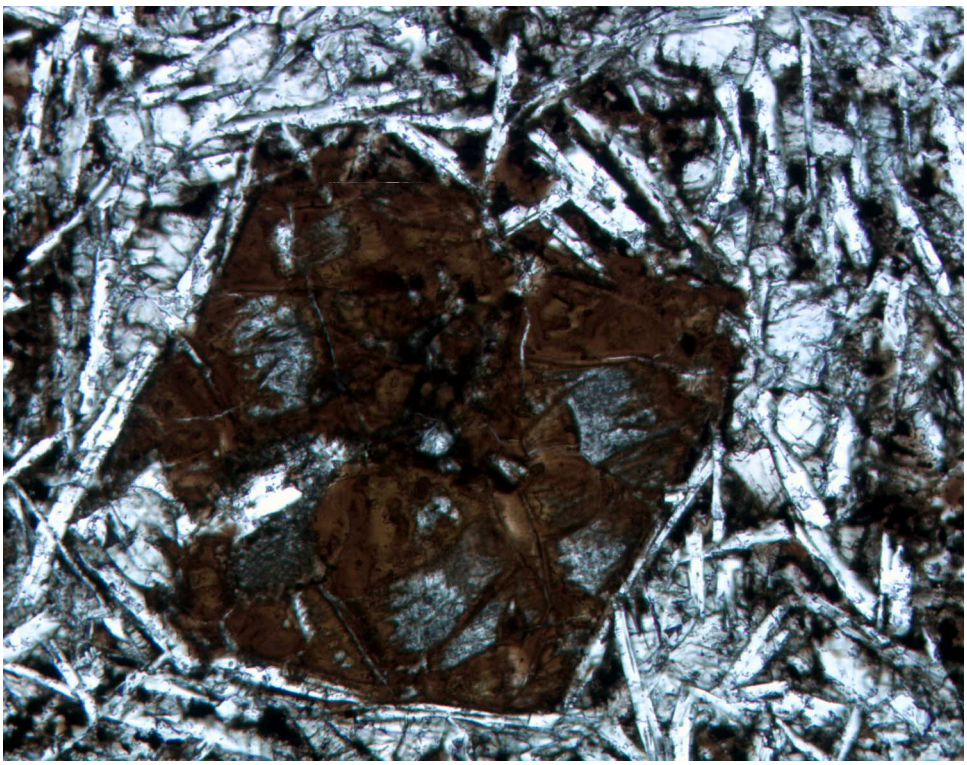

Figure F72. Interval 192-1183A-62R-2 (Piece 8, 84–110 cm) showing 7.5-mm-wide black halos on both sides of a hairline vein filled with smectite in dark gray basalt.

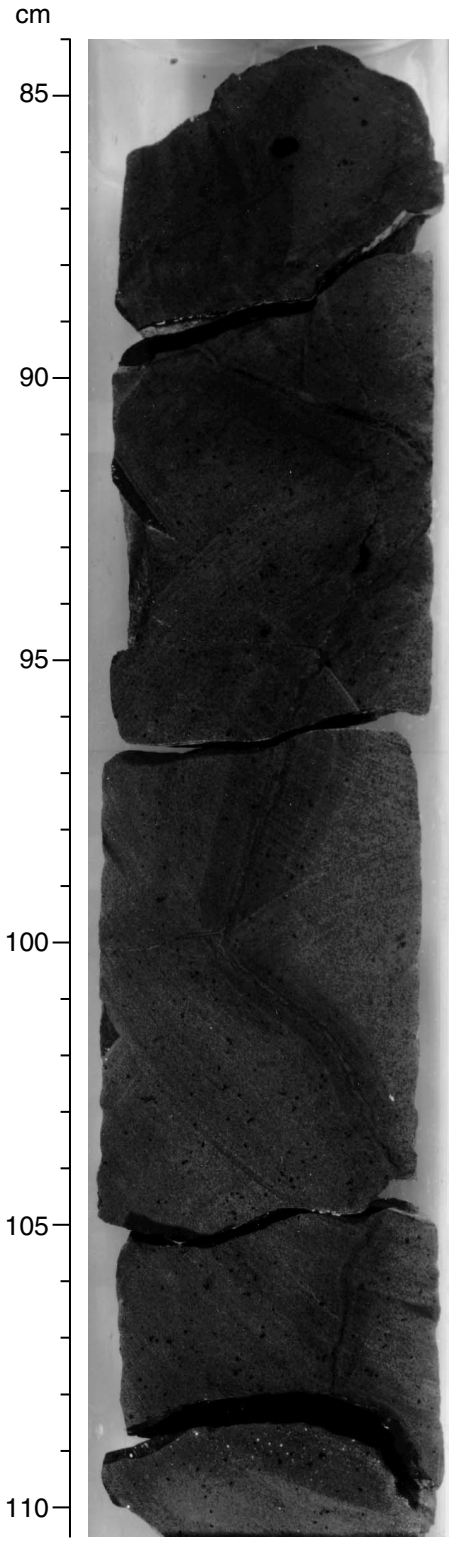

Figure F73. Interval 192-1183A-66R-2 (Piece 3, 30–48 cm) showing 10-mm-wide black halos on both sides of a 3- to 5-mm-wide vertical vein filled with calcite, smectite, and minor chalcedony (multiple reopenings) in dark gray basalt.

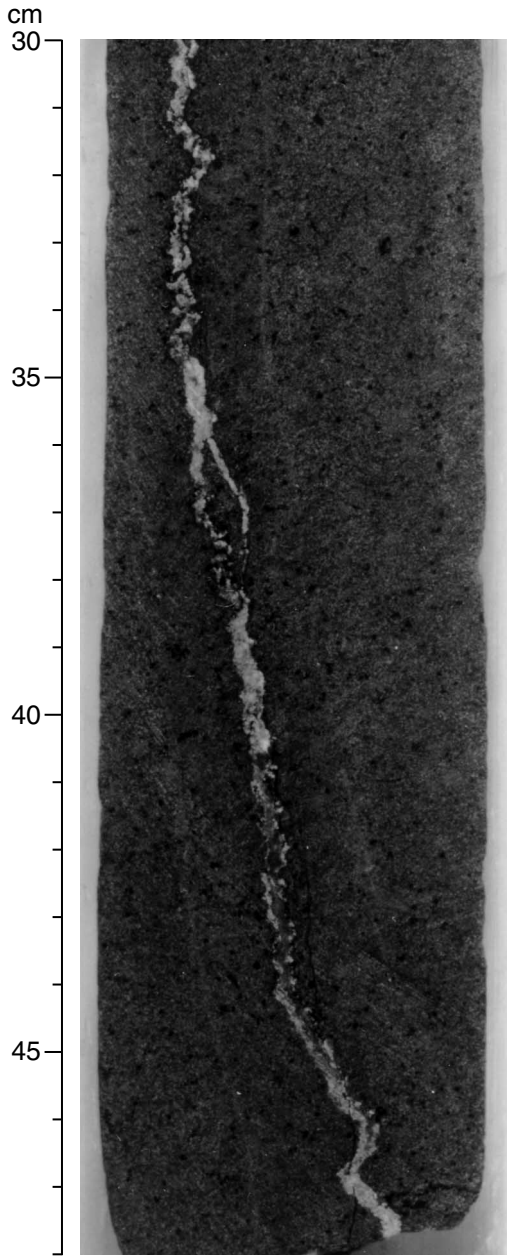

Figure F74. Euhedral olivine pseudomorph (consisting of celadonite) in a black halo in Sample 192-1183A-64R-2 (Piece 2, 15–17 cm) (field of view = 1.4 mm; plane-polarized light; photomicrograph ID# 1183A_038).

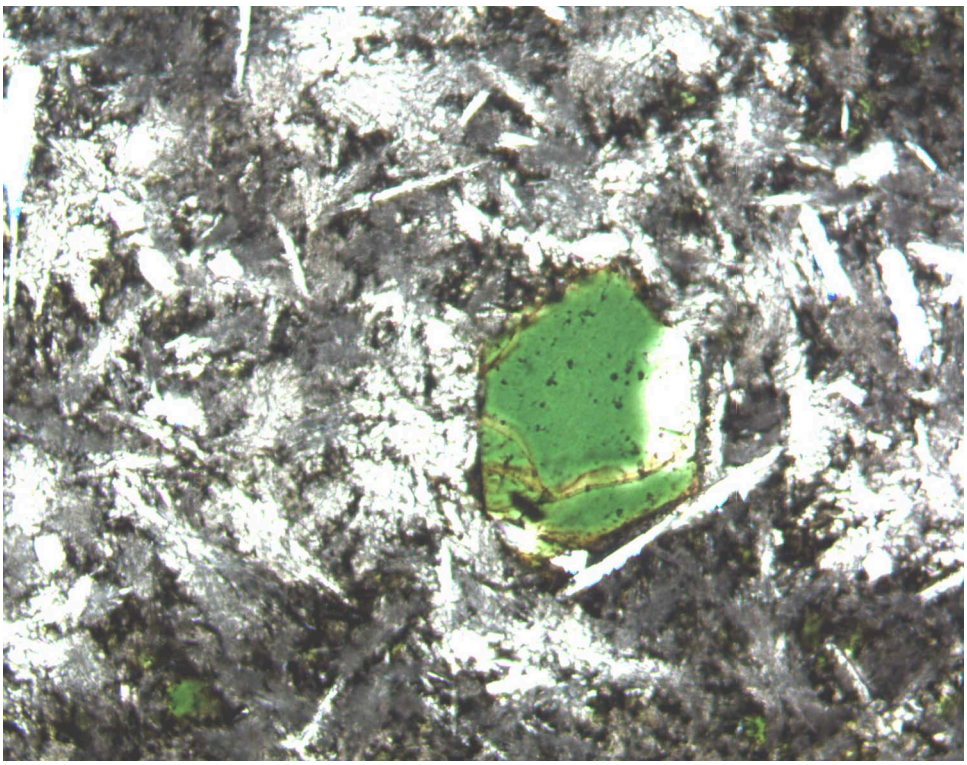

Figure F75. Euhedral olivine pseudomorph (consisting of celadonite and pyrite) in a black halo in Sample 192-1183A-64R-2 (Piece 2, 15–17 cm) (field of view = 1.4 mm; plane-polarized light; photomicrograph ID# 1183A_037).

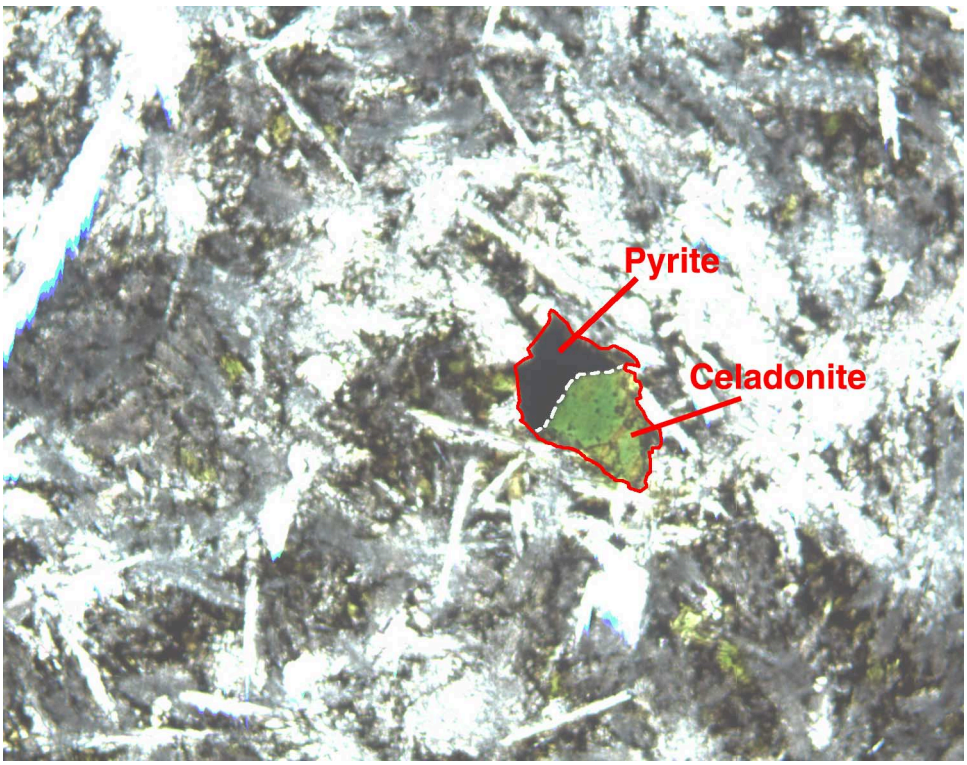

Figure F76. Euhedral olivine pseudomorphs (nontronite) in a gray pillow basalt interior in Sample 192-1183A-57R-3 (Piece 2, 15–17 cm). The vein (upper right) is filled with nontronite and minor celadonite (field of view = 5.5 mm; plane-polarized light; photomicrograph ID# 1183A_034).

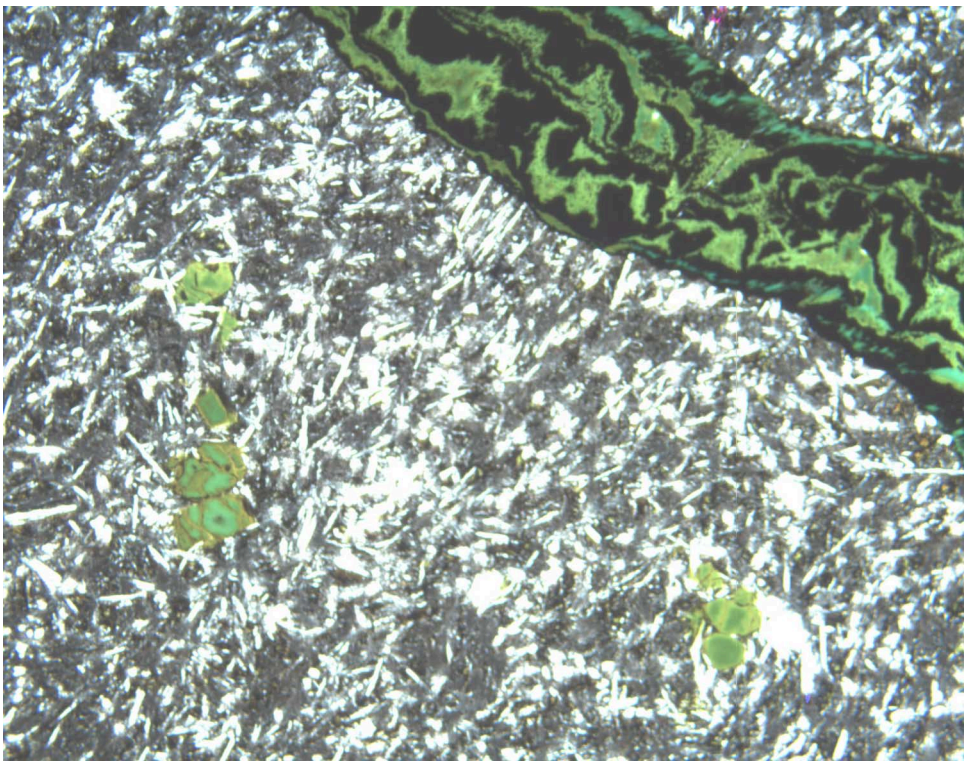

Figure F77. Olive halos (1–8 mm wide) on either side of a 1- to 3-mm-wide celadonite + goethite vein in Sample **192-1183A-60R-2 (Piece 11, 71–74 cm)** (field of view = 5.5 mm; plane-polarized light; photomicrograph ID# 1183A_041).

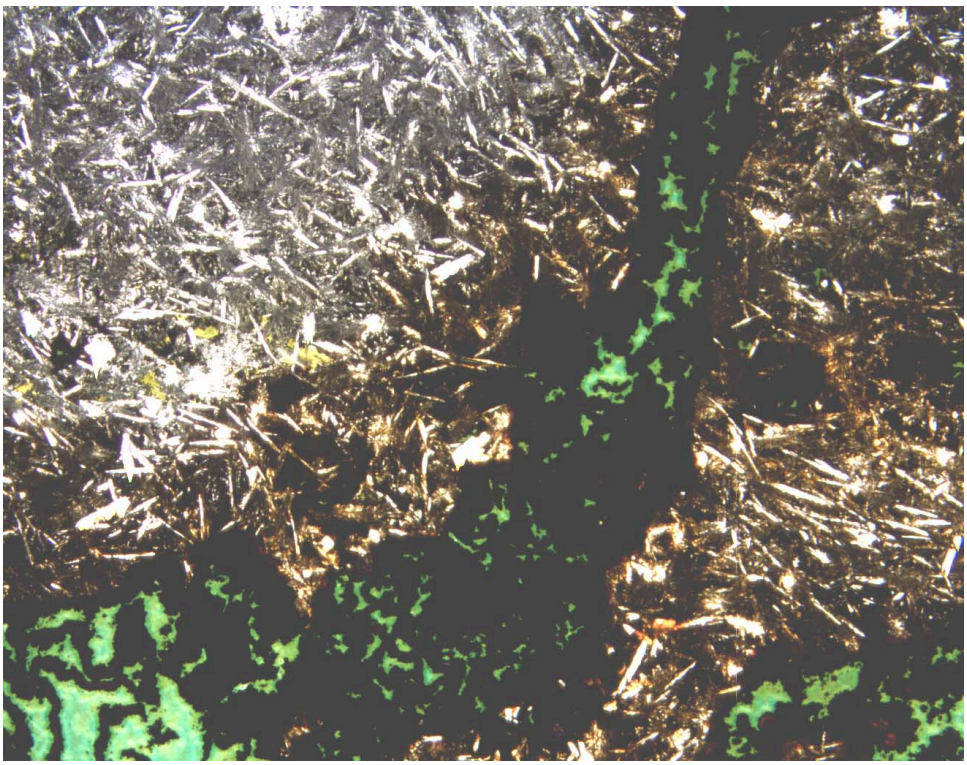

Figure F78. Vein filled with goethite and celadonite in Sample **192-1183A-65R-2 (Piece 8, 84–88 cm)** (field of view = 5.5 mm; plane-polarized light; photomicrograph ID# 1183A_027).

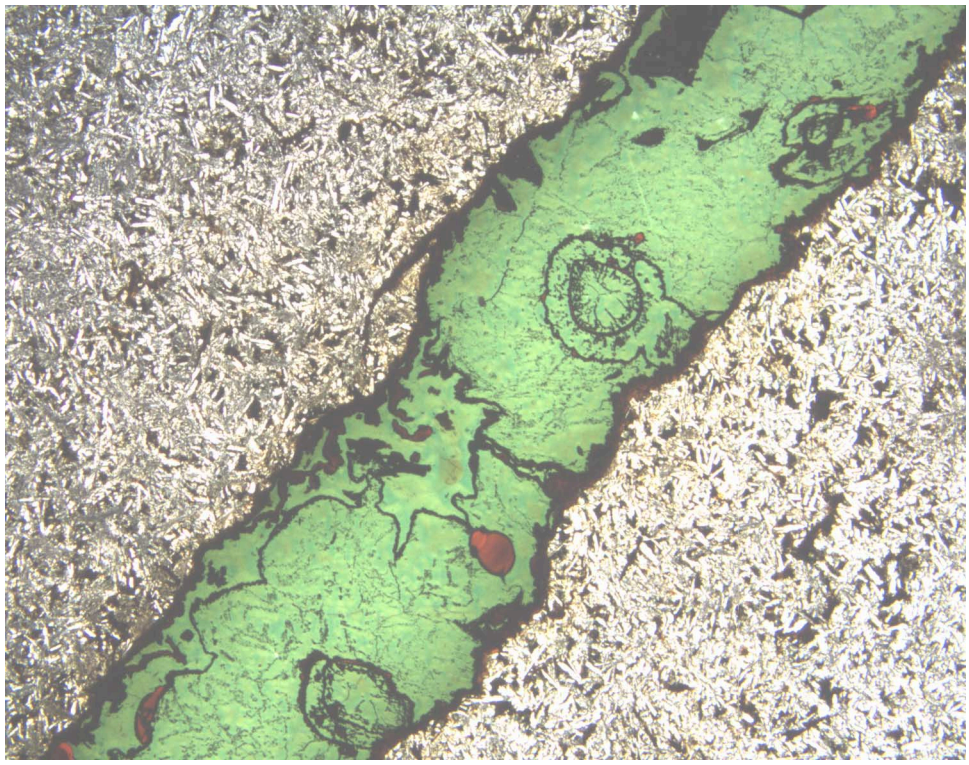

Figure F79. Vein-mineral distribution with depth in Hole 1183A.

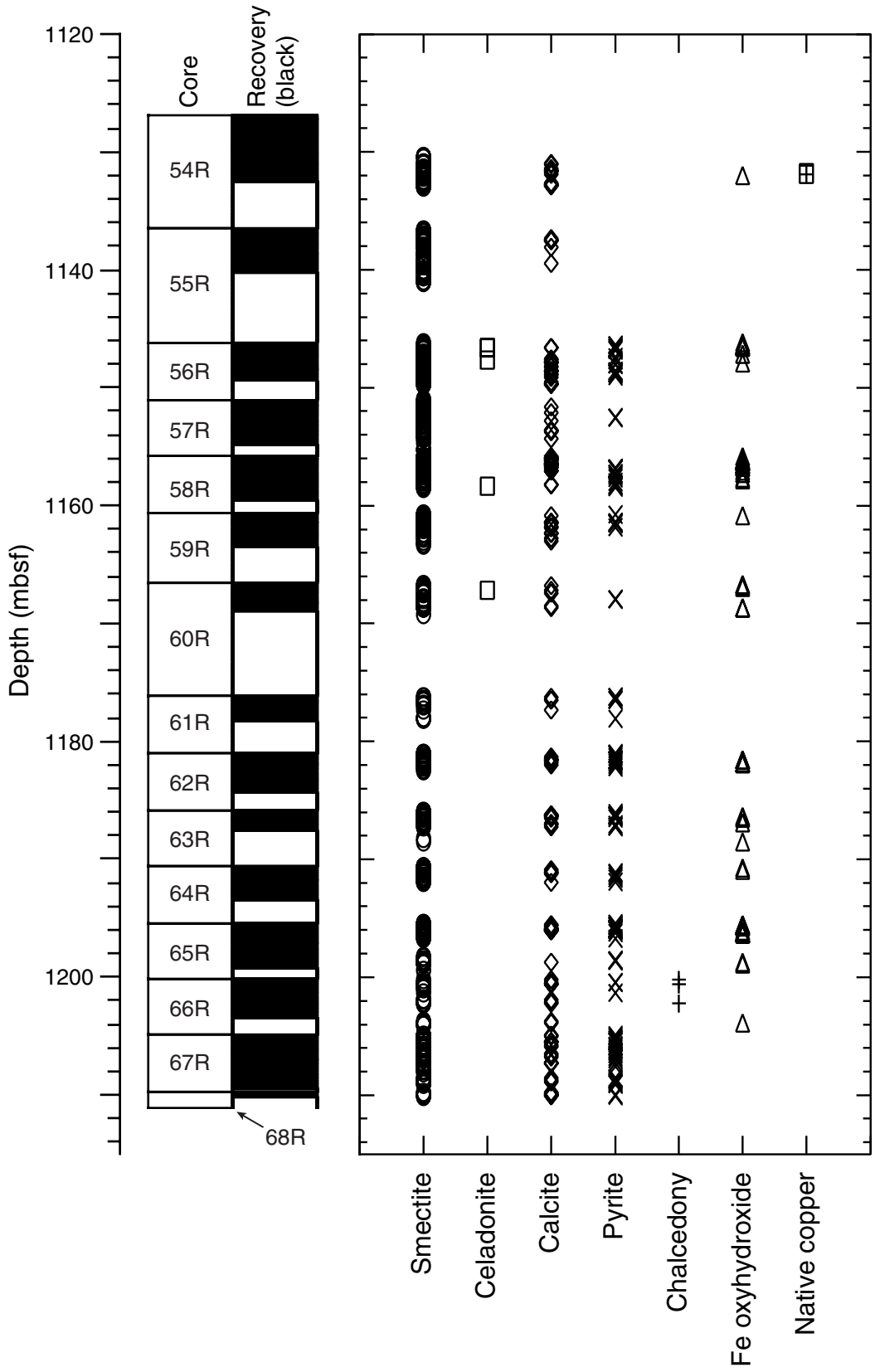

Figure F80. A 3- to 4-mm-wide vein of calcite (near walls) with chalcedony and quartz (center) in Sample 192-1183A-66R-2 (Piece 4B, 60–64 cm) (field of view = 5.5 mm; plane-polarized light; photomicrograph ID# 1183A_032).

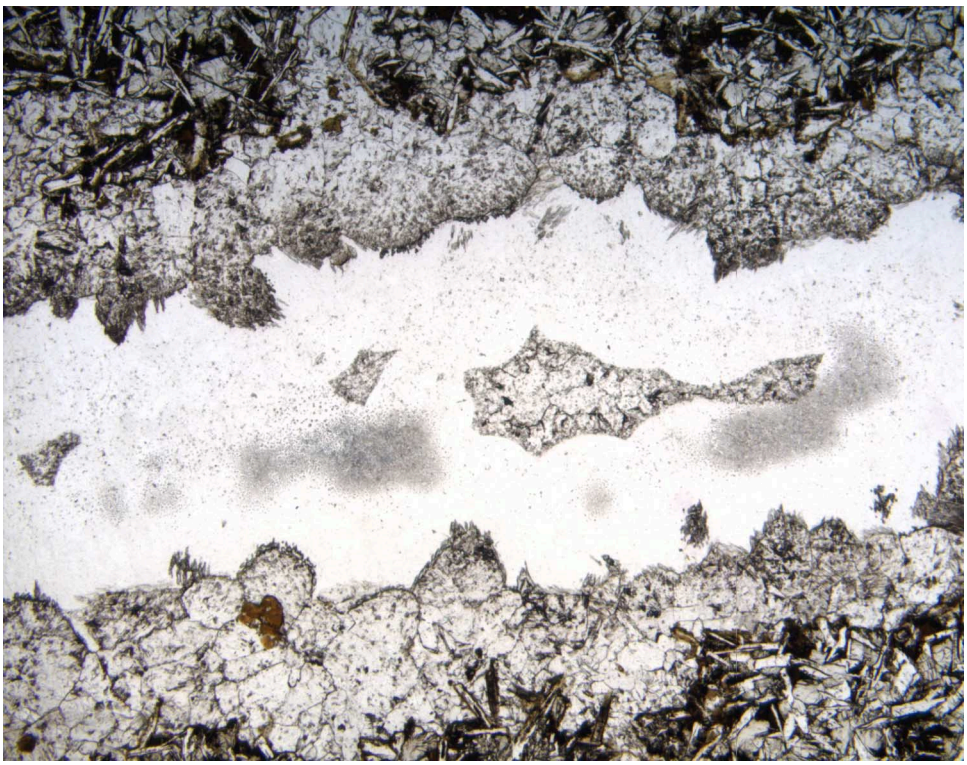

Figure F81. A 3- to 4-mm-wide vein of calcite (near walls) with chalcedony and quartz (center) in Sample 192-1183A-66R-2 (Piece 4B, 60–64 cm) (field of view = 5.5 mm; crossed polars; photomicrograph ID# 1183A_031).

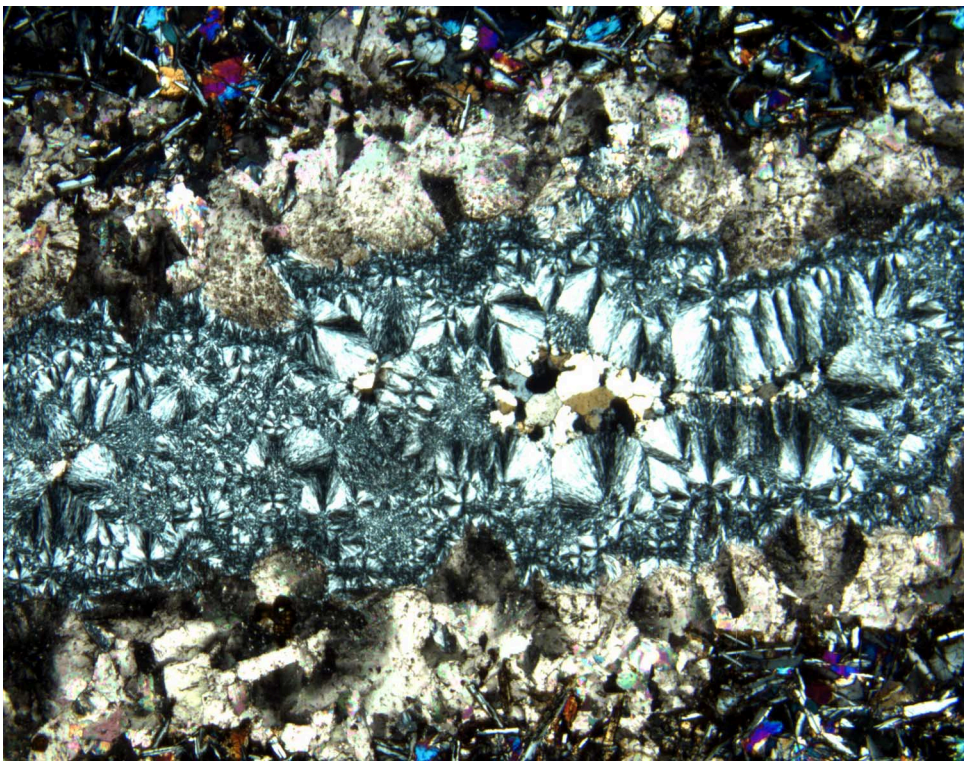

Figure F82. A 1- to 2-mm-wide vein of calcite (near walls), with successive fillings of goethite, celadonite, and chalcedony (center) in Sample **192-1183A-67R-1 (Piece 2C, 46–48 cm)** (field of view = 5.5 mm; plane-polarized light; photomicrograph ID# 1183A_028).

Figure F83. A 1- to 2-mm-wide vein of calcite (near walls), with successive fillings of goethite, celadonite, and chalcedony (center) in Sample **192-1183A-67R-1 (Piece 2C, 46–48 cm)** (field of view is 2.8 mm; crossed polars; photomicrograph ID# 1183A_029).

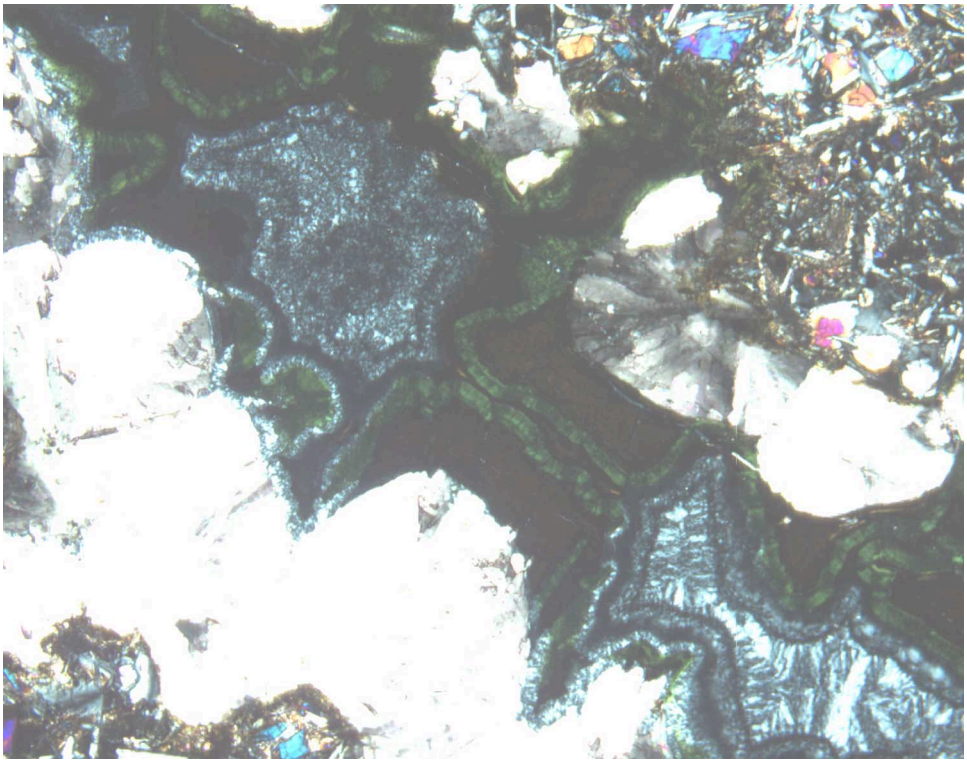

Figure F84. Vein-width distribution with depth in Hole 1183A.

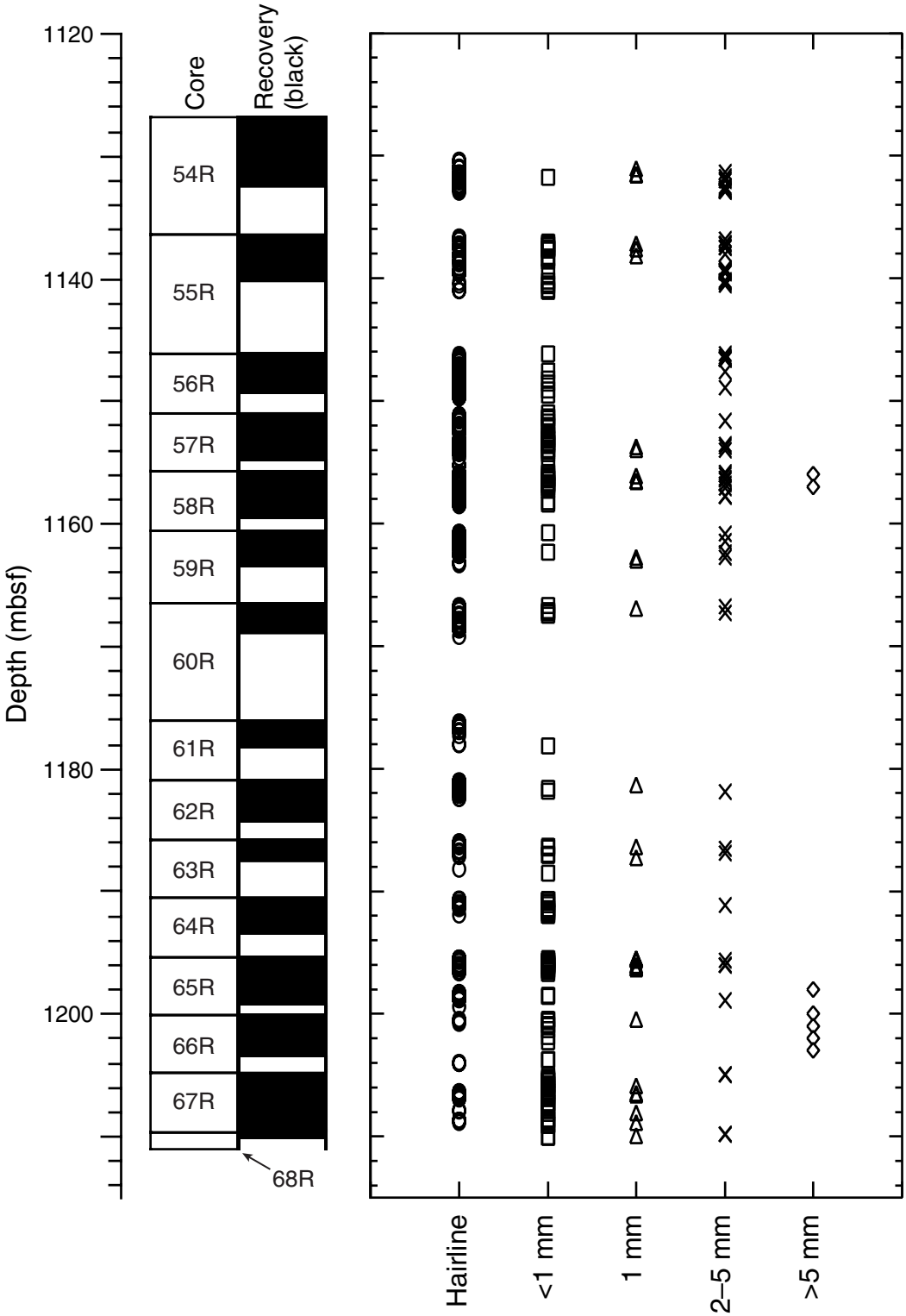

Figure F85. Large miarolitic cavities filled with smectite (black) and calcite (white) in interval 192-1183A-57R-1 (Piece 9, 62–78 cm). A horizontal 1- to 2-mm-wide vein of calcite, with minor smectite and disseminated pyrite, connects the miarolitic cavities located 63 cm from the top of the section.

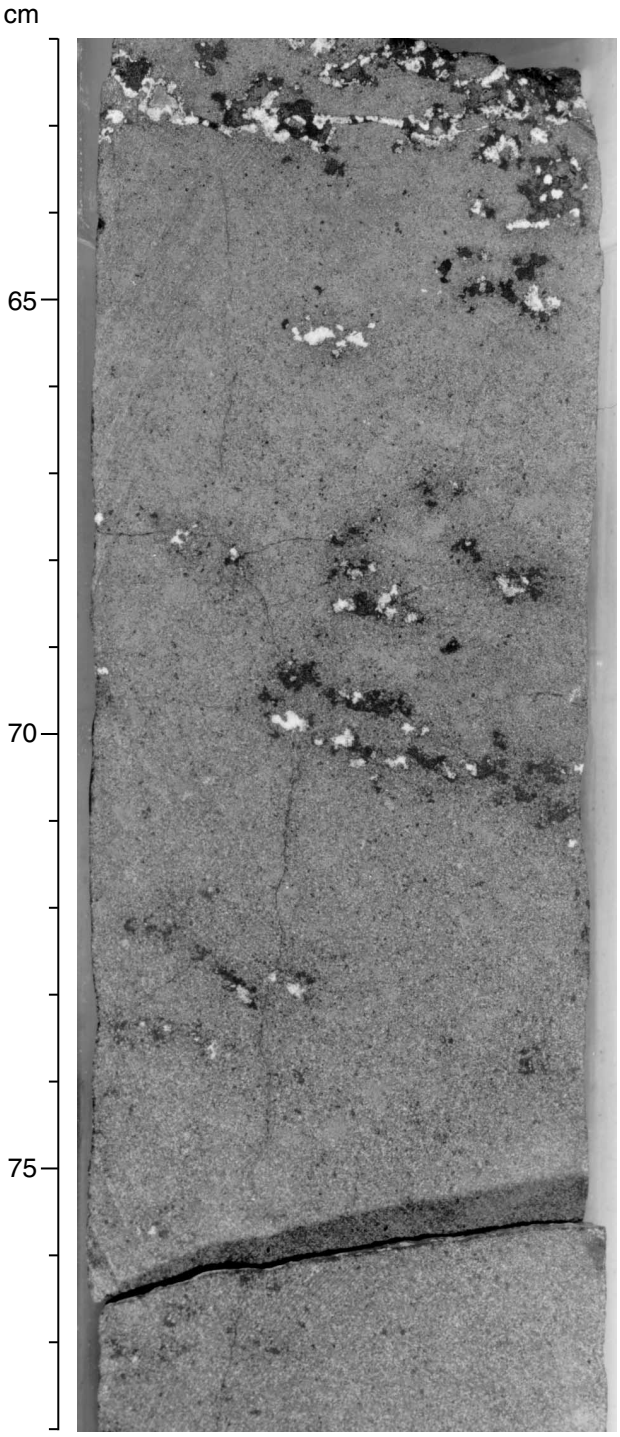

Figure F86. Miarolitic cavity filled with nontronite and celadonite (lining walls), with successive fillings of goethite, calcite, and, possibly, blue chalcedony (center) in Sample **192-1183A-66R-2 (Piece 4B, 60–64 cm)** (field of view = 2.8 mm; plane-polarized light; photomicrograph ID# 1183A_026).

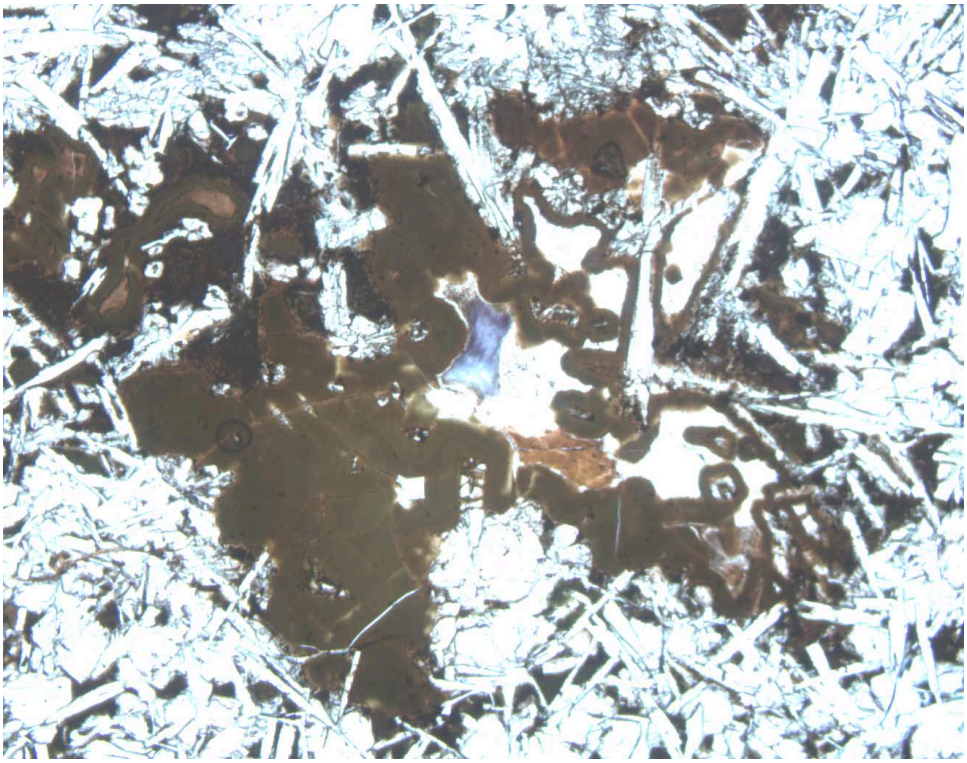

Figure F87. Graphic presentation of the true dip, fracture density, and vein abundance for Hole 1183A. There were 303 measured vein orientations and 849 measured veins. The calculated true dip was obtained from two measured apparent-dip directions; the true-dip values were measured directly from the core.

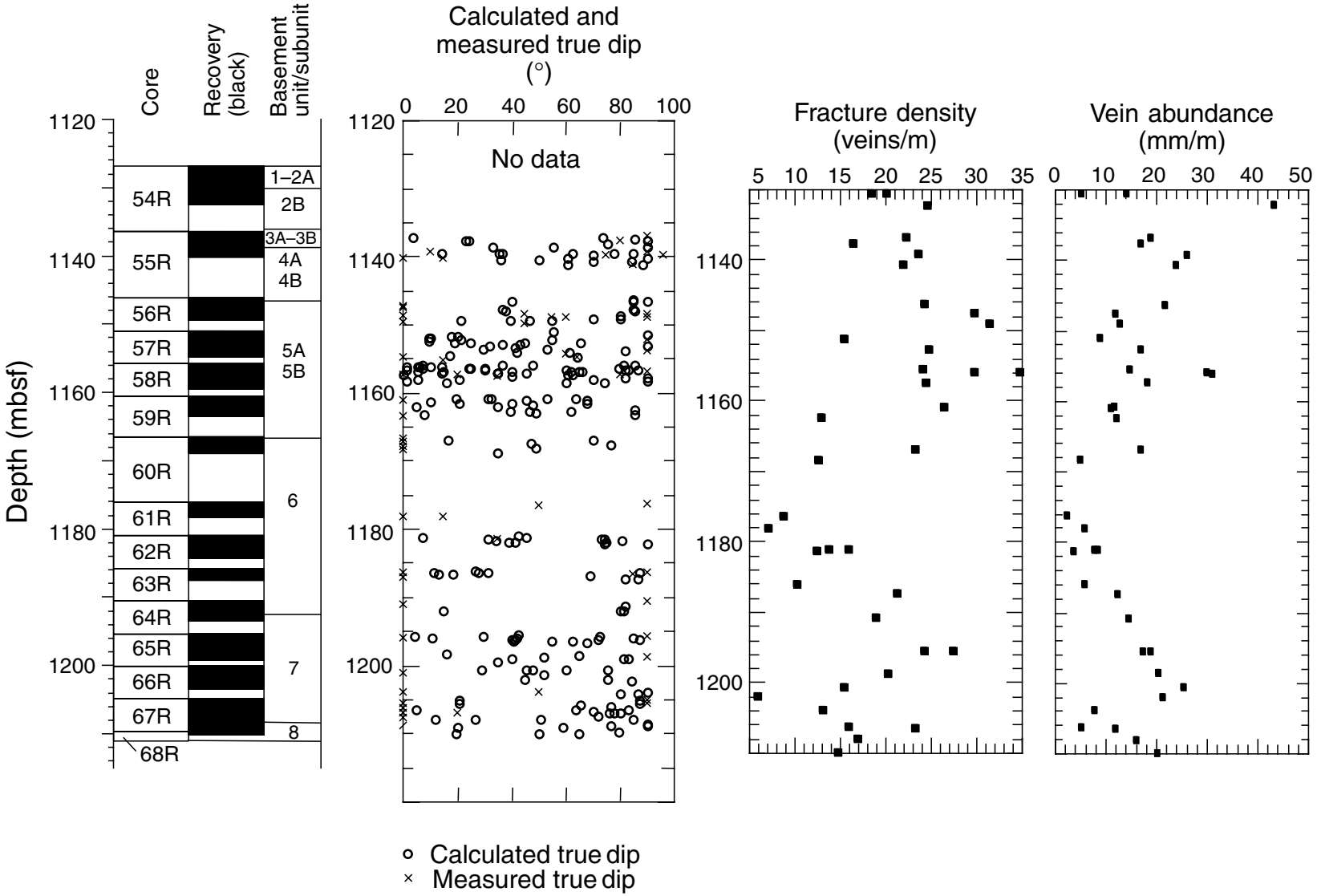

Figure F88. Examples of high-quality Zijderveld diagrams for (**A**) sediments and (**B**) basalts.

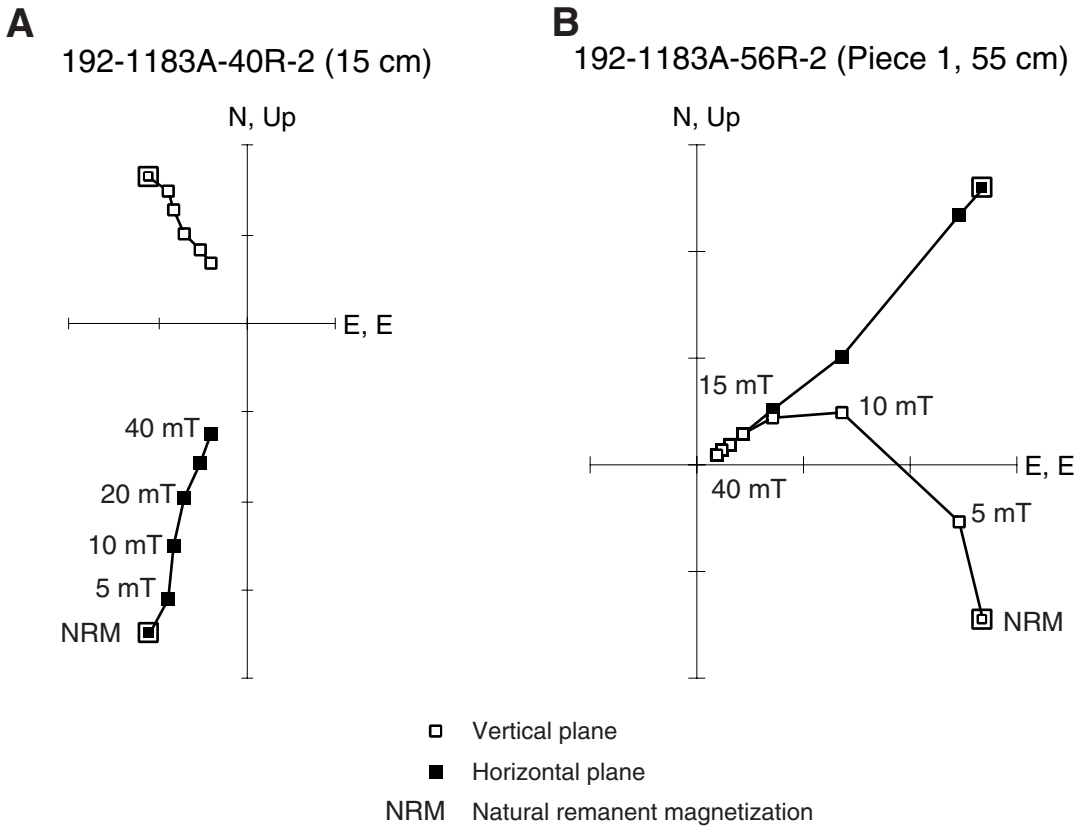

Figure F89. Downhole variation in magnetic susceptibility (κ) and natural remanent magnetization (NRM) for the sedimentary units. Note that the diamagnetic contribution of calcite (-13.8×10^{-6} SI) has been subtracted from the susceptibility.

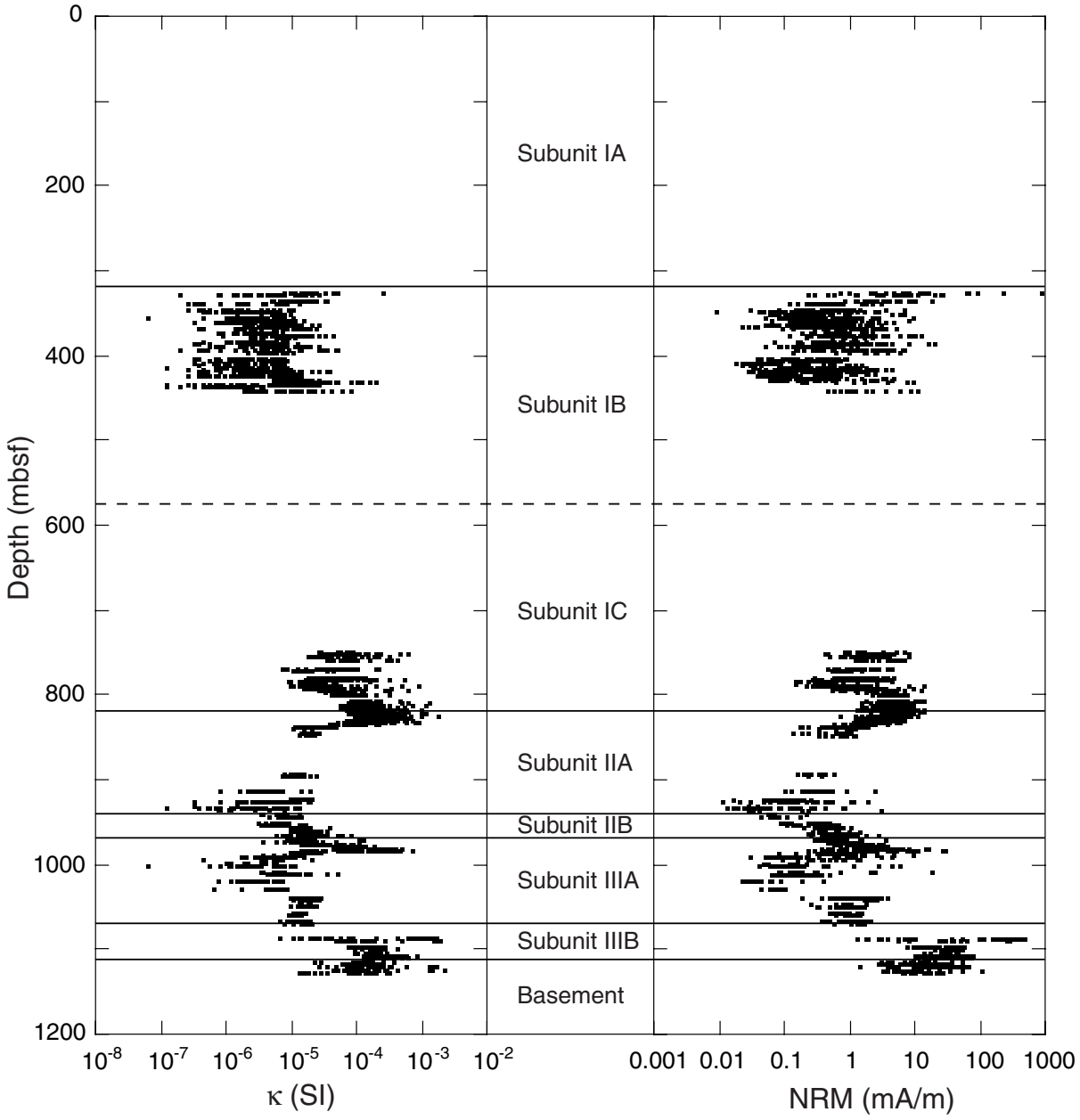

Figure F90. Magnetic polarity and biostratigraphic data for Cores 192-1183A-36R to 41R (left column) and our proposed correlation with the geomagnetic polarity timescale (right column).

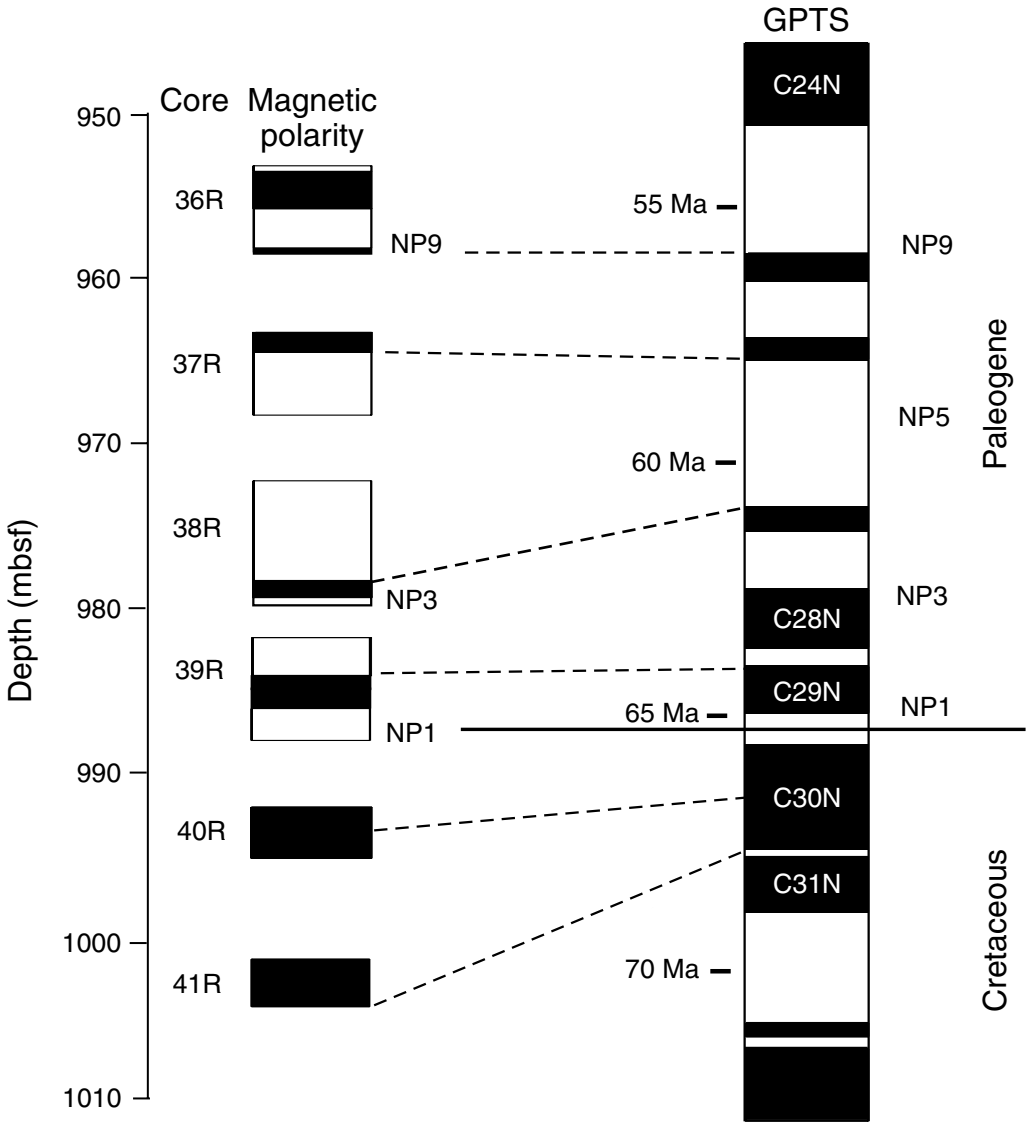

Figure F91. Downcore variation in the direction of the characteristic remanent magnetization for Core 192-1183A-21R. Shifts in declination correspond to changes in the relative azimuthal orientation of intact pieces of the core.

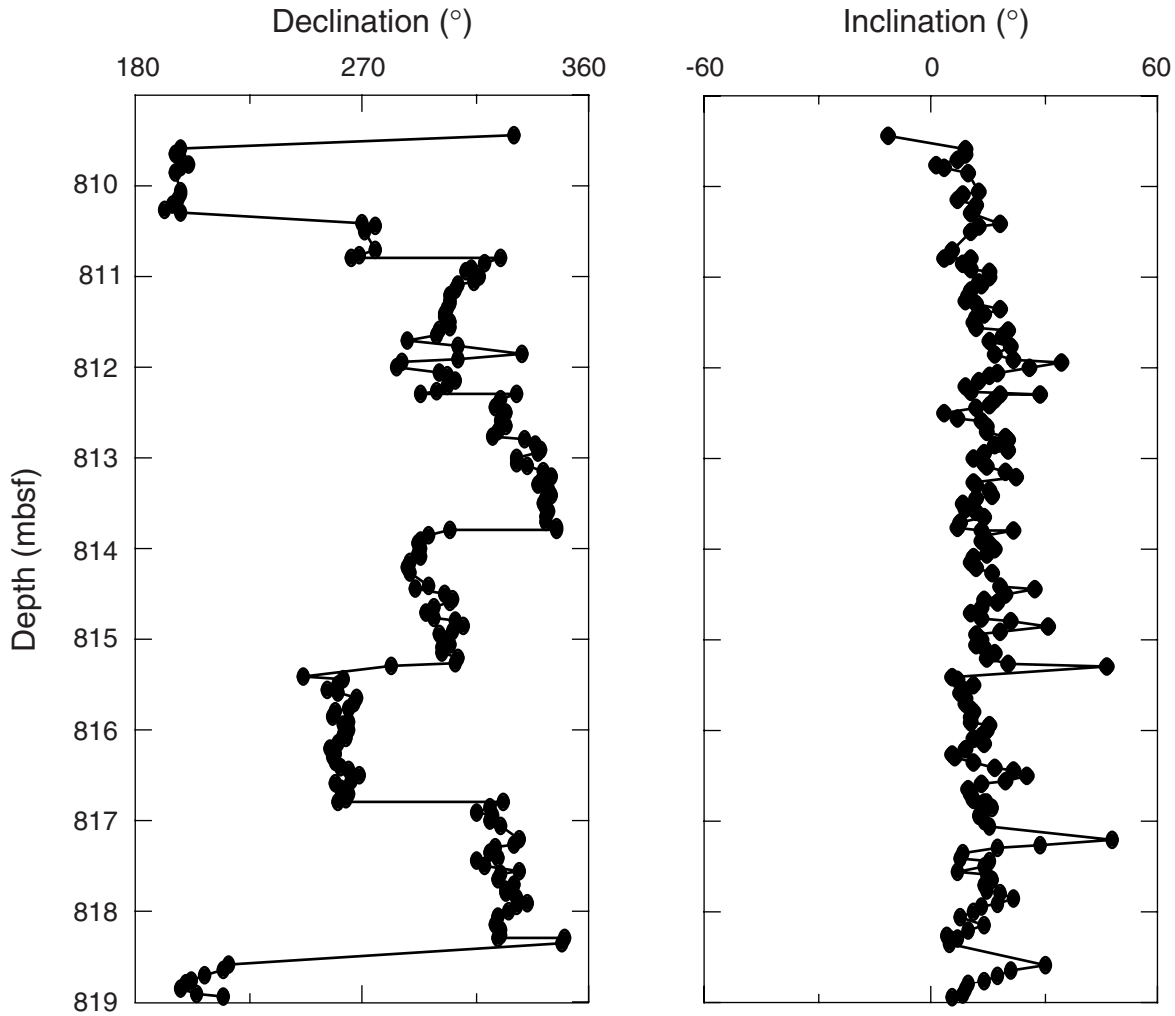

Figure F92. Paleolatitude vs. age for Hole 1183A, based on paleomagnetic inclination data.

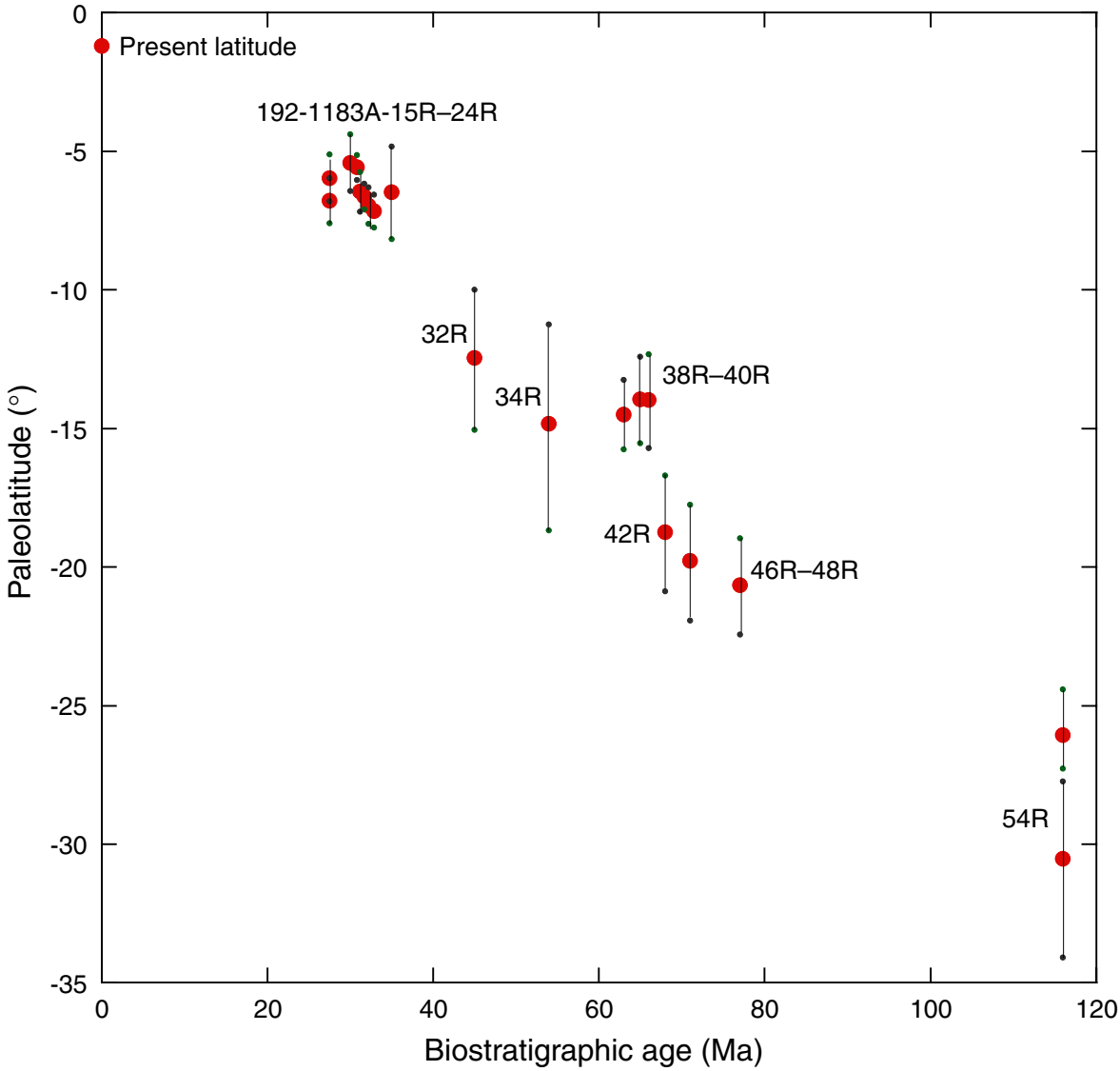

Figure F93. Variations in declination and inclination (defined by principal component analysis) and natural remanent magnetization intensity through Section 192-1183A-55R-1 (Pieces 4A–4E). See **"Results from Basaltic Units,"** p. 35, for discussion.

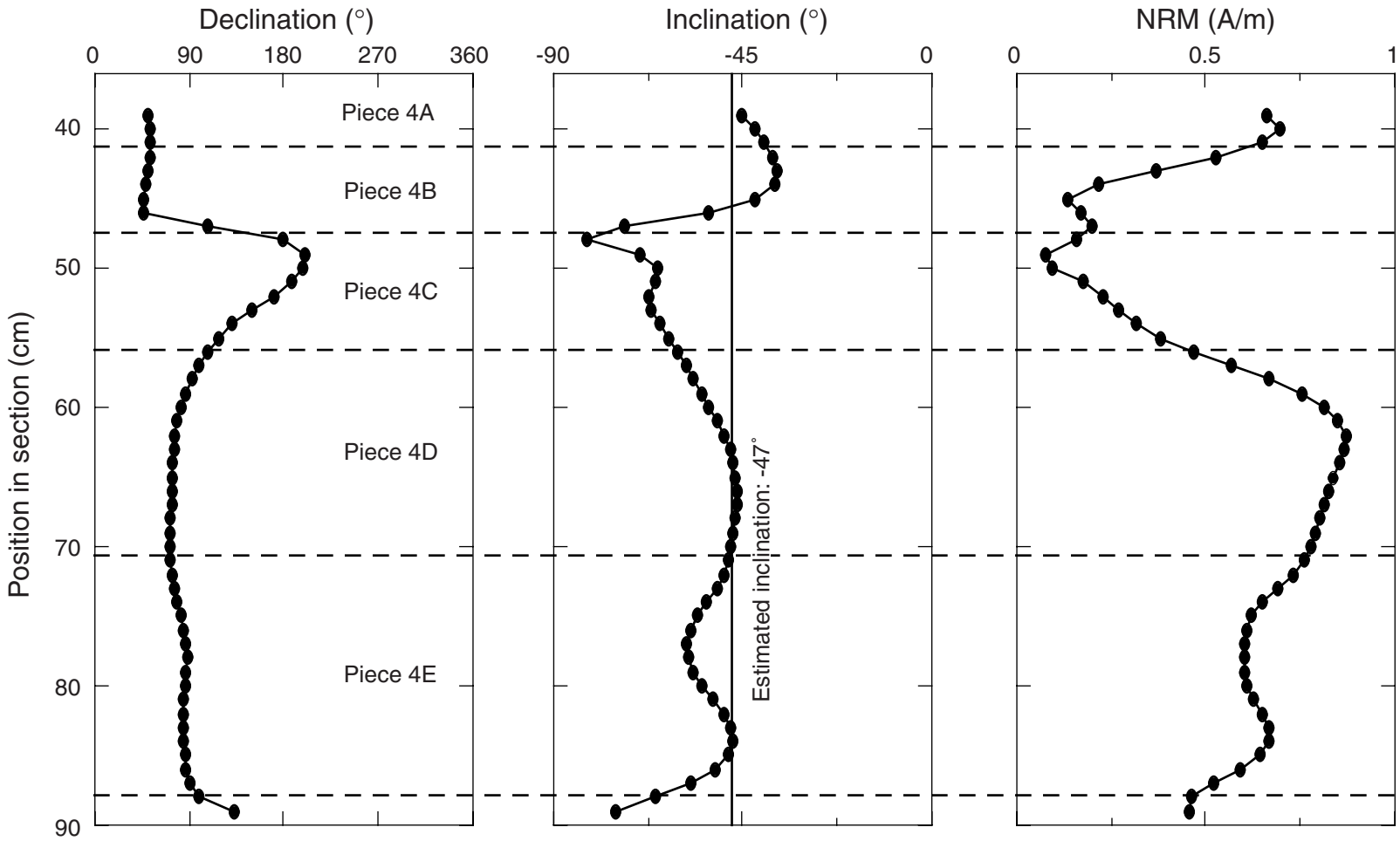

Figure F94. Index properties and thermal conductivity vs. depth at Hole 1183A correlated with lithologic units. Sedimentary units are shaded in the "Lithologic unit" column; basement units are unshaded.

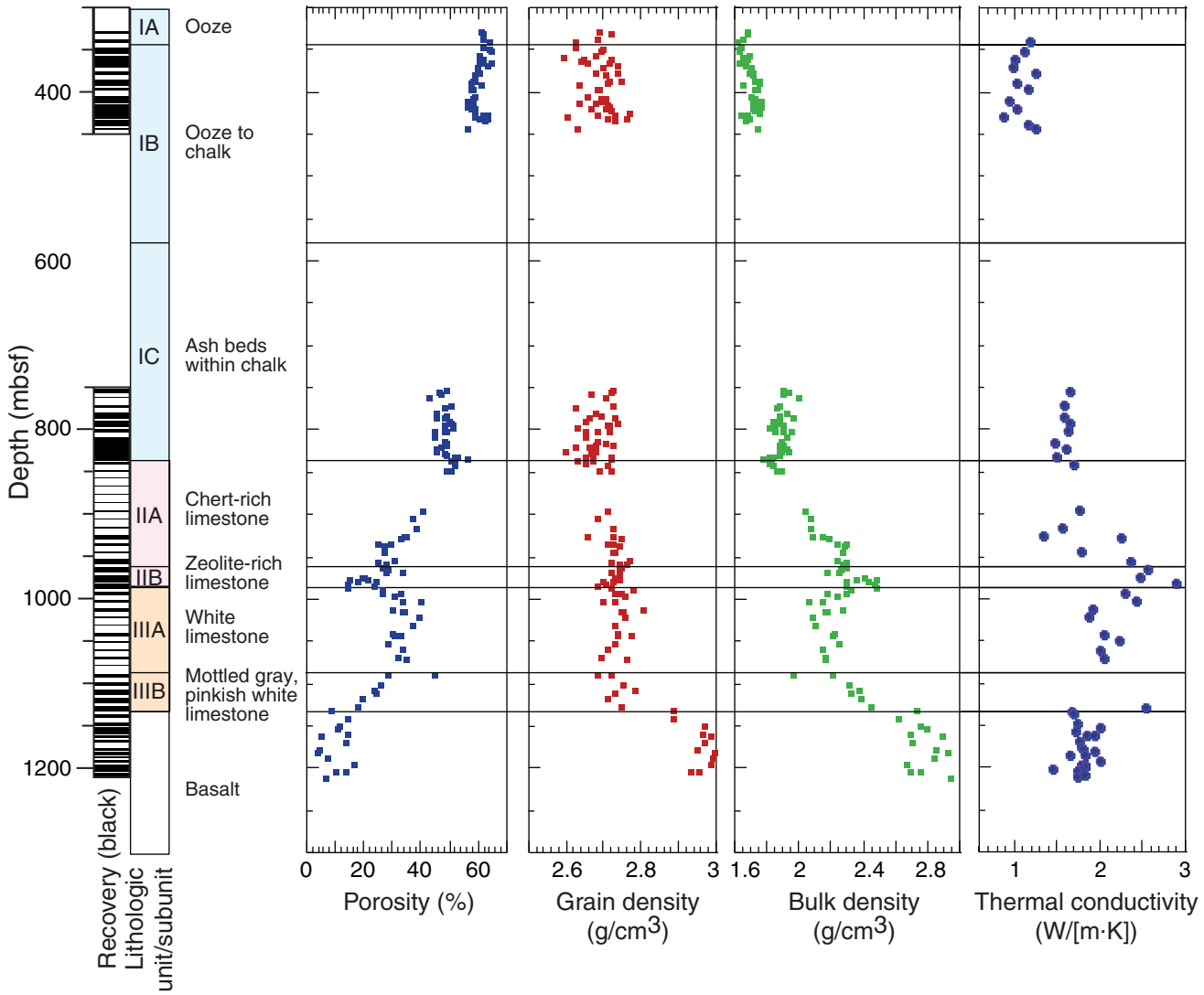

Figure F95. *P*-wave velocity and whole-core measurements vs. depth for Hole 1183A. Sedimentary units are shaded in the "Lithologic unit" column; basement units are unshaded. Velocities determined in the horizontal plane (x and y) and in the z-direction are indicated by dashed black and solid red lines, respectively.

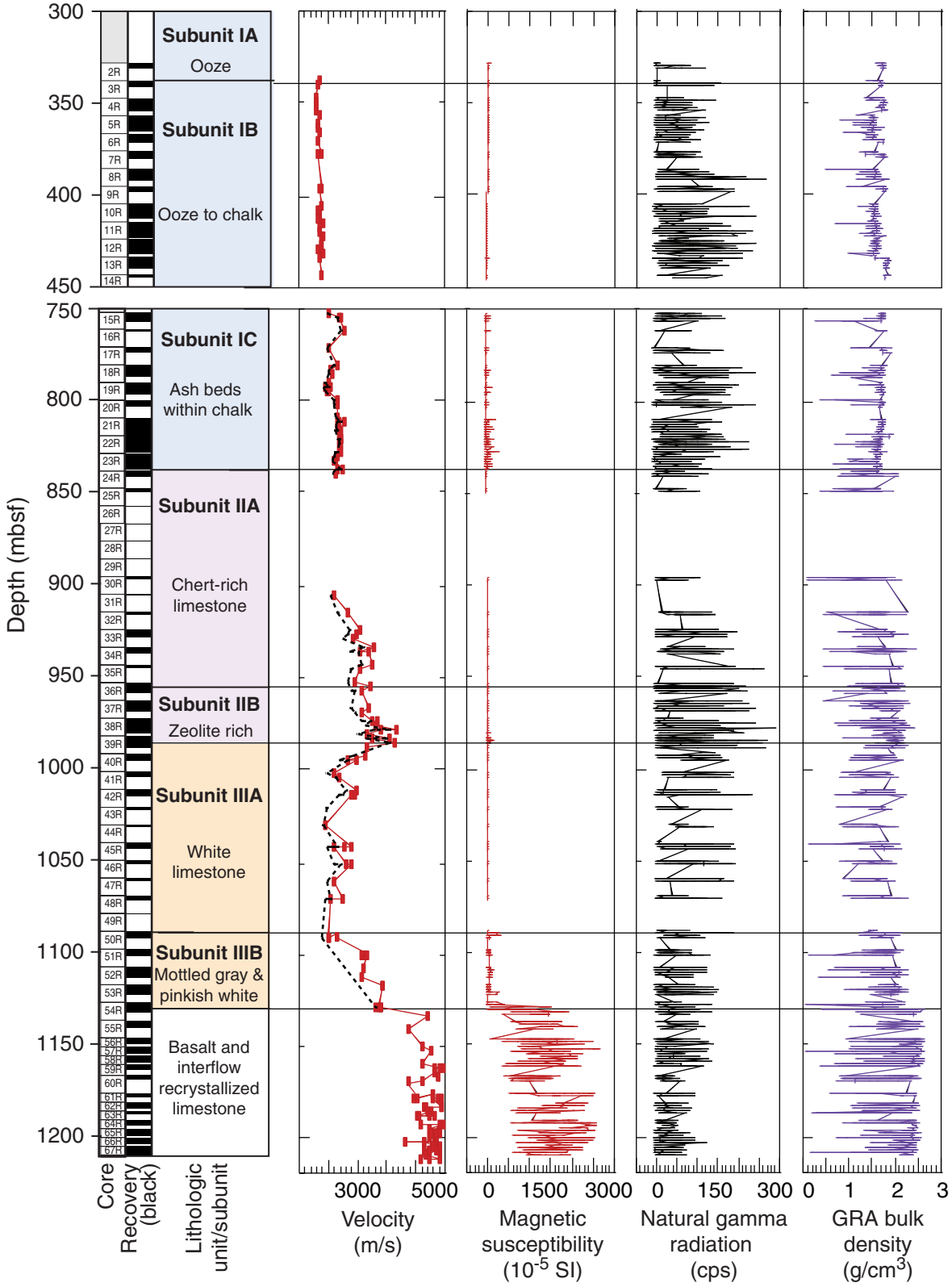

Table T1. Coring summary, Hole 1183A.

Core	Date (Sept 2000)	Time (local)	Depth (mbsf) Top	Depth (mbsf) Bottom	Length (m) Cored	Length (m) Recovered	Recovery (%)
192-1183A-							
1W	19	0245	0.0	328.0	0.0	NA	NA
2R	19	0340	328.0	337.6	9.6	2.84	29.6
3R	19	0430	337.6	347.2	9.6	3.27	34.1
4R	19	0510	347.2	356.8	9.6	6.94	72.3
5R	19	0545	356.8	366.3	9.5	8.66	91.2
6R	19	0625	366.3	375.9	9.6	4.75	49.5
7R	19	0705	375.9	385.5	9.6	4.28	44.6
8R	19	0745	385.5	395.1	9.6	6.53	68.0
9R	19	0825	395.1	404.7	9.6	2.88	30.0
10R	19	0905	404.7	414.3	9.6	8.00	83.3
11R	19	0940	414.3	423.9	9.6	8.45	88.0
12R	19	1020	423.9	433.5	9.6	8.25	85.9
13R	19	1110	433.5	443.1	9.6	6.52	67.9
14R	19	1155	443.1	452.7	9.6	1.73	18.0
150	19	0220	452.7	752.0	0.0	NA	NA
15R	20	0405	752.0	761.1	9.1	5.19	57.0
16R	20	0525	761.1	770.8	9.7	1.06	10.9
17R	20	0645	770.8	780.5	9.7	2.98	30.7
18R	20	0800	780.5	790.1	9.6	6.51	67.8
19R	20	0910	790.1	799.7	9.6	6.52	67.9
20R	20	1030	799.7	809.3	9.6	3.44	35.8
21R	20	1155	809.3	819.0	9.7	9.99	103.0
22R	20	1320	819.0	828.6	9.6	9.12	95.0
23R	20	1440	828.6	838.2	9.6	8.47	88.2
24R	20	1555	838.2	847.4	9.2	3.09	33.6
25R	20	1700	847.4	857.0	9.6	1.95	20.3
26R	20	1840	857.0	866.6	9.6	0.37	3.9
27R	20	1940	866.6	876.2	9.6	0.37	3.9
28R	20	2045	876.2	885.9	9.7	0.19	2.0
29R	20	2150	885.9	895.5	9.6	0.13	1.4
30R	20	2310	895.5	905.1	9.6	1.64	17.1
31R	21	0040	905.1	914.7	9.6	0.80	8.3
32R	21	0210	914.7	924.3	9.6	1.72	17.9
33R	21	0355	924.3	933.9	9.6	4.37	45.5
34R	21	0525	933.9	943.5	9.6	3.14	32.7
35R	21	0700	943.5	953.1	9.6	1.75	18.2
36R	21	0930	953.1	962.7	9.6	5.62	58.5
37R	21	1120	962.7	972.4	9.7	6.01	62.0
38R	21	1435	972.4	982.0	9.6	8.02	83.5
39R	21	1720	982.0	991.7	9.7	6.43	66.3
40R	21	1840	991.7	1001.4	9.7	3.87	39.9
41R	21	2000	1001.4	1011.1	9.7	2.89	29.8
42R	21	2125	1011.1	1020.8	9.7	3.81	39.3
43R	21	2240	1020.8	1030.4	9.6	1.31	13.6
44R	21	2359	1030.4	1040.0	9.6	0.91	9.5
45R	22	0145	1040.0	1049.6	9.6	3.35	34.9
46R	22	0325	1049.6	1059.2	9.6	2.08	21.7
47R	22	0505	1059.2	1068.8	9.6	1.53	15.9
48R	22	0630	1068.8	1078.5	9.7	2.34	24.1
49R	22	0755	1078.5	1088.2	9.7	0.21	2.2
50R	22	1010	1088.2	1097.9	9.7	3.63	37.4
51R	22	1310	1097.9	1107.5	9.6	3.74	39.0
52R	22	1710	1107.5	1117.2	9.7	5.93	61.1
53R	22	2045	1117.2	1126.8	9.6	5.41	56.4
54R	23	0110	1126.8	1136.5	9.7	5.66	58.4
55R	23	0745	1136.5	1146.1	9.6	3.67	38.2
56R	23	1215	1146.1	1151.0	4.9	3.32	67.8
57R	23	1725	1151.0	1155.8	4.8	3.80	79.2
58R	23	2245	1155.8	1160.6	4.8	3.73	77.7
59R	25	1140	1160.6	1166.5	5.9	2.91	49.3
60R	25	1910	1166.5	1176.1	9.6	2.39	24.9
61R	25	2335	1176.1	1181.0	4.9	2.18	44.5
62R	26	0450	1181.0	1185.8	4.8	3.33	69.4
63R	26	0955	1185.8	1190.6	4.8	1.75	36.5
64R	26	1450	1190.6	1195.4	4.8	2.84	59.2
65R	26	2215	1195.4	1200.1	4.7	3.82	81.3
66R	27	0455	1200.1	1204.9	4.8	3.32	69.2
67R	27	1120	1204.9	1209.7	4.8	4.51	94.0
68R	27	1255	1209.7	1211.1	1.4	0.47	33.6
				Cored:	583.8	260.69	44.7
				Drilled:	627.3		
				Total:	1211.1		

Note: NA = not applicable. This table is also available in **ASCII format.**

Table T2. Expanded coring summary, Hole 1183A. (See table notes. Continued on next eight pages.)

Core	Date (Sep 2000)	Time (local)	Core depth (mbsf) Top	Core depth (mbsf) Bottom	Length (m) Cored	Length (m) Recovered	Recovery (%)	Section	Length (m) Liner	Length (m) Curated	Section depth (mbsf) Top	Section depth (mbsf) Bottom	Catwalk samples	Comment
192-1183A-														
1W	19	0245	0.0	328.0										
2R	19	0340	328.0	337.6	9.6	2.84	29.6							
								1	1.50	1.50	328.00	329.50		
								2	1.08	1.08	329.50	330.58		
								CC (w/2)	0.26	0.26	330.58	330.84	PAL	
								Totals:	2.84	2.84				
3R	19	0430	337.6	347.2	9.6	3.27	34.1							
								1	1.50	1.50	337.60	339.10		
								2	1.50	1.50	339.10	340.60		
								CC	0.27	0.27	340.60	340.87	PAL	
								Totals:	3.27	3.27				
4R	19	0510	347.2	356.8	9.6	6.94	72.3							
								1	1.50	1.50	347.20	348.70		
								2	1.50	1.50	348.70	350.20		
								3	1.50	1.50	350.20	351.70		
								4	1.50	1.50	351.70	353.20		
								5	0.68	0.68	353.20	353.88		
								CC (w/5)	0.26	0.26	353.88	354.14	PAL	
								Totals:	6.94	6.94				
5R	19	0545	356.8	366.3	9.5	8.66	91.2							
								1	1.50	1.50	356.80	358.30		
								2	1.50	1.50	358.30	359.80		
								3	1.50	1.50	359.80	361.30		
								4	1.50	1.50	361.30	362.80		
								5	1.50	1.50	362.80	364.30		
								6	0.91	0.91	364.30	365.21		
								CC (w/6)	0.25	0.25	365.21	365.46	PAL	
								Totals:	8.66	8.66				
6R	19	0625	366.3	375.9	9.6	4.75	49.5							
								1	1.50	1.50	366.30	367.80		
								2	1.50	1.50	367.80	369.30		
								3	1.47	1.47	369.30	370.77		
								CC	0.28	0.28	370.77	371.05	PAL	
								Totals:	4.75	4.75				
7R	19	0705	375.9	385.5	9.6	4.28	44.6							
								1	1.50	1.50	375.9	377.40		
								2	1.50	1.50	377.4	378.90		
								3	1.00	1.00	378.9	379.90		
								CC (w/3)	0.28	0.28	379.9	380.18	PAL	
								Totals:	4.28	4.28				
8R	19	0745	385.5	395.1	9.6	6.53	68.0							
								1	1.50	1.50	385.50	387.00		
								2	1.50	1.50	387.00	388.50		
								3	1.50	1.50	388.50	390.00		

Table T2 (continued).

Core	Date (Sep 2000)	Time (local)	Core depth (mbsf) Top	Core depth (mbsf) Bottom	Length (m) Cored	Length (m) Recovered	Recovery (%)	Section	Length (m) Liner	Length (m) Curated	Section depth (mbsf) Top	Section depth (mbsf) Bottom	Catwalk samples	Comment
								4	1.00	1.00	390.00	391.00		
								5	0.70	0.70	391.00	391.70		
								CC (w/5)	0.33	0.33	391.70	392.03	PAL	
								Totals:	6.53	6.53				
9R	19	0825	395.1	404.7	9.6	2.88	30							
								1	1.50	1.50	395.10	396.60		
								2	1.09	1.09	396.60	397.69		
								CC (w/2)	0.29	0.29	397.69	397.98	PAL	
								Totals:	2.88	2.88				
10R	19	0905	404.7	414.3	9.6	8.00	83.3							
								1	1.50	1.50	404.70	406.20		
								2	1.50	1.50	406.20	407.70		
								3	1.50	1.50	407.70	409.20		
								4	1.50	1.50	409.20	410.70		
								5	1.00	1.00	410.70	411.70		
								6	0.72	0.72	411.70	412.42		
								CC (w/6)	0.28	0.28	412.42	412.70	PAL	
								Totals:	8.00	8.00				
11R	19	0940	414.3	423.9	9.6	8.45	88.0							
								1	1.50	1.50	414.30	415.80		
								2	1.50	1.50	415.80	417.30		
								3	1.50	1.50	417.30	418.80	PAL	
								4	1.50	1.50	418.80	420.30	PAL	
								5	1.50	1.50	420.30	421.80		
								6	0.64	0.64	421.80	422.44	PAL	
								CC (w/6)	0.31	0.31	422.44	422.75	PAL	
								Totals:	8.45	8.45				
12R	19	1020	423.9	433.5	9.6	8.25	85.9							
								1	1.50	1.50	423.90	425.40		
								2	1.50	1.50	425.40	426.90		
								3	1.50	1.50	426.90	428.40		
								4	1.50	1.50	428.40	429.90		
								5	1.50	1.50	429.90	431.40		
								6	0.42	0.42	431.40	431.82		
								CC (w/6)	0.33	0.33	431.82	432.15	PAL	
								Totals:	8.25	8.25				
13R	19	1110	433.5	443.1	9.6	6.52	67.9							
								1	1.50	1.50	433.50	435.00		
								2	1.50	1.50	435.00	436.50		
								3	1.50	1.50	436.50	438.00		
								4	1.00	1.00	438.00	439.00		
								5	0.78	0.78	439.00	439.78		
								CC (w/5)	0.24	0.24	439.78	440.02	PAL	
								Totals:	6.52	6.52				
14R	19	1155	443.1	452.7	9.6	1.73	18.0							
								1	1.40	1.40	443.10	444.50		

Table T2 (continued).

Core	Date (Sep 2000)	Time (local)	Core depth (mbsf) Top	Core depth (mbsf) Bottom	Length (m) Cored	Length (m) Recovered	Recovery (%)	Section	Length (m) Liner	Length (m) Curated	Section depth (mbsf) Top	Section depth (mbsf) Bottom	Catwalk samples	Comment
								CC	0.33	0.33	444.50	444.83	PAL	
								Totals:	1.73	1.73				
150	20	0220	452.7	752.0										
15R	20	0405	752.0	761.1	9.1	5.19	57.0							
								1	1.50	1.50	752.00	753.50		
								2	1.50	1.50	753.50	755.00		
								3	1.50	1.50	755.00	756.50		
								4	0.42	0.42	756.50	756.92		
								CC (w/4)	0.27	0.27	756.92	757.19	PAL	
								Totals:	5.19	5.19				
16R	20	0525	761.1	770.8	9.7	1.06	10.9							
								1	0.88	0.88	761.10	761.98		
								CC (w/1)	0.18	0.18	761.98	762.16	PAL	
								Totals:	1.06	1.06				
17R	20	0645	770.8	780.5	9.7	2.98	30.7							
								1	1.50	1.50	770.80	772.30		
								2	1.11	1.11	772.30	773.41		
								CC (w/2)	0.37	0.37	773.41	773.78	PAL	
								Totals:	2.98	2.98				
18R	20	0800	780.5	790.1	9.6	6.51	67.8							
								1	1.50	1.50	780.50	782.00		
								2	1.50	1.50	782.00	783.50		
								3	1.42	1.42	783.50	784.92		
								4	1.50	1.50	784.92	786.42		
								5	0.38	0.38	786.42	786.80		
								CC (w/5)	0.21	0.21	786.80	787.01	PAL	
								Totals:	6.51	6.51				
19R	20	0910	790.1	799.7	9.6	6.52	67.9							
								1	1.50	1.50	790.10	791.60		
								2	1.50	1.50	791.60	793.10		
								3	1.50	1.50	793.10	794.60		
								4	1.42	1.42	794.60	796.02		
								5	0.36	0.36	796.02	796.38		
								CC (w/5)	0.24	0.24	796.38	796.62	PAL	
								Totals:	6.52	6.52				
20R	20	1030	799.7	809.3	9.6	3.44	35.8							
								1	1.50	1.50	799.70	801.20		
								2	1.00	1.00	801.20	802.20		
								3	0.68	0.68	802.20	802.88		
								CC (w/3)	0.26	0.26	802.88	803.14	PAL	
								Totals:	3.44	3.44				
21R	20	1155	809.3	819.0	9.7	9.99	103.0							
								1	1.50	1.50	809.30	810.80		
								2	1.50	1.50	810.80	812.30		
								3	1.50	1.50	812.30	813.80		

Table T2 (continued).

Core	Date (Sep 2000)	Time (local)	Core depth (mbsf) Top	Core depth (mbsf) Bottom	Length (m) Cored	Length (m) Recovered	Recovery (%)	Section	Length (m) Liner	Length (m) Curated	Section depth (mbsf) Top	Section depth (mbsf) Bottom	Catwalk samples	Comment
								4	1.50	1.50	813.80	815.30		
								5	1.50	1.50	815.30	816.80		
								6	1.50	1.50	816.80	818.30		
								7	0.72	0.72	818.30	819.02		
								CC (w/7)	0.27	0.27	819.02	819.29	PAL	
								Totals:	9.99	9.99				
22R	20	1320	819.0	828.6	9.6	9.12	95.0							
								1	1.50	1.50	819.00	820.50		
								2	1.50	1.50	820.50	822.00		
								3	1.50	1.50	822.00	823.50		
								4	1.50	1.50	823.50	825.00		
								5	1.50	1.50	825.00	826.50		
								6	1.34	1.34	826.50	827.84		
								CC	0.28	0.28	827.84	828.12	PAL	
								Totals:	9.12	9.12				
23R	20	1440	828.6	838.2	9.6	8.47	88.2							
								1	1.50	1.50	828.60	830.10		
								2	1.50	1.50	830.10	831.60		
								3	1.50	1.50	831.60	833.10		
								4	1.50	1.50	833.10	834.60		
								5	1.50	1.50	834.60	836.10		
								6	0.75	0.75	836.10	836.85		
								CC (w/6)	0.22	0.22	836.85	837.07	PAL	
								Totals:	8.47	8.47				
24R	20	1555	838.2	847.4	9.2	3.09	33.6							
								1	1.50	1.50	838.20	839.70	PAL	
								2	1.36	1.36	839.70	841.06	PAL	
								CC	0.23	0.23	841.06	841.29	PAL	
								Totals:	3.09	3.09				
25R	20	1700	847.4	857.0	9.6	1.95	20.3							
								1	1.04	1.04	847.40	848.44	PAL	
								2	0.64	0.64	848.44	849.08	PAL	
								CC (w/2)	0.27	0.27	849.08	849.35	PAL	
								Totals:	1.95	1.95				
26R	20	1840	857.0	866.6	9.6	0.37	3.9							
								CC	0.37	0.37	857.00	857.37	PAL	
								Totals:	0.37	0.37				
27R	20	1940	866.6	876.2	9.6	0.37	3.9							
								CC	0.37	0.37	866.60	866.97	PAL	
								Totals:	0.37	0.37				
28R	20	2045	876.2	885.9	9.7	0.19	2.0							
								CC	0.19	0.19	876.20	876.39	PAL	
								Totals:	0.19	0.19				

Table T2 (continued).

Core	Date (Sep 2000)	Time (local)	Core depth (mbsf) Top	Core depth (mbsf) Bottom	Length (m) Cored	Length (m) Recovered	Recovery (%)	Section	Length (m) Liner	Length (m) Curated	Section depth (mbsf) Top	Section depth (mbsf) Bottom	Catwalk samples	Comment
29R	20	2150	885.9	895.5	9.6	0.13	1.4							
								CC	0.13	0.13	885.90	886.03	PAL	
								Totals:	0.13	0.13				
30R	20	2310	895.5	905.1	9.6	1.64	17.1							
								1	0.90	0.90	895.50	896.40		
								2	0.74	0.74	896.40	897.14	PAL	
								Totals:	1.64	1.64				
31R	21	0040	905.1	914.7	9.6	0.80	8.3							
								1	0.80	0.80	905.10	905.90	PAL	
								Totals:	0.80	0.80				
32R	21	0210	914.7	924.3	9.6	1.72	17.9							
								1	1.50	1.50	914.70	916.20		
								CC	0.22	0.22	916.20	916.42	PAL	
								Totals:	1.72	1.72				
33R	21	0355	924.3	933.9	9.6	4.37	45.5							
								1	1.46	1.46	924.30	925.76		
								2	1.50	1.50	925.76	927.26		
								3	1.36	1.36	927.26	928.62		
								CC (NS)	0.05	0.05	928.62	928.67	PAL	All to PAL
								Totals:	4.37	4.37				
34R	21	0525	933.9	943.5	9.6	3.14	32.7							
								1	1.50	1.50	933.90	935.40		
								2	0.98	0.98	935.40	936.38		
								3	0.66	0.66	936.38	937.04	PAL	
								Totals:	3.14	3.14				
35R	21	0700	943.5	953.1	9.6	1.75	18.2							
								1	1.27	1.27	943.50	944.77		
								2	0.48	0.48	944.77	945.25	PAL	
								Totals:	1.75	1.75				
36R	21	0930	953.1	962.7	9.6	5.62	58.5							
								1	1.45	1.45	953.10	954.55		
								2	1.50	1.50	954.55	956.05		
								3	1.50	1.50	956.05	957.55		
								4	0.92	0.92	957.55	958.47	PAL	
								CC (w/4)	0.25	0.25	958.47	958.72	PAL	
								Totals:	5.62	5.62				
37R	21	1120	962.7	972.4	9.7	6.01	62.0							
								1	1.50	1.50	962.70	964.20		
								2	1.50	1.50	964.20	965.70		
								3	1.47	1.47	965.70	967.17		
								4	1.33	1.33	967.17	968.50	PAL	
								CC	0.21	0.21	968.50	968.71		
								Totals:	6.01	6.01				

Table T2 (continued).

Core	Date (Sep 2000)	Time (local)	Core depth (mbsf) Top	Core depth (mbsf) Bottom	Length (m) Cored	Length (m) Recovered	Recovery (%)	Section	Length (m) Liner	Length (m) Curated	Section depth (mbsf) Top	Section depth (mbsf) Bottom	Catwalk samples	Comment
38R	21	1435	972.4	982.0	9.6	8.02	83.5							
								1	1.50	1.50	972.40	973.90	PAL	
								2	1.50	1.50	973.90	975.40		
								3	1.50	1.50	975.40	976.90		
								4	1.50	1.50	976.90	978.40		
								5	1.50	1.50	978.40	979.90		
								6	0.36	0.36	979.90	980.26	PAL	
								CC (w/6)	0.16	0.16	980.26	980.42	PAL	
								Totals:	8.02	8.02				
39R	21	1720	982.0	991.7	9.7	6.43	66.3							
								1	1.50	1.50	982.00	983.50		
								2	1.50	1.50	983.50	985.00		
								3	1.50	1.50	985.00	986.50		
								4	1.01	1.01	986.50	987.51	PAL	
								5	0.70	0.70	987.51	988.21		
								CC (w/5)	0.22	0.22	988.21	988.43	PAL	
								Totals:	6.43	6.43				
40R	21	1840	991.7	1001.4	9.7	3.87	39.9							
								1	1.45	1.45	991.70	993.15		
								2	1.50	1.50	993.15	994.65		
								3	0.71	0.71	994.65	995.36		
								CC (w/3)	0.21	0.21	995.36	995.57	PAL	
								Totals:	3.87	3.87				
41R	21	2000	1001.4	1011.1	9.7	2.89	29.8							
								1	1.50	1.50	1001.40	1002.90		
								2	1.36	1.36	1002.90	1004.26		
								CC (NS)	0.03	0.03	1004.26	1004.29	PAL	All to PAL
								Totals:	2.89	2.89				
42R	21	2125	1011.1	1020.8	9.7	3.81	39.3							
								1	1.50	1.50	1011.10	1012.60		
								2	1.50	1.50	1012.60	1014.10		
								3	0.64	0.64	1014.10	1014.74		
								CC (w/3)	0.17	0.17	1014.74	1014.91	PAL	
								Totals:	3.81	3.81				
43R	21	2240	1020.8	1030.4	9.6	1.31	13.6							
								1	1.28	1.28	1020.80	1022.08		
								CC (NS)	0.03	0.03	1022.08	1022.11	PAL	All to PAL
								Totals:	1.31	1.31				
44R	21	2359	1030.4	1040.0	9.6	0.91	9.5							
								1	0.88	0.88	1030.40	1031.28		
								CC (NS)	0.03	0.03	1031.28	1031.31	PAL	All to PAL
								Totals:	0.91	0.91				
45R	22	0145	1040.0	1049.6	9.6	3.35	34.9							
								1	1.50	1.50	1040.00	1041.50		
								2	1.20	1.20	1041.50	1042.70		

Table T2 (continued).

Core	Date (Sep 2000)	Time (local)	Core depth (mbsf) Top	Core depth (mbsf) Bottom	Length (m) Cored	Length (m) Recovered	Recovery (%)	Section	Length (m) Liner	Length (m) Curated	Section depth (mbsf) Top	Section depth (mbsf) Bottom	Catwalk samples	Comment
								3	0.62	0.62	1042.70	1043.32	PAL	
								CC (NS)	0.03	0.03	1043.32	1043.35	PAL	All to PAL
								Totals:	3.35	3.35				
46R	22	0325	1049.6	1059.2	9.6	2.08	21.7							
								1	1.40	1.40	1049.60	1051.00	PAL	
								2	0.65	0.65	1051.00	1051.65	PAL	
								CC (NS)	0.03	0.03	1051.65	1051.68	PAL	All to PAL
								Totals:	2.08	2.08				
47R	22	0505	1059.2	1068.8	9.6	1.53	15.9							
								1	1.50	1.50	1059.20	1060.70		
								CC (NS)	0.03	0.03	1060.70	1060.73	PAL	All to PAL
								Totals:	1.53	1.53				
48R	22	0630	1068.8	1078.5	9.7	2.34	24.1							
								1	1.50	1.50	1068.80	1070.30		
								2	0.62	0.62	1070.30	1070.92		
								CC (w/2)	0.22	0.22	1070.92	1071.14	PAL	
								Totals:	2.34	2.34				
49R	22	0755	1078.5	1088.2	9.7	0.21	2.2							
								CC	0.21	0.21	1078.50	1078.71	PAL	
								Totals:	0.21	0.21				
50R	22	1010	1088.2	1097.9	9.7	3.63	37.4							
								1	1.50	1.50	1088.20	1089.70	PAL	
								2	1.50	1.50	1089.70	1091.20	PAL	
								3	0.40	0.40	1091.20	1091.60	PAL	
								CC (w/3)	0.23	0.23	1091.60	1091.83	PAL	
								Totals:	3.63	3.63				
51R	22	1310	1097.9	1107.5	9.6	3.74	39. 0							
								1	1.50	1.50	1097.90	1099.40		
								2	1.50	1.50	1099.40	1100.90		
								3	0.46	0.46	1100.90	1101.36		
								CC (w/3)	0.28	0.28	1101.36	1101.64	PAL	
								Totals:	3.74	3.74				
52R	22	1710	1107.5	1117.2	9.7	5.93	61.1							
								1	1.50	1.50	1107.50	1109.00	PAL	
								2	1.50	1.50	1109.00	1110.50		
								3	1.50	1.50	1110.50	1112.00		
								4	1.23	1.23	1112.00	1113.23		
								CC (w/4)	0.20	0.20	1113.23	1113.43	PAL	
								Totals:	5.93	5.93				
53R	22	2045	1117.2	1126.8	9.6	5.41	56.4							
								1	1.47	1.47	1117.20	1118.67	PAL	
								2	1.50	1.50	1118.67	1120.17		
								3	1.27	1.27	1120.17	1121.44		
								4	1.14	1.14	1121.44	1122.58		
								CC (NS)	0.03	0.03	1122.58	1122.61		All to PAL
								Totals:	5.41	5.41				

Table T2 (continued).

Core	Date (Sep 2000)	Time (local)	Core depth (mbsf) Top	Core depth (mbsf) Bottom	Length (m) Cored	Length (m) Recovered	Recovery (%)	Section	Length (m) Liner	Length (m) Curated	Section depth (mbsf) Top	Section depth (mbsf) Bottom	Catwalk samples	Comment
54R	23	0110	1126.8	1136.5	9.7	5.66	58.4							
								1	1.50	1.50	1126.80	1128.30		
								2	1.44	0.87	1128.30	1129.17	PAL	
								3	1.40	1.50	1129.17	1130.67	PAL	
								4	1.19	1.46	1130.67	1132.13		
								5	0.13	1.00	1132.13	1133.13		
								Totals:	5.66	6.33				
55R	23	0745	1136.5	1146.1	9.6	3.67	38.2							
								1	0.26	1.25	1136.50	1137.75		
								2	1.50	1.39	1137.75	1139.14		
								3	1.43	1.39	1139.14	1140.53		
								4	0.48	0.62	1140.53	1141.15		
								Totals:	3.67	4.65				
56R	23	1215	1146.1	1151.0	4.9	3.32	67.8							
								1	0.37	1.35	1146.10	1147.45		
								2	1.45	1.48	1147.45	1148.93		
								3	1.50	0.87	1148.93	1149.80		
								Totals:	3.32	3.70				
57R	23	1725	1151.0	1155.8	4.8	3.80	79.2							
								1	0.25	1.45	1151.00	1152.45		
								2	1.21	1.50	1152.45	1153.95		
								3	1.03	0.79	1153.95	1154.74		
								4	1.31	0.00				
								Totals:	3.80	3.74				
58R	23	2245	1155.8	1160.6	4.8	3.73	77.7							
								1	1.03	1.42	1155.80	1157.22		
								2	0.92	1.39	1157.22	1158.61		
								3	0.87	1.2	1158.61	1159.81		
								4	0.91	0.00				
								Totals:	3.73	4.01				
59R	25	1140	1160.6	1166.5	5.9	2.91	49.3							
								1	0.48	1.45	1160.6	1162.05		
								2	1.09	1.39	1162.05	1163.44		
								3	1.34	0.00				
								Totals:	2.91	2.84				
60R	25	1910	1166.5	1176.1	9.6	2.39	24.9							
								1	0.17	1.48	1166.50	1167.98		
								2	1.06	1.31	1167.98	1169.29		
								3	1.16	0.00				
								Totals:	2.39	2.79				
61R	25	2335	1176.1	1181.0	4.9	2.18	44.5							
								1	1.11	1.38	1176.10	1177.48		
								2	1.07	0.77	1177.48	1178.25		
								Totals:	2.18	2.15				

Table T2 (continued).

Core	Date (Sep 2000)	Time (local)	Core depth (mbsf) Top	Core depth (mbsf) Bottom	Length (m) Cored	Length (m) Recovered	Recovery (%)	Section	Length (m) Liner	Length (m) Curated	Section depth (mbsf) Top	Section depth (mbsf) Bottom	Catwalk samples	Comment
62R	26	0450	1181.0	1185.8	4.8	3.33	69.4							
								1	0.96	1.40	1181.00	1182.40		
								2	1.16	1.50	1182.40	1183.90		
								3	1.21	0.64	1183.90	1184.54		
								Totals:	3.33	3.54				
63R	26	0955	1185.8	1190.6	4.8	1.75	36.5							
								1	0.59	1.40	1185.80	1187.20		
								2	1.16	0.30	1187.20	1187.50		
								Totals:	1.75	1.70				
64R	26	1450	1190.6	1195.4	4.8	2.84	59.2							
								1	0.81	1.40	1190.60	1192.00		
								2	1.07	1.40	1192.00	1193.40		
								3	0.96	0.00				
								Totals:	2.84	2.80				
65R	26	2215	1195.4	1200.1	4.7	3.82	81.3							
								1	0.63	1.40	1195.40	1196.80		
								2	1.06	1.36	1196.80	1198.16		
								3	1.02	1.04	1198.16	1199.20		
								4	1.11	0.00				
								CC	0.00	0.00				
								Totals:	3.82	3.80				
66R	27	0455	1200.1	1204.9	4.8	3.32	69.2							
								1	1.31	1.40	1200.10	1201.50		
								2	0.89	1.44	1201.50	1202.94		
								3	1.12	0.61	1202.94	1203.55		
								Totals:	3.32	3.45				
67R	27	1120	1204.9	1209.7	4.8	4.51	94.0							
								1	0.69	1.45	1204.90	1206.35		
								2	1.20	1.49	1206.35	1207.84		
								3	1.34	1.40	1207.84	1209.24		
								4	1.28	0.00				
								Totals:	4.51	4.34				
68R	27	1255	1209.7	1211.1	1.4	0.47	33.6							
								1	0.47	0.46	1209.70	1210.16		
								Totals:	0.47	0.46				
				Coring totals:	583.8	260.69	44.65							

Notes: CC = core catcher, NS = not stored. PAL = paleontology. This table is also available in **ASCII format.**

Table T3. Lithologic units with depth interval, distinguishing characteristics, and main sediment facies, Hole 1183A.

Core, section, interval (cm)	Depth interval (mbsf)	Unit/Subunit	Distinguishing characteristic	Stage/Epoch	Main sediment facies	Other characteristic features
192-1183A-						
2R-1, 0, to 24R-1, 43	328.00-838.63	I	Ooze to chalk	Oligocene to Miocene	Foraminifer nannofossil chalk	
2R-1, 0, to 3R-1, 0	328.00-337.60	IA	Ooze	middle Miocene	Foraminifer nannofossil ooze	
3R-1, 0, to 14R-CC, 33	337.60-444.83	IB	Chalk	early and middle Miocene	Foraminifer nannofossil chalk	Upper limit to significant volcanic ash is located within the 300-m noncored interval.
15R-1, 0, to 24R-1, 43	752.00-838.60	IC	Ash beds within chalk	Oligocene	Nannofossil foraminifer chalk with volcanic ash layers	
24R-1, 43, to 39R-4, 15	838.60-986.65	II	Limestone	Paleocene-Eocene	Chert-rich limestone and limestone with zeolitic chalk	
24R-1, 43, to 36R-4, 71	838.60-958.26	IIA	Chert	Eocene	Nannofossil foraminifer limestone and chert	Low recovery.
36R-4, 71, to 39R-4, 15	958.26-986.65	IIB	Zeolite-rich bands	Paleocene	Foraminifer limestone and zeolitic chalk	Chertification is common but minor.
39R-4, 15, to 54-3, 120	986.65-1130.37	III	Limestone	Aptian-Maastrichtian		
39R-4, 15, to 50R-1, 60	986.65-1088.80	IIIA	White limestone	Campanian-Maastrichtian	Nannofossil foraminifer limestone	Chertification is common but minor. Color cycles range from white to yellowish in Cores 45R-49R.
50R-1, 60, to 54R-3, 120	1088.80-1130.37	IIIB	Mottled gray and pinkish white limestone	Aptian-Albian and Santonian-Coniacian	Nannofossil limestone	Upper 1.7 m is condensed. Cores 53R and 54R contain ferruginous calcareous claystone intervals and vitric tuff interbeds.
54R-3, 120, to base of hole	1130.37-1211.10	Basement	Basalt flows with rare beds of ferruginous micrite limestone	early Aptian	Basalt	Limestone interbeds are partially recrystallized and light yellowish brown.

Table T4. Inorganic carbon, $CaCO_3$ contents, and mineral components by X-ray diffraction of sediments, Hole 1183A. (**See table note.** Continued on next page.)

Core, section, interval, (cm)	Depth (mbsf)	Subunit	Lithology	Inorganic carbon (wt%)	$CaCO_3$ (wt%)	Mineral components (by XRD)
192-1183A-						
2R-1, 23	328.23	IA	Chalk	11.27	93.85	Calcite
3R-1, 25	337.85	IB	Chalk	11.14	92.77	Calcite
4R-2, 18	348.88	IB	Chalk	11.03	91.88	Calcite
5R-3, 48	360.28	IB	Chalk	10.93	91.07	Calcite
6R-1, 64	366.94	IB	Chalk	10.92	90.98	Calcite
7R-1, 33	376.23	IB	Chalk	11.08	92.30	Calcite
8R-1, 84	386.34	IB	Chalk	11.02	91.80	Calcite
9R-1, 25	395.35	IB	Chalk	11.23	93.53	Calcite
10R-1, 85	405.55	IB	Chalk	10.71	89.23	Calcite
10R-1, 145	406.15	IB	Chalk	11.43	95.23	Calcite
10R-2, 45	406.65	IB	Chalk	NA	NA	Calcite
10R-2, 131	407.51	IB	Chalk	11.27	93.85	Calcite
11R-5, 62	420.92	IB	Chalk	11.31	94.24	Calcite
12R-3, 45	427.35	IB	Chalk	11.44	95.32	Calcite
13R-3, 10	436.60	IB	Chalk	11.34	94.45	Calcite
14R-CC, 9	444.59	IB	Chalk	11.00	91.66	Calcite
15R-1, 86	752.86	IC	Chalk	11.19	93.19	Calcite
16R-1, 46	761.56	IC	Chalk	11.05	92.06	Calcite
17R-2, 13	772.43	IC	Chalk	11.39	94.90	NA
17R-2, 80	773.10	IC	Chalk	10.74	89.49	Calcite
18R-3, 15.5	783.66	IC	Chalk	11.25	93.69	Calcite
19R-2, 83	792.43	IC	Chalk	11.27	93.87	Calcite
19R-4, 19	794.79	IC	Chalk, volcanic ash	5.91	49.26	Calcite, anorthite (minor); contains volcanic glass?
20R-1, 131	801.01	IC	Chalk	10.83	90.20	Calcite
20R-3, 6	802.26	IC	Chalk	11.11	92.58	Calcite
21R-4, 112	814.92	IC	Chalk	10.82	90.10	Calcite
22R-CC, 0	827.84	IC	Chalk	10.77	89.70	Calcite
23R-6, 68	836.78	IC	Chalk	11.43	95.20	Calcite
24R-1, 62	838.82	IIA	Limestone	11.40	94.98	Calcite
24R-CC, 6	841.12	IIA	Limestone	11.37	94.72	Calcite
25R-CC, 6	849.14	IIA	Limestone	11.63	96.91	Calcite
26R-CC, 14	857.14	IIA	Limestone	11.60	96.66	Calcite
27R-CC, 18	866.78	IIA	Limestone	11.53	96.06	Calcite
30R-1, 40	895.90	IIA	Limestone	11.70	97.48	Calcite
31R-1, 27	905.37	IIA	Limestone	11.62	96.77	Calcite
32R-1, 77	915.47	IIA	Limestone	11.70	97.46	Calcite
33R-1, 41	924.71	IIA	Limestone	11.65	97.01	Calcite
34R-1, 71	934.61	IIA	Limestone	11.87	98.88	Calcite
35R-1, 97	944.47	IIA	Limestone	11.84	98.65	Calcite
36R-2, 61	955.16	IIA	Limestone	11.86	98.80	Calcite
36R-4, 87	958.42	IIA	Limestone	11.70	97.45	Calcite
37R-1, 103	963.73	IIB	Limestone	11.72	97.64	NA
37R-4, 67	967.84	IIB	Limestone	11.38	94.82	Calcite
38R-6, 15	980.05	IIB	Limestone	11.31	94.25	Calcite
39R-3, 45	985.45	IIB	Limestone	11.55	96.24	Calcite
40R-1, 39	992.09	IIIA	Limestone	12.08	100.65	Calcite
40R-3, 57	995.22	IIIA	Limestone	11.83	98.56	NA
41R-1, 74	1002.14	IIIA	Limestone	11.85	98.74	Calcite
42R-2, 28	1012.88	IIIA	Limestone	11.72	97.59	Calcite
43R-1, 98	1021.78	IIIA	Limestone	11.67	97.24	Calcite
45R-2, 19	1041.69	IIIA	Limestone	11.87	98.85	Calcite
45R-2, 95	1042.45	IIIA	Limestone	11.47	95.54	Calcite
46R-1, 42	1050.02	IIIA	Limestone	11.71	97.52	Calcite
47R-1, 21	1059.41	IIIA	Limestone	11.87	98.86	Calcite
48R-1, 9	1068.89	IIIA	Limestone	11.88	98.99	Calcite
49R-CC, 14	1078.64	IIIA	Limestone	11.86	98.79	Calcite
50R-1, 138	1089.58	IIIB	Limestone	8.41	70.07	Calcite, illite, or quartz (volcanic ash)
50R-2, 81	1090.51	IIIB	Limestone	11.48	95.64	Calcite
50R-2, 113	1090.83	IIIB	Limestone	11.69	97.35	Calcite
50R-3, 32	1091.52	IIIB	Limestone	11.36	94.63	Calcite
51R-3, 13	1101.03	IIIB	Limestone	11.45	95.36	Calcite
52R-1, 140	1108.90	IIIB	Limestone	10.50	87.43	Calcite
52R-4, 117	1113.17	IIIB	Limestone	11.25	93.75	Calcite
53R-2, 83	1119.50	IIIB	Brown claystone	11.45	95.37	Calcite, goethite, nontronite
53R-4, 49	1121.93	IIIB	Limestone	NA	NA	Calcite
53R-4, 84	1122.28	IIIB	Brown claystone	4.91	40.88	NA

Table T4 (continued).

Core, section, interval, (cm)	Depth (mbsf)	Subunit	Lithology	Inorganic carbon (wt%)	$CaCO_3$ (wt%)	Mineral components (by XRD)
53R-4, 87	1122.31	IIIB	Limestone	11.38	94.79	NA
54R-1, 48	1127.28	IIIB	Brown claystone	1.58	13.14	Calcite, goethite (greater peak area than in 53R-2 sample), nontronite
54R-1, 66	1127.46	IIIB	Limestone	11.59	96.54	Calcite
54R-2, 29	1128.59	IIIB	Limestone	11.25	93.69	Calcite
54R-3, 26	1129.43	IIIB	Vitric tuff	NA	NA	Glauconite, anorthite, diopside, sanidine, orthoclase, magnetite, etc.; several peaks were not interpreted
54R-3, 78	1129.95	IIIB	Vitric tuff	NA	NA	Glauconite, anorthite, sanidine, diopside, orthoclase, magnetite, etc.; several peaks were not interpreted
55R-1, 9	1136.59	Basement	Limestone	11.33	94.40	Calcite
60R-1, 84	1167.34	Basement	Limestone	NA	NA	Calcite, glauconite

Note: XRD = X-ray diffraction, NA = not analyzed.

Table T5. Depth-age summary of Cretaceous stages and Cenozoic epochs, Hole 1183A.

Depth (mbsf)	Stage/Epoch
330.79-432.10	middle Miocene
439.97-444.78	lower Miocene
Core gap	
757.14-761.98	upper Oligocene
773.73-838.95	lower Oligocene
839.95-857.06	upper Eocene
866.69-924.40	middle Eocene
927.36-936.99	lower Eocene
943.91-982.37	middle-upper Paleocene
985.00-987.37	lower Paleocene
987.40-1040.56	Maastrichtian
1042.71-1089.90	Campanian
1090.05-1090.30	Santonian
1090.35-1090.44	upper Coniacian
1090.48-1108.29	upper Albian
1111.57-1121.12	lower Albian
1121.40-1128.64	upper Aptian
1130.13-1130.74	lower Aptian

Note: This table is also available in **ASCII format.**

Table T6. Summary of depths and estimated duration of unconformities, Hole 1183A.

Depth (mbsf)	Core, section, interval (cm)	Estimated age (Ma)	Duration (m.y.)	Stage/Epoch
419.56-422.40	R-4, 76 to 11R-6, 60	12.7(13.9)-(15.7)16.4	1.8-3.7	middle Miocene
757.14-761.98	15R-CC to 16R-CC	23.80-27.50	3.70	upper Oligocene
924.4-927.36	33R-1, 10 to 33R-3,10	49.70-50.60	0.90	middle/lower Eocene boundary
982.37-985.00	39R-1, 37 to 39R-3, 125	61.0-64.80	3.80	upper/lower Paleocene
987.33-987.40	39R-4, 87 to 39R-4, 100	65.0-68.2	3.20	Cretaceous/Paleogene boundary
1031.28-1040.56	44R-CC to 45R-1, 56	69.73-70.07	0.34	upper/lower Maastrichtian
1050.50-1051.22	46R-1, 100 to 46R-2, 22	72.70-74.00	1.30	upper Campanian
1089.90-1090.05	50R-2,20 to 50R-2, 35	83.17-83.90	0.63	Campanian/Santonian boundary
1090.44-1090.48	50R-2, 74 to 50R-2, 78	86.50-99.75	13.25	upper Coniacian/upper Albian
1110.05-1111.57	52R-2, 105 to 52R-3, 107	100.5-111.1	10.60	upper/lower Albian
1128.61-1128.64	54R-2, 31 to 54R-2, 35	116.2-116.75	0.55	upper Aptian

Notes: Ages in parentheses indicate an apparent discrepancy between calcareous nannofossil and planktonic foraminifer datums. This table is also available in **ASCII format.**

Table T7. List of Cenozoic planktonic foraminifer and calcareous nannofossil lowest, highest, and highest common occurrences, Hole 1183A. (See table notes. Continued on next page.)

Core, section, interval (cm)	Event	Species	Epoch	Zone	Depth (mbsf)	Age (Ma)
192-1183A-						
2R-CC	LCO	*D. kugleri*	middle Miocene	NN7	330.79	11.79
2R-CC	HO	*F. fohsi robusta*	middle Miocene	M9b	330.79	11.80
3R-CC	HO	*C. floridanus*	middle Miocene	NN7	340.82	11.50
3R-CC	HO	*F. fohsi lobata*	middle Miocene	M9b	340.82	11.90
3R-CC	LO	*D. kugleri*	middle Miocene	NN7	340.82	11.83
4R-CC	HO	*C. nitesecens*	middle Miocene	NN6	354.09	12.10
5R-CC	LO	*F. fohsi robusta*	middle Miocene	M9a	365.41	12.30
6R-CC	HO	*T. serratus*	middle Miocene	NN6	371.00	12.67
6R-CC	LO	*F. fohsi lobata*	middle Miocene	M8	371.00	12.50
7R-CC	LO	*T. rugosus*	middle Miocene	NN6	380.13	13.15
8R-CC	HO	*S. heteromorphus*	middle Miocene	NN5	391.98	13.52
9R-CC	HO	*H. waltrans*(?)	middle Miocene	NN5	397.93	13.95
11R-4, 76	LO	*G. fohsi fohsi*	middle Miocene	M7	419.56	12.70
11R-6, 60	HO	*P. sicanus*	middle Miocene	M4b	422.40	16.40
12R-CC	HO	*D. deflandrei* (5 ray)	middle Miocene	NN4	432.10	15.70
12R-CC	HCO	*D. deflandrei*	middle Miocene	NN4	432.10	16.15
13R-CC	LO	*P. sicanus*	lower Miocene	M4b	439.97	16.70
13R-CC	LO	*C. premacintyrei*	lower Miocene	NN4	439.97	17.07
14R-CC	HO	*D. drugii*(?)	lower Miocene	NN4	444.78	17.32
14R-CC	LO	*F. birnageae*	lower Miocene	M4a	444.78	17.30
15R-CC	HO	*C. fenestratus*	lower Miocene	NN1	757.14	23.65
15R-CC	LO	*G. praedehiscens*	upper Oligocene	P22	757.14	23.80
16R-CC	HO	*S. ciperoensis*	upper Oligocene	NP24	761.98	23.80
16R-CC	HO	*S. distentus*	upper Oligocene	NP23	761.98	27.50
16R-CC	HO	*S. predistentus*	upper Oligocene	NP23	761.98	27.50
16R-CC	LO	*P. opima opima*	upper Oligocene	P21	761.98	29.40
16R-CC	LO	*G. angulisuturalis*	upper Oligocene	P21	761.98	29.40
16R-CC	LO	*S. ciperoensis*	upper Oligocene	NP23	761.98	29.90
17R-CC	HO	*S. pseudoradians*	lower Oligocene	NP23	773.73	29.10
17R-CC	LO	*S. distentus*	lower Oligocene	NP23	773.73	31.50
18R-CC	HO	*L. minutus*	lower Oligocene	NP23	786.96	31.37
19R-CC	HO	*G. angiporoides*	lower Oligocene	P20	796.57	29.90
23R-CC	HO	*P. micra*	lower Oligocene	P18	838.79	32.00
23R-CC	HO	*R. umbilica*	lower Oligocene	NP22	838.79	32.30
23R-CC	HO	*R. hillae*	lower Oligocene	NP22	838.79	32.30
24R-1, 75	HO	*E. formosa*	lower Oligocene	NP21	838.95	32.80
24R-2, 25	HO	*D. saipanensis*	upper Eocene	NP20	839.95	34.20
24R-2, 114	HO	*H. primitiva*	upper Eocene	P17	840.84	33.70
24R-2, 114	HO	*D. barbadiensis*	upper Eocene	NP20	840.84	34.30
24R-2, 114	HO	*C. consuetus*	upper Eocene	NP19	840.84	
24R-CC	HO	*T. cerroazulensis*	upper Eocene	P17	840.99	33.80
25R-1, 56	HO	*C. reticulata*	upper Eocene	NP19	847.96	35.00
25R-2, 1	HO	*S. intercalaris*	upper Eocene	NP18	848.45	
26R-CC	HO	*G. index*	upper Eocene	P15	857.06	34.30
26R-CC	HO	*H. lophota*	upper Eocene	NP18	857.06	
27R-CC	HO	*C. grandis*	middle Eocene	NP17	866.69	37.10
27R-CC	LO	*D. bisectus*	middle Eocene	NP17	866.69	38.00
27R-CC	LO	*S. intercalaris*	middle Eocene	NP17	866.69	
28R-CC	HO	*C. solitus*	middle Eocene	NP16	876.36	40.40
29R-CC	LO	*C. reticulatus*	middle Eocene	NP16	886.00	42.00
29R-CC	HO	*S. furcatolithoides*	middle Eocene	NP16	886.00	
29R-CC	LO	*R. umbilica*	middle Eocene	NP16	886.00	43.70
30R-1, 17	HO	*S. spiniger*	middle Eocene	NP15	895.97	
30R-2	HO	*C. gigas*	middle Eocene	NP15	897.12	44.50
31R-1, 31	LO	*G. pomeroli*	middle Eocene	P12	905.41	42.40
32R-1, 19	LO	*C. gigas*	middle Eocene	NP15	914.89	46.10
32R-1, 19	LO	*S. furcatolithoides*	middle Eocene	NP15	914.89	
32R-CC	HO	*A. soldadoensis*	lower Eocene	P9	916.28	49.00
32R-CC	LO	*S. spiniger*	middle Eocene	NP15	916.28	
32R-CC	LO	*N. fulgens*	middle Eocene	NP15	916.28	47.30
33R-1, 10	HO	*D. lodoensis*	middle Eocene	NP14	924.40	
33R-1, 10	HO	*D. kuepperi*	middle Eocene	NP14	924.40	
33R-1, 10	LO	*D. sublodoensis*	middle Eocene	NP14	924.40	49.70
33R-3, 10	HO	*T. crassus*	lower Eocene	NP13	927.36	
33R-3, 10	HO	*T. occultatus*	lower Eocene	NP13	927.36	

Table T7 (continued).

Core, section, interval (cm)	Event	Species	Epoch	Zone	Depth (mbsf)	Age (Ma)
33R-3, 10	HO	*T. orthostylus*	lower Eocene	NP12	927.36	50.60
33R-3, 21	LO	*P. palmerae*	lower Eocene	P9	927.47	50.40
33R-CC	HO	*D. salisburgensis*	lower Eocene	NP12	928.62	
33R-CC	HO	*S. editus*	lower Eocene	NP12	928.62	
34R-1, 24	HO	*S. anarrhopus*	lower Eocene	NP11	934.14	
34R-3, 17	HO	*S. primus*	lower Eocene	NP11	936.60	
34R-3, 17	HO	*D. multiradiatus*	lower Eocene	NP11	936.60	
34R-3, 17	HO	*C. eodela*	lower Eocene	NP10	936.60	
34R-3, 56	LO	*T. orthostylus*	lower Eocene	NP10	936.99	53.64
35R-2, 48	HO	*middle velascoensis*	upper Paleocene	P5	943.91	54.70
35R-2, 48	HO	*F. tympaniformis*	upper Paleocene	NP9	943.91	55.33
36-4, 88	LO	*middle marginodentata*	upper Paleocene	P5	958.43	54.80
36R-CC	LO	*D. multiradiatus*	upper Paleocene	NP9	958.67	56.20
37R-3, 19	LO	*H. kleinpellii*	middle Paleocene	NP6	965.89	58.40
37R-3, 19	LO	*S. anarrhopus*	middle Paleocene	NP6	965.89	58.40
37-4, 17	HO	*G. pseudomenardii*	upper Paleocene	P4	967.34	55.90
38-3, 68	HO	*middle angulata*	upper Paleocene	P4a	976.08	57.10
38-3, 68	LO	*G. pseudomenardii*	upper Paleocene	P4	976.08	59.20
38R-3, 59	LO	*F. tympaniformis*	middle Paleocene	NP5	975.99	59.70
38R-3, 59	LO	*C. consuetus*	middle Paleocene	NP5	975.99	59.70
38R-3, 59	LO	*S. primus*	middle Paleocene	NP4	975.99	60.60
38-6, 15	LO	*I. albeari*	middle Paleocene	P3b	980.05	60.00
38R-CC	LO	*C. danicus*	lower Paleocene	NP3	980.37	63.80
38R-CC	LO	*C. intermedius*	lower Paleocene	NP2	980.37	64.50
39-1, 37	LO	*middle angulata*	upper Paleocene	P3a	982.37	61.00
39R-3, 125	LO	*C. primus*	lower Paleocene	NP1	985.00	64.80
39R-4, 9	LO	*middle pseudobulloides*	lower Paleocene	P1a	986.59	64.90
39R-4, 87	HO	*H. holmsdelensis*	lower Paleocene	P0	987.33	64.97

Notes: LCO = lowest common occurrence, HCO = highest common occurrence, HO = highest occurrence, LO = lowest occurrence, shaded = planktonic foraminifer, unshaded = calcareous nannofossil. Ages are from Berggren et al. (1995). This table is also available in **ASCII format.**

Table T8. List of Cretaceous planktonic foraminifer and calcareous nannofossil highest, lowest, and lowest common occurrences, Hole 1183A.

Event	Species	Stage	Core, section, interval (cm)	Zone/Subzone	Depth (mbsf)	Age (Ma)
HO	*M. mura*	upper Maastrichtian	39R-4, 100	CC25B	987.40	68.66
HO	*G. fornicata*	upper Maastrichtian	40R-3, 58	*Gansseri*	995.23	68.01
LO	*C. gallica*	upper Maastrichtian	41R-1, 55	CC25B	1001.95	68.66
HO	*R. pennyi*	upper Maastrichtian	41R-CC	*Gansseri*	1004.26	68.20
LO	*G. gansseri*	upper Maastrichtian	41R-CC	*Gansseri*	1004.26	71.37
LO	*M. praemura*	upper Maastrichtian	43R-1, 62	CC25B	1021.42	69.16
HO	*S. biarcus* (closed)	upper Maastrichtian	43R-1, 62	CC25B	1021.42	69.20
HO	*G. bicrescenticus*	upper Maastrichtian	43R-CC	CC25B	1022.08	68.33
LO	*S. biarcus* (elliptical)	upper Maastrichtian	43R-CC	CC25B	1022.08	69.73
LO	*R. subpennyi*	lower Maastrichtian	43R-CC	*Aegyptiaca*	1022.08	?
LO	*Cribcrocorona* spp.	upper Maastrichtian	44R-CC	CC25A	1031.28	?
HO	*U. trifidum*	lower Maastrichtian	45R-1, 56	CC24	1040.56	70.07
HO	*U. gothicum*	lower Maastrichtian	45R-1, 56	CC24	1040.56	70.07
HO	*Q. gartneri*	lower Maastrichtian	45R-1, 56	CC24	1040.56	70.40
LO	*P. excolata*	upper Campanian	45R-3, 1	*Aegyptiaca*	1042.71	72.70
HO	*R. elegans*	upper Campanian	46R-2, 22	CC22B	1051.22	74.00
HO	*A. cymbiformis* var. NT	upper Campanian	46R-2, 22	CC22B	1051.22	74.60
HO	*Tranolithus* sp. 1	upper Campanian	46R-2, 22	CC22B	1051.22	74.60
LO	*R. levis*	upper Campanian	47R-CC	CC22B	1060.70	74.72
LO	*G. ventricosa*	upper Campanian	47R-CC	*Ventricosa*	1060.70	77.60
LO	*P. costulata*	upper Campanian	47R-CC	*Elevata*	1060.70	79.10
LO	*U. trifidum*	upper Campanian	48R-1, 49	CC22A	1069.29	75.30
HO	*A. parcus parcus*	upper Campanian	48R-2, 49	CC 21	1070.79	75.18
HO	*B. bevieri*	upper Campanian	48R-2, 49	CC 21	1070.79	75.20
HO	*W. fossacincta*	upper Campanian	48R-2, 49	CC 21	1070.79	76.03
HO	*E. eximius*	upper Campanian	49R-CC	CC 21	1078.66	76.33
HO	*C. ovalis*	upper Campanian	49R-CC	CC 21	1078.66	77.15
LO	*U. gothicum*	upper Campanian	49R-CC	CC 21	1078.66	77.20
LO	*B. magnus*	upper Campanian	49R-CC	CC 21	1078.66	77.18
HO	*B. hayii*	lower Campanian	50R-1, 88	CC19A	1089.08	78.90
HO	*C. crassus*	lower Campanian	50R-1, 112	CC18	1089.32	80.70
HO	*M. furcatus*	lower Campanian	50R-1, 112	CC18	1089.32	81.24
LO	*A. parcus constrictus*	lower Campanian	50R-2, 20	CC18	1089.90	82.42
LO	*A. parcus parcus*	lower Campanian	50R-2, 20	CC18	1089.90	83.17
LO	*C. crassus*	upper Santonian	50R-2, 35	KN24	1090.05	83.90
HO	*Q. enebrachium*	lower Santonian	50R-2, 60	KN25	1090.30	85.27
HO	*E. floralis*	upper Coniacian	50R-2, 68	KN28	1090.38	86.20
LO	*M. cubiformis*	upper Coniacian	50R-2, 74	KN28	1090.44	86.50
LO	*M. staurophora*	middle Coniacian	50R-2, 74	KN28	1090.44	86.92
LO	*M. furcatus*	lower Coniacian	50R-2, 74	KN28	1090.44	89.03
HO	*M. chiastius*	upper Cenomanian	50R-2, 78	NC10A	1090.48	93.48
HO	*G. bentonensis*	upper Cenomanian	50R-2, 78	*Archaeocretacea*	1090.48	93.50
HO	*A. infracretacea*	upper Albian	50R-2, 78	NC10A	1090.48	99.75
LO	*R. appenninica*	upper Albian	50R-CC	*Oppenninica*	1091.78	?
LO	*E. turriseiffelii*	upper Albian	51R-CC	NC10A	1101.59	100.00
HO	*H. irregularis*	upper Albian	52R-1, 79	NC9B	1108.29	100.02
TR	*C. burwellensis*	upper Albian	52R-1, 79	NC9B	1108.29	100.53
HO	*C. erbae*	Aptian/Albian boundary	52R-3, 107	NC8A	1111.57	112.20
LO	*H. rischi*	lower Albian	52R-CC	*Rischi*	1113.38	110.06
LO	*P. columnata*	base Albian	53R-3, 21	NC8A	1120.38	112.03
HO	*G. barri*	base Albian	53R-3, 21	*Cheniourensis*	1121.12	112.03
LO	*H. trochoidea*	upper Aptian	53R-3, 95	*Gorbachikae*	1121.40	?
LCO	*R. achlyostaurion*	upper Aptian	54R-2, 5	NC7C	1128.35	?
LO	*G. algerianus*	upper Aptian	54R-2, 31	*Algerianus*	1128.61	116.20
HO	*L. salomonii*	upper Aptian	54R-2, 35	NC7A	1128.64	116.75
HO	*L. cabri*	top lower Aptian	54R-3, 96	*Cabri*	1130.13	117.00
LO	*E. floralis*	top lower Aptian	54R-3, 119	NC7A	1130.36	118.10
LO	*R. gallagheri*	middle lower Aptian	54R-3, 119	NC7A	1130.36	120.78
HO	*P. sigali*	middle lower Aptian	54R-4, 7	*Cabri*	1130.74	?

Notes: HO = highest occurrence, LO = lowest occurrence, LCO = lowest common occurrence. Shaded = planktonic foraminifer, unshaded = calcareous nannofossil. ? = uncertain age assignment. Ages are from University of Utah Paleontology Database and calibrated to the Gradstein et al. (1995) timescale. This table is also available in **ASCII format.**

Table T9. Relative (qualitative) paleobathymetric trend for Hole 1183A from the middle Cretaceous through lower Paleogene.

Core, section	Stage/Epoch	Depth (mbsf)	Age (Ma)	Mid shelf	Outer shelf	Upper slope	Middle slope	Lower slope	Abyssal
192-1183A-									
29R-CC	middle Eocene	886.00	40.50						■
32R-CC	middle Eocene	916.00	48.00						■
33R-CC	early Eocene	929.00	50.60					■	■
38R-3	late Paleocene	976.00	57.10					■	■
39R-1	middle Paleocene	982.00	59.20				■	■	
42R-CC	late Maastrichtian	1015.00	69.00				■		
43R-CC	late Campanian	1022.00	70.00			■	■		
44R-CC	late Campanian	1031.00	71.50			■	■		
45R-CC	late Campanian	1043.00	72.70				■	■	
47R-CC	middle Campanian	1061.00	75.00				■	■	
48R-CC	middle Campanian	1069.00	76.00					■	
49R-CC	middle Campanian	1071.00	77.00					■	
50R-1	early Campanian	1079.00	79.00						■
50R-2	late Coniacian	1091.00	89.00						■
50R-3	late Albian	1101.00	100.00				■	■	
52R-2	late Albian	1111.00	100.50				■	■	
52R-3	middle early Albian	1113.00	110.00			■	■		
53R-3	early Albian	1120.00	112.00			■	■		
53R-3	late Aptian	1122.00	112.30		■	■			
54R-2	late Aptian	1129.00	116.20		■	■			
55R-1	middle Aptian	1136.00	117.00	■	■				

Notes: Dark shading = estimated paleobathymetry range. Absolute age values are approximate, based upon the calibration of calcareous nannofossil and planktonic foraminifer zonations in Berggren et al. (1995). (See **"Biostratigraphy,"** p. 10, in the "Explanatory Notes" chapter.)

Table T10. Basement unit boundaries and curated unit thicknesses, Hole 1183A.

Boundary	Curated depth (mbsf)	Core, section	Piece*	Depth in section (cm)	Unit thickness† (m)	Boundary rationale
		192-1183A-				
Top of basement	1130.37	54R-3	4-5	120		Beginning of basalt flows beneath sediment
1-2A	1130.73	54R-4	1-2	6	0.36	Limestone interbed between flows
2A-2B	1130.75	54R-4	2-3	8	0.02	Pillow basalts beneath limestone
2B-3A	1136.50	55R-1	NA	0	5.75	Limestone interbed between flows
3A-3B	1136.62	55R-1	1-2	12	0.12	Pillow basalts beneath limestone
3B-4A	1138.52	55R-2	5-6	77	1.90	Limestone interbed between flows
4A-4B	1138.60	55R-2	6-7	85	0.08	Pillow basalts beneath limestone
4B-5A	1146.10	56R-1	NA	0	7.50	Recrystallized limestone cobble + hyaloclastite between flows
5A-5B	1146.17	56R-1	1-2	7	0.07	Pillow basalts continue beneath limestone
5B-6	1166.50	60R-1	NA	0	20.33	Presence of hyaloclastite, poor recovery (more fractured rock, top of flow)
6-7	1192.19	64R-2	2-3	19	25.69	Presence of hyaloclastite between flows, pillow basalts beneath
7-8	1208.37	67R-3	7-8	53	16.18	Small piece (<1 cm) of hyaloclastite, pillow basalts beneath

Notes: * = no actual contacts were recovered; boundary locations are inferred between the indicated pieces. † = calculated using curated depths. NA = not applicable because the boundary is between the top of the indicated core and the bottom of the overlying core.

Table T11. Geochemical data for whole-rock samples analyzed by shipboard ICP-AES, Hole 1183A.

	192-1183A-										
Core, section:	54R-3	55R-2	55R-3	55R-4	58R-3	59R-1	60R-1	64R-2	64R-2	65R-3	67R-3
Piece:	5	1A	5B	4	13	7C	19	2	10B	2	16
Interval (cm):	125-127	12-15	128-129	38-39	109-112	107-109	139-141	15-17	136-138	18-19	119-121
Unit/Subunit:	1	3B	4B	4B	5B	5B	6	6	7	7	7
Depth (mbsf):	1130.42	1137.87	1140.42	1140.91	1159.7	1161.67	1167.89	1192.15	1193.36	1198.34	1209.02
Major element (wt%):											
SiO_2	49.66	49.62	50.34	49.49	49.10	49.95	50.00	50.70	49.87	47.92	49.39
TiO_2	1.20	1.11	1.21	1.08	1.12	1.09	1.12	1.08	1.08	1.09	1.10
Al_2O_3	15.54	14.39	15.57	13.81	14.58	14.21	14.33	14.39	13.81	14.75	14.27
Fe_2O_3T	10.92	12.15	9.73	13.69	11.91	12.50	12.58	12.40	13.52	12.11	12.26
MnO	0.16	0.19	0.19	0.24	0.22	0.20	0.23	0.20	0.22	0.22	0.24
MgO	7.35	7.22	8.40	7.31	7.68	7.64	7.94	7.78	7.35	7.50	7.76
CaO	11.63	11.63	11.82	11.70	12.30	12.15	12.36	11.97	11.76	12.46	12.38
Na_2O	2.38	2.19	2.30	2.00	2.15	2.15	2.10	2.07	2.03	2.15	2.10
K_2O	0.43	0.58	0.07	0.46	0.10	BD	0.09	0.10	0.51	BD	0.14
P_2O_5	0.11	0.12	0.12	0.09	BD	BD	BD	BD	0.11	0.17	BD
Total:	99.37	99.18	99.74	99.87	99.16	99.89	100.73	100.69	100.27	98.37	99.64
LOI	2.38	2.18	1.75	0.09	0.30	–0.59	0.09	0.57	0.19	0.29	0.19
Mg#	0.60	0.57	0.66	0.54	0.59	0.58	0.60	0.59	0.55	0.59	0.60
CIPW norms:											
Q	0.0	0.0	0.0	0.0	0.0	0.0	0.0	0.5	0.0	0.0	0.0
Or	2.6	3.5	0.4	2.7	0.6	0.1	0.5	0.6	3.1	0.1	0.8
Ab	20.4	18.8	19.7	17.1	18.5	18.4	17.8	17.5	17.3	18.7	18.0
An	30.9	28.2	32.3	27.7	30.4	29.4	29.5	29.8	27.3	31.4	29.5
Di	22.0	24.4	21.2	25.2	25.9	25.8	26.2	24.4	25.4	24.4	26.7
Hy	14.9	17.1	20.7	19.7	16.0	20.9	18.6	22.8	19.7	13.0	16.5
Ol	4.5	3.3	1.3	2.7	4.2	0.9	3.0	0.0	2.4	6.6	3.9
Il	2.3	2.2	2.3	2.1	2.2	2.1	2.1	2.1	2.1	2.1	2.1
Mt	1.9	2.2	1.7	2.4	2.1	2.2	2.2	2.2	2.4	2.2	2.2
Ap	0.2	0.3	0.3	0.2	0.0	0.0	0.0	0.0	0.2	0.4	0.0
Trace element (ppm):											
Ni	112	88	117	93	—	—	—	—	108	—	—
Cr	215	203	215	198	201	198	197	193	19	219	196
V	343	324	353	317	326	316	322	315	313	331	319
Sc	53	48	55	48	49	50	50	49	48	49	49
Zr	65	56	66	69	68	61	60	57	58	66	59
Y	25	23	23	24	25	24	24	24	24	22	27
Sr	143	124	141	113	120	114	119	113	109	119	115
Ba	10	9	9	10	10	13	12	17	12	12	13

Notes: All analyses were conducted on ignited samples. Fe_2O_3T = total Fe expressed as Fe_2O_3. LOI = weight loss on ignition at 1100°C. BD = below detection limit (0.01% is assumed for norm calculations). Mg# and CIPW norms were calculated assuming 12% of the total iron is Fe^{3+}, which is equivalent to $Fe_2O_3/(Fe_2O_3 + FeO) = 0.13$ or $Fe_2O_3/FeO = 0.15$. — = not determined. This table is also available in **ASCII format.**

Table T12. Average natural remanent magnetization intensity and magnetic susceptibility for each of the sedimentary subunits assuming a log-normal distribution, Hole 1183A.

Subunit	NRM (±σ) (mA/m)	κ (±σ) (10^{-5} SI)
1A	5.52 (–4.64/+29.23)	0.75 (–0.54/+1.95)
1B	0.42 (–0.30/+1.10)	0.46 (–0.29/+0.77)
1C	2.71 (–1.54/+3.58)	8.69 (–5.26/+13.31)
2A	0.25 (–0.17/+0.54)	0.94 (–0.55/+1.31)
2B	1.26 (–0.74/+1.78)	3.28 (–2.05/+5.43)
3A	0.42 (–0.31/+1.20)	0.94 (–0.50/+1.07)
3B	25.68 (–15.92/+41.90)	21.07 (–8.25/+53.82)

Notes: NRM = natural remanent magnetization, κ = magnetic susceptibility. The diamagnetic susceptibility of calcite (-13.8×10^{-6} SI) has been subtracted from all susceptibility measurements.

Table T13. Characteristic remanent magnetization direction, natural remanent magnetization, median destructive field, magnetic susceptibility, and Koenigsberger ratio for selected basalt pieces.

Core, section, piece	Basement unit/ subunit	Dec (°)	Inc (°)	NRM (A/m)	MDF (mT)	κ (10^{-3} SI)	Q-ratio
192-1183A-							
54R-5 (Piece 4)	2B	179.4	–46.1	1.19	11	9.7	4.1
55R-1 (Piece 4)	3B	84.9	–47.2	0.67	13	11.8	1.9
55R-2 (Piece 1)	3B	139.3	–42.5	2.37	17	11.4	7.0
55R-3 (Piece 3)	4B	86.7	–40.9	1.83	16	12.6	4.9
56R-1 (Piece 5)	5B	233.3	–41.5	1.15	10	13.4	2.9
56R-1 (Piece 12)	5B	139.2	–30.5	4.20	6	12.0	11.7
56R-2 (Piece 1)	5B	250.1	–34.8	3.54	6	9.4	12.6
56R-2 (Piece 2)	5B	54.3	–29.9	4.40	9	11.7	12.5
56R-2 (Piece 5)	5B	273.7	–32.0	2.51	11	15.2	5.5
56R-2 (Piece 7)	5B	21.8	–32.2	5.31	16	10.6	16.7
56R-3 (Piece 1)	5B	63.2	–32.4	6.10	16	8.5	24.0
57R-3 (Piece 9)	5B	13.3	–31.0	5.87	7	15.1	12.9
58R-3 (Piece 3)	5B	16.4	–38.6	1.28	25	12.4	3.4
59R-1 (Piece 2)	5B	45.1	–39.8	2.71	12	11.3	8.0
61R-1 (Piece 2)	6	210.1	–35.3	5.63	11	12.4	15.2
62R-2 (Piece 8)	6	8.7	–32.1	2.64	9	13.5	6.5
65R-1 (Piece 3)	7	272.8	–38.7	2.85	6	12.6	7.5
65R-2 (Piece 7)	7	58.7	–33.3	1.45	19	10.2	4.8
65R-3 (Piece 2)	7	124.2	–31.5	4.65	6	14.1	11.0
66R-1 (Piece 5)	7	65.3	–23.9	6.20	6	15.2	13.6
66R-1 (Piece 9)	7	34.8	–18.2	3.48	7	12.1	9.6
66R-3 (Piece 4)	7	14.7	–18.0	6.95	9	10.8	21.5
67R-1 (Piece 2)	7	18.5	–35.5	2.52	10	11.8	7.1
67R-1 (Piece 5)	7	133.0	–41.1	3.20	7	10.6	10.1
67R-2 (Piece 7)	7	270.7	–41.5	2.37	6	14.8	5.3

Notes: Dec = declination, Inc = inclination, NRM = natural remanent magnetization, MDF = median destructive field, κ = magnetic susceptibility, Q-ratio = Koenigsberger ratio. A present-day field of 30 A/m was used for Q-ratio calculations. See **"Paleomagnetism,"** p. 32. This table is also available in **ASCII format.**

Table T14. Index properties data, Hole 1183A. (See table note. Continued on next two pages.)

Core, section, interval (cm)	Depth (mbsf)	Water content (%)		Density (g/cm^3)			Porosity (%)	Void ratio
		Bulk	Dry	Bulk	Dry	Grain		
192-1183A-								
2R-1, 39-41	328.39	37.345	59.603	1.673	1.048	2.689	61.015	1.565
2R-2, 39-41	329.89	37.570	60.179	1.676	1.047	2.718	61.502	1.598
3R-1, 33-35	337.93	38.270	61.997	1.656	1.022	2.682	61.891	1.624
3R-2, 33-35	339.43	40.513	68.104	1.607	0.956	2.625	63.583	1.746
4R-1, 43-45	347.63	38.317	62.119	1.642	1.013	2.625	61.428	1.593
4R-2, 67-69	349.37	40.250	67.365	1.627	0.972	2.698	63.963	1.775
4R-3, 65-67	350.85	40.605	68.365	1.621	0.963	2.693	64.260	1.798
5R-1, 36-38	357.16	36.360	57.134	1.686	1.073	2.674	59.874	1.492
5R-2, 42-44	358.72	37.544	60.112	1.645	1.027	2.589	60.317	1.520
5R-3, 40-42	360.20	37.142	59.088	1.665	1.047	2.644	60.408	1.526
5R-4, 45-47	361.75	37.541	60.104	1.677	1.048	2.721	61.496	1.597
5R-5, 56-58	363.36	36.901	58.481	1.668	1.053	2.639	60.113	1.507
5R-6, 47-49	364.77	40.246	67.351	1.631	0.975	2.716	64.116	1.787
6R-1, 31-33	366.61	38.286	62.037	1.650	1.018	2.656	61.673	1.609
6R-2, 42-44	368.22	38.707	63.151	1.660	1.018	2.733	62.758	1.685
6R-3, 40-42	369.70	36.000	56.250	1.698	1.087	2.698	59.708	1.482
7R-1, 45-47	376.35	35.920	56.054	1.709	1.095	2.734	59.948	1.497
7R-2, 57-59	377.97	36.247	56.856	1.688	1.076	2.674	59.756	1.485
7R-3, 48-50	379.38	35.399	54.797	1.710	1.105	2.702	59.114	1.446
8R-1, 23-25	385.73	34.730	53.209	1.725	1.126	2.714	58.510	1.410
8R-2, 59-61	387.59	34.119	51.789	1.745	1.150	2.747	58.146	1.389
8R-3, 15-17	388.65	33.417	50.189	1.748	1.164	2.709	57.037	1.328
8R-4, 89-91	390.89	37.860	60.927	1.651	1.026	2.635	61.058	1.568
9R-1, 28-30	395.38	34.607	52.921	1.720	1.125	2.688	58.142	1.389
9R-2, 18-20	396.78	33.927	51.348	1.731	1.144	2.683	57.363	1.345
10R-1, 27-29	404.97	35.505	55.052	1.696	1.094	2.656	58.813	1.428
10R-2, 99-101	407.19	34.681	53.094	1.724	1.126	2.705	58.376	1.402
10R-3, 5-7	407.75	34.664	53.054	1.721	1.125	2.694	58.264	1.396
10R-4, 6-8	409.26	32.523	48.198	1.760	1.187	2.692	55.892	1.267
10R-5, 93-95	411.63	34.865	53.528	1.712	1.115	2.674	58.295	1.398
10R-6, 32-34	412.02	33.382	50.110	1.727	1.151	2.634	56.315	1.289
11R-1, 74-76	415.04	32.982	49.214	1.756	1.177	2.709	56.557	1.302
11R-2, 41-43	416.21	32.841	48.901	1.760	1.182	2.712	56.433	1.295
11R-3, 3-5	417.33	32.646	48.470	1.764	1.188	2.714	56.227	1.285
11R-4, 71-73	419.51	34.296	52.199	1.720	1.130	2.667	57.621	1.360
11R-5, 33-35	420.63	35.404	54.809	1.710	1.105	2.703	59.127	1.447
11R-6, 33-35	422.13	34.754	53.266	1.726	1.126	2.719	58.581	1.414
12R-1, 139-141	425.29	34.500	52.672	1.744	1.142	2.769	58.752	1.424
12R-2, 72-74	426.12	37.769	60.692	1.675	1.043	2.729	61.791	1.617
12R-3, 32-34	427.22	39.267	64.655	1.640	0.996	2.682	62.874	1.694
12R-4, 4-6	428.44	35.900	56.005	1.676	1.074	2.603	58.742	1.424
12R-5, 23-25	430.13	39.119	64.255	1.659	1.010	2.760	63.392	1.732
12R-6, 38-40	431.78	36.519	57.528	1.692	1.074	2.708	60.342	1.522
13R-1, 8-10	433.58	38.455	62.482	1.663	1.024	2.728	62.467	1.664
14R-1, 5-7	443.15	33.075	49.420	1.731	1.159	2.628	55.912	1.268
15R-1, 22-24	752.22	26.270	35.629	1.897	1.399	2.724	48.660	0.948
15R-2, 71-73	754.21	24.263	32.036	1.939	1.469	2.717	45.947	0.850
15R-3, 95-97	755.95	25.031	33.389	1.903	1.426	2.667	46.510	0.870
16R-1, 73-75	761.83	21.826	27.920	1.991	1.556	2.703	42.432	0.737
17R-1, 46-48	771.26	27.278	37.509	1.876	1.364	2.726	49.964	0.999
17R-2, 5-7	772.35	26.484	36.024	1.856	1.364	2.623	47.992	0.923
18R-1, 57-59	781.07	24.314	32.125	1.923	1.455	2.677	45.649	0.840
18R-2, 79-81	782.79	26.866	36.736	1.872	1.369	2.691	49.118	0.965
18R-3, 79-81	784.29	26.124	35.362	1.878	1.387	2.662	47.898	0.919
18R-4, 92-94	785.84	23.744	31.137	1.956	1.492	2.729	45.354	0.830
19R-1, 63-65	790.73	27.622	38.163	1.842	1.333	2.651	49.696	0.988
19R-2, 47-49	792.07	27.510	37.951	1.874	1.359	2.737	50.356	1.014
19R-3, 41-43	793.51	28.249	39.371	1.849	1.326	2.707	51.001	1.041
19R-4, 10-12	794.70	26.128	35.369	1.897	1.401	2.715	48.392	0.938
19R-5, 6-8	796.08	29.082	41.007	1.806	1.281	2.629	51.282	1.053
20R-1, 141-143	801.11	27.150	37.269	1.852	1.349	2.650	49.095	0.964
20R-2, 13-15	801.33	23.347	30.457	1.946	1.492	2.681	44.363	0.797
20R-3, 6-8	802.26	26.171	35.449	1.895	1.399	2.713	48.436	0.939
21R-1, 8-10	809.38	23.807	31.246	1.922	1.465	2.648	44.693	0.808
21R-3, 8-10	812.38	26.264	35.618	1.882	1.387	2.682	48.259	0.933
21R-4, 119-121	814.99	26.477	36.012	1.885	1.386	2.703	48.731	0.950

Table T14 (continued).

Core, section, interval (cm)	Depth (mbsf)	Water content (%)		Density (g/cm³)			Porosity (%)	Void ratio
		Bulk	Dry	Bulk	Dry	Grain		
21R-5, 124-126	816.54	26.254	35.600	1.897	1.399	2.722	48.625	0.946
21R-6, 3-5	816.83	26.363	35.801	1.878	1.383	2.676	48.341	0.936
22R-1, 146-148	820.46	24.990	33.316	1.902	1.426	2.662	46.411	0.866
22R-2, 26-28	820.76	25.725	34.634	1.871	1.389	2.621	46.995	0.887
22R-3, 20-22	822.20	24.285	32.075	1.921	1.454	2.671	45.552	0.837
22R-4, 78-80	824.28	24.640	32.696	1.883	1.419	2.595	45.316	0.829
22R-5, 11-13	825.11	23.961	31.511	1.930	1.468	2.676	45.162	0.824
22R-6, 62-64	827.12	26.567	36.179	1.870	1.373	2.667	48.518	0.942
23R-1, 69-71	829.29	26.605	36.250	1.871	1.373	2.671	48.600	0.946
23R-2, 69-71	830.79	29.062	40.968	1.813	1.286	2.651	51.468	1.061
23R-3, 48-50	832.08	29.104	41.052	1.835	1.301	2.721	52.168	1.091
23R-4, 84-86	833.94	32.539	48.234	1.768	1.193	2.721	56.174	1.282
23R-5, 127-129	835.87	28.920	40.686	1.823	1.296	2.671	51.488	1.061
23R-6, 65-67	836.75	28.125	39.130	1.826	1.312	2.631	50.138	1.006
24R-1, 34-36	838.54	29.392	41.628	1.808	1.276	2.652	51.882	1.078
24R-2, 36-38	840.06	28.764	40.378	1.838	1.309	2.706	51.618	1.067
25R-1, 53-55	847.93	27.756	38.419	1.863	1.346	2.720	50.510	1.021
25R-2, 7-9	848.51	26.440	35.944	1.880	1.383	2.688	48.551	0.944
30R-1, 45-47	895.95	20.287	25.450	2.032	1.619	2.710	40.249	0.674
31R-1, 28-30	905.38	18.243	22.314	2.070	1.692	2.680	36.872	0.584
32R-1, 83-85	915.53	18.890	23.290	2.074	1.682	2.725	38.259	0.620
33R-1, 69-71	924.99	17.156	20.709	2.085	1.727	2.654	34.929	0.537
33R-2, 65-67	926.41	16.376	19.583	2.142	1.791	2.725	34.257	0.521
33R-3, 81-83	928.07	15.201	17.926	2.187	1.855	2.746	32.467	0.481
34R-1, 59-61	934.49	10.948	12.294	2.295	2.044	2.708	24.538	0.325
34R-2, 41-43	935.81	13.164	15.160	2.236	1.941	2.724	28.739	0.403
34R-3, 7-9	936.45	12.082	13.743	2.278	2.003	2.739	26.882	0.368
35R-1, 54-56	944.04	12.047	13.697	2.271	1.997	2.726	26.717	0.365
35R-2, 19-21	944.96	12.017	13.658	2.273	2.000	2.727	26.672	0.364
36R-1, 25-27	953.35	13.822	16.038	2.238	1.929	2.764	30.212	0.433
36R-2, 83-85	955.38	11.187	12.596	2.294	2.038	2.719	25.066	0.335
36R-3, 99-101	957.04	12.237	13.943	2.287	2.007	2.762	27.329	0.376
36R-4, 14-16	957.69	12.472	14.249	2.266	1.983	2.739	27.598	0.381
37R-1, 95-97	963.65	11.590	13.109	2.296	2.030	2.743	25.991	0.351
37R-2, 99-101	965.19	12.793	14.669	2.258	1.969	2.742	28.204	0.393
37R-3, 83-85	966.53	15.586	18.464	2.174	1.835	2.742	33.083	0.494
37R-4, 78-80	967.95	12.765	14.633	2.245	1.959	2.720	27.991	0.389
38R-1, 101-103	973.41	7.996	8.691	2.407	2.214	2.727	18.794	0.231
38R-2, 53-55	974.43	8.326	9.082	2.405	2.204	2.740	19.552	0.243
38R-3, 51-53	975.91	9.368	10.336	2.359	2.138	2.727	21.582	0.275
38R-4, 32-34	977.22	6.187	6.595	2.482	2.328	2.739	14.996	0.176
38R-5, 103-105	979.43	7.354	7.938	2.429	2.250	2.726	17.443	0.211
38R-6, 23-25	980.13	10.941	12.284	2.289	2.038	2.698	24.455	0.324
39R-1, 65-67	982.65	5.970	6.349	2.463	2.316	2.705	14.361	0.168
39R-2, 58-60	984.08	10.518	11.755	2.292	2.051	2.683	23.548	0.308
39R-3, 89-91	985.89	5.780	6.135	2.480	2.337	2.718	14.001	0.163
39R-5, 37-39	987.88	11.556	13.066	2.320	2.052	2.779	26.181	0.355
40R-1, 78-80	992.48	11.686	13.233	2.295	2.027	2.747	26.195	0.355
40R-2, 90-92	994.05	15.512	18.360	2.171	1.834	2.732	32.879	0.490
40R-3, 31-33	994.96	14.071	16.375	2.228	1.914	2.758	30.608	0.441
41R-1, 76-78	1002.16	19.778	24.654	2.053	1.647	2.730	39.657	0.657
41R-2, 26-28	1003.16	15.847	18.831	2.142	1.803	2.697	33.155	0.496
42R-1, 112-114	1012.22	13.354	15.412	2.275	1.971	2.802	29.666	0.422
42R-2, 117-119	1013.77	15.818	18.790	2.171	1.828	2.751	33.544	0.505
42R-3, 52-54	1014.62	16.004	19.053	2.164	1.818	2.747	33.820	0.511
43R-1, 67-69	1021.47	18.970	23.411	2.086	1.690	2.755	38.643	0.630
44R-1, 53-55	1030.93	18.007	21.961	2.100	1.722	2.730	36.928	0.585
45R-1, 78-80	1040.78	13.732	15.918	2.224	1.918	2.734	29.821	0.425
45R-2, 80-82	1042.30	14.188	16.534	2.211	1.897	2.735	30.636	0.442
45R-3, 3-5	1042.73	15.094	17.778	2.203	1.871	2.771	32.480	0.481
46R-2, 40-42	1051.40	13.084	15.053	2.239	1.946	2.727	28.613	0.401
47R-1, 62-64	1059.82	15.894	18.897	2.148	1.806	2.710	33.335	0.500
48R-1, 46-48	1069.26	15.235	17.973	2.157	1.828	2.693	32.092	0.473
48R-2, 8-10	1070.38	16.320	19.503	2.163	1.810	2.763	34.479	0.526
50R-1, 84-86	1089.04	13.104	15.080	2.212	1.922	2.681	28.302	0.395
50R-2, 67-69	1090.37	23.481	30.687	1.958	1.498	2.719	44.902	0.815
51R-2, 49-51	1099.89	11.281	12.715	2.311	2.050	2.751	25.460	0.342
52R-1, 48-49	1107.98	10.104	11.239	2.370	2.130	2.780	23.380	0.305
52R-3, 78-79	1111.28	10.667	11.941	2.319	2.072	2.732	24.159	0.319

Table T14 (continued).

Core, section, interval (cm)	Depth (mbsf)	Water content (%)		Density (g/cm³)			Porosity (%)	Void ratio
		Bulk	Dry	Bulk	Dry	Grain		
53R-1, 77-79	1117.97	8.360	9.123	2.380	2.181	2.708	19.434	0.241
54R-1, 88-90	1127.68	7.383	7.972	2.444	2.264	2.748	17.622	0.214
54R-5, 36-38	1132.49	3.158	3.261	2.727	2.641	2.883	8.410	0.092
55R-3, 131-133	1140.45	5.697	6.042	2.611	2.462	2.881	14.527	0.170
56R-3, 18-20	1149.11	4.186	4.369	2.749	2.634	2.968	11.240	0.127
57R-1, 131-133	1152.31	3.903	4.062	2.794	2.684	3.004	10.648	0.119
58R-3, 58-60	1159.19	5.360	5.663	2.689	2.545	2.962	14.076	0.164
59R-1, 60-62	1161.20	1.664	1.692	2.892	2.844	2.984	4.700	0.049
60R-1, 136-138	1167.86	5.138	5.416	2.703	2.564	2.966	13.562	0.157
61R-1, 134-136	1177.44	1.653	1.680	2.858	2.811	2.947	4.613	0.048
62R-1, 63-65	1181.63	1.131	1.144	2.932	2.899	2.996	3.240	0.033
63R-1, 94-96	1186.74	2.665	2.738	2.845	2.769	2.991	7.406	0.080
65R-1, 45-47	1195.85	6.171	6.577	2.670	2.506	2.986	16.092	0.192
66R-3, 12-14	1203.06	5.025	5.291	2.695	2.560	2.950	13.226	0.152
67R-1, 2-4	1204.92	3.578	3.711	2.749	2.650	2.932	9.604	0.106
68R-1, 40-42	1210.10	2.314	2.369	2.934	2.866	3.070	6.631	0.071

Note: This table is also available in **ASCII format.**

Table T15. *P*-wave velocity measured using the contact probe system, Hole 1183A. (See table notes. Continued on next three pages.)

Core, section, interval (cm)	Depth (mbsf)	Direction	Velocity (m/s)	Anisotropy
192-1183A-				
2R-1, 124-126	329.24	Cx	1573.7	
3R-1, 38-40	337.98	Cx	1704.7	0.0275
3R-1, 38-40	337.98	Cz	1658.4	
3R-1, 38-40	337.98	Cy	1692.2	
3R-2, 39-41	339.49	Cx	1653.8	0.0353
3R-2, 39-41	339.49	Cz	1604.6	
3R-2, 39-41	339.49	Cy	1596.6	
4R-1, 79-81	347.99	Cx	1642.6	0.0234
4R-1, 79-81	347.99	Cz	1621.1	
4R-1, 79-81	347.99	Cy	1604.6	
4R-2, 75-77	349.45	Cx	1618.5	0.0225
4R-2, 75-77	349.45	Cz	1582.4	
4R-2, 75-77	349.45	Cy	1601.9	
4R-3, 95-97	351.15	Cx	1626.6	0.0372
4R-3, 95-97	351.15	Cz	1567.5	
4R-3, 95-97	351.15	Cy	1568.6	
4R-4, 75-77	352.45	Cx	1599.9	0.0139
4R-4, 75-77	352.45	Cz	1622.2	
4R-4, 75-77	352.45	Cy	1600.1	
4R-5, 57-59	353.77	Cx	1649.6	0.0360
4R-5, 57-59	353.77	Cz	1602.0	
4R-5, 57-59	353.77	Cy	1591.5	
5R-1, 40-42	357.20	Cy	1669.2	
5R-1, 40-42	357.20	Cx	1727.0	
5R-3, 40-42	360.20	Cx	1679.2	0.0192
5R-3, 40-42	360.20	Cz	1647.3	
5R-3, 40-42	360.20	Cy	1669.4	
5R-4, 45-47	361.75	Cx	1663.2	0.0263
5R-4, 45-47	361.75	Cz	1620.0	
5R-4, 45-47	361.75	Cy	1645.7	
5R-5, 56-58	363.36	Cx	1715.6	0.0563
5R-5, 56-58	363.36	Cy	1636.5	
5R-5, 56-58	363.36	Cz	1622.3	
5R-6, 47-49	364.77	Cx	1739.1	0.0803
5R-6, 47-49	364.77	Cy	1654.2	
5R-6, 47-49	364.77	Cz	1605.3	
6R-1, 31-33	366.61	Cx	1737.8	0.0596
6R-1, 31-33	366.61	Cy	1688.2	
6R-1, 31-33	366.61	Cz	1637.2	
6R-3, 40-44	369.70	Cx	1694.6	0.0467
6R-3, 40-44	369.70	Cy	1617.8	
6R-3, 40-44	369.70	Cz	1624.0	
7R-1, 45-47	376.35	Cx	1773.6	
7R-1, 45-47	376.35	Cz	1737.3	
7R-2, 57-59	377.97	Cx	1671.1	0.0118
7R-2, 57-59	377.97	Cy	1677.6	
7R-2, 57-59	377.97	Cz	1690.9	
7R-3, 48-50	379.38	Cz	1716.5	
7R-3, 48-50	379.38	Cy	1700.9	
8R-1, 23-25	385.73	Cz	1669.6	
9R-1, 28-30	395.38	Cx	1767.7	0.0072
9R-1, 28-30	395.38	Cy	1775.2	
9R-1, 28-30	395.38	Cz	1762.4	
9R-2, 18-20	396.78	Cx	1699.3	0.0136
9R-2, 18-20	396.78	Cy	1680.5	
9R-2, 18-20	396.78	Cz	1676.3	
10R-1, 27-29	404.97	Cx	1776.5	0.0283
10R-1, 27-29	404.97	Cy	1748.0	
10R-1, 27-29	404.97	Cz	1727.0	
10R-2, 99-101	407.19	Cx	1681.2	0.0083
10R-2, 99-101	407.19	Cy	1676.6	
10R-2, 99-101	407.19	Cz	1667.3	
10R-3, 5-7	407.75	Cx	1742.7	0.0491
10R-3, 5-7	407.75	Cy	1675.7	
10R-3, 5-7	407.75	Cz	1659.6	
10R-4, 6-8	409.26	Cx	1713.4	0.0067
10R-4, 6-8	409.26	Cy	1705.8	
10R-4, 6-8	409.26	Cz	1701.9	
10R-5, 93-95	411.63	Cx	1722.0	0.0113
10R-5, 93-95	411.63	Cy	1702.6	
10R-5, 93-95	411.63	Cz	1703.5	
10R-6, 32-34	412.02	Cx	1646.6	0.0136
10R-6, 32-34	412.02	Cy	1624.4	
10R-6, 32-34	412.02	Cz	1627.7	
11R-1, 74-76	415.04	Cx	1823.5	0.0206
11R-1, 74-76	415.04	Cy	1827.1	
11R-1, 74-76	415.04	Cz	1789.8	
11R-2, 41-43	416.21	Cy	1749.1	
11R-2, 41-43	416.21	Cz	1722.2	
11R-3, 3-5	417.33	Cz	1728.9	0.0089
11R-3, 3-5	417.33	Cy	1740.3	
11R-3, 3-5	417.33	Cx	1744.3	
11R-4, 71-73	419.51	Cx	1710.4	0.0149
11R-4, 71-73	419.51	Cy	1685.1	
11R-4, 71-73	419.51	Cz	1686.9	
11R-5, 33-35	420.63	Cx	1737.1	0.0171
11R-5, 33-35	420.63	Cy	1707.7	
11R-5, 33-35	420.63	Cz	1719.5	
11R-6, 33-35	422.13	Cy	1808.6	0.0119
11R-6, 33-35	422.13	Cz	1829.9	
11R-6, 33-35	422.13	Cx	1830.3	
12R-1, 139-141	425.29	Cx	1810.3	0.0189
12R-1, 139-141	425.29	Cy	1783.9	
12R-1, 139-141	425.29	Cz	1776.4	
12R-2, 72-74	426.12	Cx	1789.6	0.0175
12R-2, 72-74	426.12	Cy	1758.7	
12R-2, 72-74	426.12	Cz	1763.2	
12R-3, 32-34	427.22	Cx	1750.9	0.0052
12R-3, 32-34	427.22	Cy	1744.3	
12R-3, 32-34	427.22	Cz	1741.8	
12R-4, 4-6	428.44	Cx	1787.9	0.0087
12R-4, 4-6	428.44	Cy	1777.4	
12R-4, 4-6	428.44	Cz	1772.4	
12R-5, 23-25	430.13	Cx	1677.5	0.0060
12R-5, 23-25	430.13	Cy	1667.5	
12R-5, 23-25	430.13	Cz	1674.6	
12R-6, 38-40	431.78	Cx	1851.0	0.0189
12R-6, 38-40	431.78	Cy	1845.7	
12R-6, 38-40	431.78	Cz	1816.2	
13R-1, 8-10	433.58	Cx	1689.5	0.0207
13R-1, 8-10	433.58	Cy	1686.6	
13R-1, 8-10	433.58	Cz	1654.8	
14R-1, 5-7	443.15	Cx	1792.2	0.0256
14R-1, 5-7	443.15	Cy	1792.6	
14R-1, 5-7	443.15	Cz	1747.1	
15R-1, 22-24	752.22	Cx	2010.5	0.0563
15R-1, 22-24	752.22	Cz	1925.9	
15R-1, 22-24	752.22	Cy	2038.0	
15R-2, 71-73	754.21	Cx	2410.1	0.0526
15R-2, 71-73	754.21	Cz	2302.9	
15R-2, 71-73	754.21	Cy	2428.0	
15R-3, 95-97	755.95	Cx	2397.9	
15R-3, 95-97	755.95	Cy	2394.8	
16R-1, 73-75	761.83	Cx	2529.9	0.0494
16R-1, 73-75	761.83	Cz	2407.0	
16R-1, 73-75	761.83	Cy	2519.6	
17R-1, 45-47	771.25	Cx	1984.8	0.0317
17R-1, 45-47	771.25	Cz	1981.9	
17R-1, 45-47	771.25	Cy	2045.5	
17R-2, 6-8	772.36	Cx	2045.9	0.0416
17R-2, 6-8	772.36	Cz	1962.7	
17R-2, 6-8	772.36	Cy	1987.4	
18R-1, 56-58	781.06	Cx	2302.5	0.0526
18R-1, 56-58	781.06	Cz	2183.7	
18R-1, 56-58	781.06	Cy	2283.6	

Table T15 (continued).

Core, section, interval (cm)	Depth (mbsf)	Direction	Velocity (m/s)	Anisotropy
18R-2, 79-81	782.79	Cx	2072.8	0.0246
18R-2, 79-81	782.79	Cz	2022.2	
18R-2, 79-81	782.79	Cy	2071.9	
18R-3, 79-81	784.29	Cx	2086.5	0.0325
18R-3, 79-81	784.29	Cz	2019.4	
18R-3, 79-81	784.29	Cy	2082.6	
18R-4, 92-94	785.84	Cx	2095.0	0.0598
18R-4, 92-94	785.84	Cz	1995.0	
18R-4, 92-94	785.84	Cy	2118.7	
19R-1, 63-65	790.73	Cx	1985.4	0.0389
19R-1, 63-65	790.73	Cy	1983.9	
19R-1, 63-65	790.73	Cz	1909.1	
19R-2, 47-49	792.07	Cx	2092.7	0.0143
19R-2, 47-49	792.07	Cy	2063.4	
19R-2, 47-49	792.07	Cz	2009.8	
19R-3, 41-43	793.51	Cx	1879.7	0.0212
19R-3, 41-43	793.51	Cy	1875.5	
19R-3, 41-43	793.51	Cz	1840.1	
19R-4, 10-12	794.70	Cx	1935.7	0.0315
19R-4, 10-12	794.70	Cy	1951.6	
19R-4, 10-12	794.70	Cz	1891.0	
19R-5, 6-8	796.08	Cz	1910.0	0.0501
19R-5, 6-8	796.08	Cy	1989.4	
19R-5, 6-8	796.08	Cx	2008.6	
20R-1, 141-143	801.11	Cx	2342.6	0.0597
20R-1, 141-143	801.11	Cy	2320.5	
20R-1, 141-143	801.11	Cz	2205.9	
20R-3, 6-8	802.26	Cx	2301.8	0.0557
20R-3, 6-8	802.26	Cy	2276.5	
20R-3, 6-8	802.26	Cz	2176.4	
21R-1, 8-10	809.38	Cx	2327.1	0.0388
21R-1, 8-10	809.38	Cy	2311.7	
21R-1, 8-10	809.38	Cz	2238.2	
21R-2, 24-26	811.04	Cx	2542.1	0.0688
21R-2, 24-26	811.04	Cy	2576.4	
21R-2, 24-26	811.04	Cz	2403.8	
21R-3, 8-10	812.38	Cx	2352.4	0.0310
21R-3, 8-10	812.38	Cy	2360.8	
21R-3, 8-10	812.38	Cz	2288.5	
21R-4, 119-121	814.99	Cx	2307.1	0.0341
21R-4, 119-121	814.99	Cy	2317.2	
21R-4, 119-121	814.99	Cz	2239.1	
21R-5, 124-126	816.54	Cx	2435.1	0.0557
21R-5, 124-126	816.54	Cy	2379.5	
21R-5, 124-126	816.54	Cz	2303.0	
21R-6, 3-5	816.83	Cx	2360.0	0.0534
21R-6, 3-5	816.83	Cy	2350.5	
21R-6, 3-5	816.83	Cz	2236.3	
22R-1, 146-148	820.46	Cx	2382.7	0.0511
22R-1, 146-148	820.46	Cy	2425.1	
22R-1, 146-148	820.46	Cz	2304.0	
22R-2, 26-28	820.76	Cx	2390.0	0.0452
22R-2, 26-28	820.76	Cy	2406.3	
22R-2, 26-28	820.76	Cz	2299.5	
22R-3, 20-22	822.20	Cx	2427.4	0.0536
22R-3, 20-22	822.20	Cy	2477.7	
22R-3, 20-22	822.20	Cz	2348.0	
22R-4, 78-80	824.28	Cx	2417.8	0.0348
22R-4, 78-80	824.28	Cy	2434.3	
22R-4, 78-80	824.28	Cz	2350.7	
22R-5, 11-13	825.11	Cx	2377.1	
22R-5, 11-13	825.11	Cy	2417.9	
22R-6, 62-64	827.12	Cx	2426.4	0.0471
22R-6, 62-64	827.12	Cy	2450.8	
22R-6, 62-64	827.12	Cz	2337.6	
23R-1, 69-71	829.29	Cx	2421.7	0.0730
23R-1, 69-71	829.29	Cy	2382.0	
23R-1, 69-71	829.29	Cz	2250.0	
23R-2, 69-71	830.79	Cx	2341.8	0.0533
23R-2, 69-71	830.79	Cy	2290.9	
23R-2, 69-71	830.79	Cz	2220.0	
23R-3, 48-50	832.08	Cx	2277.6	
23R-3, 48-50	832.08	Cy	2246.4	
23R-4, 84-86	833.94	Cx	2184.1	0.0150
23R-4, 84-86	833.94	Cy	2182.9	
23R-4, 84-86	833.94	Cz	2151.5	
23R-5, 127-129	835.87	Cy	2404.3	
23R-6, 65-67	836.75	Cy	2487.8	0.0288
23R-6, 65-67	836.75	Cz	2416.9	
23R-6, 65-67	836.75	Cx	2482.3	
24R-1, 34-36	838.54	Cx	2296.2	0.0356
24R-1, 34-36	838.54	Cy	2335.4	
24R-1, 34-36	838.54	Cz	2253.8	
24R-2, 36-38	840.06	Cx	2262.2	0.0487
24R-2, 36-38	840.06	Cy	2223.9	
24R-2, 36-38	840.06	Cz	2154.3	
25R-2, 7-9	848.51	Cx	1950.6	
31R-1, 28-30	905.38	Cx	2127.5	0.0709
31R-1, 28-30	905.38	Cz	2063.8	
31R-1, 28-30	905.38	Cy	2215.1	
32R-1, 83-85	915.53	Cx	2676.7	0.1381
32R-1, 83-85	915.53	Cz	2324.2	
32R-1, 83-85	915.53	Cy	2654.5	
33R-1, 69-71	924.99	Cx	3023.1	0.1370
33R-1, 69-71	924.99	Cz	2732.6	
33R-1, 69-71	924.99	Cy	3138.7	
33R-2, 65-67	926.41	Cy	3016.1	0.1174
33R-2, 65-67	926.41	Cz	2679.4	
33R-2, 65-67	926.41	Cx	2911.4	
33R-3, 81-83	928.07	Cx	2820.3	0.1363
33R-3, 81-83	928.07	Cz	2474.7	
33R-3, 81-83	928.07	Cy	2844.5	
34R-1, 58-60	934.48	Cx	3549.4	0.1064
34R-1, 58-60	934.48	Cz	3185.4	
34R-1, 58-60	934.48	Cy	3532.2	
34R-2, 41-43	935.81	Cx	3012.9	0.1461
34R-2, 41-43	935.81	Cz	2713.5	
34R-2, 41-43	935.81	Cy	3145.7	
34R-3, 7-9	936.45	Cx	3405.1	0.1198
34R-3, 7-9	936.45	Cz	3015.1	
34R-3, 7-9	936.45	Cy	3347.1	
35R-1, 54-56	944.04	Cx	3555.5	0.1304
35R-1, 54-56	944.04	Cz	3115.0	
35R-1, 54-56	944.04	Cy	3462.3	
35R-2, 19-21	944.96	Cx	3007.3	0.1275
35R-2, 19-21	944.96	Cz	2761.9	
35R-2, 19-21	944.96	Cy	3140.5	
36R-1, 25-27	953.35	Cx	2909.9	0.0806
36R-1, 25-27	953.35	Cy	2923.7	
36R-1, 25-27	953.35	Cz	2694.7	
36R-2, 83-85	955.38	Cx	3482.9	
36R-2, 83-85	955.38	Cy	3457.2	
36R-3, 99-101	957.04	Cz	2774.5	
36R-4, 14-16	957.69	Cx	3100.6	0.0994
36R-4, 14-16	957.69	Cy	3183.8	
36R-4, 14-16	957.69	Cz	2880.2	
37R-1, 95-97	963.65	Cy	3501.3	
37R-2, 99-101	965.19	Cy	3222.0	
37R-3, 83-85	966.53	Cx	3142.4	0.2679
37R-3, 83-85	966.53	Cy	3631.6	
37R-3, 83-85	966.53	Cz	2778.7	
37R-4, 78-80	967.95	Cx	3113.8	0.0791
37R-4, 78-80	967.95	Cy	3119.4	
37R-4, 78-80	967.95	Cz	2879.0	
38R-1, 101-103	973.41	Cx	3475.2	0.1116
38R-1, 101-103	973.41	Cy	3518.8	
38R-1, 101-103	973.41	Cz	3141.6	
38R-2, 53-55	974.43	Cx	3610.5	0.0964

Table T15 (continued).

Core, section, interval (cm)	Depth (mbsf)	Direction	Velocity (m/s)	Anisotropy
38R-2, 53-55	974.43	Cy	3766.7	
38R-2, 53-55	974.43	Cz	3419.7	
38R-3, 51-53	975.91	Cx	3587.9	0.1050
38R-3, 51-53	975.91	Cy	3633.1	
38R-3, 51-53	975.91	Cz	3265.9	
38R-4, 32-34	977.22	Cx	4349.2	0.0661
38R-4, 32-34	977.22	Cy	4304.5	
38R-4, 32-34	977.22	Cz	4069.0	
38R-5, 103-105	979.43	Cx	3755.4	0.0612
38R-5, 103-105	979.43	Cy	3784.6	
38R-5, 103-105	979.43	Cz	3558.3	
38R-6, 23-25	980.13	Cx	3322.6	0.0839
38R-6, 23-25	980.13	Cy	3273.5	
38R-6, 23-25	980.13	Cz	3052.7	
39R-1, 65-67	982.65	Cx	4115.9	0.0294
39R-1, 65-67	982.65	Cz	3996.9	
39R-1, 65-67	982.65	Cy	4044.0	
39R-2, 58-60	984.08	Cz	3319.3	0.0664
39R-2, 58-60	984.08	Cy	3474.7	
39R-2, 58-60	984.08	Cx	3548.1	
39R-3, 89-91	985.89	Cx	4245.5	0.0456
39R-3, 89-91	985.89	Cz	4071.6	
39R-3, 89-91	985.89	Cy	4262.7	
39R-5, 37-39	987.88	Cx	3321.8	
39R-5, 37-39	987.88	Cy	3355.9	
40R-1, 78-80	992.48	Cx	3164.8	0.1563
40R-1, 78-80	992.48	Cz	2872.3	
40R-1, 78-80	992.48	Cy	3362.1	
40R-2, 90-92	994.05	Cx	2632.4	0.1197
40R-2, 90-92	994.05	Cz	2369.3	
40R-2, 90-92	994.05	Cy	2675.5	
40R-3, 31-33	994.96	Cx	2929.2	0.1250
40R-3, 31-33	994.96	Cz	2640.3	
40R-3, 31-33	994.96	Cy	2997.3	
41R-1, 76-78	1002.16	Cx	2186.8	0.1288
41R-1, 76-78	1002.16	Cz	1972.6	
41R-1, 76-78	1002.16	Cy	2247.6	
41R-2, 25-27	1003.15	Cx	2527.6	0.1119
41R-2, 25-27	1003.15	Cz	2264.1	
41R-2, 25-27	1003.15	Cy	2270.0	
42R-1, 112-114	1012.22	Cx	2884.7	0.1516
42R-1, 112-114	1012.22	Cy	3058.8	
42R-1, 112-114	1012.22	Cz	2625.9	
42R-2, 117-119	1013.77	Cx	2868.2	0.1399
42R-2, 117-119	1013.77	Cz	2513.2	
42R-2, 117-119	1013.77	Cy	2899.3	
42R-3, 52-54	1014.62	Cx	2761.1	0.1482
42R-3, 52-54	1014.62	Cz	2397.6	
42R-3, 52-54	1014.62	Cy	2790.2	
43R-1, 67-69	1021.47	Cx	2171.0	
43R-1, 67-69	1021.47	Cz	1977.1	
44R-1, 53-55	1030.93	Cx	1906.7	0.0440
44R-1, 53-55	1030.93	Cz	1824.2	
44R-1, 53-55	1030.93	Cy	1896.3	
45R-1, 78-80	1040.78	Cz	2313.1	0.1987
45R-1, 78-80	1040.78	Cy	2838.7	
45R-1, 78-80	1040.78	Cx	2782.7	
45R-2, 80-82	1042.30	Cx	2536.1	0.1799
45R-2, 80-82	1042.30	Cz	2106.8	
45R-2, 80-82	1042.30	Cy	2517.5	
45R-3, 3-5	1042.73	Cx	2132.2	0.1218
45R-3, 3-5	1042.73	Cz	1945.7	
45R-3, 3-5	1042.73	Cy	2200.5	
46R-1, 85-87	1050.45	Cx	2592.5	0.2048
46R-1, 85-87	1050.45	Cz	2162.6	
46R-1, 85-87	1050.45	Cy	2669.4	
46R-2, 40-42	1051.40	Cx	2719.0	0.1637
46R-2, 40-42	1051.40	Cz	2430.5	
46R-2, 40-42	1051.40	Cy	2868.1	
47R-1, 62-64	1059.82	Cx	2156.3	0.1360
47R-1, 62-64	1059.82	Cz	1953.4	
47R-1, 62-64	1059.82	Cy	2241.4	
48R-1, 46-48	1069.26	Cx	2496.7	0.1892
48R-1, 46-48	1069.26	Cz	2055.3	
48R-1, 46-48	1069.26	Cy	2445.3	
48R-2, 8-10	1070.38	Cx	2068.3	0.1042
48R-2, 8-10	1070.38	Cz	1910.3	
48R-2, 8-10	1070.38	Cy	2122.3	
50R-1, 84-86	1089.04	Cx	2325.8	
50R-2, 67-69	1090.37	Cx	2020.0	0.1178
50R-2, 67-69	1090.37	Cy	2017.0	
50R-2, 67-69	1090.37	Cz	1791.1	
51R-2, 49-51	1099.89	Cx	3172.5	
51R-2, 49-51	1099.89	Cy	3341.8	
52R-1, 48-49	1107.98	Mx	3226.1	
52R-3, 78-79	1111.28	Mx	3168.4	
53R-1, 77-79	1117.97	Cx	3836.6	
53R-1, 77-79	1117.97	Cy	3839.2	
54R-1, 88-90	1127.68	Cx	3763.4	0.0502
54R-1, 88-90	1127.68	Cz	3627.8	
54R-1, 88-90	1127.68	Cy	3815.2	
54R-5, 36-38	1132.49	Mx	5417.5	
55R-3, 131-133	1140.45	Mx	4768.3	
56R-3, 18-20	1149.11	Mx	5232.5	
57R-1, 131-133	1152.31	Mx	5553.1	
58R-3, 58-60	1159.19	Mx	5254.7	
59R-1, 60-62	1161.20	Mx	5824.7	
59R-1, 60-62	1161.20	_x	5923.4	
59R-1, 113-115	1161.73	_x	5662.2	
59R-2, 65-67	1162.70	_x	5643.5	
60R-1, 136-138	1167.86	Mx	5253.1	
60R-1, 144-146	1167.94	_x	5736.9	
60R-2, 9-11	1168.07	_x	4728.6	
61R-1, 8-10	1176.18	_x	5604.6	
61R-1, 74-76	1176.84	_x	5603.9	
61R-1, 76-78	1176.86	_x	5064.7	
61R-1, 134-136	1177.44	Mx	5851.5	
61R-2, 7-9	1177.55	_x	5769.5	
61R-2, 52-54	1178.00	_x	4921.4	
62R-1, 63-65	1181.63	Mx	5868.0	
62R-1, 70-72	1181.70	_x	5910.7	
62R-1, 115-117	1182.15	_x	5289.7	
62R-2, 100-102	1183.40	_x	5343.6	
62R-2, 145-147	1183.85	_x	5426.6	
62R-3, 35-37	1184.25	_x	5500.6	
63R-1, 94-96	1186.74	Mx	5485.1	
63R-1, 115-117	1186.95	_x	5025.7	
63R-1, 125-127	1187.05	_x	5648.2	
63R-2, 26-28	1187.46	_x	5112.5	
64R-1, 85-87	1191.45	_x	5175.3	
64R-2, 75-77	1192.75	_x	5942.0	
64R-2, 81-83	1192.81	Mx	5809.1	
64R-2, 130-132	1193.30	_x	5493.9	
65R-1, 15-17	1195.55	_x	5596.8	
65R-1, 40-42	1195.80	_x	5754.0	
65R-1, 45-47	1195.85	Mx	5531.8	
65R-1, 90-92	1196.30	_x	5704.0	
65R-1, 120-122	1196.60	_x	5793.8	
65R-2, 39-41	1197.19	_x	5498.4	
65R-2, 120-122	1198.00	_x	5625.4	
65R-3, 26-28	1198.42	_x	5480.4	
65R-3, 90-92	1199.06	_x	5487.1	
66R-1, 46-48	1200.56	_x	5679.4	
66R-1, 133-135	1201.43	_x	4626.8	
66R-2, 10-12	1201.60	_x	5728.4	
66R-2, 86-88	1202.36	_x	5285.2	
66R-2, 140-142	1202.90	_x	5699.6	
66R-3, 10-12	1203.04	_x	5654.3	

Table T15 (continued).

Core, section, interval (cm)	Depth (mbsf)	Direction	Velocity (m/s)	Anisotropy
66R-3, 12-14	1203.06	Mx	5845.1	
66R-3, 54-56	1203.48	_x	5585.3	
67R-1, 2-4	1204.92	Mx	5488.8	
67R-1, 15-17	1205.05	_x	5265.0	
67R-1, 18-20	1205.08	_x	5841.4	
67R-1, 50-52	1205.40	_x	5478.9	
67R-1, 92-94	1205.82	_x	5763.0	
67R-1, 137-139	1206.27	_x	5438.9	
67R-2, 8-10	1206.43	_x	5747.7	
67R-2, 58-60	1206.93	_x	5696.4	
67R-2, 98-100	1207.33	_x	5324.5	
68R-1, 13-15	1209.83	_x	5850.0	
68R-1, 30-32	1210.00	_x	5487.1	
68R-1, 40-42	1210.10	Mx	5159.6	

Notes: x = into the core, y = across the core, z = along the core. _ = uncut split core, C = cut sample, M = minicore. This table is also available in **ASCII format.**

Table T16. Thermal conductivity values, Hole 1183A.

Core, section, interval (cm)	Depth (mbsf)	Thermal conductivity (W/[m·K])
192-1183A-		
3R-2, 75-77	339.85	1.195
4R-4, 75-77	352.45	1.130
5R-4, 75-77	362.05	1.015
6R-3, 75-77	370.05	0.977
7R-2, 75-77	378.15	1.244
8R-3, 75-77	389.25	1.028
9R-2, 54-56	397.14	1.155
10R-4, 75-77	409.95	0.943
11R-4, 75-77	419.55	1.041
12R-4, 75-77	429.15	0.888
13R-3, 75-77	437.25	1.158
14R-1, 75-77	443.85	1.248
15R-3, 15-17	755.15	1.654
17R-1, 77-79	771.57	1.587
18R-3, 23-25	783.73	1.580
19R-1, 140-142	791.50	1.654
20R-2, 82-84	802.02	1.625
21R-4, 93-95	814.73	1.485
22R-3, 1-3	822.01	1.614
23R-3, 30-32	831.90	1.486
24R-2, 82-84	840.52	1.704
30R-1, 55-57	896.05	1.760
32R-1, 43-45	915.13	1.569
33R-1, 77-79	925.07	1.336
33R-3, 65-67	927.91	2.252
35R-1, 104-106	944.54	1.791
36R-2, 115-117	955.70	2.358
37R-2, 8-10	964.28	2.557
38R-1, 112-114	973.52	2.480
39R-1, 74-76	982.74	2.898
40R-2, 48-50	993.63	2.304
41R-1, 117-119	1002.57	2.432
42R-2, 55-57	1013.15	1.926
43R-1, 56-58	1021.36	1.877
45R-2, 27-29	1041.77	2.047
46R-1, 55-57	1050.15	2.217
47R-1, 128-130	1060.48	2.014
48R-1, 118-120	1069.98	2.044
54R-3, 111-113	1130.28	2.544
54R-5, 54-56	1132.67	1.670
55R-1, 50-52	1137.00	1.692
56R-2, 8-10	1147.53	1.729
57R-1, 83-85	1151.83	1.995
58R-2, 30-32	1157.52	1.711
59R-1, 56-58	1161.16	1.947
59R-2, 64-66	1162.69	1.856
60R-1, 144-146	1167.94	1.765
60R-2, 10-12	1168.10	1.757
61R-1, 76-78	1176.90	1.784
61R-2, 7-9	1177.60	1.798
62R-1, 60-62	1181.60	1.944
62R-3, 33-35	1184.20	1.833
63R-1, 43-45	1186.20	1.652
64R-2, 75-77	1192.80	2.004
65R-1, 90-92	1196.30	1.835
65R-2, 68-70	1197.50	1.792
65R-3, 25-27	1198.40	1.828
66R-1, 98-100	1201.10	1.446
66R-2, 86-88	1202.40	1.786
66R-3, 54-56	1203.50	1.754
67R-1, 21-23	1205.10	1.729
67R-3, 113-115	1209.00	1.829
68R-1, 30-32	1210.00	1.746

Note: This table is also available in **ASCII format.**

CHAPTER NOTE*

N1. 5 November 2001—The URL listed in the Michael, P.J., 1999, reference has changed since it was cited by the author. The article can be found at <http://g-cubed.org/gc2000/1999GC000025/fs1999GC000025.html>.

*Dates reflect file corrections or revisions.